Magnetic Excitations in Single and Coupled Atoms on Surfaces: From the Kondo Effect to Yu-Shiba-Rusinov States

Dissertation

zur Erlangung des naturwissenschaftlichen Doktorgrades
der Julius-Maximilians-Universität Würzburg

vorgelegt von Felix Friedrich
aus Stuttgart

Würzburg 2022

Eingereicht am: 23.11.2022
bei der Fakultät für Physik und Astronomie

1. Gutachter: Prof. Dr. Matthias Bode
2. Gutachter: Prof. Dr. Friedrich Reinert
3. Gutachter: Prof. Dr. Richard Berndt
der Dissertation

Vorsitzender: Prof. Dr. Matthias Kadler

1. Prüfer: Prof. Dr. Matthias Bode
2. Prüfer: Prof. Dr. Friedrich Reinert
3. Prüfer: Prof. Dr. Giorgio Sangiovanni
4. Prüfer: Prof. Dr. Richard Berndt
im Promotionskolloquium

Tag des Promotionskolloquiums: 16.06.2023

Doktorurkunde ausgehändigt am:

ABSTRACT

Magnetic systems underlie the physics of quantum mechanics when reaching the limit of few or even single atoms. This behavior limits the minimum size of magnetic bits in data storage devices as spontaneous switching of the magnetization leads to the loss of information. On the other hand, exactly these quantum mechanic properties allow to use such systems in quantum computers. Proposals to realize qubits involve the spin states of single atoms as well as topologically protected Majorana zero modes, that emerge in coupled systems of magnetic atoms in proximity to a superconductor. In order to implement and control the proposed applications, a detailed understanding of atomic spins and their interaction with the environment is required.

In this thesis, two different systems of magnetic adatoms coupled to metallic and superconducting surfaces are studied by means of scanning tunneling microscopy (STM) and spectroscopy: Co atoms on the clean Cu(111) were among the first systems exhibiting signatures of the Kondo effect in an individual atom. Yet, a recent theoretical work proposed an alternative interpretation of these early experimental results, involving a newly described many-body state. Spin-averaged and -polarized experiments in high magnetic fields presented in this thesis confirm effects beyond the Kondo effect that determine the physics in these Co atoms and suggest a potentially even richer phenomenology than proposed by theory.

The second studied system are single and coupled Fe atoms on the superconducting Nb(110) surface. Magnetic impurities on superconducting surfaces locally induce Yu-Shiba-Rusinov (YSR) states inside the superconducting gap due to their pair breaking potential. Coupled systems of such impurities exhibit YSR bands and, if the bands cross the Fermi level such that the band structure is inverted, host Majorana zero modes. Using the example of Fe atoms on Nb(110), the YSR states' dependence on the adatom−substrate interaction as well as the interatomic YSR state coupling is investigated. In the presence of oxygen on the Nb surface, the adatom−substrate interaction is shown to be heavily modified and the YSR states are found to undergo a quantum phase transition, which can be directly linked to a modified Kondo screening.

STM tips functionalized with CO molecules allow to resolve self-assembled one-dimensional chains of Fe atoms on the clean Nb(110) surface to study the YSR states' coupling. Mapping out the states' wave functions reveals their symmetry, which is shown to alter as a function of the states' energy and number of atoms in the chain. These experimental results are reproduced in a simple tight-binding model, demonstrating a straightforward possibility to describe also more complex YSR systems toward engineered, potentially topologically non-trivial states.

ZUSAMMENFASSUNG

Magnetische Systeme unterliegen im Limit von wenigen Atomen den Gesetzen der Quantenmechanik. Diese Tatsache beschränkt die minimale Größe magnetischer Bits in der Datenspeicherung, da spontane Änderungen der Magnetisierung zu Datenverlust führen. Gleichzeitig ist es genau jenes quantenmechanische Verhalten, welches es erlaubt, diese Systeme in Quantencomputern zu verwenden. Vorschläge, die dafür notwendigen Qubits zu realisieren, umfassen die Spinzustände einzelner Atome sowie topologisch geschützte Majorana-Nullmoden, welche in Systemen gekoppelter magnetischer Atome in Supraleitern auftreten. Für die Umsetzung dieser Anwendungen sind detaillierte Kenntnisse über die Wechselwirkung atomarer Spins mit ihrer Umgebung nötig.

In dieser Arbeit werden zwei verschiedene solcher Systeme aus magnetischen Adatomen auf Oberflächen mit der Methode der Rastertunnelmikroskopie (RTM) und -spektroskopie untersucht: Lange galten einzelne Co-Atome auf der Cu(111)-Oberfläche als prototypisches Modell für den Kondo-Effekt in Einzelatomen. Dies wurde jedoch vor Kurzem durch eine Theoriearbeit infrage gestellt, welche die bisherigen experimentellen Daten durch das Auftreten eines neu beschriebenen Vielteilchen-Zustands erklärt. In dieser Arbeit werden neue, spingemittelte und -aufgelöste Messungen in hohen Magnetfeldern präsentiert, welche das Auftreten von Effekten jenseits des Kondo-Effekts in diesem System bestätigen.

Im zweiten Teil der Arbeit werden einzelne und gekoppelte Fe-Atome auf der supraleitenden Nb(110)-Oberfläche untersucht. Magnetische Defekte erzeugen in Supraleitern aufgrund ihres Paarbrechungspotentials Yu-Shiba-Rusinov(YSR)-Zustände innerhalb der supraleitenden Bandlücke. Die Kopplung dieser Zustände resultiert in YSR-Bändern, und kann durch Inversion der Bandlücke zum Auftreten von Majorana-Nullmoden führen. Am Beispiel von Fe-Atomen auf Nb(110) wird hier der Einfluss der Adatom–Oberflächen-Wechselwirkung auf die YSR-Zustände sowie deren interatomare Kopplung untersucht. Es wird gezeigt, dass Sauerstoff die Wechselwirkung stark beeinflusst und die atomaren YSR-Zustände infolge dessen einen Quantenphasenübergang durchlaufen. Dieser kann direkt auf eine veränderte Kondo-Abschirmung zurückgeführt werden.

Weiter werden mittels mit CO-Molekülen funktionalisierter RTM-Spitzen eindimensionale Ketten aus Fe-Atomen auf der sauberen Nb(110)-Oberfläche identifiziert, anhand derer die Kopplung der YSR-Zustände untersucht wird. Ortsaufgelöste Messungen der zugehörigen Wellenfunktionen decken die Symmetrie dieser Zustände auf, welche ein alternierendes Verhalten zwischen Ketten mit gerader und ungerader Atomzahl aufweist. Diese experimentellen Ergebnisse werden anschließend in einem *tight-binding*-Modell, welches auch auf komplexere Systeme angewandt werden kann, beschrieben.

CONTENTS

Chapter 1

1 INTRODUCTION

In 1934, W. J. de Haas *et al.* detected a logarithmic increase of the resistance of gold samples below a temperature of 4 K [1], contrasting the up to this date universally observed monotonic decrease of the resistivity of any metal with decreasing temperature. Subsequent experiments with different metallic samples, that were in contrast to the first gold samples purposefully doped with magnetic impurities, established the latter as the cause for the observed resistance increase [2]. However, only 30 years later, in 1964, J. Kondo was able to theoretically explain these observations by an enhanced scattering of the conduction electrons with the impurities due to an antiferromagnetic exchange coupling between both [3]. This exchange coupling was later shown to cause an effective screening of the impurities' spins by the conduction electrons and to give rise to a new state at the Fermi level, leading to the increased scattering already described by J. Kondo [4–6]. The described effect is today known as the Kondo effect and constitutes an important example of magnetic atoms interacting with the electronic bath of a metal.

Looking back, these experiments define the beginning of still ongoing efforts at understanding the interactions of spins with their environment and the resulting consequences on the behavior of magnetic atoms in different host materials. Research investigating e.g. excitations of the atoms' spins or the spin lifetime were further motivated by potential applications of these systems: The minimal size of magnetic bits for data storage is limited by thermal excitations of the bit's magnetization, that becomes increasingly stronger with decreasing physical size of the bit. However, single Ho atoms on MgO were shown to exhibit finite lifetimes of their spin state even at zero magnetic field, pushing the limit for the bit size down to the atomic level [7]. And while magnetic storage bits have today been mostly replaced by solid-state drives due to their longer durability and higher speed, atomic spin systems made their path into a new field of computing. In quantum computers, the non-degenerate spin levels of individual magnetic systems can be used as qubits, and basic qubit operations were already demonstrated in e.g. nitrogen-vacancy centers in diamond [8, 9], single phosphorus atoms in silicon [10–13], magnetic molecules in electromigrated junctions [14–16], and magnetic atoms and molecules on insulating surfaces [17–19].

Just like the various systems investigated over the years, experimental methods and techniques to study them similarly cover a wide range of fields in physics: Tunneling measurements uncover the density of states of magnetic atoms and spins embedded into insulators in tunnel junctions [20–22] and coupled to the metallic leads of electromigrated junctions [23]. SQUID (superconducting quantum interference device) measurements [24–26] and x-ray magnetic circular dichroism (XMCD) [27, 28] directly probe the magnetization of small magnetic clusters and even single atoms, and optical fluorescence spectroscopy [29] and transport measurements [30] were able to indirectly detect changes of the atomic spin states. One drawback of these techniques when investigating atomic systems is that many of them can only probe ensembles of dilute magnetic atoms or molecules rather than individual ones, or cannot control the exact environment of the spins. Scanning tunneling microscopy (STM, also used for "scanning tunneling microscope") in contrast is able to produce real space images at the atomic scale and to probe the electronic structure of single atoms [31, 32]. Scanning tunneling spectroscopy (STS) experiments measure the differential tunnel conductance between the STM tip and the sample revealing the local density of states, and signatures consistent with the Kondo effect in e.g. single Co atoms on various surfaces were detected [33–37]. Other measurements were able to identify excitations between different spin states of individual atoms and molecules [18, 38–42].
The ability of the STM to move atoms across the surface based on the forces acting between the STM tip and sample [43, 44] has further opened possibilities to study interatomic spin coupling in engineered assemblies of magnetic adatoms [45–47]. The manipulation of atoms also plays a crucial role in a very recently proposed new application of magnetic adatom systems. When coupled to a superconducting host, the magnetic moments associated with spins act as a pair-breaking potential and give rise to so-called Yu-Shiba-Rusinov (YSR) states [48–51], which were for the first time observed on individual Mn and Gd atoms atop of a Nb(110) surface [52]. Coupling these states in chains of magnetic atoms on a superconducting surface is predicted to result in the formation of a topological superconductor [53–60]. Edge states in these systems, so-called Majorana zero modes (MZMs) are topologically protected and might therefore allow for fault-tolerant quantum computing, overcoming the limitation of conventional quantum computers that require immense efforts to correct computation errors [61, 62]. Such atomically engineered structures revealing signatures of MZMs were only very recently realized in Mn atom chains on Nb(110) [63].

The experimental work presented in this thesis is divided into two parts and aims at contributing to a better or even revised understanding of this large field of atomic spin systems interacting with their environment: The first part of this thesis concerns magnetic atoms on normal metal surfaces, more specifically the system of a single Co atom on the Cu(111) surface. Co atoms on all noble metal

(111) surfaces were among the first systems that showed signatures in agreement with the Kondo effect in STM experiments [33–36]. However, a recent theoretical work suggests that the observed signatures rather originate from spin excitations in the system, that overlap with a newly proposed many-body state formed by an attractive interaction of those spin excitations and the conduction electrons [64]. Motivated by this controversy, the experiments presented in this part of the thesis intend to shine light on the underlying physics of this system.
The second part of this work is dedicated to the investigation of magnetic atoms on a superconducting surface and of the concomitant YSR states. Although a variety of coupled spin systems has shown signatures of MZMs [63, 65–68], recent works also demonstrated that care must be taken to distinguish them from other, topologically trivial, states [69]. Therefore, in order to be able to both understand and deterministically engineer these complex systems, an understanding of the underlying building blocks, i.e. the interaction of the adatoms with the superconducting surface as well as the interatomic coupling, is crucial. These properties will be investigated for single and coupled Fe atoms on the Nb(110) surface, providing the basis for more complex structures.

OUTLINE OF THIS THESIS

At the beginning of Part I, chapter 2 reviews the basics of magnetism in single atoms in an anisotropic environment. The fundamental properties of related magnetic states and excitations relevant for the first part of this thesis are introduced and evaluated in light of STM/STS experiments.

In chapter 3, the principles of STM are introduced. In addition, I will specifically discuss inelastic tunneling spectroscopy as well as spin-polarized STS, techniques that both are important throughout the presented work. In the final part of that chapter, the experimental setup used for all presented measurements will be introduced.

The experimental results of the first part of this thesis will be presented in chapter 4. After reviewing the current state of experimental and theoretical work on the Co/Cu(111) system, magnetic field-dependent STS data on single Co atoms will be presented and discussed. Further, spin-polarized STS will be employed to assess the spin character of the observed spectroscopic features.

Chapter 5 builds the relevant physical background for Part II of this thesis. The main ideas of superconductivity will be reviewed within the Bardeen-Cooper-Schrieffer (BCS) and Ginzburg-Landau theory. Based on these results, I will present the origin of Caroli-de Gennes-Matricon (CdGM) states in vortices and of YSR states in the proximity of spin impurities on superconductors, and discuss the appearance of MZMs in superconducting hybrid systems.

Chapter 6 gives a brief overview over the properties of the Nb(110) surface, which is the platform for the experiments presented in the subsequent chapters.

The properties of the Nb(110) surface are further studied in chapter 7 by investigating vortices on the surface of the type II superconductor. I will show that the emerging in-gap CdGM states lead to an apparent anisotropic shape of the vortices, reflecting the symmetry of the 2D Fermi surface of Nb(110).

In chapter 8, the adatom−surface interaction of single Fe atoms with the Nb(110) surface will be studied. Strongly adsorption position-dependent YSR states are revealed and can be consistently matched to Kondo resonances appearing in the normal state of the surface, demonstrating the close relation between both effects.

The coupling of the Fe atoms is investigated in chapter 9. The hybridized YSR states in short self-assembled chains and the corresponding wave functions are analyzed, and will be rationalized in a simple tight-binding model.

Finally, the results obtained in this thesis are summarized in chapter 10 and a brief outlook is presented.

Part I

THE KONDO EFFECT AND SPIN EXCITATIONS IN MAGNETIC ATOMS ON A NORMAL METAL SURFACE

Chapter 2

2 INTERACTIONS OF MAGNETIC ATOMS WITH NORMAL METALS

This chapter provides a general background on magnetic states and excitations of single atoms on normal metal surfaces relevant for the experimental chapters 4 and 8. The physical effects that are unique to magnetic adatoms on superconducting surfaces, which is the main topic of Part II of this thesis, will be introduced in chapter 5.

In this chapter, I will first briefly review the origin of magnetism in single atoms and the influence of the presence of a metallic surface on the atoms' magnetic moment in section 2.1. Afterwards, I will introduce a formalism that allows to describe spin excitations in single atoms in section 2.2, followed by a discussion of the Kondo effect in section 2.3. Both effects play a major role in the results presented in chapter 4. I will further describe their experimental signatures in STM measurements in the respective sections, while the principles and technique of scanning tunneling microscopy will be introduced in chapter 3.

2.1 MAGNETISM IN SINGLE ATOMS

The magnetic moment of an atom in vacuum is determined by the electronic occupation of the atomic orbitals according to Hund's rules [70]. For the transition metal atoms Fe, Co, and Ni, that were studied in different environments throughout this work, the electronic configuration given in Figure 2.1 exhibits only partially filled d orbitals, that carry the angular momentum of the atoms, separated into spin and orbital moments S and L specified in Figure 2.1. The effect of spin-orbit interaction couples both L and S to a total angular momentum J, which leads to a total magnetic moment of $-g_J \mu_B J$, with g_J being the Landé-factor and μ_B the Bohr magneton. For atoms in the gas phase, the $2J+1$ possible orientations J_z of this magnetic moment relative to a chosen quantization axis z are fully degenerate in the absence of an external magnetic field.

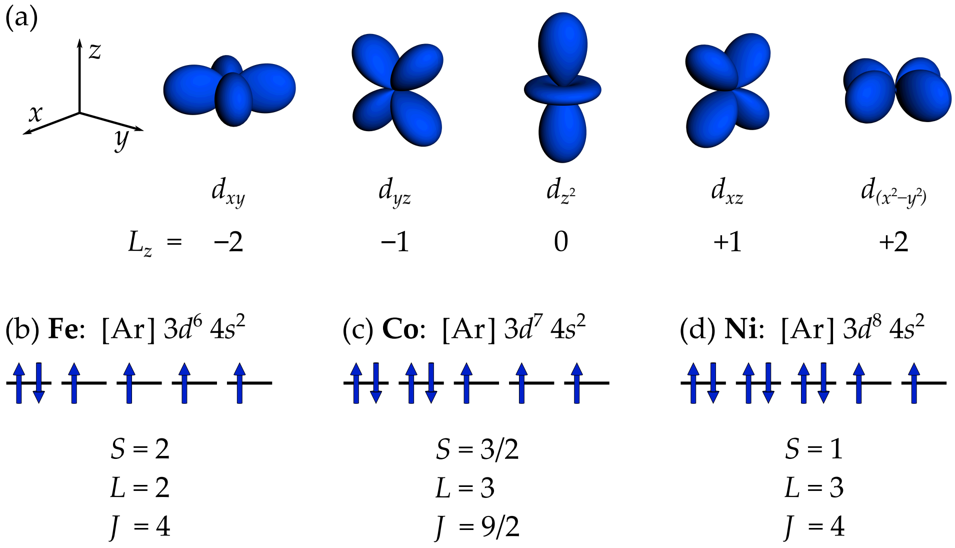

Figure 2.1: (a) Wave functions of the five $3d$ orbitals and the corresponding projection of the orbital momentum onto the z-axis. (b)-(d) Electronic configuration and sketched occupation of the $3d$ orbitals for Fe, Co and Ni in the gas phase, respectively, including their spin, orbital and total angular momentum.

This situation changes when the atoms are placed into an anisotropic environment. In e.g. a crystal lattice, the orbital motion of the atom's electrons interferes with the electrons of the surrounding atoms via an electrostatic field. Due to the broken rotational symmetry of both the environment and the atomic orbitals (cf. Figure 2.1), the resulting energy shift varies for different values of L_z. Spin-orbit coupling translates this effect to the spin moment of the atom, thus finally lifting the degeneracy of states with different J_z [71]. The same effect occurs for magnetic atoms placed onto a surface or within the ligands of a molecule, where also the translation invariance is broken [72, 73]. Additional effects arise when the magnetic adatoms are coupled to metallic substrates, as this can alter the number of electrons in the adatom and hence the adatom's total magnetic moment [73] and often leads to a reduction of the orbital momentum for $3d$ atoms [74].

The discussed influences on the atomic magnetic moment can be described in an effective spin model, that will be introduced in the following section. For this purpose, all changes to the total angular momentum of the atom when placed into a metallic environment are absorbed in an effective spin S_{eff} with a multiplicity of $2S_{\text{eff}} + 1$. In the discussions in the following sections, the subscript "eff" will be dropped for simplicity, as the "effective" spin behaves like a "real" spin, i.e. a quantum mechanical angular momentum, in both theory and experiment. The interaction of the electrostatic field of the surrounding material is captured by the so-called crystal field, which will be introduced in the following.

2.2 SPIN EXCITATIONS

Experimentally, the coupling between magnetic adatoms with their environment can be investigated by exciting the atomic spin $\vec{S}$ into states at higher energy and measuring the excitation energy as a function of an applied external magnetic field $\mu_0\vec{H}$. The Hamiltonian introduced in the following can in turn be mapped to the experimentally obtained values, providing insight into the magnitude of the atom's magnetic moment as well as the strength and symmetry of the magnetic anisotropy induced by the substrate.
The effect of the external magnetic field is described by the Zeeman Hamiltonian and energetically splits the atom's spin states according to

$$\mathcal{H}_{\mathrm{Z}} = -\mu_0\vec{\mu}\cdot\vec{H} = g\mu_0\mu_{\mathrm{B}}\vec{S}\cdot\vec{H}. \tag{2.1}$$

Here, the Landé-factor g might significantly differ from 2 due to the combination of orbital and spin angular momentum in the effective spin model as well as interactions of the effective spin with itinerant quasiparticles of the environment [75].
The effect of broken inversion symmetry on the spin is described in terms of the crystal field, acting on the spin as given by the crystal field Hamiltonian

$$\mathcal{H}_{\mathrm{CF}} = \vec{S}\cdot\boldsymbol{D}\cdot\vec{S}, \tag{2.2}$$

where $\boldsymbol{D}$ is a real-valued, symmetric tensor [76]. By choosing the correct coordinate system, $\boldsymbol{D}$ becomes diagonal with eigenvalues D_{xx}, D_{yy} and D_{zz}. In this case, Equation (2.2) can be rewritten as [76]

$$\mathcal{H}_{\mathrm{CF}} = DS_z^2 + E\left(S_x^2 - S_y^2\right), \tag{2.3}$$

with the uniaxial anisotropy $D = D_{zz} - \frac{1}{2}(D_{xx} + D_{yy})$ and the transverse anisotropy $E = \frac{1}{2}(D_{xx} - D_{yy})$. From these definitions it is clear that for an axial system, i.e. $D_{xx} = D_{yy}$, E vanishes and the eigenstates of the system are described by the pure spin states of the free atom. For $E \neq 0$, the new eigenstates are linear combinations of the free atom's spin states at energies determined by the eigenvalues of the full Hamiltonian describing the adatom system:

$$\mathcal{H} = \mathcal{H}_{\mathrm{Z}} + \mathcal{H}_{\mathrm{CF}} = g\mu_0\mu_{\mathrm{B}}\vec{S}\cdot\vec{H} + DS_z^2 + E\left(S_x^2 - S_y^2\right). \tag{2.4}$$

Exemplarily, the eigenenergies and eigenenstates as a function of a magnetic field applied along the z-axis are displayed in Table 2.1 and Figure 2.2 as obtained for a $S = 1$ system with $D, E = 0$ (panel (a)), $D = -1$ meV, $E = 0$ (panel (b)), and $D = -1$ meV, $E = 0.3$ meV (panel (c)). The values chosen for D and E are similar

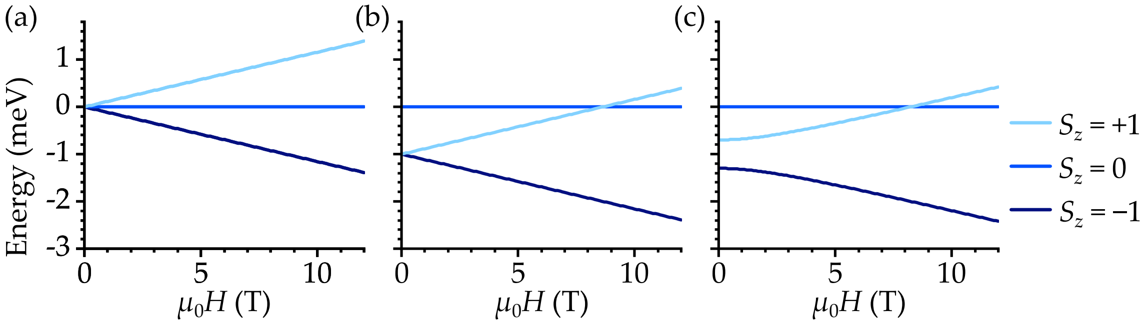

Figure 2.2: Splitting of the spin levels of a $S = 1$ system in an external magnetic field of up to 12 T applied along the z-axis; g was chosen to be 2. (a) $D, E = 0$, (b) $D = -1$ meV, $E = 0$, and (c) $D = -1$ meV, $E = 0.3$ meV. While D shifts levels with the same absolute spin value $|S_z|$ (cf. panel (b)), E leads to a mixing of spin states and lifts their zero-field degeneracy (panel (c)). In this case the spin expectation value indicated in the legend is only valid at high fields, where E is small compared to the Zeeman energy, such that the mixing of states becomes negligible.

Table 2.1: Composition of the eigenstates φ of the $S = 1$ system in Figure 2.2(c) at $\mu_0 H = 0$. Values present the sign and squared amplitude of the projection of the eigenstates onto the pure spin states. States are listed by their energy in ascending order.

	$S_z = -1$	$S_z = 0$	$S_z = +1$
φ_0	0.5	0	−0.5
φ_1	0.5	0	0.5
φ_2	0	1	0

to experimentally obtained values for different adatom–substrate systems [42, 77, 78]. As expected for the free spin in panel (a), the magnetic field causes a Zeeman splitting proportional to the value of S_z. For a finite value of D as presented in panel (b), an additional zero-field splitting of size DS_z^2 between states with different $|S_z|$ is induced. For $E \neq 0$, the axial symmetry of the system is broken and an additional splitting of the energetically two lowest states as well as a deviation from the linear Zeeman shift is observed in panel (c). The latter is caused by the earlier mentioned mixing of the pure spin states, which in the presented example leads to a linear combination of the $S_z = +1$ and $S_z = -1$ state with equal weight at $\mu_0 H = 0$ (see also Table 2.1). Thus, at $\mu_0 H = 0$, the expectation value $\langle S_z \rangle$ of both states is zero, such that the Zeeman field does induce an energy shift. Noteworthy, independent on the magnitude of E, the mixing of the free atom's spin states is restricted exclusively to states with $\Delta S_z = \pm 2$ [76].

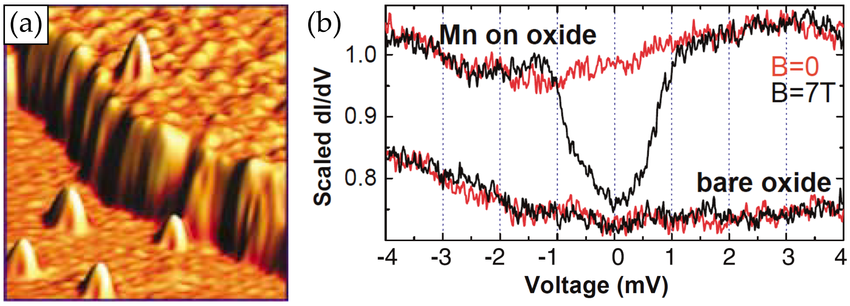

Figure 2.3: (a) Topography (scan range: $20 \times 10\ \mathrm{nm}^2$) and (b) spectroscopy of a single Mn atom adsorbed onto a layer of aluminum oxide on NiAl(110). At a field of 7 T, bias voltage-symmetric steps indicate the excitation of the Mn atom's spin. *From Ref. [38]. Reprinted with permission from AAAS.*

The presented model now allows to describe excitations of an atomic spin from an initial state φ_i to an excited final state φ_f. In an STM experiment, spin excitations conventionally occur by the inelastic tunneling of electrons [79].[1] Considering energy conservation, the excitation can only occur if $eU_\mathrm{bias} \geq (E(\varphi_\mathrm{f}) - E(\varphi_\mathrm{i}))$, and leads to a step in the $\mathrm{d}I/\mathrm{d}U$ signal of an inelastic scanning tunneling spectroscopy (IETS) experiment as will be shown in chapter 3. Due to the conservation of angular momentum, only excitations with $\Delta S_z = 0, \pm 1$ are allowed,[2] as the change in angular momentum of the atom needs to be compensated by a flip of the electron's spin. Experimentally, the excitation of an individual atom's spin was first observed by A. Heinrich *et al.* in a Mn atom on a layer of aluminum oxide on NiAl(110) [38]. The results are displayed in Figure 2.3. Due to the low anisotropy of the system, the steps in the $\mathrm{d}I/\mathrm{d}U$ signal indicating the excitation of the Mn atom's spin only appear at finite magnetic fields as can be seen from panel (b) of Figure 2.3. In contrast to this, later measurements by C. F. Hirjibehedin *et al.* on Fe/$\mathrm{Cu_2N}$ reproduced in Figure 2.4 revealed multiple steps already at zero field, indicative of a large anisotropy of the system and excitations to various energetically higher spin states, which were well explained by the effective spin model [77]. The height of the differential conductance steps reflects the transition probability between φ_i and φ_f and is quantified by

$$|M_\mathrm{if}|^2 = \frac{1}{2}\,|\langle\varphi_\mathrm{f}|S_-|\varphi_\mathrm{i}\rangle|^2 + \frac{1}{2}\,|\langle\varphi_\mathrm{f}|S_+|\varphi_\mathrm{i}\rangle|^2 + |\langle\varphi_\mathrm{f}|S_z|\varphi_\mathrm{i}\rangle|^2, \qquad (2.5)$$

---

[1] A more recent technique to detect spin excitations in single atoms in STM is electron spin resonance, relying on the absorption of microwave photons that excite the spin. The spin change is then detected with a spin-polarized tip [39]. The extremely high energy resolution of this technique allows even the detection of excitations of the nuclear spin [80].

[2] Excitations with $\Delta S_z = 0$ can occur for finite values of the transverse anisotropy E when both ground and excited states are linear combinations of the same free atom's spin states [76].

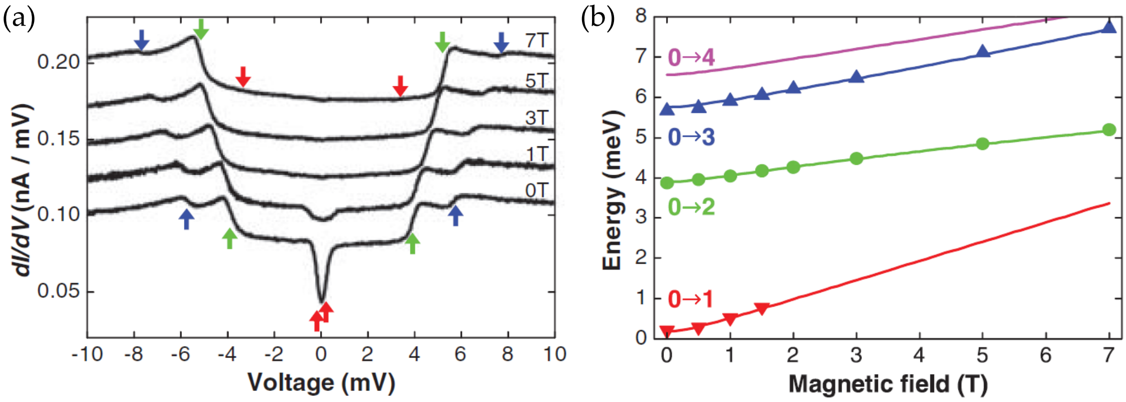

Figure 2.4: (a) Spin excitation spectra of a single Fe atom atop a layer of Cu_2N on Cu(001) at various in-plane fields. Excitations at 0 T reveal the strong magnetic anisotropy of the system. (b) Fit of the spin Hamiltonian in Equation (2.4) (lines) to the excitation energies extracted from the experiment (arrows/dots in (a)/(b)). The different excitations from the ground to the n^{th} excited state are labeled "$0 \rightarrow n$". *From Ref. [77]. Reprinted with permission from AAAS.*

where M_{if} is the tunneling matrix element as will be introduced in chapter 3, and S_+ and S_- are the spin raising and lowering operators acting on the atom's spin [77, 79].

In spin-averaged STS measurements, the resulting spectrum is symmetric with respect to zero bias. This picture changes in experiments conducted with spin-polarized tips (see also section 3.1.2), where the conservation of angular momentum leads to an asymmetry between the step heights at positive and negative bias and allows to assign a spin character to the observed spin excitations [81]. The sketch in Figure 2.5 illustrates the spin excitation process for a $S = 1/2$ adatom in an external magnetic field that fixes the ground state spin orientation at $S_z = -1/2$. The excitation of the atom's ground state to the excited $S_z = +1/2$ state requires the tunneling electrons to flip their spin in the opposite direction, i.e. from "up" to "down", to conserve the total angular momentum of the system. For a spin-averaged tip with equal density of states (DOS) for both spin channels, this process is equally likely to occur for electrons tunneling from the surface to the tip at negative bias voltage and from the tip to the surface at positive bias voltage. The conductance spectrum is therefore symmetric around zero bias as measured on a Mn atom on Cu_2N/Cu(001) and displayed in Figure 2.5(d).[3]

---

[3] Mn on Cu_2N/Cu(001) is a $S = 5/2$ system with almost vanishing anisotropy [45]. In a spin-polarized measurement, the only detectable excitation from the $S_z = -5/2$ state to the $S_z = -3/2$ state behaves equivalently to a $S = 1/2$ system.

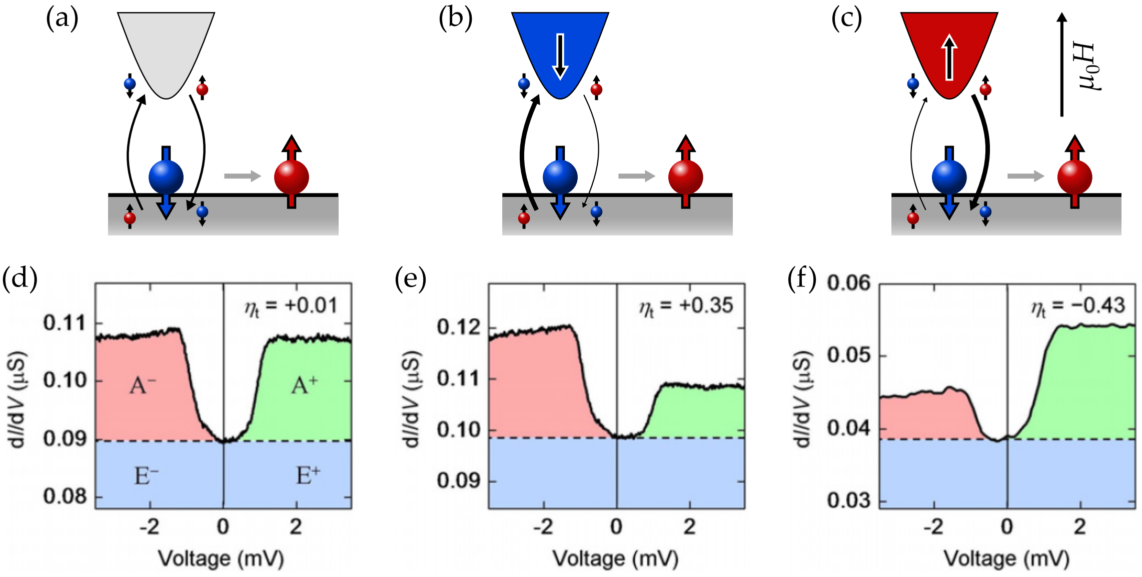

Figure 2.5: (a)-(c) Illustration of the spin excitation process of a magnetic adatom in an external magnetic field for a spin-averaged tip and spin-polarized tips oriented parallel and antiparallel to the field, respectively. (d)-(f) Corresponding spectra as measured on top of a Mn atom on a layer of Cu_2N on Cu(001). The extracted tip polarization η_t is indicated. *(d)-(f) reprinted from Ref. [81] under a Creative Commons 3.0 License (CC BY-NC-SA 3.0 [82]).*

Panels (b) and (c) in Figure 2.5 illustrate why this symmetry is broken for spin-polarized tips: Identically to the spin excitations with a spin-averaged tip, the tunneling electrons change their spin from “up” to “down” in the process. This means that for an inelastic tunneling process at negative bias, i.e from the sample to the tip, the electron spin at the tip position is “down”, while for tunneling at positive bias, i.e. from tip to sample, the electron spin must be “up” at the tip position to be able to excite the adatom’s spin. Therefore, if the tip polarization in the relevant energy range is parallel to the adatom’s ground state spin orientation (“down”) (panel (b)), inelastic tunneling can only occur at negative bias, as there are no “spin-up” electrons available that could tunnel from the tip to the surface. In reality, the spin polarization is never 100 %, such that the spin-polarized IETS signal exhibits a large step at negative bias, but also a reduced step at positive bias (cf. panel (e)). The opposite is true for tips polarized antiparallel to the adatom’s ground state (panel (c)). Here, electrons with spin “down” that would be the result of spin excitations at negative bias, can not enter the tip DOS, resulting in a reduced spectral weight of the IETS step at $U < 0$, as presented in panel (f).

It is important to note that these measurements do not reflect spin-resolved measurements of the sample’s local density of states (LDOS), but are rather a result of selection rules for the spin excitation process [81]. Nevertheless, it is common to assign a majority (minority) character to those spin excitations that show an increased (decreased) weight when measured with a tip exhibiting a spin-polarized DOS that is dominated by majority electrons at the Fermi energy E_F. In the presented scenario of a $S = 1/2$ system the majority spin excitation hence occurs at negative bias, while the minority spin excitation appears at positive bias. Generally, this holds if S_z is increased in the excitation process whereas the picture is reversed if S_z is decreased. Further, one finds that all spin excitations with majority character shift to lower bias voltages with increasing field strength, while the opposite is true for minority excitations.

This illustrative derivation of the dependence of the excitation spectrum on the tip polarization η_t is expressed in the extension of the tunneling matrix element in Equation (2.5) to account for the tip polarization [79]:

$$U > 0: \; |M_\mathrm{if}|^2 = \frac{1+\eta_\mathrm{t}}{2} \, |\langle \varphi_\mathrm{f} | S_- | \varphi_\mathrm{i} \rangle|^2 + \frac{1-\eta_\mathrm{t}}{2} \, |\langle \varphi_\mathrm{f} | S_+ | \varphi_\mathrm{i} \rangle|^2 + |\langle \varphi_\mathrm{f} | S_z | \varphi_\mathrm{i} \rangle|^2 , \tag{2.6}$$

$$U < 0: \; |M_\mathrm{if}|^2 = \frac{1-\eta_\mathrm{t}}{2} \, |\langle \varphi_\mathrm{f} | S_- | \varphi_\mathrm{i} \rangle|^2 + \frac{1+\eta_\mathrm{t}}{2} \, |\langle \varphi_\mathrm{f} | S_+ | \varphi_\mathrm{i} \rangle|^2 + |\langle \varphi_\mathrm{f} | S_z | \varphi_\mathrm{i} \rangle|^2 . \tag{2.7}$$

Equations (2.6) and (2.7) were successfully applied to measurements on e.g. Mn atoms on $\mathrm{Cu_2N}$/Cu(001) [81], and nickelocene molecules adsorbed on an STM tip [83].

2.3 The Kondo effect

In the previous section, the effect of the conduction electrons interacting with a magnetic adatom was restricted to the rise of anisotropy in the system, and potential changes of the atom's magnetic moment and Landé-factor were absorbed in the effective spin model. However, many-body interactions between the conduction electrons and the adatom can lead to the complete screening of the adatom spin, accompanied by the appearance of a new electronic state at the Fermi level. In the following, this effect known as the Kondo effect [3] will be qualitatively introduced within the Anderson model of a spin 1/2 impurity [84]. In the second part of this section, the experimental signatures of the Kondo effect will be discussed. An extensive review of the Kondo effect in STM experiments is given in Ref. [85].

In the Anderson model, the singly occupied spin-carrying d orbital of the magnetic adatom is located below the Fermi level at an energy E_d, as displayed in Figure 2.6(a). Double occupation of this orbital shifts the second electron's energy by the Coulomb repulsion U above the Fermi level, such that the adatom's

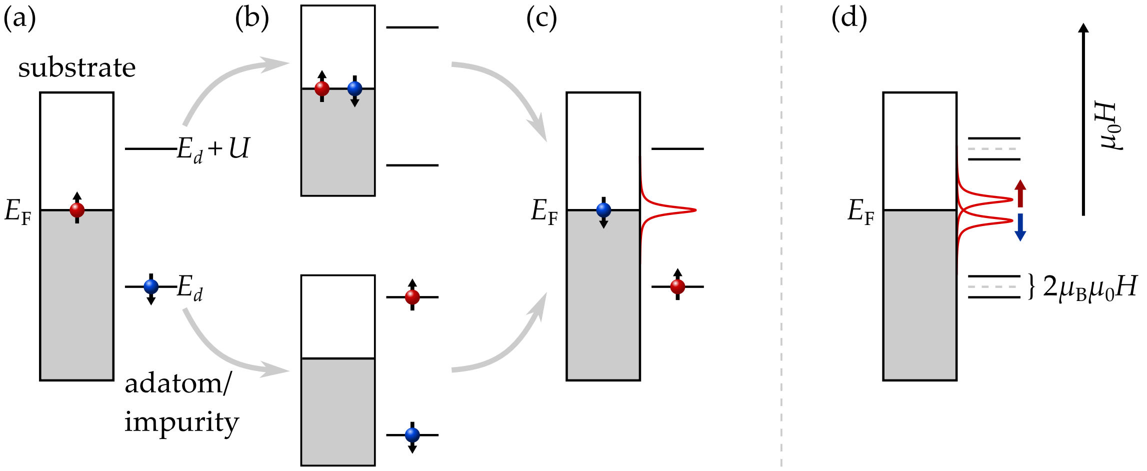

Figure 2.6: (a)-(c) Illustration of the Anderson model describing the spin-flip processes involved in the screening of the $S = 1/2$ impurity spin and the formation of the Kondo resonance at the Fermi level. (d) An external magnetic field leads to the splitting of the d levels, resulting in a splitting of the Kondo resonance away from E_F. Arrows indicate the spin polarization of the split resonances.

ground state is a doublet state with $S = 1/2$. Within the Heisenberg uncertainty relation, the adatom can undergo a spin-flip at zero energy cost as illustrated in Figure 2.6(b) and (c): For a short time, the d level can either be doubly occupied by transferring an electron with opposing spin from the electronic bath of the substrate to the adatom, or emptied, by transferring the electron from the d level to the substrate. In the next step the electron with opposing spin occupies the d level while the other electron enters the surface electronic bath. Multiple of these spin-flip processes lead to a net zero and hence effectively screened atomic spin and create a new electronic state at the Fermi level, the so-called Kondo or Abrikosov-Suhl resonance [4–6]. It can be shown that the physics of the Kondo effect is defined by the Kondo temperature T_K, which is given by

$$k_B T_K \approx \sqrt{2U\frac{\Delta}{\pi}} \exp\left(-\frac{\pi}{2\Delta}\left(\left|\frac{1}{E_d}\right| + \left|\frac{1}{E_d + U}\right|\right)^{-1}\right) = \Gamma, \tag{2.8}$$

and also defines the width Γ of the Kondo resonance. Here, Δ is the width of the d level in the Anderson model [86]. Further analysis of the system shows that the resonance position can be shifted from E_F if the average filling level n_d of the d level differs from 1, as it is the case in a non-electron–hole symmetric system. In that case, the center of the resonance E_K is given by [86]

$$E_K = \Gamma \tan\left(\frac{\pi}{2}(1 - n_d)\right). \tag{2.9}$$

The occurrence of this (close to) zero-energy state also explains the increasing resistivity at low temperatures, that is observed in metallic alloys containing

magnetic impurities [1]: The emergence of the Kondo resonance at the impurity sites below T_K constitutes new scattering centers for the conduction electrons and hence results in a minimum of the measured resistivity at T_K.
Applying an external magnetic field to the Kondo system leads to the splitting of the Kondo resonance as is displayed in Figure 2.6(d) [87]. For $\mu_0 H \neq 0$, the d levels are not degenerate anymore, hence spin-flips either require or release energy determined by the Zeeman Hamiltonian defined in Equation (2.1). Accordingly, the zero-energy state is split and each resonance is shifted by $\pm g\mu_\mathrm{B}\mu_0 H$. Both states are fully spin-polarized, with the majority (minority) state moving to lower (higher) energies with increasing field as has been experimentally demonstrated by K. von Bergmann *et al.* on a single Co atom atop a $\mathrm{Cu_2N}$ layer on Cu(001) [78].
Originally, J. Kondo derived the first understanding of the Kondo effect from the so-called $s-d$ model [88–92], which describes the interaction of the 4s conduction electrons of e.g. Cu with the spin carrying d orbitals of the transition metal atoms. The Hamiltonian describing the $s-d$ model consists of a term accounting for the exchange coupling J between the conduction electrons' spin $\vec{s}$ and the impurity spin $\vec{S}$ and a term accounting for the spin-independent potential scattering V of the conduction electrons at the impurity:

$$\mathcal{H}_{s-d} = -J\vec{s}\cdot\vec{S} + V\mathbb{1}. \tag{2.10}$$

In the limit of small impurity−substrate interaction, the Anderson model can be transformed into the $s-d$ model via the Schrieffer-Wolff transformation introducing the effective scattering potentials

$$J = \frac{2}{\pi}\Delta^2\left(\frac{1}{E_d} - \frac{1}{E_d+U}\right), \qquad V = -\frac{2}{\pi}\Delta^2\left(\frac{1}{E_d} + \frac{1}{E_d+U}\right), \tag{2.11}$$

valid for energies $E \ll |E_d|,\ |E_d+U|$ [86, 93]. For a spin 1/2 impurity, necessarily $E_d < 0$ and $E_d + U > 0$, such that J is always smaller than zero, ensuring an antiferromagnetic coupling between the conduction electrons at the Fermi level and the impurity spin. This antiferromagnetic coupling ultimately leads to the screening of the impurity spin at $T < T_\mathrm{K}$ and results in the appearance of the Kondo resonance.
The $s-d$ model allows to also describe systems with larger spin and is further employed for the description of spins on superconducting surfaces, which is the main topic of the second part of this thesis.
In an STM experiment, one might at first sight expect that the Kondo resonance can simply be detected by a $\mathrm{d}I/\mathrm{d}U$ measurement atop the magnetic atom that should reveal the Lorentzian Kondo resonance in the sample LDOS. However, tunneling electrons can not only tunnel into the Kondo state, but also into states of the surface or into atomic orbitals at the same energy [85, 94]. The interference

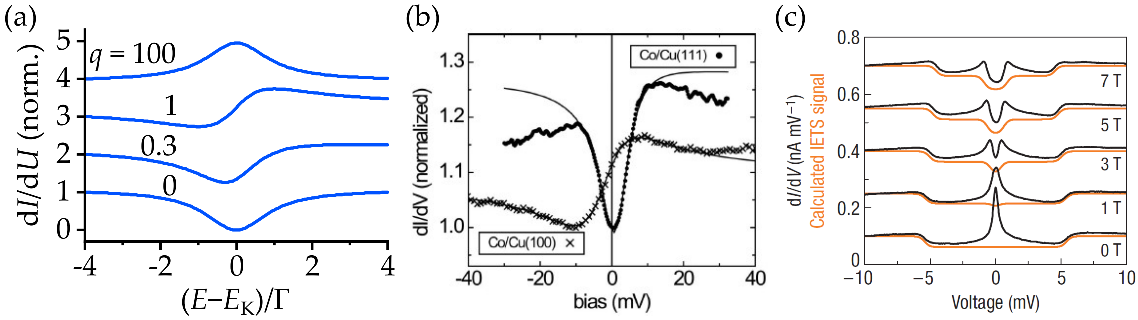

Figure 2.7: (a) Possible line shapes of the Fano resonance for different values of q. (b) Fano-like features observed in the differential conductance atop Co atoms on Cu(001) and Cu(111). (c) Spectroscopic measurements (black curves) of overlapping spin excitations (steps) and a Kondo resonance (peak) in an external field measured atop a Co atom on Cu_2N/Cu(001). The external field splits the Kondo resonance and gives rise to further spin excitation at the same energy. *(a) Adapted from Ref. [85]. (b) Reprinted with permission from Ref. [35]. Copyright ©2002 by the American Physical Society. (c) Reprinted by permission from Springer Nature: Ref. [37], Copyright ©2008.*

of these two paths can be shown to result in the appearance of a so-called Fano resonance [95] in $\mathrm{d}I/\mathrm{d}U$ spectra measured above a Kondo impurity. As presented in Figure 2.7(a), this resonance, given by

$$\frac{\mathrm{d}I}{\mathrm{d}U} = \rho_0 + A\frac{(q+\varepsilon)^2}{1+\varepsilon^2}, \qquad \varepsilon = \frac{eU - E_\mathrm{K}}{\Gamma}, \tag{2.12}$$

can take a variety of shapes determined by the form factor q, which approaches zero, when the tunneling occurs mainly via the states in the surface and takes on large values if the tunneling dominantly occurs via the Kondo resonance. The full range of curves has been observed in STM experiments as displayed in Figure 2.7(b) and (c). Yet, this variety of shapes complicates the clear identification of the Kondo effect in a single $\mathrm{d}I/\mathrm{d}U$ measurement as e.g. similar curves originating from the inelastic excitation of vibrational modes were observed when a single hydrogen atom bound to a metallic adatom [96]. This ambiguity also motivated the research presented in chapter 4, re-investigating Co atoms on noble metal (111) surfaces, one of the first ever reported Kondo systems in STM [33–36].

Finally, it should be mentioned that while especially early works widely used the Fano line to describe potential Kondo resonances in STM experiments [33–36, 97], later works increasingly employed the so-called Frota line [98, 99]. This phenomenological line shape exhibits an improved fit to the results of numerical renormalization group calculations of the Kondo effect and was also shown to yield a better agreement with experimental data when compared to the Fano line [100, 101]. However, this is not true for the cases of Co atoms on noble metal (111) surfaces [102], such that the Fano line is continued to be used to describe the zero-bias feature in STS data in these systems.

Chapter 3

3 INVESTIGATING ELECTRONIC AND MAGNETIC PROPERTIES ON THE ATOMIC SCALE BY SCANNING TUNNELING MICROSCOPY

The invention and realization of the scanning tunneling microscope by G. Binnig, H. Rohrer, Ch. Gerber, and E. Weibel in the early 1980s [31, 32] opened new possibilities in the field of surface science, allowing for the first time to study topographic and electronic properties at the atomic scale. In this chapter I will introduce the basics of scanning tunneling microscopy in section 3.1, including inelastic tunneling spectroscopy (IETS) and spin-polarized STM. More details on the principles of STM can be found in e.g. Refs. [103, 104]. In the second part of this chapter in section 3.2, I will present the experimental setup used in this work.

3.1 BASICS OF SCANNING TUNNELING MICROSCOPY

The working principle of an STM relies on the quantum mechanical tunneling of electrons through the vacuum barrier between a metallic tip and a conducting surface, which is defined by the work function ϕ. If this barrier is sufficiently low, electrons can tunnel through the junction, resulting in a finite net tunneling current if a bias voltage $U \neq 0$ is applied between tip and sample. The resulting tunneling current depends exponentially on the tip–sample distance z as

$$I(z) = I_0 e^{-2\kappa z}, \tag{3.1}$$

where κ is given by $\sqrt{2m\phi}/\hbar$ for sufficiently small voltages $eU \ll \phi$. For a typical value of 5 eV for ϕ, one obtains $\kappa \approx (0.1\,\mathrm{nm}^{-1})$. Therefore, height differences

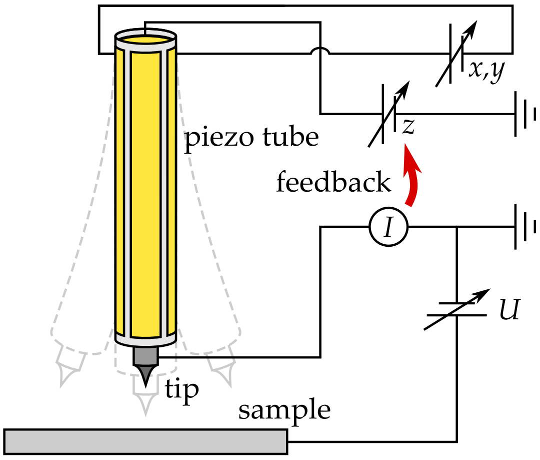

Figure 3.1: Sketch of the basic setup of an STM. The bias voltage U applied to the sample leads to a tunneling current I between tip and sample. In a standard topography measurement, the tunneling current is kept at a fixed value by adjusting the tip–sample distance via a feedback loop. The tip is moved by a piezo tube which can be stretched or bent by applying a voltage to the contacts on the tube.

on the scale of an atomic diameter can be detected on a surface by measuring the tunneling current at a fixed tip height. In practice, rather than fixing the tip–sample distance, the tunneling current is kept constant by adjusting the tip height via a feedback loop, such that the height profile of the sample is translated to the relative tip displacement. This allows to keep a stable measurement signal and prevents unintended contact of tip and sample at surface features higher than the tip–sample distance. To acquire a 2D image, the tip is scanned across the surface. Experimentally this is most commonly realized via a piezo-electric tube, which can be elongated or bent by applying a voltage to metallic contacts on the tube's surface, thereby changing the tip's z and x, y-position, respectively. A sketch of such a setup is presented in Figure 3.1.

While the above description yields an intuitive understanding of the topographic capabilities of an STM, it entirely neglects the influence of the tip and sample band structure on the tunneling current. J. Bardeen's tunneling theory [105] explicitly includes the electronic states of both tip and sample into the description of the tunneling process. Although both wave functions need to overlap to allow electrons to tunnel, the states entering the theory are assumed to be the unperturbed tip and sample states, which yields satisfactory results for the description of most STM measurements. Solving the time-dependent Schrödinger equation one finds that the tunneling rate of an electron tunneling from state ψ_μ with energy E_μ in the tip into state ψ_ν with energy E_ν in the sample is

$$T_{\mu\rightarrow\nu} = \frac{2\pi}{\hbar}\left|M_{\mu\nu}\right|^2 \delta(E_\mu - (E_\nu - eU)). \tag{3.2}$$

Here, U is considered to be applied to the sample, shifting the sample's states by $-eU$ with respect to the Fermi level of the tip. The tunneling matrix element defined as [104]

$$M_{\mu\nu} = \frac{\hbar^2}{2m}\int_\Sigma \psi_\mu \nabla \psi_\nu^* - \psi_\nu^* \nabla \psi_\mu \mathrm{d}\vec{S} \tag{3.3}$$

contains the overlap of the wave functions and implicitly the exact shape of the tunnel barrier which defines the amplitude and gradient of the wave functions at the interface Σ between the electrodes and hence determines the probability of an electron to tunnel between the two states. Often, the tunneling matrix element is assumed to not depend on the exact states that participate in the tunneling process, but only on the states' energy. This simplification then allows to integrate over all energies, to derive the tunneling current from tip to sample and vice versa without explicitly considering the individual states. The limitations of this simplification will be discussed below. Considering that tunneling can only occur from occupied into empty states and introducing the tip and sample LDOS ρ_t and ρ_s, respectively, as well as the Fermi-Dirac distribution $f(E)$, one obtains

$$I_{\mathrm{t}\rightarrow\mathrm{s}} = \frac{2\pi e}{\hbar} \int |M_{\mu\nu}|^2 \rho_\mathrm{t}(E_\mu)\rho_\mathrm{s}(E_\nu) f(E_\mu)(1 - f(E_\nu))\delta(E_\mu - (E_\nu - eU))\mathrm{d}E_\mu \mathrm{d}E_\nu \tag{3.4}$$

$$I_{\mathrm{s}\rightarrow\mathrm{t}} = -\frac{2\pi e}{\hbar} \int |M_{\mu\nu}|^2 \rho_\mathrm{t}(E_\mu)\rho_\mathrm{s}(E_\nu)(1 - f(E_\mu)) f(E_\nu)\delta(E_\mu - (E_\nu - eU))\mathrm{d}E_\mu \mathrm{d}E_\nu . \tag{3.5}$$

The total tunneling current is then given by the sum of Equations (3.4) and (3.5). Integration over E_μ yields

$$I(U) = \frac{2\pi e}{\hbar} \int |M(E)|^2 \rho_\mathrm{t}(E - eU)\rho_\mathrm{s}(E)(f(E - eU) - f(E))\mathrm{d}E. \tag{3.6}$$

Neglecting $M(E)$ for the moment, one finds that the tunneling current at positive bias voltage is determined by the convolution of all filled tip states in the interval $[E_\mathrm{F} - eU, E_\mathrm{F}]$ with the empty sample states in $[E_\mathrm{F}, E_\mathrm{F} + eU]$. The opposite holds for negative bias voltages, as illustrated in Figure 3.2.

J. Tersoff and D. R. Hamann further simplified Equation (3.6) by considering an s-wave-like tip wave function [106, 107]. In this approximation, the energy dependencies of the tunneling matrix and the tip DOS in Equation (3.6) vanish, resulting in

$$I(U) \propto \rho_\mathrm{t} \int \rho_\mathrm{s}(E, z = z_\mathrm{t})(f(E - eU) - f(E))\mathrm{d}E, \tag{3.7}$$

where the tunneling current is simply determined by the integral over the sample LDOS at the position of the tip z_t. For $E \ll \phi$, one can approximate $\rho_\mathrm{s}(E, z = z_\mathrm{t}) \approx \rho_\mathrm{s}(E, z = 0)\exp(-2\kappa z_\mathrm{t})$, which allows to interpret experimental results as a direct measurement of the sample LDOS. As will be discussed at the end of this section, this does not hold for e.g. large bias voltages or non s-wave like tip states.

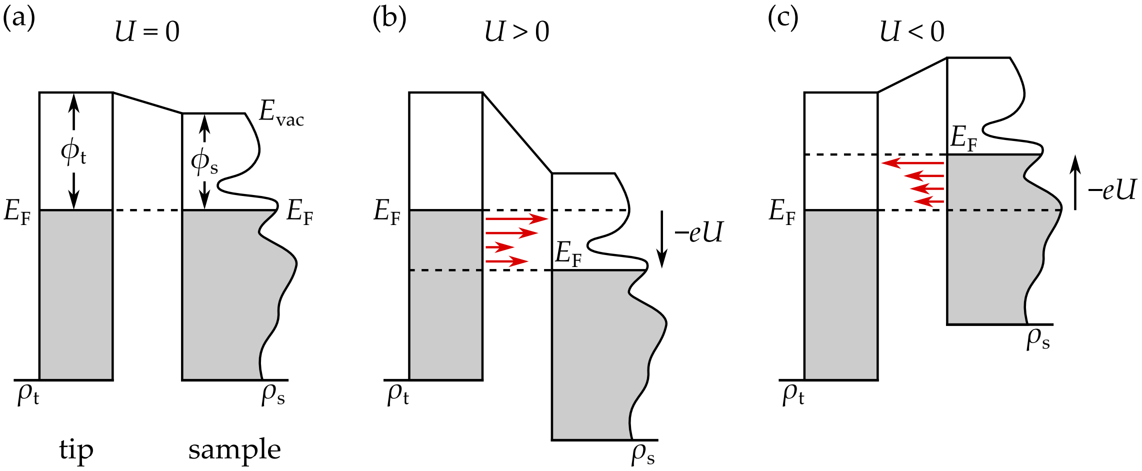

Figure 3.2: Tunneling through a vacuum barrier. For (a) $U = 0$, the Fermi levels of tip and sample are aligned such that no net tunneling current can flow. For (b) $U > 0$, the electrons from occupied tip states flow into unoccupied states of the sample, the opposite applies for (c) $U < 0$. The red arrows indicate the tunneling direction of electrons. The arrows' lengths indicate the strength of the tunneling current at a specific energy, which depends on the sample's LDOS as well as the energy difference to the vacuum level.

From Equation (3.7) it is easy to deduce that in the chosen approximation of a constant tip DOS and an energy-independent tunneling matrix element, the derivative of the tunneling current at a given bias voltage U is directly proportional to the sample LDOS at $E_F + eU$:

$$\frac{dI}{dU}(U) \propto -\rho_t \int \rho_s(E) f'(E - eU) dE. \tag{3.8}$$

The convolution of ρ_s with the derivative of the Fermi-Dirac distribution given by

$$f'(x) = -\frac{1}{4k_B T} \mathrm{sech}^2 \left(\frac{x}{2k_B T} \right). \tag{3.9}$$

leads to a broadening (full width at full maximum, FWHM) of all features in the sample LDOS by about $3.5k_B T$ in the dI/dU signal.

This finding, that by measuring the differential conductance one has local access to the density of states of the sample within a spatial resolution of < 1 nm, demonstrates one of the greatest potentials of scanning tunneling microscopy and is commonly referred to as scanning tunneling spectroscopy (STS). Experimentally, STS measurements are usually performed using a lock-in amplifier and applying a small ac modulation voltage U_{mod} that is added to the DC bias voltage.

The thermal broadening of the obtained conductance spectra generates the need for low temperatures in STS measurements, as already a temperature of 4.2 K causes

a broadening of all spectroscopic features by 1.3 meV, comparable to e.g. the size of the superconducting gap of Nb. As will be shown in chapter 8, additionally to lower experimental temperatures the issue of temperature broadening can be reduced by using superconducting tips.
Finally, the limitations of the simplifications made in the preceding derivation of especially Equation (3.8) need to be discussed: First, the energy independence of the tunneling matrix element only holds for small bias voltages. States at higher energies have a longer decay range into the vacuum, as they effectively experience a reduced barrier height. Thus, electrons at higher energies have a larger probability to tunnel than those close to $E_\mathrm{F} - eU$, as already indicated in Figure 3.2. This also leads to the effect that for $U > 0$, predominantly sample states are probed, while for $U < 0$, mostly the tip DOS determines the shape of the conductance spectrum [103] (see also Figure 3.2). Another effect that was neglected so far is the dependence of the tunneling barrier height on the in-plane momentum $k_{||}$ of the tunneling electrons. One can show that the conservation of $k_{||}$ in the tunneling event leads to an increase of the effective tunnel barrier by $\hbar^2 k_{||}/2m^*$, where m^* is the effective mass of the electrons [103]. Hence, STM and STS experiments are most sensitive to states close to the $\overline{\Gamma}$ point of the surface Brillouin zone, where $k_{||} \approx 0$, an effect that will be relevant in the discussion of the experimental results in chapter 7. Last, the orbital character of the tip and sample states cannot be neglected and has been shown to often differ from the s-wave character assumed by Tersoff and Hamann. For the commonly used tungsten tips, d orbitals protruding from the tip apex dominate the tunneling [108], and tips functionalized with a CO molecule at the tip apex, which will be introduced in chapter 9, are characterized by degenerate p_x and p_y orbitals [109]. As shown by C. J. Chen, it is crucial to consider tunneling from these non s-wave tip orbitals to explain the experimentally observed increased spatial resolution in comparison to that predicted by Tersoff and Hamann [110, 111].

A brief nomenclature of measurement modes employed in this thesis

Here, the most important measurement modes employed throughout this work are briefly introduced:

- *Constant-current topography:* All topographic measurements in this thesis were performed in a constant-current mode at fixed bias voltage, were the tunneling current is kept constant by the feedback loop of the STM controller and the topographic information is encoded in the resulting relative vertical tip displacement. The resulting images were treated in *WSxM* [112] and *Gwyddion* [113].

- *Differential conductance spectrum:* Single point spectra show the measured differential conductance over a given bias range. All spectra presented

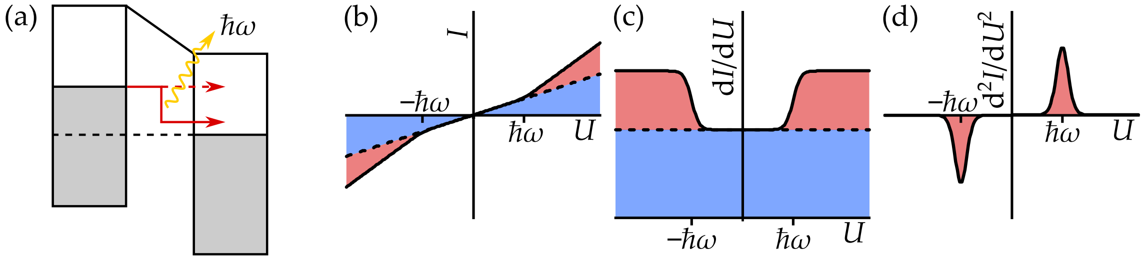

Figure 3.3: (a) Sketch of an inelastic tunneling process where an electron excites a mode with excitation energy $\hbar\omega$ in the gap of the tunneling junction. (b)-(d) The resulting tunneling current, $\mathrm{d}I/\mathrm{d}U$, and $\mathrm{d}^2I/\mathrm{d}U^2$ signal, respectively. The blue part originates from elastic tunneling events, the red part reflects the inelastic tunneling. At $\pm\hbar\omega$ a (b) current onset, (c) conductance steps, and (d) a dip/peak become visible in the respective signal.

in this thesis were recorded with open feedback loop, i.e. at a fixed tip–sample distance determined by the initial current and bias voltage setpoint.

- *dI/dU map:* Differential conductance maps display the change of the spatial variation of the $\mathrm{d}I/\mathrm{d}U$ signal at a fixed bias voltage. They are usually recorded by scanning the tip over the surface at a fixed bias voltage and tunneling current. As will be shown in chapter 7, this can lead to set-point artifacts, which can be avoided by measurements with a fixed tip–sample distance.

- *Line and full grid spectroscopy:* Multiple single point spectra recorded along a line or on a 2D grid. Cuts at a fixed bias voltage yield maps of the differential conductance.

3.1.1 *Inelastic tunneling spectroscopy*

The derivation of the tunneling current in the previous section assumed an elastic tunneling of the electrons through the junction, reflected in the δ-function in Equation (3.2). However, if the electrons can induce an excitation of energy $\hbar\omega$ of a system inside the junction, they can tunnel inelastically, such that their final state differs by an energy of $-\hbar\omega$ from the initial state. The process is sketched in Figure 3.3(a). In this case, the δ-functions in Equations (3.4) and (3.5) must be changed to $\delta(E_\mu - (E_\nu - eU + \hbar\omega))$ and $\delta(E_\mu + \hbar\omega - (E_\nu - eU))$, respectively. Assuming a constant tip and sample LDOS within the energy region of interest, the resulting inelastic tunneling current is given by [114]

$$I_{\text{inel}} = \frac{\sigma_{\text{inel}}}{e} \int f(E - eU + \hbar\omega)(1 - f(e)) + (f(E - eU - \hbar\omega) - 1) f(E) \mathrm{d}E \quad (3.10)$$

$$= \frac{\sigma_{\text{inel}}}{e} k_{\mathrm{B}} T \left(\frac{x e^{x}}{e^{x} - 1} - \frac{x' e^{x'}}{e^{x'} - 1} \right), \quad (3.11)$$

with $x = (eU - \hbar\omega)/k_{\mathrm{B}}T$ and $x' = (-eU - \hbar\omega)/k_{\mathrm{B}}T$. As illustrated in Figure 3.3(b), the inelastic tunneling current thus increases linearly above the excitation energy. This can be understood as the opening of a new, the inelastic tunneling channel at $|eU| = \hbar\omega$. In practice one measures the differential conductance or second derivative of the tunneling current, which are characterized by steps or peaks/dips at the excitation energy, respectively:

$$\frac{\mathrm{d}I_{\text{inel}}}{\mathrm{d}U} = \sigma_{\text{inel}} \left(\frac{e^{x}(e^{x} - x - 1)}{(e^{x} - 1)^2} + \frac{e^{x'}(e^{x'} - x' - 1)}{(e^{x'} - 1)^2} \right) \quad (3.12)$$

$$\frac{\mathrm{d}^2 I_{\text{inel}}}{\mathrm{d}U^2} = \sigma_{\text{inel}} \frac{e^2}{k_{\mathrm{B}} T} \left(\frac{e^{x}\left(e^{x}(x - 2) + x + 2\right)}{\left(e^{x} - 1\right)^3} - \frac{e^{x'}\left(e^{x'}(x' - 2) + x' + 2\right)}{\left(e^{x'} - 1\right)^3} \right) \quad (3.13)$$

The finite temperature leads to a broadening of the peaks in Equation (3.13) with a FWHM of $5.44 k_{\mathrm{B}} T$. Inelastic tunneling spectroscopy hence allows to determine excitation energies of systems inside the STM junction by detecting electron–hole symmetric peaks/dips in a $\mathrm{d}^2 I/\mathrm{d}U^2$ measurements as sketched in Figure 3.3(d). Such excitations via inelastic tunneling of electrons were for the first time observed in planar Al-AlO$_x$-Pb junctions containing $\mathrm{CH_3COOH}$ molecules, whose vibrational modes could be matched to the observed peaks in the $\mathrm{d}^2 I/\mathrm{d}U^2$ spectrum [115]. In STM junctions, IETS was used to detect vibrational modes of individual molecules [116, 117], phonons [118], and magnetic excitations [38, 45, 77] as already presented in section 2.2.

3.1.2 *Spin-polarized scanning tunneling spectroscopy*

Another important extension to standard STM is spin-polarized scanning tunneling microscopy and spectroscopy (SP-STM/SP-STS) [119]. SP-STM and SP-STS allow to probe the magnetic structure and spin-resolved LDOS of surfaces (e.g. Refs. [120–123]) as well as to determine the spin character of magnetic excitations in single atoms, molecules, and small clusters [78, 81, 83, 124, 125].

The tunneling magneto resistance, an effect discovered 10 years before the invention of the STM, causes the tunneling current between to ferromagnets separated by an insulating barrier to depend on the relative alignment of the magnetization in

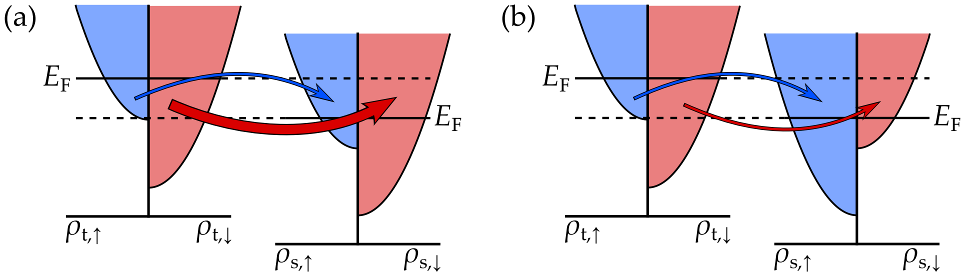

Figure 3.4: Sketch of the spin-polarized two current model for a magnetic tip and sample in the Stoner model. For elastic tunneling, electrons maintain their spin in the process, such that the "spin up" and "down" electron current can be considered separately. Due to the larger LDOS for the majority electrons, the tunneling current for (a) a parallel magnetization of both tunneling contacts, i.e. same direction of the majority spin, is larger than for (b) an antiparallel magnetization of tip and sample.

both electrodes [126]. To explain the effect, it is helpful to study the spin-resolved DOS of both electrodes, presented in Figure 3.4 in a simplified Stoner-model. In the case of elastic tunneling of the electrons the angular momentum is conserved, such that tunneling of "spin up" and "spin down" electrons needs to be considered separately [126]. As illustrated in Figure 3.4, the increased overlap of the occupied tip and unoccupied sample states for the parallel alignment of tip and sample magnetization in panel (a) leads to a higher tunneling current compared to the antiparallel alignment displayed in panel (b).

This finding can be expressed mathematically by introducing the spin-polarized LDOS $\vec{m}_{t,s}(E)$ that contains the number as well as the average orientation (polarization) of the electrons' spins at a given energy. The tunneling conductance extending the Tersoff-Hamann model to the spin-polarized case is then given by [127]

$$\frac{dI}{dU}(U) \propto \rho_t \rho_s (E_F + eU) + \vec{m}_t \vec{m}_s (E_F + eU). \tag{3.14}$$

The scalar product $\vec{m}_t \vec{m}_s$ accounts for arbitrary relative polarization directions between tip and sample with angle θ. Introducing the tip and sample polarization

$$\eta_{t,s} = \frac{\rho^{\downarrow}_{t,s} - \rho^{\uparrow}_{t,s}}{\rho^{\downarrow}_{t,s} + \rho^{\uparrow}_{t,s}}, \tag{3.15}$$

Equation (3.14) can be rewritten as

$$\frac{dI}{dU}(U) \propto \rho_t \rho_s (E_F + eU)(1 + \eta_t \eta_s (E_F + eU) \cos\theta). \tag{3.16}$$

Equation (3.16) demonstrates how magnetic tips can be used to image e.g. magnetic domain walls, which exhibit a changing contrast between domains with a parallel and antiparallel alignment with respect to the tip polarization in $\mathrm{d}I/\mathrm{d}U$ maps. SP-STS further allows to determine the spin character of specific electronic states such as the (Zeeman-split) Kondo resonance [78] (see also section 2.3) or of magnetic excitations [81]: If the tip polarization is aligned parallel to the majority states in the sample, the latter show an increased intensity of the conductance signal in comparison minority states. For magnetic excitations such as the spin excitations of a single magnetic adatom, the assignment of the spin character is more intricate as was already discussed in section 2.2. The concomitant spin-flip of the tunneling electrons in these excitations in combination with the bias-dependent tunneling direction of the electrons results in an asymmetric weight of the observed inelastic conductance steps at positive and negative bias. Although IETS does not probe the samples LDOS and the observed asymmetry in the SP-IETS measurements is rather a manifestation of selection rules of the excitation process, it is common to assign a bias-dependent majority and minority spin character to the excitations (cf. section 2.2). In the limit of an energy-independent tip DOS, one can even quantify the states' or excitations' polarization by measuring the STS signal in the parallel and antiparallel alignment of tip and sample:[1]

$$\eta_{\mathrm{s}}(U) = \frac{\mathrm{d}I/\mathrm{d}U_{\downarrow\downarrow}(U) - \mathrm{d}I/\mathrm{d}U_{\uparrow\downarrow}(U)}{\mathrm{d}I/\mathrm{d}U_{\downarrow\downarrow}(U) + \mathrm{d}I/\mathrm{d}U_{\uparrow\downarrow}(U)}. \tag{3.17}$$

In a real measurement, $\eta_{\mathrm{t}}(E)$ is never constant, since equivalent to the sample, the tip polarization depends on the spin character of the contributing bands. Hence a careful characterization of the tip polarization on a known sample is necessary and a quantitative determination of the sample polarization is usually only possible in a narrow energy range where $\eta_{\mathrm{t}} \approx$ const. is a valid approximation.

Experimentally, spin-polarized tips are realized by the deposition of thin films of ferromagnetic or antiferromagnetic materials such as Fe or Cr onto the tip apex [128, 129], or by picking up magnetic clusters [130] or single atoms [124] from a surface onto the tip. For the latter, the magnetic anisotropy of the tip is often small and it is necessary to apply an external magnetic field to stabilize the magnetization direction of the tip.

---

[1] For the Zeeman split Kondo state or spin excitations, both configurations can be probed in a single measurement, with the majority and minority state/excitation appearing at opposite bias voltages. For e.g. exchange-split bands in the surface, it is however necessary to measure in different domains or to switch the tip or sample magnetization with an external magnetic field.

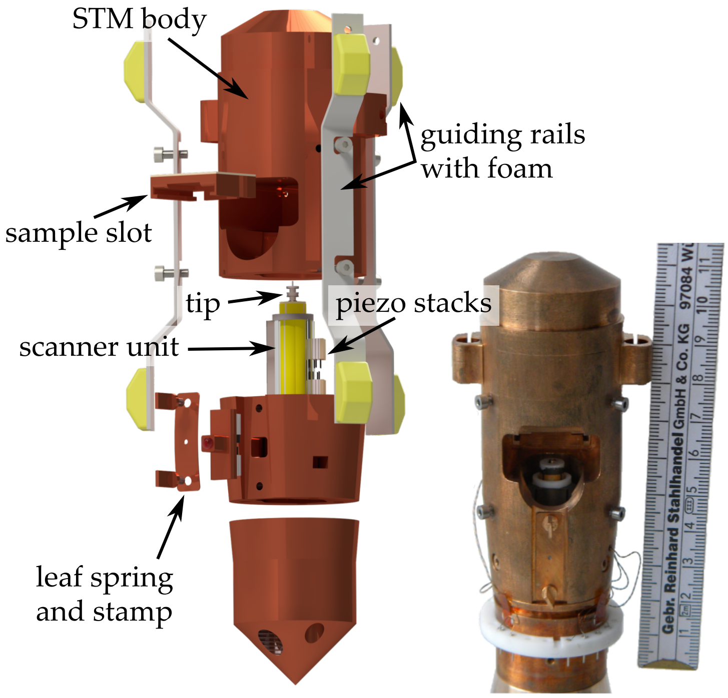

Figure 3.5: Technical drawing and photograph of the STM in the 1 K system. The phosphor bronze body hosts a Pan-style STM, which is driven by three piezo stacks pressed against a sapphire prism that contains the scanner. Rails on the side of the STM body are mounted on springs inside the cryostate, the foam on these rails damps the eigenmotion of the created pendulum. *Photograph reprinted with permission from Ref. [132].*

3.2 EXPERIMENTAL SETUP

All measurements presented in this thesis were performed in the “1 K system” that will be briefly presented in the following. The system was originally set up by Oliver Storz; the current STM was later built and installed by Stefan Wilfert. More details on the STM, the cryostat as well as the UHV system can be found in the respective PhD theses [131, 132]. The UHV system was heavily modified during this work to especially facilitate sample transfer.

A technical drawing of the STM in the 1 K system is presented together with a photograph in Figure 3.5. The STM is a Pan-style STM [133] integrated into a phosphor bronze body. The coarse motion is actuated via three pairs of piezo stacks (*PI Ceramic GmbH*) that press onto a sapphire prism. The STM’s piezo scanner tube is glued into the prism and allows for a maximum x/y scan range of $\sim$ 2.8 µm and a z stroke of $\sim$ 500 nm at 4.2 K. All tips used throughout the presented work were electrochemically etched from 0.375 mm tungsten wire (*Plano GmbH*) in a 2 molar NaOH solution. The STM is controlled by a *Nanonis* SPM controller (*SPECS Surface Nano Analysis GmbH*). The tunneling current is amplified by a *Femto DLPCA-200* low noise current amplifier and a *SR810* lock-in amplifier (*Stanford Research Systems*) was used to perform STS measurements.

The STM is integrated into a ^{4}He cryostat from *CryoVac GmbH & Co KG*. By pumping on separated He pots situated below the main He tank it is possible to cool the STM down to $\sim$ 1.3 K. The cryostat is equipped with a superconducting magnet coil with a maximum field of 12.5 T which is applied perpendicular to the sample surface in the STM. To both be able to reach minimum temperatures in the STM and to apply the maximum magnetic field to the sample, the STM is moved to the magnet center to the "measuring position", while in the "exchange position" the STM is fixed below the magnet allowing to exchange tips and samples with visual access to the STM. In the "measuring position" the STM hangs on CuBe springs, the second damping stage of the system. The cryostat itself is supported by three pneumatic vibration isolators (*Newport*). This allows to achieve a minimum noise of ~ 1 pm in a topography measurement. For more details especially on the integration of the STM into the cryostat I refer to the PhD thesis of Oliver Storz [131].

A critical characteristic of an STM, especially when investigating low-bias features, is the electronic temperature of the system, as it can strongly differ from the thermodynamic temperature measured by the temperature sensors mounted to the STM sample slot. One important source for additional high frequency noise that causes the elevated electron temperature is radiation from electronic devices, which must be minimized by appropriate filtering or by switching off the devices not needed during the measurement. In the presented system these measures led to a minimum effective temperature of 1.8 K as was shown by fits of the superconducting gap on Nb(110) (cf. chapter 6). Presumably electronic filters at low temperature but also better filtering at the in- and outputs on the cryostat could further reduce this value.

The cryostat with the STM is integrated into a UHV system consisting of three chambers used for sample preparation, and a small load lock chamber to introduce tips and samples into the system. A technical drawing of the entire system is presented in Figure 3.6. While inside the STM chamber the minimum pressure is $< 1 \times 10^{-10}$ mbar, it is $< 5 \times 10^{-10}$ mbar in the preparation system. The latter is equipped with an Ar^{+}-ion sputter gun, a radiative ($T \leq 600$ °C) heater, and a DC heater as well as an electron-beam heating stage ($T > 2500$ °C) for the preparation of clean sample surfaces. Effusion cell and electron-beam evaporators for the deposition of metals or semimetals and -conductors as well as materials with high vapor pressure are mounted onto preparation chambers I and II, respectively. Additionally, single atoms and molecules can be deposited *in-situ* onto the cold sample inside the STM, with the sample temperature ranging from 4.2 K to $\lesssim 15$ K. In addition to the STM, a LEED/AES (low-energy electron diffraction/Auger electron spectroscopy) optics from *SPECS Surface Nano Analysis GmbH* allows for a fast characterization of sample cleanliness and film growth quality and is mounted to the preparation chamber II.

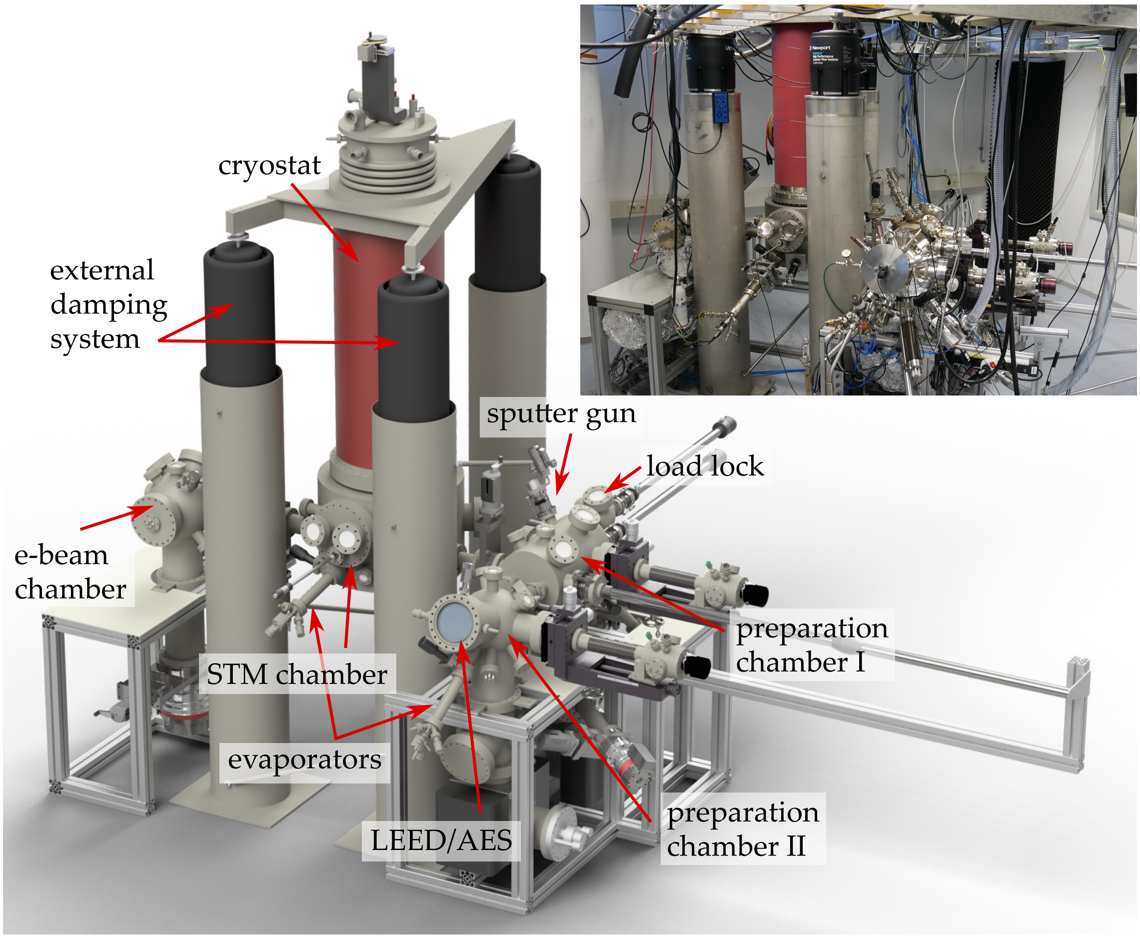

Figure 3.6: Technical drawing and photograph of the whole setup of the 1 K system. The cryostat is mounted onto three sand-filled columns equipped with pneumatic vibration insulators. Three additional UHV chambers are used for the surface preparation of single crystals as well as the growth of thin films. A LEED/AES optics for additional surface characterization is available.

4

Chapter 4

COBALT ATOMS ON NOBLE METAL (111) SURFACES – A PROTOTYPICAL KONDO SYSTEM?

Single cobalt atoms on the (111) surfaces of noble metals were for a long time considered prototypical systems of the Kondo effect in STM experiments. Spectroscopic measurements on these atoms revealed a Fano-like dip around the Fermi level, which was interpreted as the result of co-tunneling into the Kondo resonance and surface states at the same energy [33–36]. Very recently, J. Bouaziz *et al.* however proposed that the observed zero-bias feature actually originates from spin excitations of the Co atom induced by the tunneling electrons [64]. Further, interactions between these spin excitations and conduction electrons were predicted to lead to the formation of a new many-body state, called spinaron. This newly established controversy was the incentive for the re-investigation of the system, whose results will be presented in this chapter.

This chapter is organized as follows: First, I will review existing experimental and theoretical studies of Co atoms on the noble metal (111) surfaces in section 4.1. In the second part of the chapter, I will present the experimental results obtained in magnetic field-dependent (sections 4.2 and 4.3) and spin-polarized STS measurements (section 4.4) on Co/Cu(111), which are expected to shine light on the underlying physics of the system. Finally, these results will be discussed and compared to the existing theoretical descriptions in section 4.5.

4.1 THE KONDO EFFECT VS. SPIN EXCITATIONS

In this section I summarize the existing work studying single Co atoms on nobel metal (111) surfaces in the framework of the Kondo effect in section 4.1.1 and briefly introduce the competing theory presented by J. Bouaziz *et al.* that proposes a different interpretation of the experimental data in section 4.1.2.

4.1.1 Single Co atoms in the Kondo picture

The observation of a Fano-like resonance atop a Co atom was first reported and interpreted as a signature of the Kondo effect by V. Madhavan *et al.* in 1998, studying single Co atoms on the Au(111) surface [33]. Co atoms on both the fcc and hcp sites of the herringbone reconstruction were shown to exhibit a dip in the recorded $\mathrm{d}I/\mathrm{d}U$ spectrum around E_F, which could be fitted by a Fano curve with a shape factor q of ~ 0.6 and a width $\Gamma = k_\mathrm{B}T_\mathrm{K}$ corresponding to a Kondo temperature of 70 K. Later on, very similar features were observed on single Co atoms on Cu(111) [34] and Ag(111) [36], exhibiting Kondo temperatures of 50 K and 90 K, respectively.

Following these pioneering experiments, large theoretical [94, 134–147] and experimental [102, 148–160] effort was made to better understand the formation of the proposed Kondo state in Co atoms on the noble metal (111) surfaces, partly resulting in contradictory conclusions.

Significant effort was put into assessing the role of the noble metal (111) surface state: Experiments by L. Limot and R. Berndt on Co atoms close to step edges of the Ag(111) surface [151], where the LDOS of the surface state is strongly modified, and by J. Henzl and K. Morgenstern on narrow terraces of the Ag(111) surface [154], where the lower edge of the 2D electronic surface band is pushed above the Fermi level, suggested no dependence of T_K on the presence of the surface state. Contradicting experiments by M. Moro-Lagares *et al.* and Q. L. Li *et al.* however showed a linear dependence of the Kondo temperature on the surface state LDOS when moving a single Co atom through the standing wave pattern on the surface [159, 160]. This sensitivity was attributed to the energetic proximity of the surface state onset to the Fermi level in comparison to Co/Cu(111), where no modulation of the Kondo temperature as a function of the surface state LDOS has been reported until today. This is corroborated by calculations showing that for Co/Cu(111) T_K is determined by the interaction of the d orbitals with bulk states [94, 140, 142, 146, 147]. Contrary, a change of the LDOS induced by the proximity of neighboring Cu atoms on the surface has been shown to significantly change T_K in the system [102, 156]. Generally, the surface state however appears to play a crucial role in the observed shape of the Fano resonance [138, 154]. Recent publications further revealed that electron tunneling occurs mainly via the Co s orbital that hybridizes with the Cu surface state, leading to the Fano line shape based on Kondo resonance of the screened Co d_{z^2} orbital [94, 147].

Further theoretical effort was made to estimate the size of the unscreened spin of Co/Cu(111). Surprisingly, Refs. [146] and [147] both find $S = 1$ (or potentially also $S = 3/2$ [147]), where the simple Anderson model presented in section 2.3 fails to produce a zero-energy spin-flip that would result in a Kondo resonance for any system exhibiting finite magnetic anisotropy. Instead, a more complex process that screens the spin is expected for such a system [147]. The effect of magnetic interactions on the Kondo resonance has been studied theoretically [143] as well as experimentally by placing Co atoms on a thin Fe layer on top of Au(111) [158], resulting in the splitting of the resonance.

Finally, the Fano resonance has been shown to disappear if the adatom–substrate coupling is changed by studying Co atoms adsorbed to the fcc/hcp domain walls on the reconstructed Au(111) surface [150] and dimers with short interatomic distances [148].

Although the presented experiments could mostly be explained within the Kondo model, some fundamental features of the Kondo resonance have not been observed until now. Due to the high mobility of Co atoms on the noble metal (111) surfaces [161], a study of the resonance width as a function of temperature, which is expected to follow $\Gamma = \sqrt{(5.4 k_\mathrm{B} T)^2 + (2 k_\mathrm{B} T_\mathrm{K})^2}/2$ [37, 114, 162], is not possible. Further, splitting of the resonance in an external magnetic field and concomitant spin-resolved measurements as presented for Co/$\mathrm{Cu_2N}$/Cu(001) in Ref. [78] have not been presented until now, presumably due to the large width of the resonance of about 10 meV and the comparably small expected field-induced splitting. These measurements were now motivated by the work of J. Bouaziz *et al.* [64], which will be introduced in the following, and will be presented in the subsequent sections.

4.1.2 *"A new view on the origin of zero-bias anomalies of Co atoms atop noble metal surfaces"*

The title of this section, taken from Ref. [64], reflects the motivation for the experiments presented in this chapter. In their work, J. Bouaziz *et al.* present an alternative origin of the experimentally observed zero-bias anomaly (ZBA) that rejects the Kondo effect and the concomitant Fano resonance as an explanation.

Based on first-principle relativistic time-dependent density functional theory (DFT) calculations, the authors find that the Co atom atop the noble metal (111) surfaces is an unscreened $S = 1$ system with a magnetic moment of about $2.0 - 2.2\,\mu_\mathrm{B}$ and an out-of-plane easy axis magnetic anisotropy of $3.3 - 4.5$ meV, depending on the surface material. Consequently, spin excitations appear at finite energies as a result of the spin-orbit coupling in the system that is explicitly included in the calculations. In an earlier publication by the same group, spin-orbit coupling was modeled by an artificial magnetic field, leading to similar results as discussed in the following [163]. The self-energy of the system, which describes the interaction between the spin excitations and the conduction electrons of the surface is determined subsequently. The result is displayed in Figure 4.1(c). As shown in Ref. [163], excitations of the adatom's spin are accompanied by the formation of electron–hole pairs, which, depending on the transferred angular momentum and direction of the tunneling electrons are created in the occupied minority and unoccupied majority states or vice versa. Due to the different

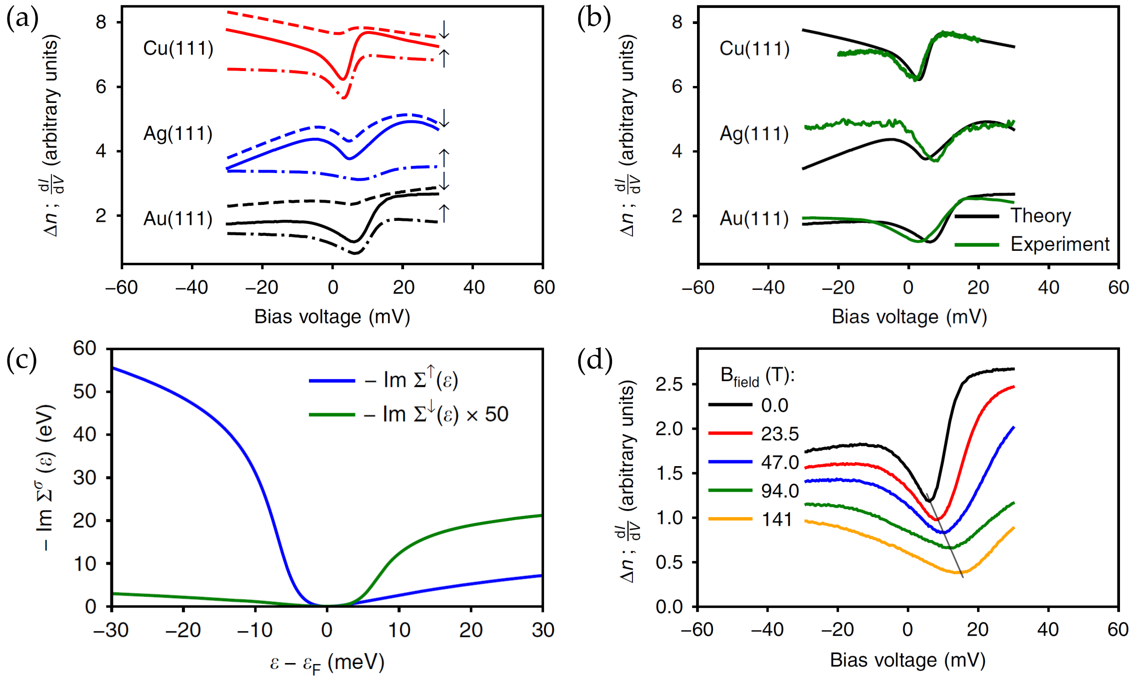

Figure 4.1: (a) Simulated total (solid line) and spin-resolved (dashed lines) LDOS above the Co atom on Cu, Ag, and Au(111), where ↑ (↓) denotes the majority (minority) spin channel. While the minority spin channel only exhibits a single step originating from intrinsic spin excitations, the majority spin channel additionally exhibits a positive-bias step inconsistent with conventional spin excitations, which is attributed to a localized state called "spinaron". (b) Comparison of the derived LDOS with experimental data. (c) Calculated self-energy, reflecting the asymmetry of the spin excitation signal at positive and negative bias voltage in (a). (d) In an external magnetic field, the calculations predict a shift of the spinaron to positive bias voltages in $\mathrm{d}I/\mathrm{d}U$ measurements, leading to an overall shift of the ZBA to higher energies. *Reprinted from Ref. [64] under a Creative Commons Attribution 4.0 International License (CC BY 4.0 [165]). The experimental data in (b) is adapted with permission from IOP Publishing for Cu (Ref. [85]) and Au (Ref. [153], ©2005 The Japan Society of Applied Physics), as well as from Springer Nature for Ag (Ref. [166]) under a Creative Commons Attribution 4.0 International License (CC BY 4.0 [165]).*

densities of states of the two spin channels, this electron–hole pair formation can have different probabilities for the different excitation processes, which leads to an asymmetric spin excitation LDOS with respect to zero bias.[1] This is in contrast to the conventionally observed symmetric $\mathrm{d}I/\mathrm{d}U$ signal as displayed e.g. in Figure 2.4 for Fe atoms on a layer of $\mathrm{Cu_2N}$.

---

[1] Within these calculations, spin excitations do not necessarily show up as steps in the differential conductance, but can also lead to more intricate signals as was shown for e.g. Cr/Nb(110) [164] and Ti/Ag(001) [64].

To estimate the differential conductance measured by STS above the Co atom, the LDOS in vacuum at the assumed tip position is calculated according to the Tersoff-Hamann model (cf. section 3.1). The resulting total as well as spin-resolved vacuum LDOS is displayed in Figure 4.1(a) (note that here the majority (minority) spin is indicated by ↑ (↓)). In agreement with the introduction of spin excitations in section 2.2, the minority $\mathrm{d}I/\mathrm{d}U$ signal hosts a single step at positive bias voltage, best seen for Co/Cu(111), originating from the intrinsic spin excitations of the atom. The majority spin channel shows the corresponding step at negative bias voltage, but additionally exhibits a step-like feature at positive bias voltage. This rise in the $\mathrm{d}I/\mathrm{d}U$ signal is explained by an electronic bound state, localized at the Co atom adsorption site due to the electron−spin excitation interactions. One might think of this effect as a change in the electronic environment caused by the fluctuations of the adatom spin and mediated via the spin-orbit coupling [167]. If this change of the electronic structure reduces the local potential for the conduction electrons, they can effectively bind to the spin excitations of the adatom [64]. In the style of other quasiparticles, such as the polaron, where electrons couple to vibrations in a crystal lattice, this bound state resulting from the coupling of electrons and spin excitations is named "spinaron".

The total vacuum LDOS exhibits an astonishing similarity to the experimental data for Co on Cu, Ag, and Au(111) as shown in Figure 4.1(b). Although the overall shape is similar to a Fano resonance, the above discussion suggests that the observed ZBA originates from intrinsic spin excitations (SE) appearing at positive bias for the minority spin channel and negative bias for the majority spin channel in combination with an energetically and spatially localized electronic state, the spinaron, that also emerges in the majority spin channel. In the following sections, this explanation will therefore be referred to as the "SE & spinaron model".

The authors of Ref. [64] present various experimental approaches that could allow to verify their theory: The (theoretically) simplest is to measure the spin-resolved LDOS by SP-STS to observe the different contributions of the minority and majority electrons to the ZBA. Contrary to the SE & spinaron model, the Kondo effect is expected to show exactly the same signal for both spin channels in the absence of a magnetic field. Yet, in contrast to theory, experiments require an external field to define the quantization direction. Further, SP-STS data is never fully spin-polarized, complicating the analysis of the experimental results. A second suggestion is to monitor the behavior of the ZBA in the presence of a magnetic field. Contrary to the Kondo effect or simple spin excitations, which both exhibit a symmetric splitting around zero bias for increasing field strength, the spinaron is predicted to shift to higher energies without splitting, resulting in an overall shift of the ZBA to positive bias voltages as displayed in Figure 4.1(d). Although the fields applied in this calculation are significantly higher than experimentally available, one can expect to observe a shift of a few meV in fields of about 10 T.

Both approaches were experimentally realized in this work and will be presented in the following.

4.2 The Co/Cu(111) system in zero magnetic field

The most suitable platform to experimentally test the hypotheses of the SE & spinaron model appears to be the Cu(111) surface, as Co/Cu(111) shows the narrowest ZBA [35], offering the best possibility to observe the predicted effects of an external magnetic field on the measured differential conductance. Further, Co/Cu(111) exhibits no or only very little dependence of the ZBA shape on the atom's adsorption position, contrary to Co/Ag(111) and Co/Au(111), where the surface state oscillation or surface reconstruction heavily influence the observed signal, as was discussed above [150, 159, 160] (for Co/Au(111) see also appendix B).

The Cu(111) surface (*MaTecK GmbH*) was cleaned by Ar-sputtering at 0.5 keV and subsequent annealing at 500 °C for 25 min. Co atoms were evaporated from a Co rod (*Alfa Aesar*, 99.995 %) onto the Cu surface at a sample temperature of 4.2 K, resulting in a coverage of 0.01 atoms/nm^2.

Figure 4.2(a) displays a topographic scan of the resulting surface, were the Co atoms appear as protrusions of about 70 pm (cf. panel (d)) and are surrounded by the standing wave pattern formed by the Friedel oscillations of the Cu(111) surface state [168]. The ZBA, that was so far interpreted as a Fano curve caused by the presence of a Kondo resonance, is revealed in a spectroscopy measurement atop a single Co atom on the clean surface displayed in Figure 4.2(b). A fit of the data according to Equation (2.12), consistent with the Kondo picture, is presented in the same panel and determines the ZBA center at $E_0 = (2.6 \pm 0.1)$ mV and a width of the ZBA of $\Gamma \approx (4.7 \pm 0.1)$ mV. The line shape factor q of the fitted Fano resonance is 0.29 ± 0.01. All parameters agree well with earlier studies [34, 35, 156]. Yet, as already shown in previous works, it is not possible to perfectly fit the ZBA of Co/Cu(111) with a Fano line shape over the full range of the spectrum [35, 169], contrary to e.g. the ZBA of Co/Au(111) [33]. Differential conductance data with changing lateral and vertical tip–sample distance, d and Δz, respectively, are presented in Figure 4.2(c) and (d). Comparison of these experiments with the data presented in Refs. [35, 155] serve as an additional control to validate the experimental setup, but also to exclude potential unknown influences on the ZBA shape, that might corrupt the results presented in the following sections. The latter can be dismissed from a qualitative assessment of the data in panels (c) and (d), as no significant change (especially in comparison to the changes reported in section 4.3) of the ZBA line shape is observable for different tip–sample distances or within lateral distances comparable to the topographic radius

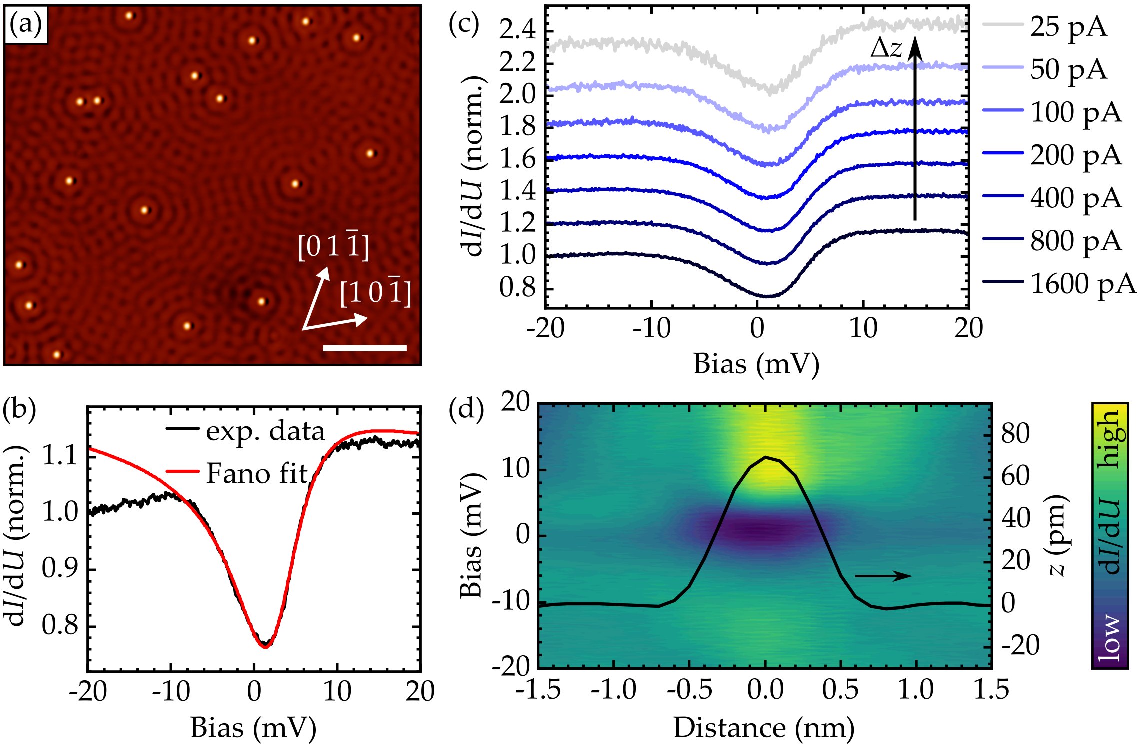

Figure 4.2: (a) Topographic scan of the Cu(111) surface with adsorbed Co atoms. The standing wave pattern formed by Friedel oscillations of the Cu(111) surface state is visible. Scale bar is 10 nm. (b) dI/dU spectrum recorded atop a single Co atom (black curve) fitted with a Fano curve (red line). The fit was performed in the range of $(-10, +10)$ mV. The fit parameters are specified in Figure 4.3. (c) Vertical tip−sample distance-dependent dI/dU measurements of the ZBA. The tip displacement scales linearly with the exponentially increasing tunneling current in steps of $\sim$ 30 pm. Spectra are vertically offset for clarity. (d) Conductance data from a line grid across a Co atom, the black line illustrates the corresponding topographic profile. Stabilization parameters: (a) $U = -20$ mV, $I = 400$ pA; (b)-(d) -20 mV, 400 pA / as indicated, $U_{\mathrm{mod}} = 1$ mV. $\mu_0 H = 0$ T; $T = 1.4$ K.

of the Co atom of about 0.4 nm. For a quantitative comparison with the works mentioned above, the data was fitted equally to the fit shown in panel (b) and the extracted parameters are shown in Figure 4.3. As already reported in Ref. [155], only little change of the ZBA anomaly is detected when changing the tip−sample distance. Most notably, q is continuously reduced with increasing Δz, which would indicate reduced tunneling into the Kondo state within this picture. For increasing lateral distance, q similarly decreases, which, within the Kondo picture, could again be explained by a decreased tunneling into the Kondo state. The same trend was reported in Ref. [35]. Although these findings can be rationalized within the Kondo picture, they are insufficient to confirm it. While Γ remains

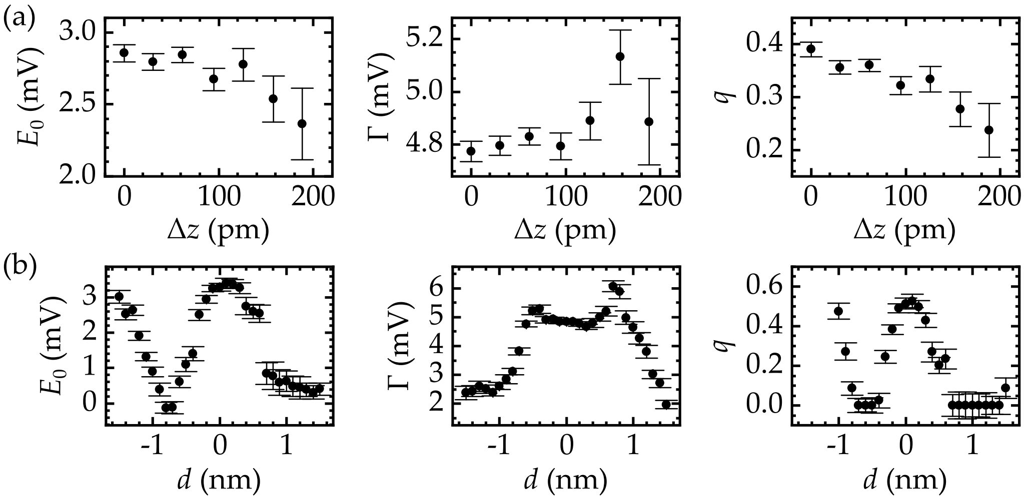

Figure 4.3: Fit parameters of the (a) vertical and (b) lateral tip–sample distance-dependent measurements displayed in panels (c) and (d) of Figure 4.2, respectively. Error bars represent the standard errors of each fit parameter.

almost constant within ±0.5 nm around the Co atom, the center of the ZBA shifts to smaller energies, which is unexpected in the Kondo picture, but might be explainable by changing contributions of the spin excitations and spinaron suggested within the SE & spinaron model of Ref. [64]. Simulations of this distance dependence in both models might give further insight into the system. For the lateral distance-dependent data, it is important to notice that for $d \gtrsim 0.5$ nm, the ZBA is strongly suppressed, i.e. the fitting is strongly influenced by the standing wave pattern formed by the surface state close to E_F. This is evident from the strongly asymmetric line shapes in Figure 4.3(b) and prevents a meaningful evaluation of the data at larger distances.

The zero-field measurements reported here agree well with previous studies of Co/Cu(111), yet do not allow to discriminate between the two existing explanations for the observed ZBA. This issue will be addressed in the following two sections.

4.3 THE CO/CU(111) SYSTEM IN AN EXTERNAL MAGNETIC FIELD

The shift of the ZBA on single Co atoms on the noble metal (111) surfaces in an external magnetic field was suggested to be one of the key signatures to confirm the SE & spinaron model [64]. Here I present measurements atop single Co atoms performed in an out-of-plane field of up to 12 T.

Figure 4.4(a) displays conductance spectra recorded atop the same Co atom at 0 T, 6 T, 8 T, 10 T, and 12 T. While the overall shape of the ZBA remains mostly

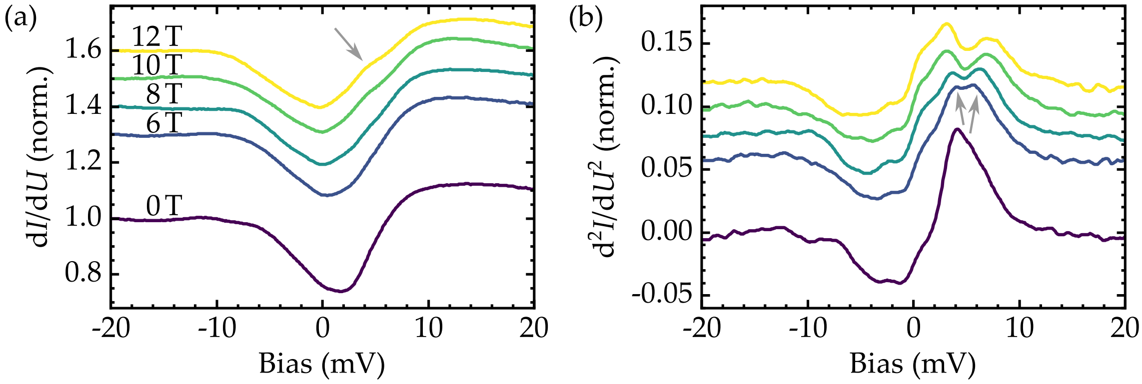

Figure 4.4: (a) Differential conductance spectra taken atop a single Co atom in an out-of-plane external magnetic field of up to 12 T. The gray arrow indicates the appearance of a kink in the rising edge of the ZBA at high magnetic fields. (b) Numerically calculated derivative of the data in (a). The kink in the $\mathrm{d}I/\mathrm{d}U$ signal is translated into a split peak as indicated by gray arrows. All spectra are vertically shifted by (a) $0.05\mu_0 H$ and (b) $0.01\mu_0 H$. Stabilization parameters: $U = -20$ mV, $I = 1$ nA, $U_{\mathrm{mod}} = 0.5$ mV. $\mu_0 H$ as indicated; $T = 1.4$ K.

unchanged, one can identify a kink appearing in the rising edge of the ZBA at fields ≥ 8 T which is marked by a gray arrow. The same measurements were conducted on four additional Co atoms as well as for the opposite field direction, all yielding the same result (see also Figure 4.7 and appendix A). The kink becomes more evident in the numerically calculated derivative of the differential conductance, displayed in Figure 4.4(b). In the $\mathrm{d}^2I/\mathrm{d}U^2$ signal, the falling edge of the ZBA appears as a dip that generally maintains its shape, showing only a slight broadening with increasing field. Contrary, the peak originating from the rising edge in the $\mathrm{d}I/\mathrm{d}U$ signal splits into two peaks.

These findings are now compared to the two prevailing theoretical models: In a first approach, the effect of the magnetic field on a Kondo resonance can be modeled by simply changing E_{K} to $E_{\mathrm{K}}(H) = E_{\mathrm{K}}(0) \pm g\mu_{\mathrm{B}}\Delta S \mu_0 H$ with $\Delta S = 1$. Here, potential changes of e.g. the resonance line shape or width, as shown in Ref. [78], are neglected. Especially altering the line shape as a function of the magnetic field will definitely modify the resulting spectrum, yet without theoretical background all attempts in this direction are speculative. Figure 4.5 depicts the splitting of a Fano resonance that is based on a fit of the zero-field measurement as presented in Figure 4.2(b). The Landé-factor was set to 4 to achieve a reasonably close correspondence to the experimental data. This choice will be further supported by the analysis in the subsequent paragraph. The splitting of the individual Fano resonances displayed as dashed lines is well seen in the $\mathrm{d}I/\mathrm{d}U$ signal in Figure 4.5(a) by the dashed lines that indicate the individual contributions. Nevertheless, to assess the agreement of the Kondo

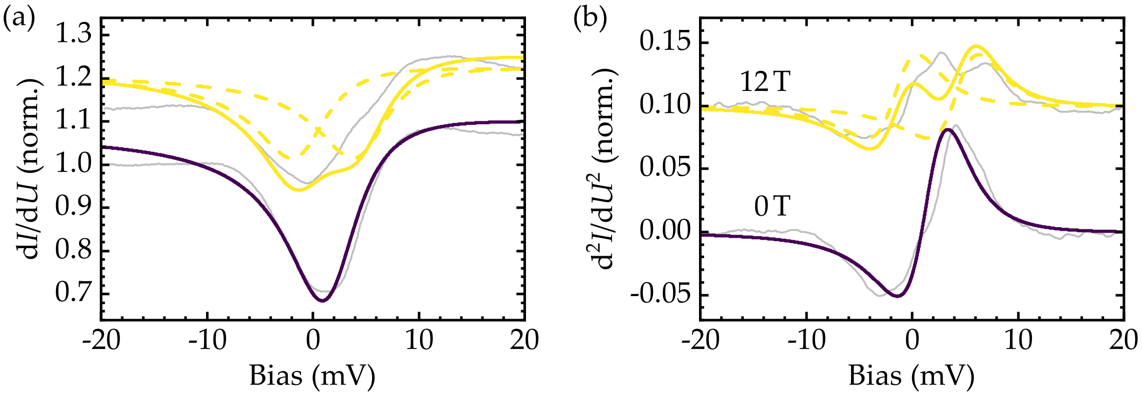

Figure 4.5: (a) Modeled magnetic field splitting of a Fano line originating from a Kondo resonance. The purple curve represents a fit to the zero-field data recorded atop a Co atom (gray line). The obtained curve is consecutively split according to the Zeeman energy with a Landé-factor of 4 (see main text). The full yellow line displays the resulting resonance at 12 T, dashed lines depict the individual contributions of the shifted Fano curves. For comparison, the experimental data at 12 T is presented. (b) Numerically calculated derivative of the data in (a).

model with the experimental data, it is helpful to again turn to the d^2I/dU^2 signal, which is displayed in Figure 4.5(b). Although equally to the experimental data, the model exhibits two peaks at positive energy at 12 T, the peaks' characteristics differ strongly from the experimentally observed d^2I/dU^2 signal. First, it is evident that the peaks' intensity or spectral weight is reversed in comparison to the experimental curves. Measurements on Co/Au(111) exhibited the same spectral weight distribution as the data on Co/Cu(111) (see appendix B). Due to the overlap of the falling edge of the Fano resonance that is shifted to higher energies and the rising edge of the one shifted to lower energies in the model, the latter is suppressed in the dI/dU signal and consequently the amplitude of the resulting peak in the d^2I/dU^2 signal is reduced. This is a common feature arising for all values of $q < 1$ and is in strong contrast to the experiment, where the low-energy peak is more intense than the high-energy peak. Further, the splitting of the peaks in the modeled Fano resonances is mostly symmetric (as imposed by the model and expected for a Kondo resonance), although the overlap of the two Fano curves slightly shifts both maxima at positive bias in the d^2I/dU^2 signal to slightly lower energies. Contrary, the experimentally observed splitting is strongly asymmetric with the low-energy peak shifting significantly less (to lower energies) than the high-energy peak (to higher energies). Hence, at least within the simple Kondo model employed here, where only E_K is changed with the external field, the experimental data cannot be explained.

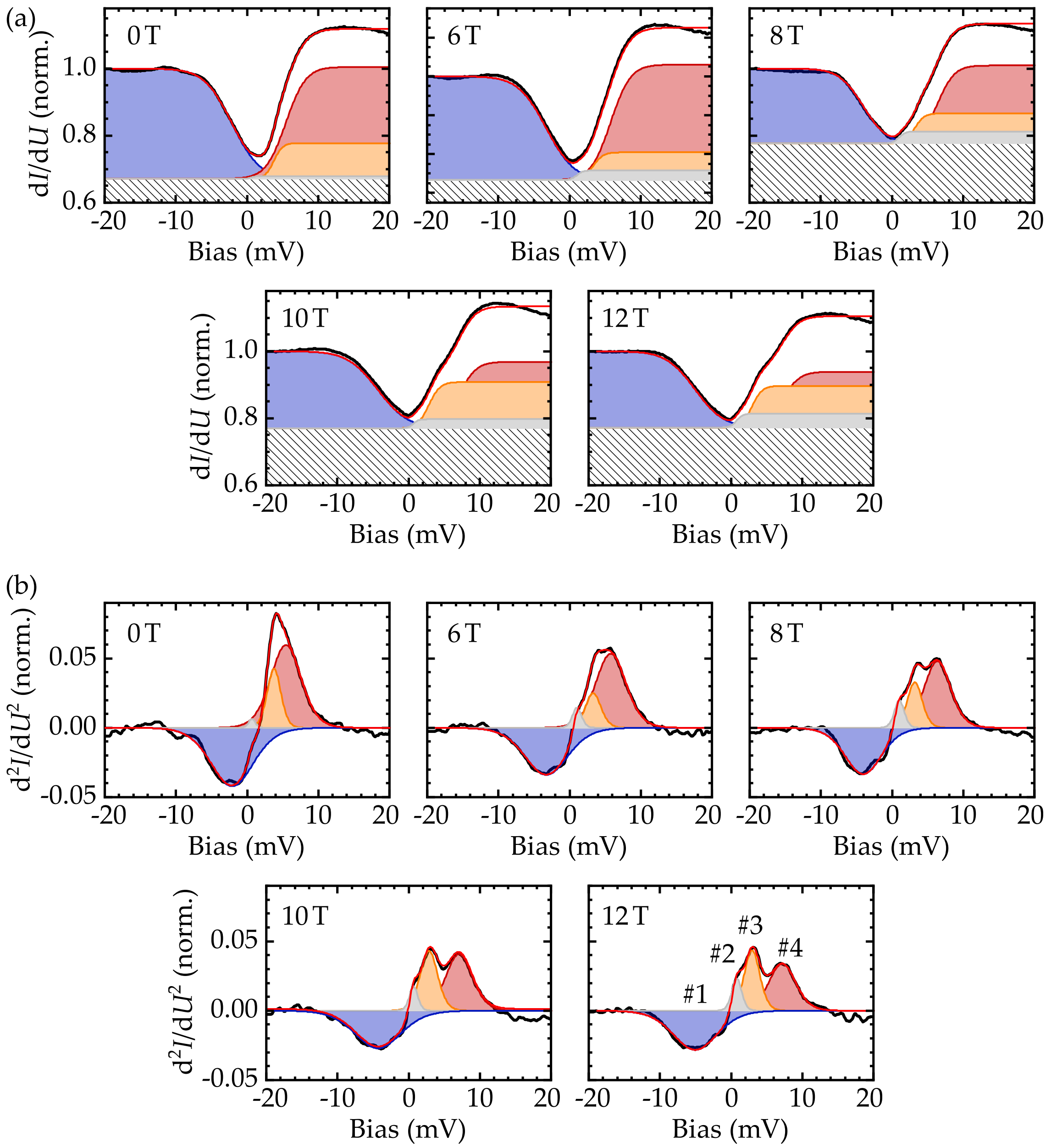

Figure 4.6: Results of the fit using four independent inelastic excitations (Equations (3.12) and (3.13), see main text). The striped area in (a) indicates the conductance offset that was added to the fit performed on the d$^2I/$dU^2 data displayed in (b), which accounts for the contribution of elastic tunneling. The color code as well as the numbering introduced in the bottom right panel of (b) is used to distinguish the contributions in the text and Figure 4.7.

Following Ref. [64], the predicted presence of the spinaron in the SE & spinaron model should induce a shift of the ZBA to higher energies. Yet, opposed to the calculations, where fields of up to 141 T were considered, the experimental data does not produce a significant shift of the ZBA.[2] Nevertheless, the changes in the ZBA line shape are further assessed in terms of the SE & spinaron model. As introduced in section 3.1.1, inelastic tunneling of electrons exciting e.g. spin excitations leads to steps in the $\mathrm{d}I/\mathrm{d}U$ and dips/peaks in the $\mathrm{d}^2I/\mathrm{d}U^2$ signal at the excitation energy. Hence, two of the observed features in the experimental $\mathrm{d}^2I/\mathrm{d}U^2$ signal, more precisely the dip at negative bias and one of the two peaks at positive bias, might be attributed to the intrinsic spin excitations of the Co atom and should therefore be described according to Equations (3.12) and (3.13). The specific description of the line shape of the spinaron signal is unknown. Yet, the calculated conductance signal displayed in Figure 4.1(a) exhibits a step like feature similar to an inelastic excitation in the majority spin channel at positive bias, which originates from the spinaron. It seems thus justified to qualitatively model the spinaron signal in the differential conductance with the same equations as the presumed intrinsic spin excitations. Careful examination of the experimental data in Figure 4.4(b) indicates that these three contributions are insufficient to fully describe the data. All $\mathrm{d}^2I/\mathrm{d}U^2$ curves exhibit a shoulder close to zero bias, that needs to be included in the description. Due to lacking additional information, this shoulder is also fitted according to Equations (3.12) and (3.13), a choice that can be justified by the interpretation of this feature suggested below.

The results of the proposed fitting model are presented in Figure 4.6. The fitting process was performed on the $\mathrm{d}^2I/\mathrm{d}U^2$ data and the corresponding $\mathrm{d}I/\mathrm{d}U$ curves were obtained by integration and addition of a suitable conductance offset. Excellent agreement between the suggested fit and the experimental data is obtained that allows to track the energetic position of the proposed excitations and states with increasing magnetic field. For this purpose, the extracted center of each peak or dip is plotted as a function of $\mu_0 H$ in Figure 4.7, also containing the results of four additional Co atoms (cf. appendix A). Line fits describing the Zeeman shift of the individual features are displayed in black and yield the parameters listed in Table 4.1. Except for peak #2 (light gray), which appears at about 1 mV, all peaks shift as a function of the magnetic field. This allows to conclude that contrary to all other peaks, peak #2 is of non-magnetic origin and might be explained by e.g. a vibrational mode of the adatom–surface system [170]; phonon modes of the pure surface can be excluded as they were shown to occur at energies > 5 meV in IETS experiments [171, 172]. The slopes $\mathrm{d}U/\mathrm{d}H$ of peaks #1 (dark blue) and

---

[2] Fitting the data with a single Fano resonance, which is from a physics point of view not meaningful within the SE & spinaron model, but allows to follow the overall curve shape, even yields a shift of the ZBA center to lower energies of about -0.2 mV/T to -0.3 mV/T. See also appendix A.

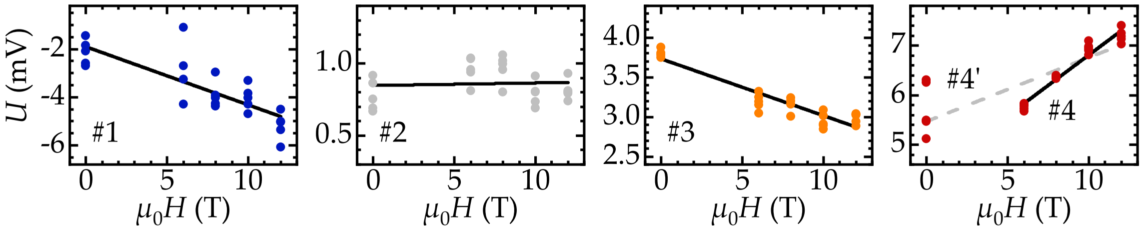

Figure 4.7: Energetic position of the excitations extracted from the fits presented in Figure 4.6 and Figure A.2 for five different Co atoms. The color code is the same as in Figure 4.6. For peak #4 (red), fits were performed over all data points (gray dashed line) and after excluding the data at 0 T (black line) (see also footnote in main text). The resulting fit parameters are summarized in Table 4.1.

#4 (dark red) exhibit the same absolute value, but opposite sign.[3] This behavior is expected for spin excitations (cf. section 2.2). Extracting the corresponding Landé-factor (with $\Delta S = 1$ for all spin excitations), one obtains $g \approx 4$, the same value employed to model the split Fano resonances in the previous paragraph. However, the zero-field positions of the dip and peak are not symmetric with respect to E_F, contradicting any inelastic excitation process in STM. Hence a direct assignment of these two peaks to the intrinsic spin excitations is not possible. Finally, peak #3 (orange) shifts to lower energies with increasing external magnetic field, yet with a much lower slope. Identifying this peak with the spinaron leads to a qualitative contradiction with theory, as the calculations anticipate a shift to higher energies. Although this prediction might be sensitive to details that are hard to determine unambiguously in the first-principles approach employed in Ref. [64], such as the energetic position of the d orbitals with respect to the Fermi level, this discrepancy between experiment and theory prevents at this point the confirmation of the suggested SE & spinaron model.

I would like to point out again that the choice of mathematically describing the line shape of the potential spinaron in the dI/dU and d^2I/dU^2 signal in the same way as intrinsic spin excitations is only an "educated guess" and is caused by a lack of more detailed information. In the calculations, it is not possible to disentangle the intrinsic spin excitation in the majority spin channel from the spinaron. Hence, choosing a different, potentially better suited line shape might seriously change the result of the fits presented here.

---

[3] Note that for fitting the data of peak #4, all data points at 0 T were excluded, as they evidently do not fall on the same line as the other points. One reason might be the overlap of peaks #3 and #4 at zero field, resulting in a larger uncertainty of the fit, reflected also in the large spread of extracted values for peak #4 at 0 T.

Table 4.1: Field-induced shift and zero-field position of the excitations as extracted from fits in Figure 4.7. For peak #4, the fit parameters for both lines displayed in Figure 4.7(d) are indicated.

Peak #	Slope (mV/T)	Position at 0 T (mV)
1 ●	-0.24 ± 0.04	-1.9 ± 0.3
2 ●	0.002 ± 0.006	0.85 ± 0.05
3 ●	-0.071 ± 0.006	3.73 ± 0.05
4 ●	0.24 ± 0.01	4.4 ± 0.1
$4'$ ●	0.13 ± 0.02	5.5 ± 0.1

The presented discussion of the field-dependent measurements demonstrates that other experiments are necessary to confirm or discard one or the other explanation for the ZBA in Co/Cu(111).

4.4 Spin-polarized measurements

The second experimentally accessible signature of the spinaron is its spin polarization, which is predicted to have a majority character, contrary to the intrinsic spin excitation at positive bias, which has a minority spin character. The spin polarization of the SE & spinaron model also manifests a qualitative difference from the Kondo model, where the spin-resolved minority and majority LDOS are fully symmetric with respect to E_F. Hence, performing SP-STS measurements in an external field that energetically splits the occurring states is expected to yield further insight into the physics of the Co/Cu(111) system.

4.4.1 *Preparation and characterization of spin-polarized tips*

The possibilities to prepare spin-polarized tips were already mentioned in section 3.1.2. As the proposed spin-sensitive measurements will be performed in an external field of 12 T, the favorable choice is a paramagnetic tip, that can be realized by picking up individual magnetic atoms or small clusters [81]. Coated or bulk magnetic tips might show unexpected and more importantly uncontrollable magnetization switching at such high field strengths.

The initial method of choice to prepare and characterize such tips was to pick up magnetic 3*d* atoms from Cu_2N grown on Cu(001), a procedure that has been shown to routinely result in tips with a spin polarization of $\eta_t > 30\ \%$ [78, 81, 124]. To this end a clean Cu(001) surface (see section 9.1 for the preparation of the Cu(001) surface) was sputtered in an N_2 atmosphere (3×10^{-6} mbar) at 0.5 keV for 60 s at a substrate temperature of 300 °C. The sample was afterwards post-annealed at the same temperature for 5 min. This process followed the

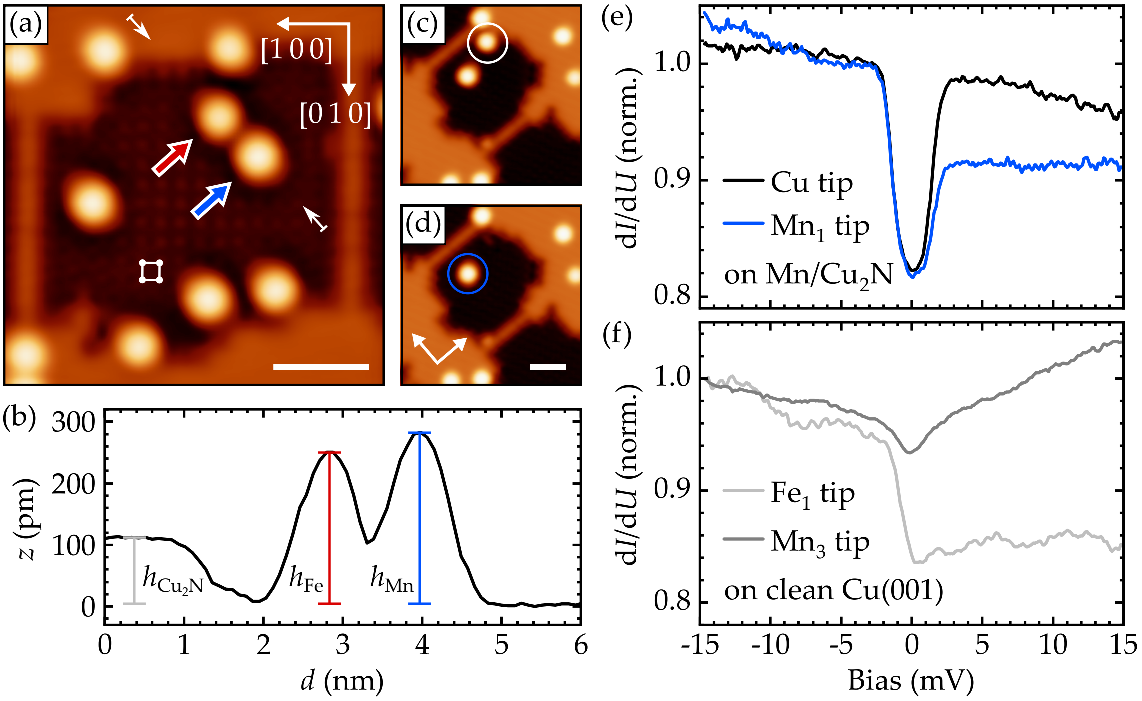

Figure 4.8: (a) Constant-current scan of a Cu_2N patch on the Cu(001) surface with adsorbed Fe (red arrow) and Mn atoms (blue arrow). The Cu_2N unit cell is indicated. White arrows mark the position of the line profile displayed in (b). (c),(d) Scans before and after picking up the Mn atom marked with a white circle. All scale bars are 2 nm. (e) $\mathrm{d}I/\mathrm{d}U$ signal recorded on the Mn atom marked with a blue circle in (d) before (black line) and after (blue line) picking up a Mn atom onto the tip. (f) Spectra recorded on the clean Cu(111) surface measured with tips functionalized with different magnetic atoms. Stabilization parameters: (a) $U = -5$ mV, $I = 5$ nA; (c)-(f) -15 mV, 1 nA, $U_{\mathrm{mod}} = 0.5$ mV. $\mu_0 H = 12$ T; $T = 1.4$ K.

procedure described in Ref. [173]. After cooling the sample to 4.2 K, Fe (*Alfa Aesar*, 99.995 %) and Mn atoms (*Mateck GmbH*, 99.8 %) were deposited from a 4-cell electron-beam evaporator (*Oxford Applied Research*) with a coverage of about 0.05 atoms/nm^2. A topographic scan of a single Cu_2N patch with several adatoms is presented in Figure 4.8(a). The Cu_2N layer appears as an almost square depression with depth $h_{Cu_2N} \approx 120$ pm. The Cu_2N unit cell with lattice constant $a_{Cu_2N} = a_{Cu} = 360$ pm, where a_{Cu} is the lattice constant of Cu, is well seen. Fe and Mn atoms can be distinguished by their apparent height, $h_{Fe} \approx 250$ pm and $h_{Mn} \approx 280$ pm, as shown in Figure 4.8(b), and their characteristic spin excitation spectra (cf. Figure 2.4 for Fe and Figure 4.8(a) for Mn). Atoms were picked up by stabilizing the tip above the atom at $U = -15$ mV and $I = 0.4 - 1$ nA, approaching by -100 pm with opened feedback loop, and applying a short voltage pulse of $+4$ V to $+5$ V. A successful pick-up sequence of a single Mn

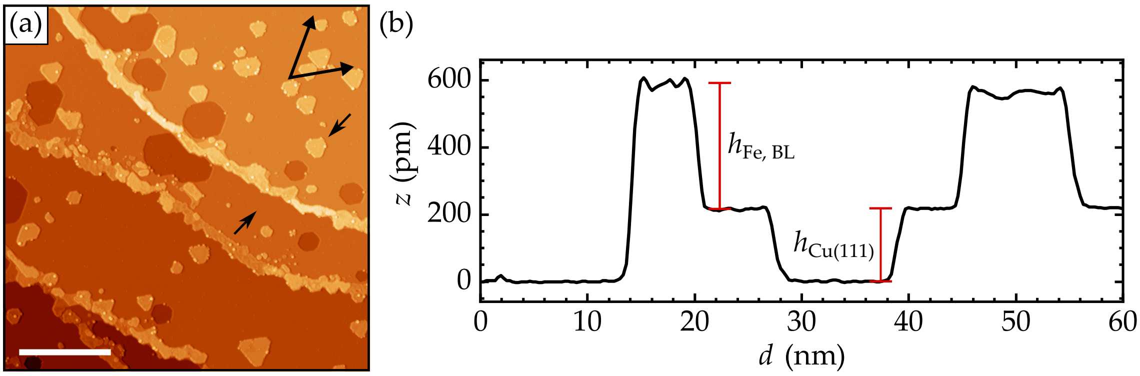

Figure 4.9: (a) Topographic scan of the Cu(111) surface decorated with Fe islands. Scale bar is 50 nm. (b) The line profile taken in between the black arrows in (a) reveals a bilayer height of the Fe islands. The large hexagonal Cu vacancy islands created upon the Fe deposition exhibit a monolayer depth. Scan parameters: $U = -50$ mV, $I = 50$ pA.

atom is presented in Figure 4.8(c)-(d). Following the transfer of the atom to the tip, the spectrum measured atop a second Mn atom exhibits a strong bias-dependent asymmetry as can be seen in Figure 4.8(e) in comparison to the spectrum recorded with a clean tip prepared on the Cu surface. As discussed in section 2.2, this asymmetry is expected for a spin-polarized tunneling current from a magnetic tip. However, the quantitative analysis of the spin polarization has to be done with care, as many of the tips functionalized with magnetic atoms showed a non-flat $\mathrm{d}I/\mathrm{d}U$ signal atop the clean Cu(001) surface as shown in Figure 4.8(f), that will contribute to the observed asymmetry on the studied atom. Similar features were found for tips functionalized with Fe, Mn, and also Co atoms or small clusters, and are assumed to result from an interaction of the magnetic atoms with the tip material, which, similar to a magnetic atom on a surface, can lead to Kondo resonances or spin excitations. This effect is especially problematic if the intensity of the sample LDOS feature under investigation is of the same magnitude as that of the feature in the tip DOS. Unfortunately, this is the case for Co/Cu(111), where the ZBA only accounts for about 20 % of the $\mathrm{d}I/\mathrm{d}U$ signal.

Therefore, a different approach was conceived for the spin-polarized measurements on Co/Cu(111): If it is possible to prepare the tip on the same surface used for the actual experiment, i.e. Cu(111) instead of Cu(001), one could perform the SP-STS measurements atop the same Co atom with different tips exhibiting different features in the tip DOS. In that case, one could conclude that features appearing in all measurements originate from the sample LDOS. For this purpose, Fe (*Alfa Aesar*, 99.995 %) was deposited onto the Cu(111) sample at room temperature [174, 175], forming bilayer high ($h_{\text{Fe,BL}} = 380$ pm) islands that covered about 25 % of the surface. The result is displayed in Figure 4.9(a) and (b). The STM tip

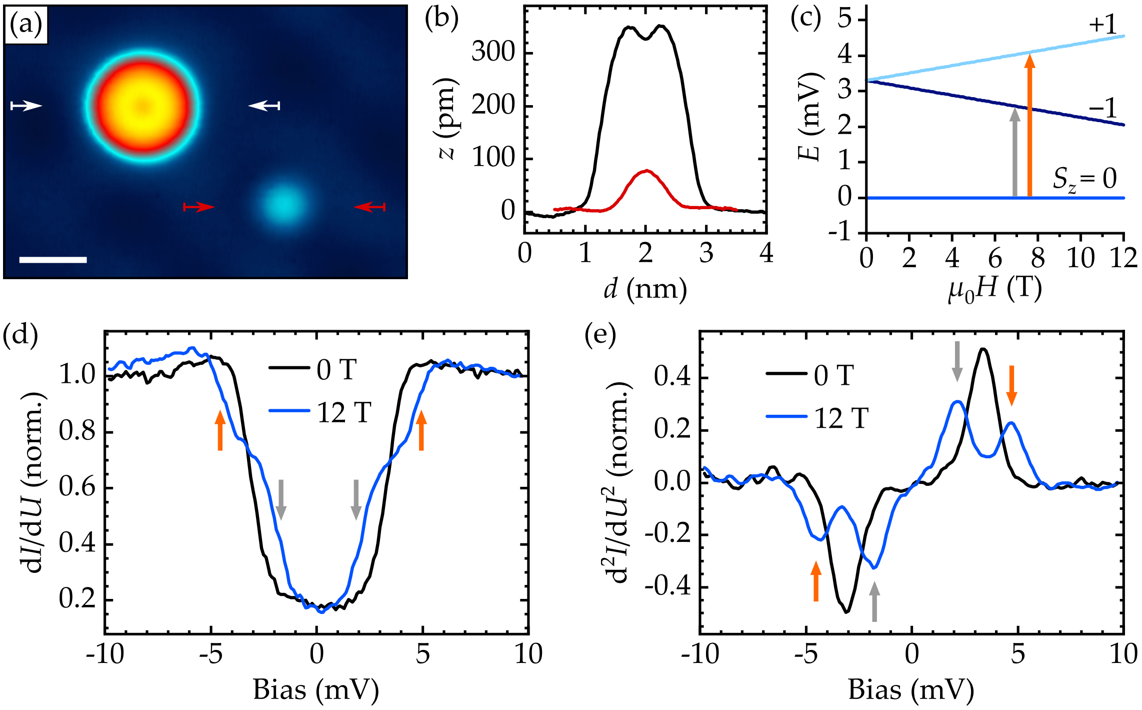

Figure 4.10: (a) Scan of a single Nc molecule and Co atom. Scale bar is 1 nm. (b) Line profiles across the Nc (black line) and Co atom (red line). (c) Energy of the $S_z = -1, 0, +1$ states as a function of magnetic field with anisotropy parameters as determined from a fit to the data in (d),(e): $D = 3.3$ meV, $E = 0.0$ meV, $g = 1.8$. (d) dI/dU and (e) numerically derived d^2I/dU^2 signal at 0 T (black line) and 12 T (blue line) recorded atop the Nc molecule with a spin-averaged tip. Arrows mark steps resulting from the transitions indicated in (c). Stabilization parameters: (a) $U =$ 20 mV, $I = 20$ pA; (d) −10 mV, 20 pA, $U_{\text{mod}} = 0.5$ mV. $T = 1.4$ K.

could then be dipped into these islands to pick up a small Fe cluster in order to create a spin-polarized tip.

In order to determine the spin polarization of the tip, a known reference system is necessary. In Refs. [41, 42], M. Ormaza *el al.* investigated spin excitations in a ($Ni(C_5H_5)_2$, $NiCp_2$), short nickelocene (Nc), molecule, that exhibits a spin of $S = 1$ and an in-plane magnetic anisotropy of about 3 meV on both the Cu(001) and Cu(111) surface. By approaching a Nc molecule adsorbed to an STM tip toward an Fe atom on the Cu(001) surface, the single spin excitation was shown to split as a function of the exchange coupling with the Fe atom, resulting in a strongly spin-polarized dI/dU signal [83]. Based on these properties, Nc constitutes an ideal reference system for the measurements presented in the following.

At ambient conditions, Nc (*Alfa Aesar*) forms a metallic-like shiny powder, that was filled into a UHV container under nitrogen atmosphere, which was subsequently

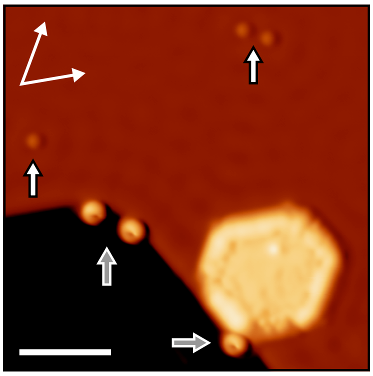

Figure 4.11: Scan of the same surface as shown in Figure 4.9 after deposition of Nc molecules (gray arrows) and Co atoms (white arrows). Nc molecules preferentially adsorb to the edges of the Cu vacancy islands, Co atoms are randomly distributed on the surface. Scale bar is 5 nm. Scan parameters: $U = -20$ mV, $I = 100$ pA.

connected to the STM chamber via a leak valve. The molecules were dosed onto the cooled Cu(111) surface by taking the sample out of the STM with the wobble stick and holding it in front of the opened leak valve ($p \approx 1 \times 10^{-10}$ mbar) for 60 s [176], resulting in a coverage of about ≤ 0.01 molecules/nm^2. On the clean surface, Nc appears as a fully isotropic ring with a height of about 350 pm, as shown in Figure 4.10(a),(b). Spin excitations that can be inferred from the energy diagram in Figure 4.10(c) lead to two (four) bias symmetric steps in the $\mathrm{d}I/\mathrm{d}U$ and corresponding dips and peaks in the $\mathrm{d}^2I/\mathrm{d}U^2$ signal at 0 T (12 T) as presented in Figure 4.10(d),(e). As the low-energy spin excitation (gray arrows) decreases the spin of the molecule, while the high-energy excitation (orange arrows) increases the spin, spin-polarized measurements are expected to alter the amplitude of both in the opposing ways. One expects that at negative bias the intensity of the high-energy excitation is increased and the intensity of the low-energy excitation is decreased for a tip probing mainly the majority spin channel; the opposite holds for positive bias.

On the surface decorated with Fe islands, the molecules prefer to adsorb to the edges of the Cu(111) vacancy islands (cf.Figure 4.9, $h_{\mathrm{Cu(111)}} = 215$ pm) that are created upon the Fe deposition, leading to a slightly distorted shape of the molecules, as can be seen in Figure 4.11. However, this change in adsorption site was shown not to alter the magnetic properties of the molecule. Solely a small enhancement of the spin-independent scattering term in Equation (2.10), apparent in an enhanced conductance above the IETS spin excitation steps, was determined (cf.Figure 4.12) [79, 176].

4.4.2 *Spin-polarized spectroscopy on Co/Cu(111)*

The setup for the following measurements was introduced in the previous section. Succeeding the Fe island and Nc deposition, single Co atoms were evaporated onto the cold surface as described in section 4.2. The resulting surface is displayed in Figure 4.11. To distinguish contributions of the tip and sample LDOS in the differential conductance spectra recorded on Co/Cu(111), measurements with

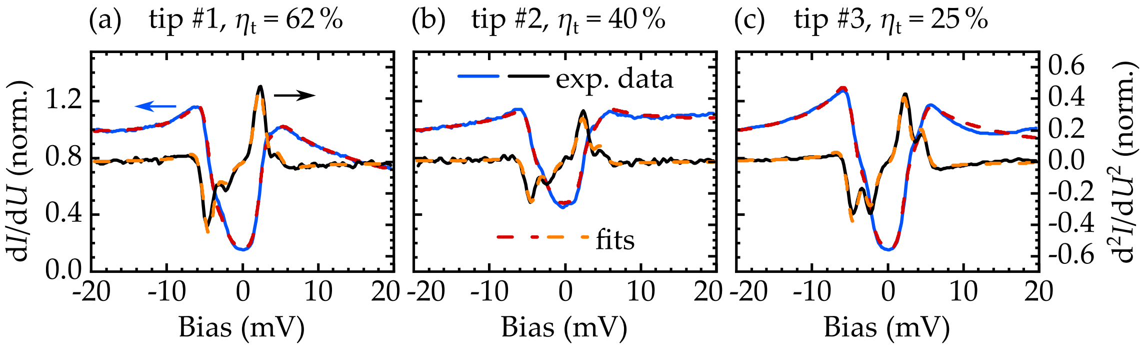

Figure 4.12: Differential conductance (blue lines) and numerically calculated $\mathrm{d}^2I/\mathrm{d}U^2$ signal (black lines) measured with different spin-polarized tips atop a Nc molecule. Dashed lines display fits to the data according to Ref. [79]. The extracted tip polarization is indicated. The less pronounced spin excitation signal in (b) is attributed to a measurement off the molecule's ring, where the IETS signal has been shown to be weaker [176]. Stabilization parameters: $U = -20$ mV, $I = 100$ pA, $U_{\mathrm{mod}} = 0.5$ mV. $\mu_0 H = 12$ T; $T = 1.4$ K.

three different microscopic tips are presented in the following. The tips were prepared by indentation into the Fe bilayer and care was taken that each tip showed a sharp topography and as small as possible spectroscopic features on the clean Cu(111) surface (cf. section 4.4.1). Spectra taken on Nc at $\mu_0 H = 12$ T displayed in Figure 4.12 demonstrate the spin polarization of these tips. Fits within the dynamical scattering model introduced by M. Ternes in Ref. [79] using the provided script allow to account for the overshooting conductance above the spin excitation energy caused by the spin-independent scattering of conductance electrons and yield a satisfactory agreement with the experimental data. The extracted spin polarizations of the three tips amount to 62 %, 40 %, and 25 %, respectively.[4] The fact that all polarizations are positive as defined in section 2.2 allows to conclude that all tips predominantly probe the majority spin channel of the sample in the bias range of -20 mV to $+20$ mV.

These tips were used to investigate the spin polarization of the observed features in Co/Cu(111). Corresponding STS data is presented in Figure 4.13(a), where the $\mathrm{d}I/\mathrm{d}U$ signal recorded atop a single Co atom (blue line) is displayed together with the $\mathrm{d}I/\mathrm{d}U$ signal measured on the bare surface (gray line) with the same tip. All spectra were recorded at 12 T to obtain a maximum splitting of the observed features above the Co atom. As mentioned in the previous section, the significant variation of the $\mathrm{d}I/\mathrm{d}U$ signal detected on the clean Cu(111) surface prevents an

---

[4] Although the script by M. Ternes does not provide the uncertainty of the fit, I expect it to be no less than 10 %, as the experimental overlap of both the spin excitations and the overshooting conductance above the spin excitations complicates the fit.

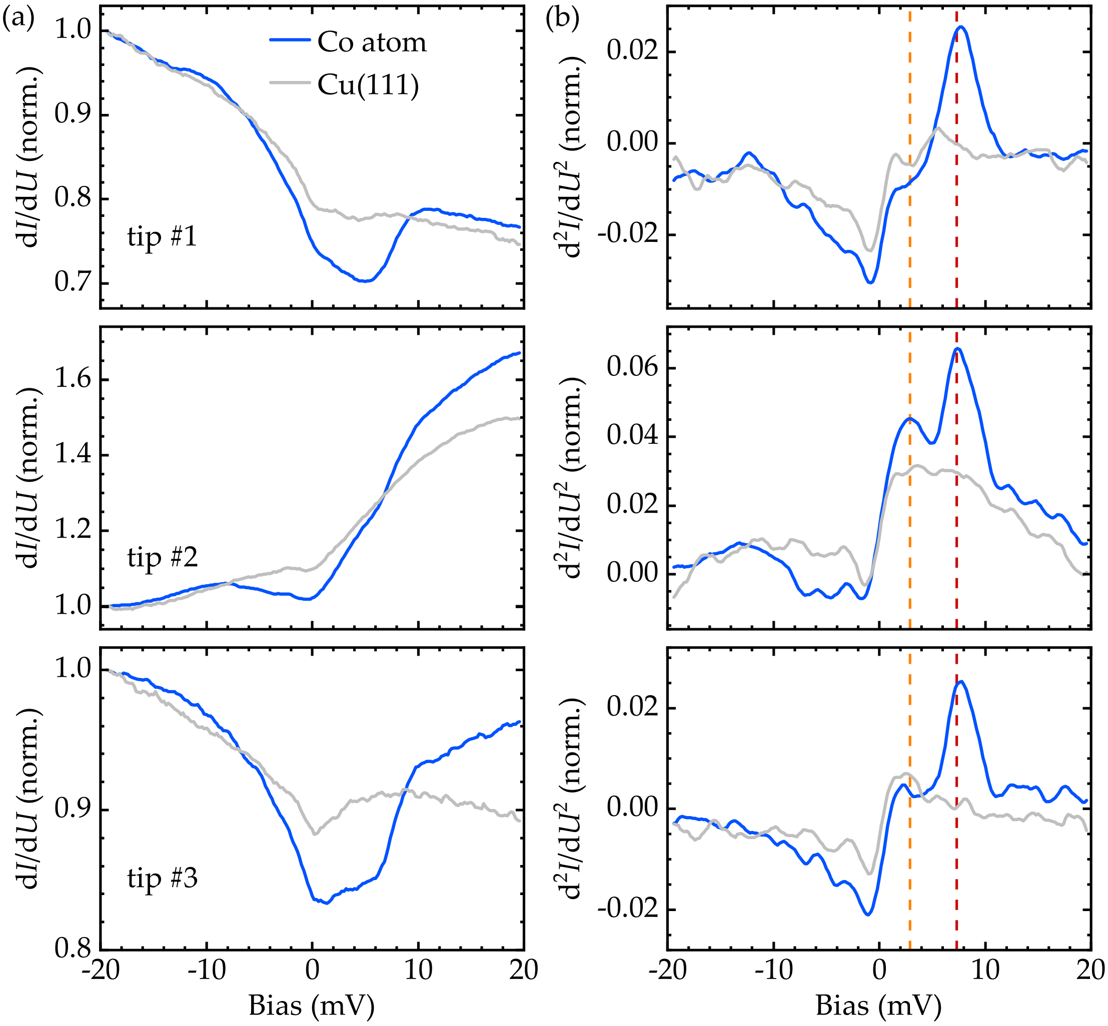

Figure 4.13: (a) Differential conductance and (b) numerically calculated d^2I/dU^2 signal measured atop single Co atoms (blue line) and on the clean Cu(111) surface with the spin-polarized tips presented in Figure 4.12. The dashed lines in (b) indicate the position of the positive-bias high- (red) and low-energy feature (orange) observed in the spin-averaged measurements. Stabilization parameters: $U = -20$ mV, $I = 400$ pA, $U_{\mathrm{mod}} = 0.5$ mV. $\mu_0 H = 12$ T; $T = 1.4$ K.

easy interpretation of the spectrum recorded on the Co atom. Once again, the numerically calculated derivative of the differential conductance displayed in Figure 4.13(b) allows to better separate the individual contributions. A significant part of the d^2I/dU^2 signal at negative bias is attributed to the tip DOS, as the spectra on Cu(111) and atop the Co atom exhibit very similar features at $U < 0$. Although the dip in the signal on Co/Cu(111) is slightly more pronounced for each tip, and hence a small falling step below E_F can be inferred for the dI/dU signal, it is difficult to assess the spin character of this feature. Contrary, the spectra taken on Co atoms and the bare Cu surface exhibit clear differences at positive bias and a strong contribution from the Co LDOS can be determined. Lines at the average position of the high- and low-energy feature found in the spin-averaged measurements (red and orange peak in Figure 4.6(b)) are displayed in all panels of Figure 4.13(b). In the spin-polarized $\mathrm{d}^2I/\mathrm{d}U^2$ signal, the peak at higher energy can clearly be identified, whereas the peak at low energy is only observed with tip #2, yet with a much lower intensity than the high-energy peak. This is in contrast with the spin-averaged data, where the low-energy peak exhibited a significantly larger spectral weight than the high-energy peak at $\mu_0 H = 12\,\mathrm{T}$. Based on the measurements on Nc, all tips are expected to enhance features in the majority spin channel of the sample LDOS, while those originating from minority states or excitations should appear with a reduced intensity.

To exclude an exchange interaction between tip and sample, that could result in an antiferromagnetic alignment of both by overcoming the ferromagnetic alignment dictated by the external field, and reverse the interpretation of the spin-polarized data, the tip–sample distance was tuned in the same range as presented in Figure 4.2(c). Based on the lacking change of the spectra, an exchange coupling, which would depend on the tip–sample distance, could be excluded. One notable oddity in the performed measurements is the fact that while although tip #3 displays the lowest spin polarization, tip #2 exhibits the smallest difference between the $\mathrm{d}^2I/\mathrm{d}U^2$ peaks' intensities. Instead, tips #1 and #3 produce very similar spectroscopic signals, despite a three times larger polarization extracted for tip #1. Nevertheless, the general observed picture can be traced back to spin-polarized tunneling, as a measurement with the same tip at zero field well reproduced the spectra observed with a Cu coated tip, such that effects based on e.g. the orbital character of the Fe cluster on the tip can be excluded. Conclusively, the high-energy $\mathrm{d}^2I/\mathrm{d}U^2$ peak is determined to result from a majority state or excitation in the Co LDOS, while the low-energy peak is attributed to a minority state or excitation.

4.5 Discussion

The experimental data obtained with spin-averaged tips at different magnetic fields up to 12 T was already discussed in light of both the Kondo effect as well as the SE & spinaron model in section 4.3. Both theories were unable to explain the experiments: Modeling the observed splitting of the measured spectra with a Fano resonance that fits the zero-field spectrum of Cu/Cu(111) failed to reproduce the asymmetric shift and spectral weights of the features in the $\mathrm{d}^2I/\mathrm{d}U^2$ signal. Describing the measured $\mathrm{d}I/\mathrm{d}U$ data in terms of excitations yielded three magnetic contributions. Yet, in contrast to the predictions of the SE & spinaron model, two of them were shown to move two lower bias voltages, while only one shifted to a higher bias voltage as a function of the applied field. Further, the splitting of those steps in the IETS signal, that could originate from the predicted intrinsic spin excitations, was shown not to be symmetric around E_F, an observation that is inconsistent with the basic theory of spin excitations.

A new puzzle arises from the spin-polarized measurements: The two most prominent features in the spin-averaged data appearing at positive bias move to lower and higher bias voltages with increasing field, respectively. Consequently, one would expect the first to be a majority state or excitation, that decreases its energy in an external field, while the latter would be expected to be a minority state or excitation. However, the spin-polarized measurements demonstrate the opposite. This behavior of a majority state/excitation moving to higher energies, and a minority state/excitation moving to lower energies can neither be explained by the $S = 1/2$ Kondo model nor by common spin excitations (cf. chapter 2). Only the spinaron is expected to be a majority state while showing a positive energy shift as a function of an external magnetic field. Hence, one could be tempted to actually assign the high-energy feature (red) in Figures 4.4 and 4.13 to this localized state created by the interaction of spin excitations and conduction electrons. Yet, in this case the origin of the other experimentally observed features would remain unexplained.

In conclusion, the experiments presented in this chapter are at this point incompatible with both existing models and suggest that the system of single Co atoms on the noble metal (111) surfaces is governed by even more complex physics than considered up to date. Hence, the question asked in the title of this chapter, whether Co atoms on the noble metal (111) surfaces constitute a prototypical Kondo system, can be negated. Yet, additional theoretical work is necessary to improve the understanding of the existing theories and to explore new potential explanations. Concerning the first, it might be helpful to artificially modify the results of the first-principle calculations to assess the stability of the model to changes of specific parameters and to thereby understand their impact on the results of the simulations. Still, the SE & spinaron model is the only approach that includes the shift of a majority states to higher energies in an external magnetic field. Ideas for a new approach explaining the experimentally observed behaviors might involve the Kondo screening of spins larger than $S = 1/2$, potentially via multiple (n) scattering channels. For $2S > n$, the Kondo impurity cannot be fully screened, such that a finite magnetic moment remains, which ferromagnetically couples to the electronic bath of the surface [86, 177, 178]. This state is called the *underscreened* Kondo effect and was experimentally observed in a molecular quantum dot transistor [179]. For $2S < n$, the impurity is overcompensated, resulting in the *overscreened* Kondo effect and an antiferromagnetic coupling to the conduction electrons [177, 178]. The response of such systems to an external magnetic field have been shown to differ from the conventional Kondo effect [179], which might

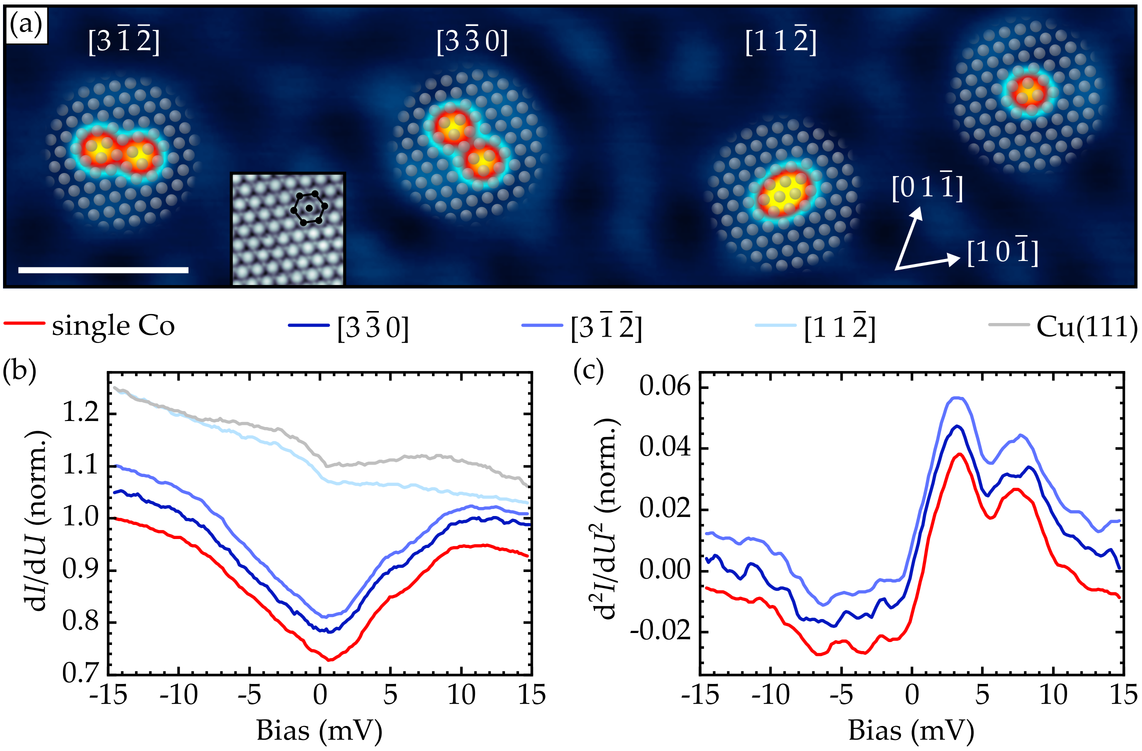

Figure 4.14: (a) Topography of Co dimers and a single Co atom assembled by atomic manipulation on the Cu(111) surface. For the manipulation, a setpoint of $U = -5$ mV, $I = 50$ nA was used. The positions of underlying Cu atoms and the dimer configurations are indicated. The inset shows a scan with atomic resolution obtained by manipulating a Co atom across the surface [181]. Scale bar is 3 nm. (b) Spectra recorded above the single Co atom, the created dimers, as well as the clean surface. (c) The numerically calculated $\mathrm{d}^2I/\mathrm{d}U^2$ signal of all ensembles exhibiting a ZBA demonstrate that the splitting of the ZBA remains unchanged down to interatomic distances < 1 nm. Stabilization parameters: (a) $U = -5$ mV, $I = 100$ pA; inset -5 mV, 40 nA; (b) -15 mV, 200 pA, $U_{\mathrm{mod}} = 0.5$ mV. $\mu_0 H = 12$ T; $T = 1.4$ K.

be an important aspect in the analysis of the experimental data presented in this chapter.

Further, STS data on Co/Cu_2N/Cu(001) [78] and Fe on Re(0001) [180] demonstrated the coexistence of a Kondo resonance and spin excitations. In these experiments both appeared as sharp features in the dI/dU signal and especially the low Kondo temperature and the negligible tunneling into states of the surface led to an easily identifiable zero-bias peak. Due to the suggested high Kondo temperature of Co on Cu, Ag or Au(111), a clear distinction of the different contributions would be experimentally difficult but might be possible in calculations.

Additional experimental efforts could aim at directly measuring the magnetic moment of the Co atoms as it is possible with XMCD [182]. By calculating the difference between absorption spectra of magnetic samples illuminated with left- and right-handed circularly polarized x-rays, this technique allows to assess the magnetic moment as well as magnetic anisotropy of a system [183]. Although XMCD has already been successfully applied to probe ensembles of dilute magnetic atom such as transition metal atoms on K and Na films [27], Co atoms on the Pt(111) surface [28], or Ho atoms on a bilayer of MgO on Ag(001) [7], no XMCD data on Co/Cu(111) is available in literature, which might be caused by the fact that Co atoms on the noble metal (111) surfaces where always considered as Kondo systems, hence exhibiting a zero magnetic moment, as well as by their high mobility and hence the required low experimental temperature.

Another potential approach is based on nanoscale transport measurements by the molecular nanoprobe (MONA), a technique developed by J. Kügel and M. Leisegang [184, 185]. MONA allows to measure charge transport across distances of less than 10 nm and with atomic precision [184] by detecting a charge current by the tautomerization of molecules that serve as detectors. By placing close-packed and larger distance dimers in between the STM tip, that constitutes the injection point of the charge carriers, and the detector molecule, one could determine the influence of the ZBA anomaly on the electric current, as the close-packed dimers do not exhibit any spectroscopic feature at E_F (cf. Figure 4.14). Ideally, one would perform the measurement at injection voltages close to 0 mV within $k_\mathrm{B}T_\mathrm{K}/e$, to mimic a conventional transport experiment with thermalized charge carriers. The currently available molecules for MONA experiments however exhibit too high activation thresholds [185]. Nevertheless, if the ZBA originates from a Kondo state, this high LDOS at E_F would increase the probability of inelastic scattering events of the hot electrons into states below the detection threshold [186] and would hence influence the observable charge transport.

Part II

YU-SHIBA-RUSINOV STATES IN MAGNETIC ATOMS ON A SUPERCONDUCTING SURFACE

Chapter 5

5 IN-GAP STATES ON SUPERCONDUCTING SURFACES

External magnetic fields and local magnetic moments lead to a variety of interesting phenomena in superconducting materials, ranging from vortices in type II superconductors over topologically trivial Yu-Shiba-Rusinov states to non-trivial Majorana fermions. This chapter will provide an overview over these effects, which become relevant in the discussion of the experimental results in the subsequent chapters. I will start by reviewing the basics of the BCS and Ginzburg-Landau theory in section 5.1, which form the groundwork for the later examined effects. Subsequently, I will introduce the formation of quasiparticle bound states in vortices in section 5.2, the appearance of Yu-Shiba-Rusinov states in proximity to magnetic impurities in superconducting host materials in section 5.3, and finally discuss the properties and possible experimental realizations of Majorana fermions in superconducting systems in section 5.4.

5.1 SUPERCONDUCTIVITY

After the experimental observation of perfect conductivity in mercury below its critical temperature $T_\mathrm{c} = 4.2$ K by H. Kamerlingh Onnes [187], W. Meissner and R. Ochsenfeld discovered the second unique characteristic of superconductivity in 1933: perfect diamagnetism [188]. These two experimental findings led to the phenomenological London equations by F. and H. London [189]:

$$\frac{\mathrm{d}\vec{j}_\mathrm{s}}{\mathrm{d}t} = \frac{n_\mathrm{s} e_\mathrm{s}^2}{m_\mathrm{s}} \vec{E} \tag{5.1}$$

$$\nabla \times \vec{j}_\mathrm{s} = -\frac{n_\mathrm{s} e_\mathrm{s}^2}{m_\mathrm{s}} \vec{B}, \tag{5.2}$$

with constants n_s, e_s and m_s for the superconducting charge carrier density, charge and mass, respectively. The first equation implies that a supercurrent of density $\vec{j}_\mathrm{s}$ is sustained without an externally applied electric field $\vec{E}$, indicating perfect conduction. The second equation tells that a magnetic flux $\vec{B}$ evokes a circulating current, which in turn generates a magnetization inside the superconductor that opposes the external field, such that the magnetic flux in the bulk material vanishes. The equation also shows that this screening current only develops at positions of finite flux. Hence the magnetic field needs to partially penetrate into the superconductor's surface to induce the current. By inserting Maxwell's equation $\nabla \times \vec{B} = \mu_0 \vec{j}_\mathrm{s}$ into Equation (5.2), one finds that an external field $\mu_0 H_\mathrm{x}$ parallel to a superconducting surface exponentially decays along the surface normal z:

$$B_\mathrm{x}(z) = \mu_0 H_\mathrm{x} e^{-z/\lambda_\mathrm{L}}. \tag{5.3}$$

The decay length is given by the London penetration depth

$$\lambda_\mathrm{L} = \sqrt{\frac{m_\mathrm{s}}{\mu_0 n_\mathrm{s} e_\mathrm{s}^2}}, \tag{5.4}$$

establishing a characteristic length for every superconductor. The second important length scale in superconductivity is the coherence length ξ, which defines at which distance from a perturbation a superconductor recovers its original properties. This quantity is a result of the Ginzburg-Landau theory that is discussed in the last part of this section. Before that, I will briefly introduce the BCS theory, which determines the microscopic understanding of superconductors. Refs. [70, 190–192] provide more detailed reviews of the BCS theory and the underlying formalism and served as the basis for the following section.

5.1.1 *The BCS theory*

The microscopic understanding of superconductivity, which constitutes itself in the BCS theory developed by J. Bardeen, L. N. Cooper and J. R. Schrieffer in 1957 [193], is based on earlier theoretical and experimental observations: As the transition from a normal metal to a superconductor below the critical temperature T_c strongly changes the electronic properties of the material, it was evident that the phase transition needs to induce significant modifications in the electronic system of the metal. In 1956, Cooper found that an arbitrarily small attractive interaction between two electrons suffices to reduce the electrons' energy, favoring a pairing of these electrons [194]. An answer to a possible origin of this interaction in superconductors is the isotope effect, which describes an experimentally found dependence of T_c on the atomic mass of the material [195, 196], suggesting phonons as a crucial ingredient in the formation of the electron pairs [197].
These findings enter the BCS theory: Starting point is the interaction of two electrons with opposite momenta k and $-k$ that are added to the filled Fermi sea. These electrons can be scattered into unoccupied states k' and $-k'$ via the

exchange of a virtual phonon within a narrow energy range equal to the phonons' Debye frequency ω_D and thereby reduce their energy by

$$\Delta E = \frac{2\hbar\omega_\mathrm{D}}{1 - \exp(4/V_0\rho_\mathrm{n}(E_\mathrm{F}))}, \tag{5.5}$$

forming a so-called Cooper pair. Here, $\rho_\mathrm{n}(E)$ is the density of states of the normal metal, which is considered to be constant close to E_F, and V_0 is a measure of the attractive interaction potential between the two electrons, which is assumed to be independent of k and k'. This second assumption implies that the spatial part of the Cooper pairs' wave function is isotropic and hence symmetric upon exchange of the two electrons. Therefore, the spin wave function must be asymmetric, resulting in a singlet state with an antiparallel alignment of the electron spins. In total, the Cooper pairs' spin is hence zero, allowing them to condensate into a common bosonic ground state. In real materials the interaction is not necessarily k-independent and can lead to non-isotropic, but still spatially symmetric wave functions like the d-wave pairing found in high-T_c superconductors [198–200], or even to asymmetric spatial and thus symmetric spin wave functions as I will discuss in section 5.4.

With this result of a finite attractive interaction between electrons leading to an energy reduction of the system by pairing electrons of momentum and spin k, σ and $-k$, $-\sigma$, one can expect that the ground state of a superconductor is formed by the creation of a finite number of Cooper pairs. Therefore, Bardeen, Cooper and Schrieffer suggested the following wave function of the BCS ground state:

$$|\phi_\mathrm{BCS}\rangle = \prod_k \left(u_k + v_k c^\dagger_{k\uparrow} c^\dagger_{-\mathrm{k}\downarrow}\right) |\phi_0\rangle \,. \tag{5.6}$$

Here, $c^\dagger_{k\sigma}$ and $c_{k\sigma}$ are the electron creation and annihilation operators, $|\phi_0\rangle$ is the vacuum state and $|v_k|^2$ $\left(|u_k|^2\right)$ is the probability of the pair $(k\uparrow, -k\downarrow)$ being (un-) occupied. The superconductor is then described by the BCS pairing Hamiltonian

$$\mathcal{H}_\mathrm{BCS} = \sum_{k,\sigma} \eta_k c^\dagger_{k\sigma} c_{k\sigma} + V_0 \sum_{k,k'} c^\dagger_{k\uparrow} c^\dagger_{-k\downarrow} c_{-k'\downarrow} c_{k'\uparrow}, \tag{5.7}$$

where η_k is the electrons' kinetic energy $(\hbar^2 k^2/2m - E_\mathrm{F})$ relative to the Fermi level. The ground state energy as well as the values of v_k and u_k in Equation (5.6) can be found by minimizing $\langle\phi_\mathrm{BCS}|\,\mathcal{H}_\mathrm{BCS}\,|\phi_\mathrm{BCS}\rangle$ with respect to both while keeping $|v_k|^2 + |u_k|^2 = 1$. As a result, one obtains

$$E_\mathrm{BCS} = \sum_k \eta_k \left(1 - \frac{\eta_k}{E_k}\right) - \frac{\Delta^2}{V_0} \tag{5.8}$$

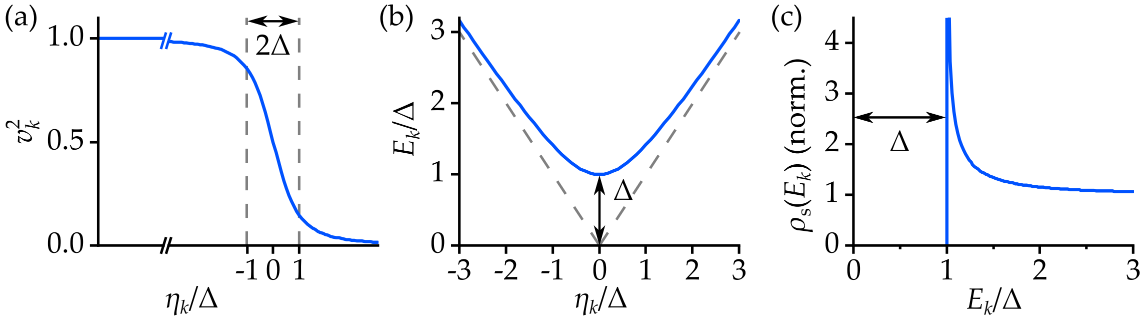

Figure 5.1: Depiction of important results derived from the BCS theory: (a) The single-particle occupation probability as a function of the kinetic energy with respect to E_F in a superconductor. Even at $T = 0\,\mathrm{K}$, the distribution is broadened at the Fermi level. (b) The dispersion relation of the Bogoliubov quasiparticles in a superconductor (solid line). The dashed line shows the electron- and hole-dispersion relations in a normal metal. (c) The quasiparticle density of states at zero-temperature exhibiting the superconducting gap and the coherence peak at the gap edge. *Adapted from Ref. [191].*

with the relations

$$\Delta = V_0 \sum_{k'} v_{k'} u_{k'} = \frac{\hbar\omega_D}{\sinh\left(2/V_0\rho_n(E_F)\right)}, \tag{5.9}$$

$$E_k = \sqrt{\eta_k^2 + \Delta^2}, \tag{5.10}$$

and ground state occupation probabilities

$$v_k^2 = \frac{1}{2}\left(1 - \frac{\eta_k}{E_k}\right), \tag{5.11}$$

$$u_k^2 = \frac{1}{2}\left(1 + \frac{\eta_k}{E_k}\right). \tag{5.12}$$

The second identity in Equation (5.9) was obtained by inserting Equations (5.11) and (5.12).

Equation (5.11) is plotted in Figure 5.1(a) and shows that even at $T = 0\,\mathrm{K}$ a superconductor has a finite probability of occupying single-particle states above E_F within an energy region $\sim 2\Delta$. This is necessary to allow the scattering processes involved in the formation of Cooper pairs, which require filled and empty states at the same energy. The excess kinetic energy of particles in these states is overcompensated by the binding energy of the Cooper pairs. To determine the meaning of the introduced quantities in Equations (5.9) and (5.10), one needs to examine the minimal energy required to excite the condensate, which is equivalent to breaking a single Cooper pair. One finds a value of $2\sqrt{\eta_k^2 + \Delta^2}$, equal to two times E_k as introduced in Equation (5.10), as breaking a Cooper pair creates two excited particles. Thus Equation (5.10) constitutes the dispersion relation of the excitation of the Cooper pair condensate, which is displayed in Figure 5.1(b). Equation (5.9) determines a gap in this excitation spectrum. The excitations' DOS is then given by

$$\rho_\mathrm{s}(E) = \begin{cases} \rho_\mathrm{n}(E_\mathrm{F}) \frac{E_k}{\sqrt{E_k^2 - \Delta^2}} & \text{for } E_k > \Delta \\ 0 & \text{for } E_k < \Delta, \end{cases} \tag{5.13}$$

and is plotted in Figure 5.1(c). One can recognize the well-known spectrum with the superconducting gap Δ and a diverging coherence peak at the gap edge.
Since creating a single electron in a state with momentum k requires the state with $-k$ to be empty, i.e. a hole to exist at $-k$ (otherwise, the two electrons would immediately form a Cooper pair), the excitations in a superconductor do not have a pure electron or hole character, but are a superposition of both and are therefore called (Bogoliubov) quasiparticles.[1] Their creation operators for the respective spin channels are defined as

$$\gamma_{k\uparrow}^\dagger = u_k^* c_{k\uparrow}^\dagger - v_k^* c_{-k\downarrow} \tag{5.14}$$
$$\gamma_{k\downarrow}^\dagger = u_k^* c_{-k\downarrow}^\dagger + v_k^* c_{k\uparrow}. \tag{5.15}$$

Depending on whether $|v_k|^2 > |u_k|^2$ or $|v_k|^2 < |u_k|^2$, i.e. η_k larger or smaller than zero, the electron or hole character of the quasiparticle is dominating. Therefore, these states are called electron- and hole-like quasiparticles, respectively.
In tunneling experiments as presented in this work, the quasiparticle DOS can be measured directly, as will be shown in the following section. Further, one also finds other tunneling processes involving Andreev reflections or Cooper pair tunneling via the Josephson effect in normal metal–superconductor and superconductor–superconductor junctions [201]. However, these are only relevant for low tunneling resistances and do not appear in the measurements presented in this thesis.

5.1.2 Quasiparticle tunneling

A simple picture which allows to understand the tunneling of (quasi-)particles in normal metal–superconductor or superconductor–superconductor junctions is the semiconductor model. In this picture, the hole-like quasiparticles are represented by mirroring the quasiparticle DOS in Figure 5.1(c) at the Fermi level

---

[1] For simplicity I will refer to them as "quasiparticles", wherever no confusion of the Bogoliubov quasiparticles with other quasiparticles is expected.

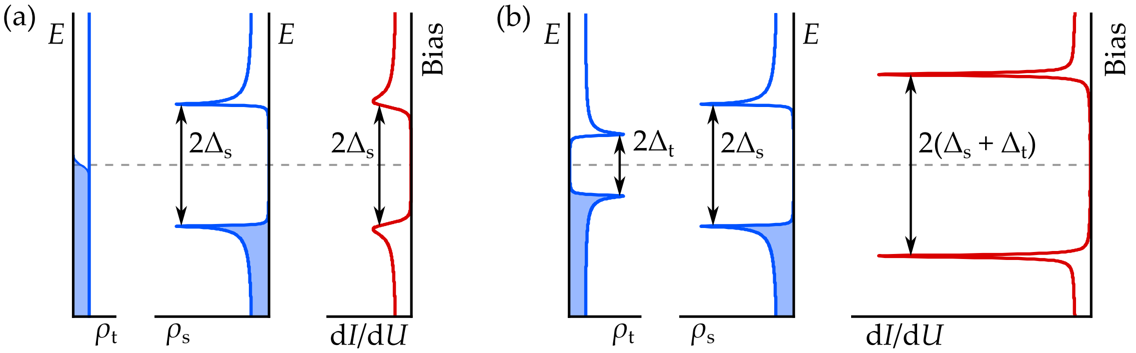

Figure 5.2: Illustration of the semiconductor model for quasiparticle tunneling in junctions with (a) one and (b) two superconducting contacts. The (extended) tip and sample DOS are shown in blue. Filled areas indicate occupied states. Red curves show the resulting conductance spectra. In contrast to the normal metal tip in (a), tunneling from a superconducting tip as shown in (b) reduces the broadening effect of finite temperature on the measured spectrum.

as shown in Figure 5.2, thereby creating occupied states below E_F. The electron-like quasiparticles are represented by the unoccupied states above E_F. Doing so, one obtains the experimentally found tunneling spectrum by convoluting the DOS of both contacts, i.e. of tip and sample in an STM experiment, as introduced in chapter 3. As sketched in Figure 5.2(a), if the tip has a constant DOS, the measured conductance spectrum is proportional to the DOS of the superconductor in the semiconductor model with a thermal broadening given by the derivative of the smeared Fermi distribution. If both tip and sample are superconducting with gap widths Δ_t and Δ_s, respectively, the convolution of both densities of states also yields a spectrum similar to that of a superconductor, but with a size of the full gap equal to $2(\Delta_\mathrm{s} + \Delta_\mathrm{t})$ and strongly pronounced coherence peaks (cf. Figure 5.2(b)). The wide gap is caused by the fact that one needs to apply a bias voltage of $(\Delta_\mathrm{s} + \Delta_\mathrm{t})/e)$ in order to get overlapping empty and filled states, as can be seen from the left side of Figure 5.2(b). Therefore, all features of the sample LDOS are shifted by Δ_t in the conductance spectrum. The increased coherence peaks are first of all due to the sum of the coherence peaks in both densities of states, but further, measurements with a superconducting tip contact are less affected by thermal broadening. Since the tip DOS exhibits a sharp edge at both $+\Delta_\mathrm{t}$ and $-\Delta_\mathrm{t}$, the thermally smeared occupation probability at E_F is irrelevant for $k_\mathrm{B}T \ll \Delta_\mathrm{t}$ [202]. This circumstance can be used to increase the energy resolution of an STS experiment beyond the thermal limit of $3.5k_\mathrm{B}T$. Corresponding experimental results of measurements of the differential conductance above a clean Nb(110) surface are shown in section 8.1.

Besides the effect of thermal broadening when measuring with a normal metal tip, the finite quasiparticle lifetime $\hbar/\Gamma$ also broadens the coherence peaks in the measurement. To account for this effect, the experimental data can be described by the Dynes formula [203]:

$$\rho(E) \propto \mathrm{Re}\left(\frac{E - i\Gamma}{\sqrt{(E - i\Gamma)^2 - \Delta^2}}\right). \tag{5.16}$$

5.1.3 The Ginzburg-Landau theory

In contrast to the BCS theory, the Ginzburg-Landau (G-L) theory [204] does not yield any insight into the microscopic origin of superconductivity, but instead allows to describe the variation of the superconducting phase in space as a consequence of disturbances like boundaries or fields. Although the theory, presented in 1950, seven years prior to the BCS theory, is based on a phenomenological approach, L. P. Gor'kov succeeded in 1959 to demonstrate that it follows as a direct result from the BCS theory close to T_c [205]. One very important result that evolves from the G-L theory is the emergence of vortices in a type II superconductor in an external magnetic field. More extended discussions of the G-L theory than the brief introduction given here can be found in e.g. Refs. [70, 190], which are also the background for the following pages.

Starting point of the G-L theory is the introduction of a local complex order parameter $\psi(\vec{r}) = |\psi(\vec{r})|e^{i\varphi(\vec{r})}$, where the squared amplitude of the order parameter $|\psi(\vec{r})|^2$ is equal to the density of superconducting charge carriers (Cooper pairs) n_s. Similar to the Landau theory, if $|\psi(\vec{r})|$ is sufficiently small, i.e. below but close to the phase transition temperature, one can expand the thermodynamic Helmholtz free energy in terms of $|\psi|$:

$$f_\mathrm{s} = f_\mathrm{n0} + \alpha|\psi|^2 + \frac{\beta}{2}|\psi|^4 + \frac{1}{2m_\mathrm{s}}\left|\left(\frac{\hbar}{i}\nabla - e_\mathrm{s}\vec{A}\right)\psi\right|^2 + \frac{B^2}{2\mu_0}, \tag{5.17}$$

where f_n0 is the free energy of the metal in the normal state in the absence of fields, α and β are coefficients of the expansion and $\vec{A}(\vec{r})$ is the position-dependent vector potential. The fourth term, accounting for the energy associated with gradients of ψ and supercurrents, and the fifth term, accounting for the energy gain in a magnetic field, were added to the expansion. Since a system will always try to reduce its free energy, the correct solution for $\psi(\vec{r})$ can be found by minimizing f_s with respect to ψ:

$$\alpha\psi + \beta|\psi|^2\psi + \frac{1}{2m_\mathrm{s}}\left(\frac{\hbar}{i}\nabla - e_\mathrm{s}\vec{A}\right)^2\psi = 0. \tag{5.18}$$

Further, it is necessary to minimize f_s with respect to $\vec{A}$ which leads to

$$\vec{j} = \frac{e_\mathrm{s}\hbar}{2im_\mathrm{s}}\left(\psi^*\nabla\psi - \psi\nabla\psi^*\right) - \frac{e_\mathrm{s}^2}{m_\mathrm{s}}|\psi|^2\vec{A}. \tag{5.19}$$

Equations (5.18) and (5.19) constitute the first and second G-L differential equation. From Equation (5.17) one finds that β needs to be positive in order for the free energy to remain finite, while for a solution with finite ψ and $f_s < f_{n0}$, α is required to be negative. In the absence of fields and far away from interfaces, the spatially homogeneous solution of Equation (5.18) is then

$$|\psi_\infty|^2 = -\frac{\alpha}{\beta}. \tag{5.20}$$

Note that the temperature dependence of the introduced parameters is not discussed here but can be found in the literature cited above.
As mentioned in the introduction of this section, the G-L theory predicts that this value is only reached within a certain distance from any disturbance. To show this one has to include the gradient in Equation (5.18), while keeping $\vec{A} = 0$. In one dimension and for a real Ansatz for ψ one obtains

$$\overline{\psi} - \overline{\psi}^3 + \frac{\hbar^2}{2m_s|\alpha|}\frac{\mathrm{d}^2}{\mathrm{d}x^2}\overline{\psi} = 0, \tag{5.21}$$

where the normalized order parameter $\overline{\psi} = \psi/\psi_\infty$ was introduced. For the boundary conditions $\psi(x=0) = 0$ and $\psi(x \to \infty) = \psi_\infty$ this equation is solved by

$$\psi = \psi_\infty \tanh\left(\frac{x}{\sqrt{2}\xi}\right) \tag{5.22}$$

with the coherence length

$$\xi = \sqrt{\frac{\hbar^2}{2m_s|\alpha|}} \tag{5.23}$$

as a measure for the distance at which $|\psi|$ recovers its undisturbed value. At this point it is important to note that STM experiments have no direct access to $|\psi|$. Instead, as shown in the previous section, STS provides a mean to probe the superconducting gap, which is influenced by the pair breaking potential of the fields and boundaries reflected in the strength of the order parameter, but is not equal to the latter [70].

Equations (5.20)–(5.23) provide a picture of the superconducting condensate in the absence of fields. However, it is known that type I superconductors fully expel an external magnetic field up to a critical field H_c, while type II superconductors host flux lines above a first critical field H_{c1} up to the second critical field H_{c2}, before becoming normal conducting. These properties will be deduced in the following.

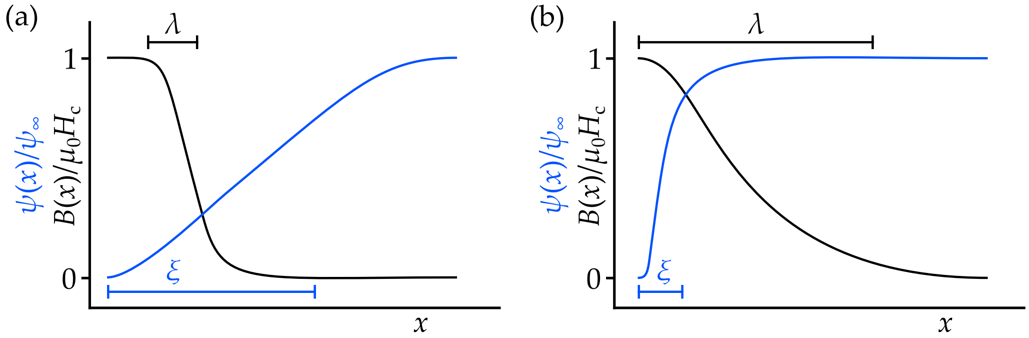

Figure 5.3: Sketched variation of the order parameter and the magnetic flux across a boundary between a normal and a superconducting region in (a) a type I ($\kappa = \lambda/\xi \ll 1$) and (b) a type II superconductor ($\kappa \gg 1$) in an external field $\mu_0 H_c$. *Adapted from Ref. [190].*

Type I superconductors

Since in an experiment rather the external field H than the magnetic flux density B is constant, the correct thermodynamic potential is the Gibbs free energy $g = f - HB$. Now the critical field of a type I superconductor can easily be found by equating this Gibbs free energy of a (infinite) superconductor that fully expels the external field H_c, i.e. $B = 0$, with that of a normal metal where $B = \mu_0 H_c$:

$$g_s = f_{n0} + \alpha|\psi_\infty|^2 + \frac{\beta}{2}|\psi_\infty|^4 = f_{n0} + \frac{\mu_0 H_c^2}{2} - \mu_0 H_c^2 = g_n. \tag{5.24}$$

This relation yields

$$\mu_0 H_c = \sqrt{\mu_0 \frac{\alpha^2}{\beta}}. \tag{5.25}$$

Above this field, the condensation energy is overcome by the energy required to expel the field and hence the superconducting state is energetically unfavorable. Below H_c, the superconductor behaves like a perfect diamagnet with magnetization $M = -H$ and $B = 0$.

Type II superconductors

To understand the origin of the different behavior of a type I and a type II superconductor in a magnetic field as well as the appearance of vortices in the latter, it is necessary to calculate the energy associated with a boundary at $x = 0$ between a normal conducting region with $B(x \to -\infty) = \mu_0 H_c$ and

$\psi(x \to -\infty) = 0$ and a superconducting region with $B(x \to +\infty) = 0$ and $\psi(x \to +\infty) = \psi_\infty$. In this case, according to the definition of H_c,

$$g_s(x \to +\infty) = g_n(x \to -\infty) = f_{n0} - \frac{\mu_0 H_c^2}{2}. \tag{5.26}$$

The additional free energy per surface area γ of the boundary is then given by the difference between the spatially altering energy across the boundary and this equilibrium value:

$$\begin{aligned}\gamma &= \int_{-\infty}^{\infty} g_s(x) - \left(f_{n0} - \frac{\mu_0 H_c^2}{2}\right) \mathrm{d}x \\ &= \int_{-\infty}^{\infty} f_s(x) - f_{n0} - \mu_0 B(x) H_c + \frac{\mu_0 H_c^2}{2} \mathrm{d}x \\ &= \ldots = \frac{\mu_0 H_c^2}{2} \int_{-\infty}^{\infty} \left(1 - \frac{B(x)}{\mu_0 H_c}\right)^2 - \frac{|\psi(x)|^4}{|\psi_\infty|^4} \mathrm{d}x. \end{aligned} \tag{5.27}$$

$B(x)$ and $\psi(x)$ are solutions of the G-L differential equations. Equation (5.27) reveals that the energy of such a normal conductor–superconductor boundary is related to the energy gain obtained by allowing the field to penetrate into the superconductor (first term in the integral) and by the loss of condensation energy where $\psi(x) < \psi_\infty$ (second term). By numerically calculating $B(x)$ and $\psi(x)$ from the G-L differential equations and evaluating Equation (5.27), one finds $\gamma > 0$ for $\kappa := \lambda/\xi < 1/\sqrt{2}$ [2] and $\gamma < 0$ for $\kappa > 1/\sqrt{2}$. The parameter κ is called Ginzburg-Landau parameter and separates type I superconductors ($\kappa < 1/\sqrt{2}$), where the free energy associated with the boundary is positive and hence prevents the formation of the latter, from type II superconductors ($\kappa > 1/\sqrt{2}$), where the formation of a boundary results in an energy gain. This sign change of γ at $\kappa = 1/\sqrt{2}$ can also be understood from the simple sketch of $B(x)$ and $\psi(x)$ shown in Figure 5.3. As illustrated in (a), for $\lambda \ll \xi$, i.e. $\kappa \ll 1$, the external field is almost completely pushed out of the superconducting region, while ψ does not reach its equilibrium value over a large range. This implies that one has to pay a large energy for expelling the field, while not benefiting from the full condensation energy. Hence such a boundary is unfavorable. Contrary, for $\lambda \gg \xi$, i.e. $\kappa \gg 1$ as illustrated in Figure 5.3(b), the system benefits from almost the full condensation energy and gains energy by letting the field penetrate into the volume for a significant distance.

In conclusion, for type II superconductors in a magnetic field one might expect the formation of atomically small domains separated by such boundaries, as this would reduce the energy of the material. However, the flux quantization in a

---

[2] For superconductors in the clean limit, $\lambda = 0.96\lambda_L$ [190].

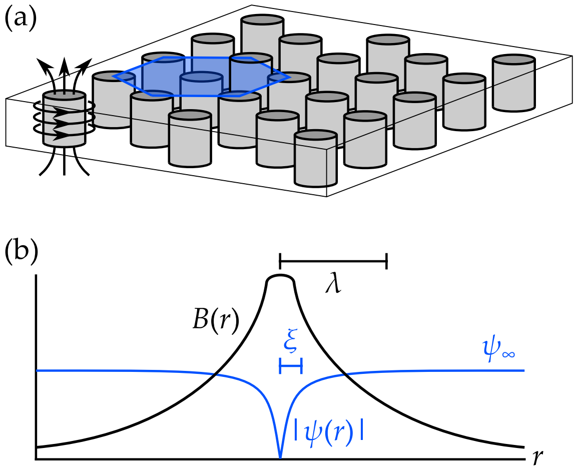

Figure 5.4: (a) 3D illustration of the hexagonal Abrikosov lattice of vortices. The blue shaded area emphasizes the unit cell of the lattice. The magnetic flux within the vortices is aligned with the external field and leads to circular screening currents as indicated by arrows. (b) Radial variation of the order parameter and the magnetic flux inside a vortex. *Adapted from Refs. (a) [70], (b) [190].*

superconductor, which is a consequence of the phase of the macroscopic order parameter, limits the minimal size of the domains. As the phase can only vary by an integer multiple of 2π on a closed loop around a domain, the flux inside this domain is limited to an integer multiple of $\Phi_0 = h/2e = 2.07 \times 10^{-15}$ Wb and cannot be smaller [190].

In 1957, A.A. Abrikosov could show that the magnetic field instead penetrates the superconductor in so-called flux tubes or vortices hosting exactly one flux quantum as illustrated in Figure 5.4(a). At the vortex core, the amplitude of the order parameter is zero and recovers its undisturbed value at a radial distance of $\sim \xi$, while the magnetic flux is maximum at the vortex center and vanishes on a length scale of $\sim \lambda_\mathrm{L}$, as sketched in Figure 5.4(b). Reversing the argument of the flux quantization shows that the circulating screening currents around the vortex change the phase of the order parameter by 2π on a path enclosing the vortex. Therefore, flux tubes must start and end at a surface of the sample or close onto themselves. As derived by Abrikosov, the flux tubes orient along the external magnetic field and form a periodic lattice in the plane perpendicular to that field. Due to the repulsive interaction of the vortices, similar to the repulsion of ordinary field lines, they seek to maximize the distance between each other, while the area of one unit cell is fixed at $\Phi_0/\mu_0 H$. As illustrated in Figure 5.4(a), this is achieved by ordering in a hexagonal lattice. In real materials, an anisotropy of the electronic properties can lead to the formation of a different lattice symmetry [206–208]. To conclude this section, the two critical fields of a type II superconductor are given. At H_c1, where the first vortex enters the superconductor, the energy required to form the vortex is overcome by the energy that would be required to keep the superconductor field free. At H_c2, the density of vortices is such that B reaches $\mu_0 H$. H_c1 and H_c2 are given by

$$H_\mathrm{c1} \approx \frac{H_\mathrm{c}}{\sqrt{2}\kappa} \ln \kappa \qquad \text{and} \qquad H_\mathrm{c2} = \sqrt{2}\kappa H_\mathrm{c}. \tag{5.28}$$

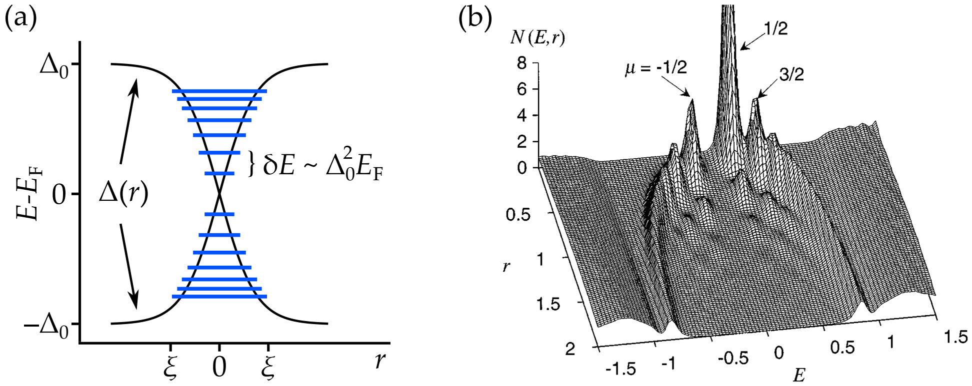

Figure 5.5: (a) Sketched potential well with depth $\sim \Delta_0$ and width $\sim \xi$ for quasiparticles inside a vortex. Due to Andreev reflections at the vortex boundary, localized Caroli-de Gennes-Matricon states with an energy spacing $\sim \Delta_0^2 / E_\mathrm{F}$ develop in the vortex core. (b) Exact LDOS as a function of r and E for an isotropic vortex. *(b) Reprinted with permission from Ref. [212]. Copyright ©1998 by the American Physical Society.*

The presented basics of superconductivity set up the basis for the following sections.

5.2 Bound states in superconducting vortices

The occurrence of in-gap states inside flux tubes of a type II superconductor can be understood in an intuitive picture: Within limits, the order parameter can be viewed as a locally varying pairing strength $\Delta(r)$ between Cooper pairs, with its equilibrium value Δ_0 being proportional to the BCS gap Δ introduced in section 5.1.1 [209]. As derived in section 5.1.3 for the order parameter, this coupling strength vanishes at the center of a vortex and reaches its equilibrium value only within a distance $\sim \xi$ from the vortex core. Thus, one can think of a vortex as a cylindrical potential well for both electron- and hole-like quasiparticles with depth Δ_0 and width ξ, as sketched in Figure 5.5(a) [210]. Quasiparticles inside this well will form bound states at discrete energy levels symmetric around E_F. Since the quasiparticles inside the vortex are Andreev reflected at the boundary, i.e. electron-like quasiparticles are reflected as hole-like quasiparticles and vice versa, resulting in the effective transmission of a Cooper pair, the resulting bound states are superpositions of both electron- and hole-like quasiparticles [211].

Mathematically, these states were first described by C. Caroli, P. G. de Gennes and J. Matricon in 1964 and are thus also referred to as Caroli-de Gennes-Matricon (CdGM) states [213]. The eigenenergies and eigenfunctions of the CdGM states can be obtained by solving the Bogoliubov-de Gennes equations for a type II superconductor hosting vortices [213, 214]. The calculated LDOS inside an isolated

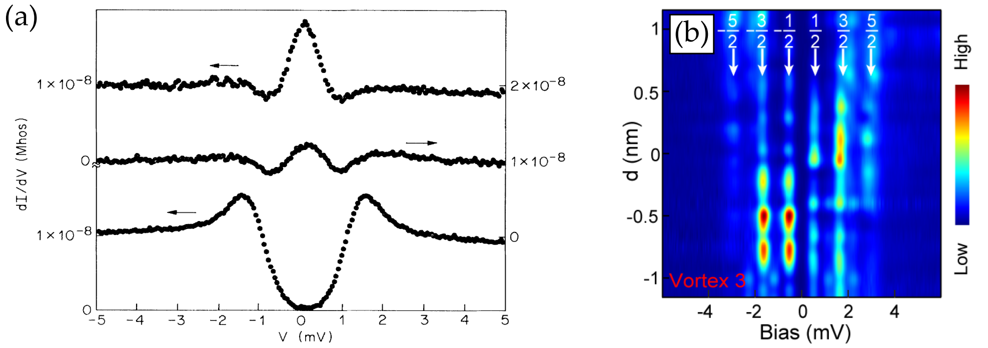

Figure 5.6: (a) Measured differential conductance at the center, ~ 7.5 nm and far away from a vortex on $NbSe_2$ (top to bottom). The finite temperature merges the individual CdGM states into a broad peak at the vortex center. (b) Individually resolved CdGM states at the center of a vortex on a single layer FeSe on $SrTiO_3(100)$. *(a) Reprinted with permission from Ref. [216]. Copyright ©1989 by the American Physical Society. (b) Reprinted with permission from Ref. [217]. Copyright ©2020 by the American Physical Society.*

vortex in a system with an isotropic Fermi surface and isotropic s-wave pairing is reproduced in Figure 5.5(b) [212]. Similar to the solutions of the hydrogen atom, the individual states can be labeled by a quantum number $\mu = \pm 1/2,\ \pm 3/2,\ ...$, defining the angular momentum of each state. As $|\mu|$ increases, the states' energy also increases and asymptotically approaches $\pm\Delta$. Simultaneously, the maxima of the states move away from the vortex core, leading to the V-shaped profile presented in Figure 5.5(b). With the qualitative explanation of the CdGM states, it is also clear that this result only holds in the limit of clean superconductors, where the quasiparticle mean free path l_F is larger than ξ [215]. For $l_F < \xi$, the quasiparticles inside the vortex core cannot interfere coherently, preventing the formation of discrete bound states.

Experimentally, CdGM states were observed in a variety of materials, although it is difficult to identify the individual states due to their usually small energy splitting of $\delta E \approx \Delta_0^2/E_F$, which is in the range of few µeV for low-T_c superconductors [213]. As a result, the high-intensity peaks at the vortex center found in Figure 5.5(b) thermally merge into a single broad peak in the measurement as can be seen in the experimental data of H. F. Hess *et al.* on $NbSe_2$ reproduced in Figure 5.6(a) and the calculations in e.g. Refs. [210, 218]. Only in high-T_c superconductors, the splitting between the states becomes sufficiently large to access them experimentally. Such a measurement of CdGM states in the quantum limit on a single layer FeSe on $SrTiO_3(100)$ is displayed in Figure 5.6(b) [217]. It is noteworthy that although the thermally broadened peak at the vortex center is centered around E_F, no CdGM state actually exists at this energy for topologically trivial superconductors. This distinguishes these states from Majorana bound states that exist at the Fermi level at the ends of flux tubes in topological superconductors, as will be discussed in section 5.4.

5.3 YU-SHIBA-RUSINOV STATES

Discrete in-gap states can not only be induced by an external magnetic field in a type II superconductor, but can also be caused by magnetic impurities in both type I and II superconductors. These Yu-Shiba-Rusinov (YSR) states, named after L. Yu, H. Shiba, and A. I. Rusinov, who first described them theoretically [48–51], are a result of the scattering potential of the impurity spin. In a simplified picture, this spin acts as a local magnetic field that tries to align the originally antiparallel spins of the electrons in a Cooper pair [49, 219]. This weakens the pairing strength in the Cooper pair and therefore leads to low-lying excitations of the superconductor within the superconducting gap.

Within the classical approach, the Hamiltonian of a single impurity with spin S_{imp} and exchange coupling J of this spin to the conduction electrons is given by

$$\mathcal{H} = \mathcal{H}_{\text{BCS}} + J\vec{s}\cdot\vec{S}_{\text{imp}} + V\mathbb{1}, \tag{5.29}$$

where the first part is the BCS Hamiltonian from Equation (5.7) and the second part describes the spin-dependent (J) and -independent (V) scattering potential of the impurity as introduced in Equation (2.10). Solving the eigenequation of this system by the Bogoliubov transformation yields a single subgap excitation at an energy of

$$E_{\text{YSR}} = \Delta\frac{1-\alpha^2+\beta^2}{\sqrt{\left(1-\alpha^2+\beta^2\right)^2+4\alpha^2}}, \tag{5.30}$$

with $\alpha = \pi\rho_{\text{n}}(E_{\text{F}})JS_{\text{imp}}$ and $\beta = \pi\rho_{\text{n}}(E_{\text{F}})V$ [51]. This energy is called YSR energy in the following and is plotted in Figure 5.7(a) for $\beta = 0$. For small exchange coupling, i.e. $\alpha \approx 0$, the YSR energy is equal to the superconducting gap as the impurity is only weakly coupled to the substrate and the Cooper pairs are hardly disturbed. In this case, the impurity remains unscreened, resulting in a YSR ground state with $S = 1/2$ for an impurity with spin $S_{\text{imp}} = 1/2$, as illustrated in Figure 5.7(b). Considering antiferromagnetic exchange coupling and the impurity spin to be "up", the YSR state can be excited from the unoccupied ground state by occupation with a quasiparticle with spin "down", which will bind to the impurity spin and change the total spin of the system to $S = 0$. For $\alpha^2 = 1+\beta^2$, E_{YSR} crosses zero, which marks the crossover to the screened regime of the impurity. For large exchange coupling, the impurity spin will be fully screened by a quasiparticle of opposite spin that occupies the YSR state and reduces the ground state spin

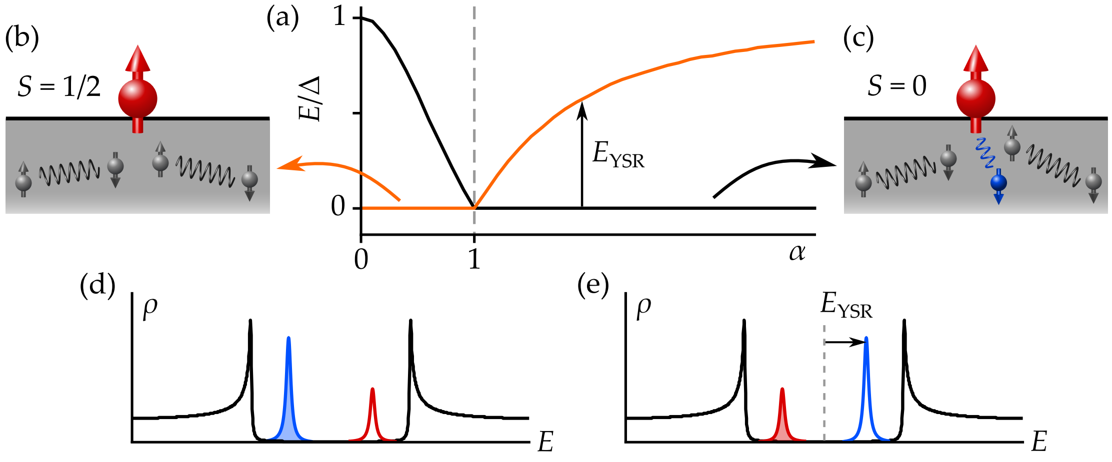

Figure 5.7: Characteristics of Yu-Shiba-Rusinov states in single magnetic impurities on a superconducting surface. (a) Energy of the screened (black) and unscreened state (orange) of a magnetic impurity in a superconducting host as a function of exchange coupling ($\alpha \propto JS_{\mathrm{imp}}$) and zero spin-independent scattering ($\beta = 0$). For $\alpha = 1$, the system undergoes a quantum phase transition, where the YSR ground state changes from (b) a free spin with total spin $1/2$ and fermion parity equal to zero to (c) a screened impurity spin with total spin 0 and fermion parity one. The excitation of the YSR state of a "spin up" impurity occurs by adding (removing) a quasiparticle with "spin down" for $\alpha < 1$ ($\alpha > 1$). This excitation leads to energetically symmetric peaks at $\pm E_{\mathrm{YSR}}$ in a conductance measurement as illustrated in (d) and (e). Due to the different excitation processes, the electron- and hole components of the excitation cross E_{F} at the quantum phase transition, leading to an inversion of the peak intensities. *Adapted with permission from Ref. [223].*

to zero, as sketched in Figure 5.7(c). In this case, the excitation of the YSR state occurs by removing the quasiparticle with spin "down" (or adding a quasiparticle with spin "up", which is equivalent in a superconductor) and increasing the total spin to $S = 1/2$. This change of the ground state spin is equivalent to a change of the fermion parity of the system [219] and marks the so-called quantum phase transition [220–222].

In an STM experiment the excitation of the YSR state can be evoked by the tunneling of quasiparticles into the impurity, which gives rise to peaks in the conductance signal at $\pm E_{\mathrm{YSR}} < \Delta$. This was first observed by A. Yazdani *et al.*, who performed STS measurements on Mn and Gd atoms on a Nb(110) surface [52]. The intensity of the conductance peaks at the YSR energy of such an experiment is given by the electron and hole-weights $|v|^2$ and $|u|^2$ of the quasiparticle creation and annihilation operators describing the excitation of the YSR state (cf. Equations (5.14) and (5.15)). The solution of the eigenstates of Equation (5.29) for a spin-up impurity is [224]

$$v \propto \sqrt{1+(\alpha+\beta)^2} \tag{5.31}$$

$$u \propto \sqrt{1+(\alpha-\beta)^2}. \tag{5.32}$$

One thus finds that the spin-independent scattering potential $V \propto \beta$ leads to an asymmetry in the electron- and hole component of the excitation. With the discussion above, i.e. that the excitation of the YSR state in the unscreened regime requires the creation of a quasiparticle $\gamma_\downarrow^\dagger = u^* c_\downarrow^\dagger + v^* c_\uparrow$, while the excitation of the YSR state in the screened regime requires the annihilation of a quasiparticle $\gamma_\downarrow = u c_\downarrow + v c_\uparrow^\dagger$, it becomes clear that at the quantum phase transition the asymmetry in the peak intensity at positive and negative bias is reversed. This has previously been demonstrated for e.g. Mn-phtalocyanine, Va-phthalocyanine and Fe-porphin molecules adsorbed on Pb(111) [202, 225–228] and defect-induced YSR states on a V(110) surface [229]. Additionally, it is noteworthy that the YSR peaks in a measured excitation spectrum are fully spin-polarized, as can be inferred from the excitation operators given above, and keep their respective spin polarization when crossing E_F at the quantum phase transition [220–222, 230–232].

Up to this point, the discussion considered only a classical spin with fixed orientation. In the framework of quantum mechanics, however, one needs to include the degrees of freedom of the quantum mechanical spin, crystal fields as discussed in section 2.2 and many-body phenomena such as the Kondo effect (cf. section 2.3). The latter is indeed closely related to the presence and nature of YSR states [202, 233–235], which will also be part of the research presented in chapter 8. An extensive discussion of the results of a quantum mechanical treatment of YSR states is given in Ref. [236].

Before reviewing the coupling of single magnetic impurities and the related YSR states, it is necessary to examine the spatial wave function of the YSR state of a single impurity. In a fully isotropic, three-dimensional system, the radial variation of the electron- and hole-component of the YSR wave function is given by

$$u(r), v(r) \propto \frac{\sin\left(k_\mathrm{F} r + \delta^\pm\right)}{k_\mathrm{F} r} \exp\left(-\left|\sin\left(\delta^+ - \delta^-\right)\right| \frac{r}{\xi}\right), \tag{5.33}$$

where ξ is the coherence length and $E_\mathrm{YSR} = \Delta\cos(\delta^+ - \delta^-)$ and $\tan\delta^\pm = (\beta \pm \alpha)$ determine the scattering phase shifts $\delta^\pm$ [51, 219, 237]. One finds that the YSR state amplitudes oscillate with a period of λ_F. The phase of this oscillation differs for the electron- and hole-component, with a phase shift of $\pi/2$ ($= \pi$ for the state's intensity) for states close to E_F. This phase shift has been resolved experimentally in e.g. Refs. [237, 238]. For $\xi k_\mathrm{F} \gg 1$, which is the case for many common superconductors with a coherence length in the µm range for e.g. aluminum, the

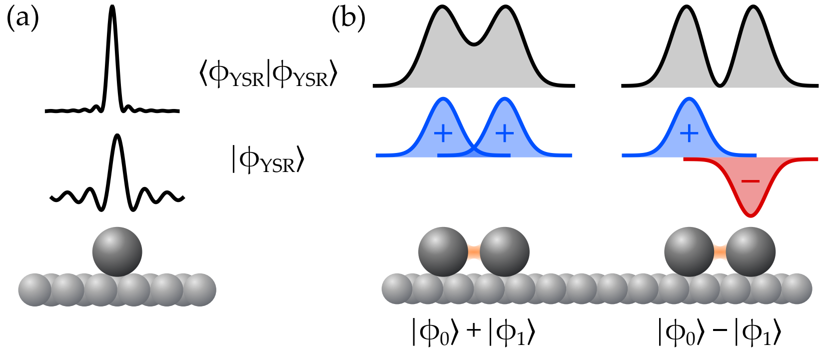

Figure 5.8: (a) Sketch of the YSR wave function for an isotropic system as given in Equation (5.33). The middle panel shows the wave function amplitude, the top panel the corresponding LDOS profile at the YSR energy. (b) Illustration of the formation of hybridized states in an impurity dimer. For simplicity, the actual $\mathrm{sinc}(x)$ type wave function is replaced by a Gaussian envelope. On the left, the sum of the two individual YSR states leads to a dimer state with even symmetry, on the right the difference of the two individual wave functions leads to an odd state. Characteristic for the odd wave function is the vanishing LDOS at the center of the dimer as shown in the top right.

decay of the YSR state is determined by the Fermi wavelength, which is in the sub-nanometer range for many metals. Therefore, it is in practice often difficult to observe the spatial variation of the YSR wave function. However, in a (quasi-)two-dimensional superconductor, the amplitude of the YSR wave function only decays as $1/\sqrt{k_\mathrm{F}r}$ [237, 239], and quasiparticle focusing in k-directions perpendicular to flat parts of the Fermi surface can also lead to widely extended YSR wave functions which allows their observation [238, 240]. Finally, the quantum mechanical treatment of the magnetic impurity predicts the appearance of individual YSR states from different orbitals [236, 241]. The symmetry of these orbitals is inherited by the corresponding YSR wave functions and has been observed in differential conductance maps at bias voltages matching the respective YSR energies [238, 242–244].

Coupling of YSR states in assemblies of magnetic impurities

If two or more magnetic impurities are brought into proximity such that their wave functions overlap, their YSR states couple and hybridize. The effect of a disordered concentration of magnetic impurities was already discussed by Shiba and Rusinov and was found to create an impurity band that eventually leads to a closing of the gap [49, 50].

In a first approach, the coupling of two individual YSR states can be treated similarly to the H_2^+-molecule [245–247]. In this case, the total YSR wave functions of the impurity dimer consist of linear combinations of the individual wave functions of the single impurities. One finds a solution with even symmetry, being the sum of the two single-impurity wave functions $|\Phi_0\rangle + |\Phi_1\rangle$, and one with odd symmetry, where the total wave function is given by the difference of the individual ones $|\Phi_0\rangle - |\Phi_1\rangle$. This model is sketched in Figure 5.8 and can easily be extended to more impurities. Indeed, first experiments found such states with even and odd states in STM experiments with magnetic adatom and molecule dimers on superconducting surfaces [248–251]. Although earlier calculations and experiments suggested that YSR states could hybridize only in ferromagnetically coupled impurities, as the single-impurity YSR wave functions of antiferromagnetically coupled impurities are orthogonal to one another [245, 249], it was found recently that in the presence of spin-orbit coupling hybridization of YSR states also occurs in antiferromagnetic dimers, as the system's effective time reversal symmetry[3] is broken [244]. It is noteworthy that for coupled YSR states also a change of the inter-impurity coupling can induce phase transitions that change the system's fermion parity and spin, similar to the quantum phase transition of single impurities driven by changes in the impurity–substrate coupling [252–254].

In more extended periodic systems of magnetic impurities, the individual YSR states form bands inside the superconducting gap [66, 255]. Very recently, quasiparticle interference [256] along a 1D chain of Mn atoms on Nb(110) was evaluated to determine the band dispersion of the present YSR bands [231]. Further, chains of magnetic impurities on *s*-wave superconductors are predicted to constitute a potential realization of Majorana fermions in solid-state systems [53–56], as will be introduced in the next section.

5.4 MAJORANA ZERO MODES

Currently, the "most wanted" in-gap states in superconducting systems are the so-called Majorana zero modes. In this section I will provide a short introduction to the properties of Majorana fermions and to possible experimental realizations of Majorana zero modes in solid-state systems, focusing on 1D atomic chains and wires.

The existence of particles which are their own antiparticles is not as unusual, as it appears in the context of Majorana fermions. Photons, neutral pions and also

---

[3] In time reversal symmetric systems, the Kramer's theorem protects the degeneracy of the paired YSR states. This symmetry is broken for ferromagnetically coupled dimers. Antiferromagnetically coupled dimers are symmetric under the combination of time reversal and a rotation by 180°, also leading to degenerate YSR states. Spin-orbit coupling breaks this symmetry, as the rotation of the spins influences the surface quasiparticles, lifting the degeneracy [244].

the suggested gauge bosons of gravity, gravitons, are their own antiparticles [257]. However, these particles all have an integer spin and are thus bosons. In 1937, E. Majorana was able to derive the existence of corresponding half-integer spin particle–antiparticle pairs, which are today called Majorana fermions, by bringing the complex-valued Dirac equations in a form that only contains real terms [258]. In contrast to the complex solutions of the original Dirac equations, where the fields ψ and $\psi^* \neq \psi$ describe fermionic particles and antiparticles such as electrons and positrons, respectively, the real solution of Majorana's equations is equal to its complex conjugate [257]. Particles and antiparticles are thus the same.

One immediate requirement when looking for Majorana fermions in nature is their charge neutrality. If Majorana fermions where charged, creation or annihilation of a particle–antiparticle pair would violate charge conservation. In the standard model of particle physics, the only candidates for a Majorana fermions are therefore neutrinos, yet to date, an experimental proof is still missing [259–262].

Within the last 20 years, the search for Majorana fermions expanded to the field of solid-state physics, first theoretically and later also experimentally. In solid-state systems, quasiparticles can carry similar properties as "true", high-energy particles and also appear as particle–antiparticle pairs, such as electrons and holes in a semiconductor. As employed earlier in this thesis, (quasi-)particles in solid-state physics are described by their creation and annihilation operators. For the example of electrons and holes, complex conjugation of the electron creation operator $c_\sigma^\dagger$ yields the creation operator c_σ of its antiparticle, the hole, which is simultaneously the annihilation operator of the electron. Therefore, Majorana fermions in solid-state systems are characterized by the equality of their creation and annihilation operators $\gamma^\dagger$ and γ, respectively. To distinguish quasiparticles in a solid-state system with this property from high-energy Majorana fermions, they are often referred to as Majorana zero modes (MZMs) [263–265], as they exist at zero energy (E_F), as will be shown below.

Starting from electrons and holes in a solid-state system, superconductors are an interesting candidate to host MZMs [224]. As discussed in section 5.1, the Bogoliubov quasiparticles exhibit both electron and hole character. Since the electron (hole) character dominates for quasiparticles above (below) the Fermi level, one might naturally expect the appearance of MZMs at $E = E_\mathrm{F}$, where electron and hole character have the same weight. Mathematically this becomes clear by creating Majorana operators from the superposition of electron creation and annihilation operators (the index j can be ignored for the moment):

$$\gamma_{j,1} = c_j^\dagger + c_j \tag{5.34}$$

$$\gamma_{j,2} = i\left(c_j^\dagger - c_j\right). \tag{5.35}$$

Clearly, both so defined operators are Hermitian. Comparing Equations (5.34) and (5.35) to Equations (5.14) and (5.15) reveals that for $u = (-)v^*$ and $v = (-)u^*$

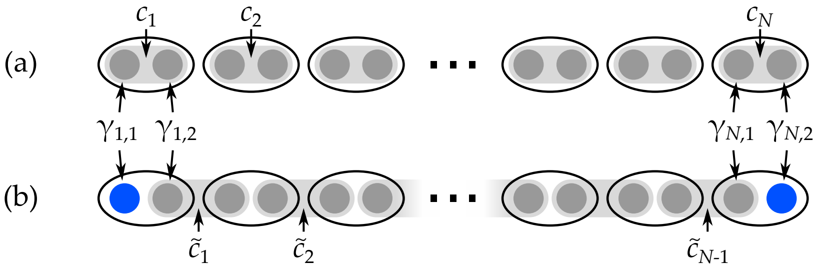

Figure 5.9: Illustration of the (a) trivial and (b) non-trivial solution of the Kitaev model. In the trivial case, two Majorana fermions (dark gray dots) on the same site (circles) are coupled to a conventional fermion (light gray). In the non-trivial case, Majorana fermions from neighboring sites couple to a conventional fermion, leaving a highly delocalized zero-energy fermionic state consisting of two spatially well separated Majorana fermions (blue dots) at the chain ends. *Adapted from Ref. [266].*

Bogoliubov quasiparticles actually are Majorana fermions, if the spin component in Equations (5.14) and (5.15) is neglected. To show that a superconductor might host Majorana fermions, I will briefly discuss the theoretical model of an effectively spinless 1D superconductor introduced by A. Y. Kitaev [61], following further explanations and the nomenclature in Refs. [224] and [266].
By inverting Equations (5.34) and (5.35), one finds that any electron (or hole) can be written as a linear combination of two Majorana fermions:

$$c_j = \frac{1}{2}\left(\gamma_{j,1} + i\gamma_{j,2}\right) \tag{5.36}$$

$$c_j^\dagger = \frac{1}{2}\left(\gamma_{j,1} - i\gamma_{j,2}\right). \tag{5.37}$$

For now, this is only a mathematical reformulation of the electron creation and annihilation operators and does not have any consequences for real systems, as the Majorana fermions are always bound to form a conventional fermion and cannot be addressed individually [260]. However, the Kitaev model shows how such Majorana fermions can be spatially separated to obtain proper MZMs. For this purpose, one can construct a 1D chain with N sites, that host a single (spinless) electron each, as sketched in Figure 5.9. Electrons in neighboring sites j and $j+1$ shall be coupled to a Cooper pair. The Hamiltonian of this system is then given by:

$$\mathcal{H}_{\text{Kitaev}} = \sum_{j=1}^{N} -t\left(c_j^\dagger c_{j+1} + c_{j+1}^\dagger c_j\right) + \Delta\left(c_j c_{j+1} + c_{j+1}^\dagger c_j^\dagger\right) - \mu\left(c_j^\dagger c_j - \frac{1}{2}\right), \tag{5.38}$$

with the hopping amplitude t, the superconducting gap Δ and the chemical potential μ. One can analytically find two distinct regimes by replacing c_j and

$c_j^\dagger$ with $\gamma_{j,1}$ and $\gamma_{j,2}$: In the trivial case, for $t = \Delta = 0$, the Hamiltonian can be rewritten as

$$\mathcal{H}_{\text{Kitaev}} = -\mu \sum_{j=1}^{N} \left(c_j^\dagger c_j - \frac{1}{2} \right) = \frac{\mu}{2i} \sum_{j=1}^{N} \gamma_{j,1}\gamma_{j,2}, \tag{5.39}$$

where the Majorana operators of a single site are coupled to a conventional fermion as depicted in Figure 5.9(a). In the non-trivial case, for $t = \Delta$ and $\mu = 0$, Equation (5.38) reduces to

$$\mathcal{H}_{\text{Kitaev}} = it \sum_{j=1}^{N} \gamma_{j,2}\gamma_{j+1,1} = 2t \sum_{j=1}^{N-1} \left(\tilde{c}_j^\dagger \tilde{c}_j - \frac{1}{2} \right), \tag{5.40}$$

with the new fermionic operators $\tilde{c}_j^{(\dagger)} = \left(\gamma_{j,2} \pm i\gamma_{j+1,1}\right)/2$ that couple Majorana fermions from neighboring sites as illustrated in Figure 5.9(b). One finds that in the non-trivial regime the Majorana fermions $\gamma_{1,1}$ and $\gamma_{N,2}$ do not appear in the Hamiltonian and must therefore have zero energy. Further, Equation (5.40) only contains $N-1$ fermionic operators. One can construct an N-th operator $\tilde{c}_0 = \left(\gamma_{1,1} + i\gamma_{N,2}\right)/2$ that has zero energy and contains the delocalized Majorana fermions at the chain ends. As $\tilde{c}_0$ and $\mathcal{H}_{\text{Kitaev}}$ commute, both states with and without occupied states $\gamma_{1,1}$ and $\gamma_{N,2}$ are ground states of the chain. The model hence predicts the existence of paired, but delocalized MZMs at the ends of a spinless superconducting chain at $E = E_{\text{F}}$. Further analysis of the Kitaev Hamiltonian shows that the appearance of MZMs is not restricted to the single point in the phase diagram, that was discussed above, but that the non-trivial phase actually extends over the full range where $|\mu| < 2t$ and $\Delta \neq 0$. One can show that this phase is topologically distinct from the trivial phase, i.e. the appearance of MZMs at the chain ends is a topologically protected property of the system [267].

Instead of spinless fermions, which do not exist, it is in practice sufficient to restrict the spin to a single direction [61]. This means that the electrons in Cooper pairs cannot be paired as singlets with an s-wave-like spatial wave function, but must pair as triplets. To maintain an antisymmetric total wave function, the spatial part must hence be p-wave-like.[4] In addition to Kitaev's model, it can be shown that in 2D, $(p_x + ip_y)$-wave pairing also leads to a topologically non-trivial phase hosting Majorana fermions [268, 269]. Such superconductors are often referred to as topological superconductors. Unfortunately, the existence of a superconductor with intrinsic p-wave paring remains to be confirmed [270], yet various artificial systems have been conceived that mimic the 1D Kitaev Hamiltonian [53–56, 271, 272] or equivalent systems in 2D [273–275].

---

[4] It could also be any other antisymmetric spatial wave function, such as f-wave-like.

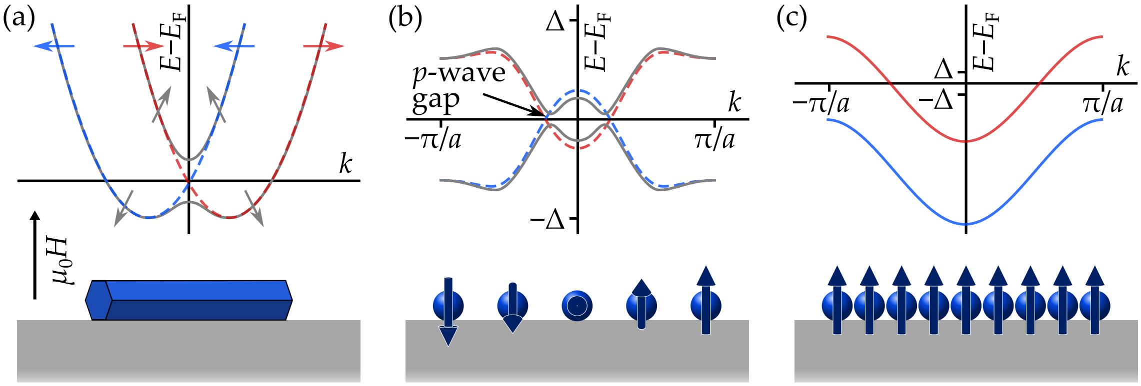

Figure 5.10: Band dispersion and illustration of possible realizations of topological superconductivity in artificial 1D systems. (a) In semiconductor nanowires, spin-orbit coupling leads to a splitting of the spin-polarized bands (dashed blue and red band). An external magnetic field gaps the dispersion at the crossing point of the two bands (gray bands) and realigns the spins. If only the lower band crosses the Fermi level, p-wave superconductivity can be induced. (b) Dilute chain of magnetic adatoms forming a spin helix. The resulting spin-polarized YSR bands (dashed lines) cross at the Fermi level and reopen a p-wave gap. (c) In a densely packed spin chain, the spin carrying orbitals form spin-polarized bands. If spin-orbit coupling is present, an s-wave superconductor can also couple to a ferromagnetically ordered chain and crossing of a single band at E_F then results in an effectively spinless Kitaev chain. *Partially adapted from Refs. (a) [266], (b) [276], and (c) [224].*

In 1D, semiconductor nanowires proximity coupled to a conventional s-wave superconductor are a promising candidate [277]. Strong spin-orbit coupling in these wires splits the spin bands and an external magnetic field can be used to generate a gap between the spin up and spin down band as illustrated in Figure 5.10(a). If the chemical potential is placed within this gap by gating, s-wave superconductivity couples only to a single spin channel, rendering the system effectively spinless [271, 272]. Several transport measurements on such devices have shown zero-bias signatures expected for MZMs [278–280]. Another one-dimensional approach is the coupling of spin chains to an s-wave superconductor, which can be realized by placing magnetic adatoms onto a superconducting surface [53–60], and is a popular approach in many STM experiments [281]. Two limits need to be distinguished within this concept: (i) In the dilute limit, where the overlap between the spin-carrying orbitals is small, the subgap physics is dominated by the emerging YSR bands, which were introduced in section 5.3. Just like the single-atom YSR states, the YSR bands are fully spin-polarized. If coupling between the individual states becomes strong enough such that the band width becomes larger than E_{YSR} and the bands cross the Fermi level, a p-wave gap opens around E_F as sketched in Figure 5.10(b) [57, 224]. (ii) In densely packed chains, the spin-carrying orbitals hybridize into spin-polarized bands. If only one of the two bands crosses the Fermi level as depicted in Figure 5.10(c), the system is effectively spinless and topologically equal to the Kitaev model [60, 224]. One important prerequisite in both limits is that the s-wave pairing of the superconductor can induce a gap into the spin chain. This is only possible, if the spins are not ferromagnetically aligned, such as in a spin helix, so that quasiparticles in neighboring sites have partially opposing spins and can couple to the singlet Cooper pairs of the substrate. Spin-orbit coupling creates an exception to this rule, as it leads to proximity-induced superconductivity also in ferromagnetically coupled chains [224]. Great effort was put into this approach in recent years, yielding a variety of systems that showed YSR band crossing [276] and zero-bias states at chain ends that were interpreted as MZMs [63, 65–67]. Further, a lot of effort is put into distinguishing these potential MZMs form trivial modes [69, 232, 282–284] and into finding new material systems that offer tunable and easily accessible topological states [68, 243, 285]. Yet, a definite proof determining the nature of detected zero-bias modes is still missing and will be very challenging.

In 2D, L. Fu and C. L. Kane predicted that a 3D topological insulator coupled to an s-wave superconductor would give rise to $p_x + ip_y$-superconductivity [273], if the chemical potential lies within the bulk band gap. The surface states of a topological insulator are spin-polarized, therefore rendering the created superconductor effectively spinless. Earlier works had already shown that vortices in p-wave superconductors would host MZMs [268, 269]. In contrast to the trivial CdGM states, MZMs appear at the Fermi level as discussed above. Yet, it is often difficult to experimentally separate both due to the small energy shift of the CdGM states from E_F (cf. section 5.2). STM experiments indicating the presence of MZMs in such heterostructures were obtained on thin films of $\mathrm{Bi_2Te_3}$ on $\mathrm{NbSe_2}$ [286, 287] as well as on Fe-based superconductors [288–290]. However, the aforementioned difficulty to individually resolve the MZMs and the fact that disorder in the Fe-based superconductors seems to play a crucial role as not every vortex shows zero-bias states demonstrates that more work is necessary to unambiguously identify MZMs.

Further proposals to create MZMs involve doping of topological insulators, to drive them into a superconducting state [291–293], proximity coupled 2D topological insulators [294], magnetic islands on s-wave superconductors [295–299], superfluidity in ^{3}He [268, 300, 301] and cold atom gases [302, 303], the natural p-wave superconductor candidate $\mathrm{Sr_2RuO_4}$ [270, 304], and the fractional quantum Hall effect [305].

Finally, after reviewing potential realizations of MZMs, their technologically most interesting property should not remain unmentioned here: MZMs show non-Abelian exchange statistics, which means that the effect of an exchange of multiple MZMs on their wave function depends on the path and order that is chosen for the process [264, 269]. Since these exchange operations, also called braiding operations, can be used for information storage and quantum computing, and MZMs are insensitive to local perturbations due to their non-local character, MZMs could be used in topologically protected quantum computing operations [61, 62]. This idea motivates the large effort put into their realization and characterization in solid-state systems.

Chapter 6

6 THE NB(110) SURFACE

Its high critical temperature of 9.2 K and large bulk gap of 1.53 meV [306] make niobium a favorable material for experimental research on a superconductor, as the liquid helium temperature lies well below T_c and the experimental resolution of in-gap states does not require as low temperatures as for e.g. aluminum. A coherence length ξ_{Nb} of 38 nm and a London penetration depth $\lambda_{L,Nb}$ of 39 nm make niobium a type II superconductor with a Ginzburg-Landau parameter of $\kappa = 0.99$ [307, 308] with an upper critical field of $H_{c2} = 400$ mT [309]. Unfortunately, contrary to its desirable electronic properties, the preparation of a single crystalline Nb surface for STM purposes is challenging. In this chapter, I will thus first review the preparation procedure leading to a clean Nb(110) surface as well as its topographic features. Afterwards, the basic electronic properties will be discussed. The general results presented in this chapter were mostly published in Ref. [310] and were obtained by Artem Odobesko and during the PhD thesis of Stefan Wilfert [132] and the Bachelor thesis of Jakob Hagen [311]. The related DFT calculations were performed by Soumyajyoti Haldar in the group of Stefan Heinze at the Christian-Albrechts-Universität zu Kiel. The individual measurements shown in the following were obtained in the course of the presented work.

6.1 SURFACE PREPARATION AND TOPOGRAPHY

Bulk niobium crystallizes in a bcc structure with lattice constant $a_{Nb} = 330$ pm. The Nb(110) surface is hence defined by a two-fold symmetric, centered rectangular unit cell with orthogonal high-symmetry directions $\langle 0\,0\,1 \rangle$ and $\langle 1\,\bar{1}\,0 \rangle$ (cf. inset in Figure 6.1(f)). By means of LEED, AES and STM studies, earlier works determined the main contamination of the polished Nb surfaces to be oxygen [312–315]. Since oxygen segregates from the bulk to the surface at temperatures lower than the required annealing temperatures to obtain a smooth surface [312], sputter−anneal cycles are not suited to produce a clean surface [310]. Instead, samples with more than 90% oxygen-free surface area can be obtained by heating the Nb sample to a temperature close to its melting point at 2477 °C [310].

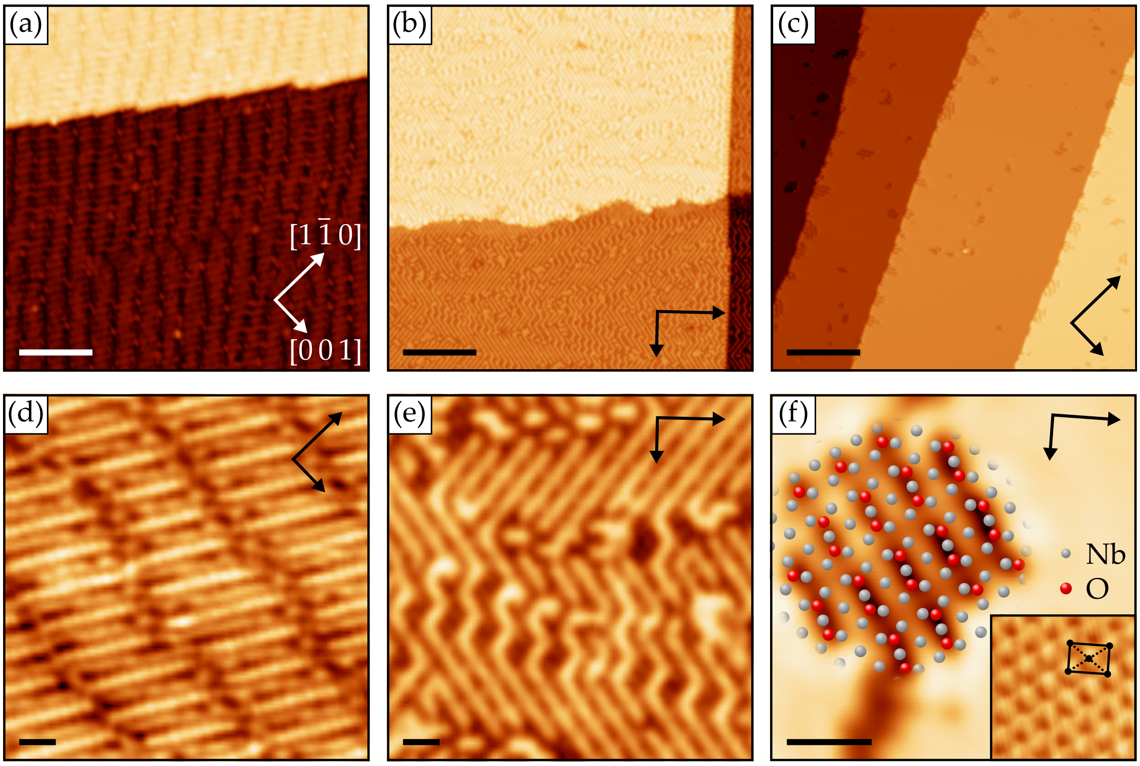

Figure 6.1: Overview scans of the two oxygen reconstructions (a) NbO_x phase I and (b) NbO_x phase II of the Nb(110) surface and (c) the clean surface. Scale bars are 10 nm. (d),(e) Close-ups of the surfaces in (a) and (b), respectively. The oxygen reconstruction of NbO_x phase II appears to be more ordered than that of NbO_x phase I. (f) Scan of a small patch of the NbO_x phase II oxygen reconstruction on the otherwise clean surface, overlain with the ball model revealing the oxygen dimers on the surface. The inset shows a scan with atomic resolution of the clean surface. Scale bars are 1 nm. Scan parameters: (a),(b),(e) $U = -100$ mV, $I = 400$ pA; (c) -1 V, 400 pA; (d) -100 mV, 200 pA; (f) -10 mV, 8 nA.

The Nb(110) single crystals (*MaTecK GmbH* and *Surface Preparation Laboratory*) for the experiments presented in the following chapters were prepared by multiple flashes of electron beam heating, each usually 30 s long, with the sample surface facing the e-beam filament. The surface temperature was measured with an *Ircon UX 70P* pyrometer in the single wavelength mode and a set emissivity of 0.293 through a window in the UHV chamber.

When new crystals are heated to temperatures below 2000 °C, they initially exhibit smooth step edges with atomically straight segments oriented along the ⟨1 1 1⟩ directions as can be seen in Figure 6.1(a). Additionally, a quasiperiodic structure with small, few nanometer long stripes oriented closely along the ⟨1 1 1⟩ directions can be observed in the close-up in Figure 6.1(d). As shown in Refs. [314, 315], this pattern originates from the formation of a single-atomic fcc NbO(111) layer with

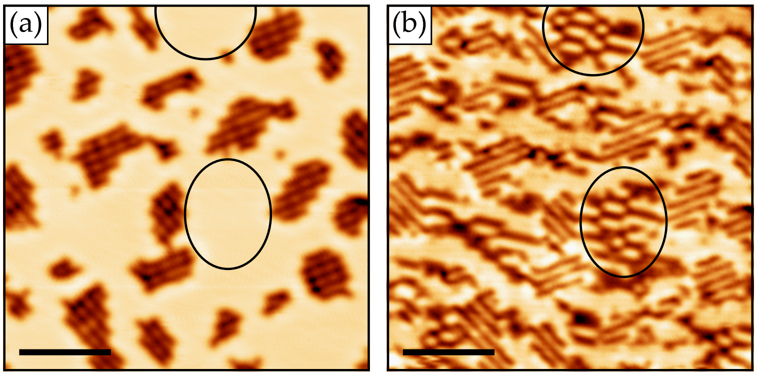

Figure 6.2: Scans of the same area on a partially clean Nb sample at different bias voltages. (a) At $U > 0.2$ V, only oxygen is visible as depressions in the topography. (b) For lower bias voltages, hydrogen in between the oxygen patches becomes visible. The circles mark exemplary areas where hydrogen forms an ordered reconstruction on the oxygen-free Nb surface. Scale bars are 5 nm. Scan parameters: (a) $U = -1$ V, $I = 400$ pA; (b) -50 mV, 400 pA.

on-top rows of Nb (bright protrusions) and oxygen atoms (dark areas). This phase of the Nb(110) surface will be called "NbO_x phase I" in the following.

To remove the NbO layer, the crystals were exposed to several cycles of Ar^+-ion sputtering with an energy of 1 keV and electron beam heating to temperatures > 2000 °C.[1] The result is a surface exhibiting mostly single-atomic, unordered step edges and an ordered pattern of alternating bright and dark rows along the $\langle 1 1 2 \rangle$ directions of the surface as displayed in Figure 6.1(b). Individual domains observed along the $[\bar{1} 1 2]$ and $[\bar{1} 1 \bar{2}]$ direction only extend over few tens of nanometers. A higher resolution scan in the same area displayed in Figure 6.1(e) reveals ordered boundaries between the two domains. Further, one can identify individual segments within the dark rows, which are attributed to dimers of atomic oxygen. As displayed in the ball model in Figure 6.1(f), the individual oxygen atoms sit in the threefold hollow sites of the Nb(110) lattice with the dimers being oriented along the $\langle 1 1 3 \rangle$ directions [310]. This phase will be called "NbO_x phase II".

To obtain an almost completely oxygen-free, clean Nb surface, the samples were heated multiple times to up to 2400 °C. The result is displayed in Figure 6.1(c), showing large areas of the bare surface and only small patches of the remaining NbO_x phase II oxygen reconstruction. Atomic resolution of the surface (cf. inset

---

[1] After removing the NbO layer, I did not succeed in recreating the NbO_x phase I surface on the same crystal. Also extensive sputtering and low-temperature annealing, exposure to oxygen inside the UHV chamber at room temperature and higher temperatures or exposure to atmosphere only reconstituted the NbO_x phase II surface.

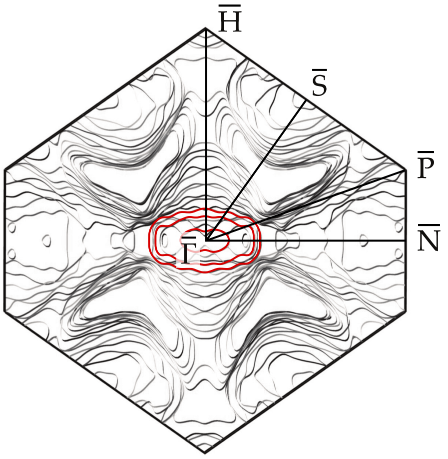

Figure 6.3: The calculated Fermi surface of clean Nb(110) exhibits a multitude of bands crossing E_F. Bands close to $\overline{\Gamma}$, to which STM experiments are particularly sensitive, are marked in red and serve as the starting point for the simulations presented in chapter 7. *Adapted from Ref. [316]. Copyright ©2020 by the American Physical Society.*

in Figure 6.1(f)) confirms the expected centered rectangular unit cell of the Nb(110) lattice.

Another contaminant of the Nb(110) surface is hydrogen, which is visible in STM scans at bias voltages < 200 mV [310]. Figure 6.2 shows scans of the same area at $U = -1$ V and -50 mV, the latter revealing ordered structures of hydrogen that appear as depressions in the measurement. Presumably, the hydrogen originates from both the bulk of the sample as well as the UHV system. The initial amount of hydrogen on the surface can be reduced by hundreds of flashing cycles, however even samples stored at 4.2 K will be covered with hydrogen from the UHV system over time (significant changes of the surface contamination were observed on timescales of several days to weeks). By repeatedly scanning a small surface area at a high bias voltage and tunneling current (usually -1 V and $\sim$ 6 nA), hydrogen can be removed from the area due to its high mobility [310]. The electronic properties of the surface described in the following as well as the results in chapters 8 and 9 seem not to be influenced by the presence of hydrogen, while oxygen strongly influences the coupling of adatoms to the surface (cf. chapter 8) and suppresses the Nb(110) surface resonance discussed below.

6.2 ELECTRONIC PROPERTIES OF THE NB(110) SURFACE

Figure 6.3 presents the Fermi surface of clean Nb(110) [316] as calculated using the plane-wave-based VASP code [317, 318] within the projector augmented-wave method [319, 320]. As already reported in Ref. [310], a variety of bands originating from different *d* orbitals of the Nb atoms crosses the Fermi level. Close to the center of the Brillouin zone at $\overline{\Gamma}$, several stadium-shaped pockets (marked in red) are visible. As will be shown in chapter 7, they substantially influence the observed CdGM states in vortices on the surface.

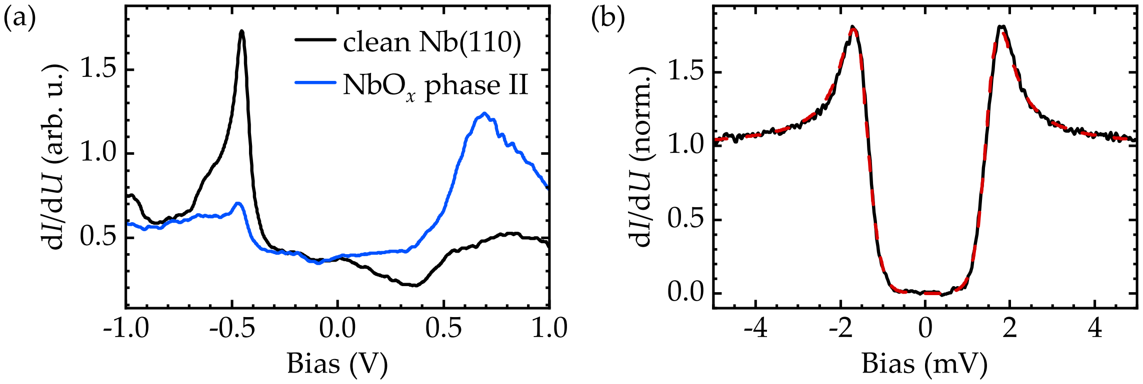

Figure 6.4: Differential conductance measurements on the clean an oxygen-reconstructed Nb(110) surface. (a) Wide-range spectroscopy revealing a surface resonance peak on the clean surface at -0.45 V, which is absent in areas of NbO$_x$ phase II. (b) Superconducting gap measured on the clean Nb surface (black curve) and the corresponding fit (red, dashed curve). Fit parameters are $\Delta = 1.50$ meV, $T_{\mathrm{eff}} = 1.80$ K, $\Gamma = 0.3$ µeV. Stabilization parameters: (a) $U = -1$ V, $I = 400$ pA, $U_{\mathrm{mod}} = 10$ mV; (b) -7 mV, 400 pA, 0.1 mV. $T = 1.4$ K.

The measured surface spectrum of clean Nb(110) is characterized by a sharp peak at -0.45 V as presented in the STS signal in Figure 6.4(a). The origin of this peak can be identified by DFT calculations as a flat band surface resonance close to $\overline{\Gamma}$ in the surface Brillouin zone arising from the $4d_{z^2}$ orbitals of the Nb atoms [310]. The measured LDOS on a small patch of NbO$_x$ phase II on the same surface (blue curve in Figure 6.4(a)) exhibits a strongly reduced intensity of that peak, confirming its surface nature.

The low-energy STS data in Figure 6.4(b) displays the gapped excitation spectrum of a BCS superconductor. Fitting the data with the Dynes formula in Equation (5.16) and including broadening by an effective temperature T_{eff} yields a gap size of 1.50 meV, $T_{\mathrm{eff}} = 1.80$ K, and a quasiparticle lifetime broadening of in the range of 1 µeV.[2] The value of Δ agrees well with the literature value for bulk Nb and the fitted effective temperature defines the electronic temperature of the STM mentioned in section 3.2. In contrast to the wide-range surface spectrum in Figure 6.4(a), the measured superconducting gap does not depend on the cleanliness of the surface and is not affected by the presence of oxygen or hydrogen within the experimental resolution. This observation confirms that the gap size on the Nb surface is defined by the bulk.

---

[2] At this relatively high temperature in comparison to Γ, the fit is rather insensitive to variations of Γ by a few µeV.

7 Chapter 7

ANISOTROPIC VORTICES ON NB(110)

The observation and analysis of the Abrikosov vortex lattice in type II superconductors can yield estimates for the London penetration depth [321], coherence length [216], and electron mean free path [215], and provide insight into further electronic properties such as the superconducting gap and pairing symmetry [322–324] as well as into the structure of the Fermi surface [325]. The prediction of MZMs inside vortices of topological superconductors discussed in section 5.4 led to a further increased interest in the trivial CdGM states inside the vortex cores: Whereas for the few superconductors that are in the quantum limit at experimentally accessible temperatures the identification of zero-bias modes is possible [289, 290], the differentiation of such modes from CdGM states is more challenging for most other superconductors. One observation that is often referred to in corresponding experiments is the spatial distribution of the bound states, more specific a lacking spatial dispersion, that is used to distinguish the sought-after MZMs from trivial CdGM states [286, 288, 326]. Yet, as I will shown in this chapter, such conclusions need to be taken with care.

In the first part of this chapter, I will discuss the methods used to image vortices on Nb(110) and present the experimental results obtained on the clean surface, exposing heavily bias-dependent and anisotropic apparent shapes of the observed vortices.[1] In the second part, I will elaborate the influence of surface adsorbates on the CdGM states and the concomitant vortex shape. Finally, I will discuss the experimental results in light of solutions of the Bogoliubov–de Gennes equations determined by Song-Bo Zhang and Björn Trauzettel, revealing the physical origin of the observed behavior. Most results presented in this chapter were published in Ref. [316].

---

[1] Here the word "apparent" shall highlight, that the described shape is that of a constant differential conductance contour at a given bias voltage. The actual shape of a vortex might rather be defined by the radial variation of the order parameter or the magnetic field inside the flux tube, which are both energy-independent.

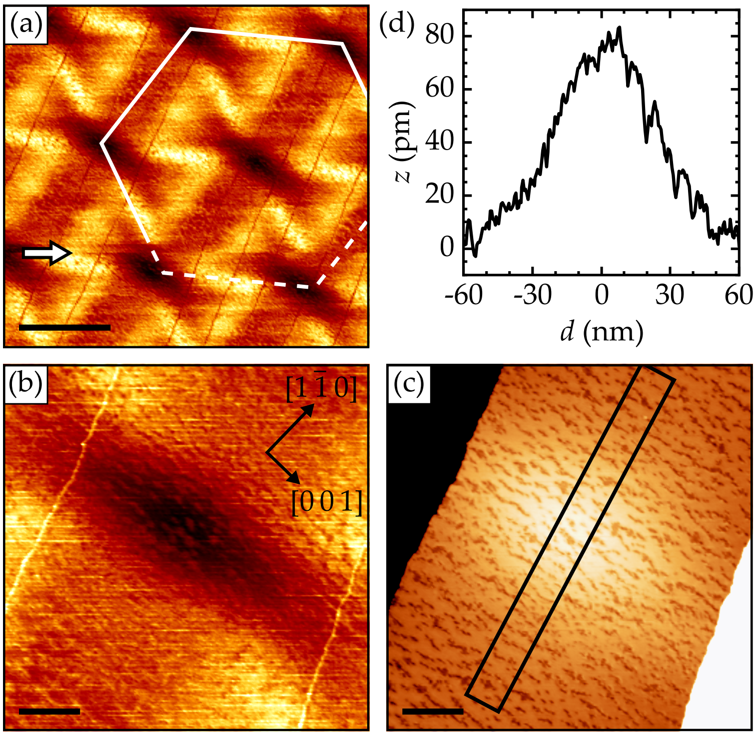

Figure 7.1: Artifacts in measurements of vortices on a clean Nb(110) surface. (a) Constant current $\mathrm{d}I/\mathrm{d}U$ map of the Nb surface in an external field of 100 mT. The hexagonal vortex lattice is indicated. A synchronous movement of the vortices during the measurements indicated by the white arrow caused a displacement of the whole lattice. This is presumably caused by a temporary, but unstable pinning of the vortices at e.g. defects in the crystal. This pinning also explains an area per vortex that is different from the expected value of $\Phi_0/\mu_0 H$, here by about +10 %. Scale bar is 100 nm. (b) Constant current $\mathrm{d}I/\mathrm{d}U$ map of a single vortex, (c) the simultaneously recorded topography and (d) the averaged line profile taken from the area marked in (c). The strongly varying LDOS across the vortex leads to different tip–sample distances at and away from the vortex, causing an incorrect representation of the latter in the $\mathrm{d}I/\mathrm{d}U$ map. Scale bars are 20 nm. Stabilization parameters: $U = -0.8$ mV, $I = 50$ pA, $U_{\mathrm{mod}} = 0.1$ mV. $\mu_0 H = 100$ mT; $T = 1.4$ K.

7.1 ARTIFACT-FREE IMAGING OF VORTICES ON CLEAN NB(110)

First images of the Abrikosov lattice of vortices in a type II superconductor in real space were obtained by depositing small magnetic particles on the surface of a superconductor exposed to an external magnetic field [327]. Subsequent imaging of the surface by either light or scanning electron microscopy showed the accumulation of these particles where the magnetic flux penetrated the surface. In contrast to this technique, generally called the Bitter technique [328], which is based on the magnetic properties of the sample, scanning tunneling microscopy relies on changes of the LDOS, which is caused by the reduction of the order parameter and the appearance of in-gap states inside the vortices. Far away from a vortex, one can expect a BCS-like excitation spectrum.[2] At the center of the vortex, the measured LDOS is expected to become gapless. It is thus possible to visualize the Abrikosov vortex lattice in $\mathrm{d}I/\mathrm{d}U$ maps at a fixed bias voltage $U \lesssim \Delta/e$. An example of such a measurement is shown in Figure 7.1(a). One can identify the hexagonal Abrikosov lattice and a very peculiar pattern arising around the vortices. However, a more careful analysis indicates that the results of such measurements need to be treated with care and even have limited value: Although at the given bias voltage of $-\Delta < -0.8\,\mathrm{mV} < \Delta$ the LDOS inside the vortex is expected to be higher than outside due to the reduced gap, the vortices appear as depressions in the produced image. As further elaborated in Figure 7.1(b)-(d), this artifact originates from a changing z-setpoint in the constant current image across the vortex despite an actually flat surface caused by the strongly varying LDOS between the bias setpoint and E_F. This changing tip−sample distance also causes the increased $\mathrm{d}I/\mathrm{d}U$ signal in between the vortices, which was already mentioned in the PhD thesis of Stefan Wilfert [132], but could not be explained by the author. Therefore, a different approach that circumvents these setpoint artifacts is required to correctly record and present the LDOS of the observed vortices.

Figure 7.2 displays experimental results obtained by two different approaches that do not suffer from the above-mentioned problems. The first is a full grid spectroscopy recorded on a single vortex, where each spectrum is stabilized sufficiently far away from the gap such that a correct normalization of the spectra is possible when processing the data. Exemplarily, both a spectrum far away from and at the center of a vortex are shown in Figure 7.2(a). The spectrum at the vortex center exhibits a broad zero-bias peak, characteristic for the presence of thermally merged CdGM states as already shown in Figure 5.6. The result of the full grid spectroscopy is depicted in Figure 7.2(b), where slices at different bias voltages were stacked to obtain an impression of the variation of the apparent vortex shape at different energies. If imaged at a bias voltage of $-2\,\mathrm{mV}$, corresponding to the position of the coherence peaks, the vortex appears as an almost fully isotropic depression with a diameter (FWHM) of about 80 nm, which corresponds well to the expected length scale of $2\xi_\mathrm{Nb} \approx 76\,\mathrm{nm}$ over which the order parameter varies across a vortex. At lower absolute bias voltages, the depression turns into a protrusion as is expected, and the vortex clearly changes its apparent shape. First, the vortex seems to split, reaching a coffee bean-like shape at a bias voltage

---

[2] Although the magnetic field penetrates the superconductor within the flux tubes, the exponential decay of the flux on a length scale $> \lambda_\mathrm{L}$ [190] still influences the excitation spectrum in between the vortices, causing the discrepancy between the spectrum shown as a black line in Figure 7.2(a) measured in between the vortices at 100 mT and the zero-field data in Figure 6.4(b).

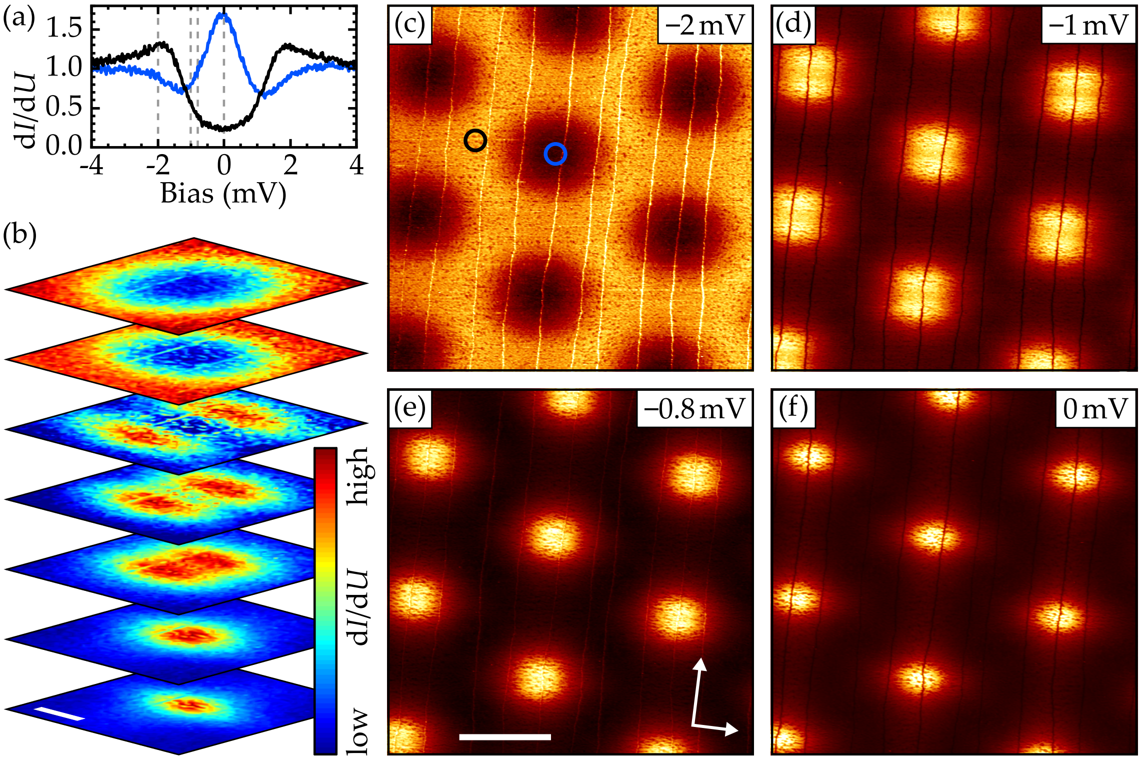

Figure 7.2: Vortices on clean Nb(110). (a) Spectra recorded far away from (black line) and at the center of a vortex (blue line) as indicated in (c). The enhanced $\mathrm{d}I/\mathrm{d}U$ signal at zero bias indicates the presence of CdGM states in the vortex core. (b) Stacked differential conductance data measured on a single vortex in a full grid spectroscopy. Slices were taken at $U = (-2.0,\ -1.6,\ -1.2,\ -1.0,\ -0.8,\ -0.4,\ 0.0)$ mV (top to bottom). Scale bar is 30 nm. (c)-(f) Constant tip–sample separation $\mathrm{d}I/\mathrm{d}U$ maps recorded at the indicated bias voltages. Scale bar is 100 nm. In (b) as well as (c)-(f), the transformation of the apparent vortex shape from circular at higher bias voltages to elliptical at 0 mV is visible. At an intermediate bias range between -1.4 mV and -0.8 mV the vortices appears to split along the $\langle 0\,0\,1\rangle$ direction. Stabilization parameters: (a) $U = -7$ mV, $I = 150$ pA, $U_\mathrm{mod} = 0.1$ mV; (b) -10 mV, 200 pA, 0.1 mV; (c)-(f) -100 mV, 200 pA, 0.1 mV. Scanning bias voltage in (c)-(f) as indicated in the individual panels. z-offset: (c) -170 pm; (d)-(f) -180 pm. $\mu_0 H = 100$ mT; $T = 1.4$ K. *Adapted from Ref. [316]. Copyright ©2020 by the American Physical Society.*

of approximately -1 mV, and becomes elliptical at 0 mV. To demonstrate that this observation is not unique to a single vortex, measurements over a larger area including several vortices were performed. Here, it is not suitable to perform a full grid spectroscopy, as the spatial resolution would need to be significantly reduced to maintain a reasonable measuring time. Instead, the topography of the surface was recorded at a bias voltage sufficiently far away from E_F, such that small LDOS variations in the gap region become negligible. After every line, the

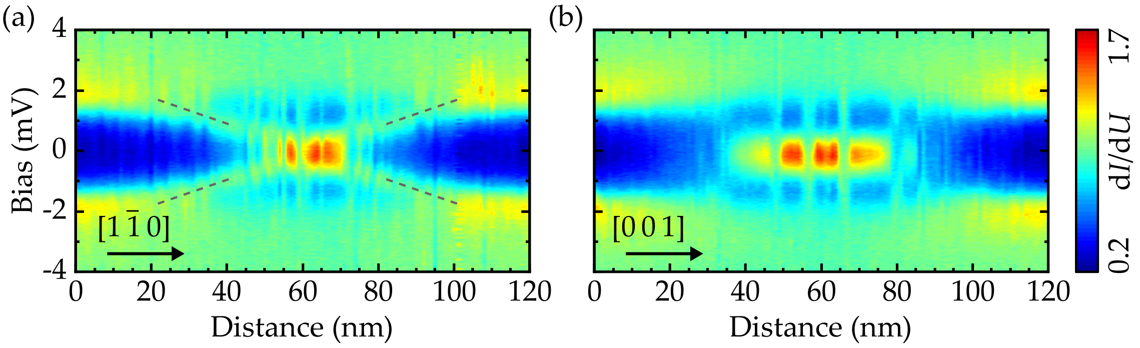

Figure 7.3: Line grids recorded across a single vortex along the (a) $[1\,\bar{1}\,0]$ and (b) $[0\,0\,1]$ direction revealing direction-dependent spatial dispersions of the in-gap states. In (a), the x-shaped dispersion expected for CdGM states is visible and highlighted with dashed lines. This dispersion is absent along the orthogonal direction displayed in (b), where the CdGM states seem to remain centered around 0 mV. The positions with an almost flat LDOS in both line grids coincide with the presence of hydrogen on the surface, which acts detrimental on the CdGM states (cf. section 7.2). Stabilization parameters: $U = -7$ mV, $I = 150$ pA, $U_{\text{mod}} = 0.1$ mV. $\mu_0 H = 100$ mT; $T = 1.4$ K.

bias voltage was changed to the desired value and the recorded topography was retraced, including a constant z-offset to enhance the measured $\mathrm{d}I/\mathrm{d}U$ signal. The results are displayed in Figure 7.2(c)-(f). At the selected bias voltages the main features described above are clearly visible. Imaged at -2 mV, the vortices are round-shaped and acquire a coffee bean shape at -1 mV. Below this value, the splitting disappears and gives way to an elliptical shape. These measurements further allow to determine the orientation of the anisotropic shapes. The ellipsis' long axis in Figure 7.2(f) as well as the trench in the split vortices in panel (d) align with the $\langle 0\,0\,1 \rangle$ direction of the Nb(110) lattice indicated in (e), while the ellipsis' short axis aligns with the crystallographic $\langle 1\,\bar{1}\,0 \rangle$ direction. Equally, the $(1\,1)$ and $(1\,\bar{1})$ directions of the Abrikosov lattice itself align with the high-symmetry directions of the Nb(110) surface.

To further assess the difference between the $\langle 1\,\bar{1}\,0 \rangle$ and $\langle 0\,0\,1 \rangle$ direction, spectroscopic data recorded along lines across a single vortex in these two directions is presented in Figure 7.3. At the center of the vortex, the intense zero-bias peak already shown in Figure 7.2(a) is visible for both line grids. Along the $[1\,\bar{1}\,0]$ direction, this peak splits into two energetically symmetric ridges when moving away from the center, forming an x-shaped LDOS profile. This spatially dispersing feature can be identified as the thermally merged CdGM states as described in section 5.2 and is expected for a clean surface. Along the $[0\,0\,1]$ direction, a qualitatively different picture is observed. Within the energy resolution of the experiment, the central peak does not split but instead remains at the same energy while its intensity decays away from the vortex center. This lacking x-shaped dispersion along the $\langle 0\,0\,1 \rangle$ direction can be directly related to the vortex splitting along this direction. These findings indicate that the CdGM states play a crucial role in the observed anisotropic vortex shapes on the clean Nb(110) surface at different bias voltages.

As discussed in section 5.2 the existence of the CdGM states depends on the length of the mean free path in comparison to the vortex size which is determined by $\xi_{\mathrm{Nb}} \approx 38$ nm. If for the clean surface one considers the same mean free path as for bulk Nb, $l_{\mathrm{F,bulk}} = 100$ nm [329], the appearance of CdGM states on the clean Nb(110) surface is expected. It is possible to tune the surface mean free path by introducing surface disorder. In the following I will therefore review the influence of surface adsorbates on the CdGM states and the concomitant vortex shape.

7.2 INFLUENCE OF SURFACE DISORDER ON THE OBSERVED VORTEX SHAPE

The most abundant contaminant on the "clean" Nb(110) surface is hydrogen, as discussed in section 6.1. Although the measured superconducting gap is not influenced by the presence of hydrogen within the resolution of the presented experiments, the observed CdGM states are. Figure 7.4 displays $\mathrm{d}I/\mathrm{d}U$ maps of a single vortex, similar to those presented in Figure 7.2(c)-(f). Especially at voltages $|U| \leq 1$ mV, i.e. at energies inside the gap, the characteristic structure of hydrogen emerges as elongated depressions along the $\langle 0\,0\,1 \rangle$ direction, also seen in the simultaneously recorded topography in Figure 7.4(f). Setpoint effects can be excluded as the origin of this observation, as at the stabilization voltage of -100 mV the tip is in fact slightly closer to the surface when measuring on top of hydrogen in comparison to the truly clean surface. Thus, the $\mathrm{d}I/\mathrm{d}U$ signal should actually be enhanced if setpoint effects were dominating. One can thus conclude, that the CdGM states' intensity is locally reduced by the presence of hydrogen. If the concentration of hydrogen on the surface is too high, the spatial dispersion of the CdGM states and the bias-dependent vortex shape vanish [132].

The different oxygen surface reconstructions described in chapter 6 provide an ideal platform to further study the influence of surface disorder on the CdGM states without altering e.g. the superconducting gap, the penetration depth or the coherence length of the material. The quasiparticle mean free path is expected to be considerably reduced by the presence of oxygen. While NbO_x phase II has a periodic structure and exhibits translation invariance at least within a single domain, NbO_x phase I is only quasiperiodic and should thus possess an even shorter quasiparticle mean free path in comparison to NbO_x phase II. Hence, a significant reduction or complete vanishing of the CdGM states is anticipated.

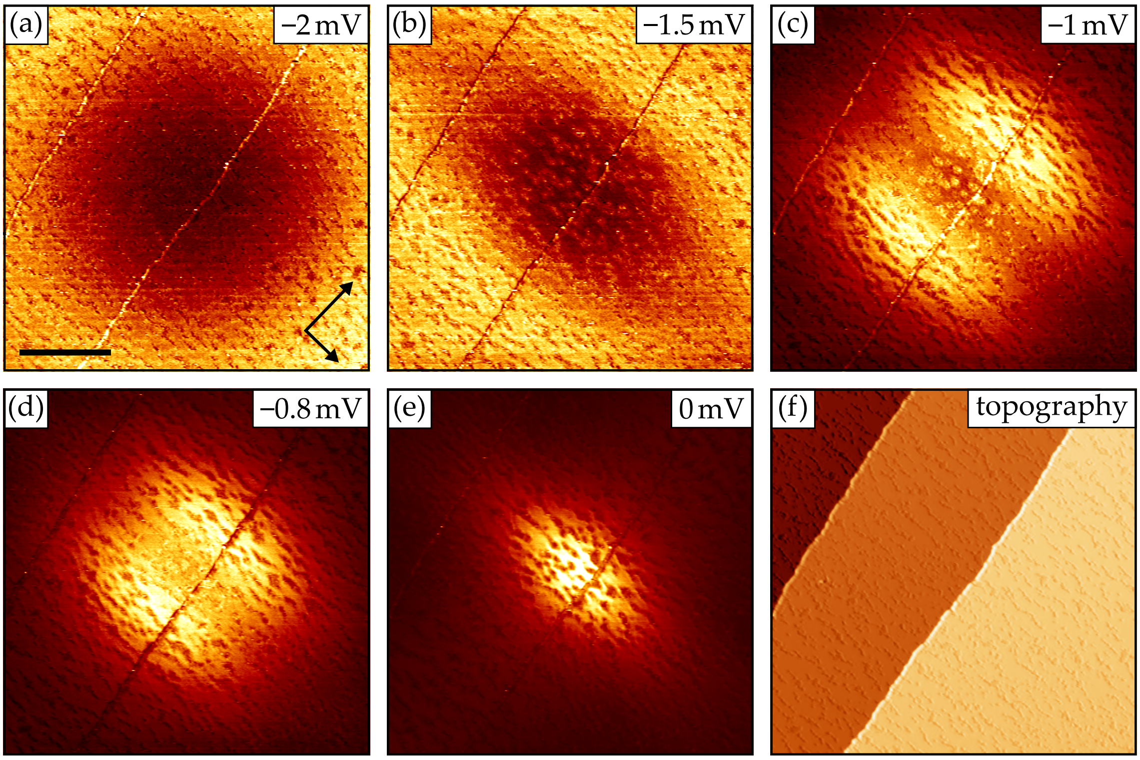

Figure 7.4: (a)-(e) Constant tip–sample separation dI/dU maps of a single vortex on a clean Nb(110) surface recorded at the indicated bias voltages. Scale bar is 30 nm. (f) The simultaneously recorded topography. At bias voltages $|U| \leq 1$ mV, hydrogen adsorbates are visible in the dI/dU maps, indicating the detrimental effect of hydrogen on the CdGM states. Stabilization parameters: $U = -100$ mV, $I = 200$ pA, $U_{\text{mod}} = 0.1$ mV. Scanning bias voltage as indicated in the individual panels. z-offset: (a),(b) -180 pm; (c)-(f) -220 pm. $\mu_0 H = 100$ mT; $T = 1.4$ K.

Single spectra recorded at the center of vortices on all three Nb (110) surfaces presented in Figure 7.5 confirm this hypothesis. As shown before, on clean Nb(110) the presence of CdGM states manifests itself in a pronounced electron-hole symmetric peak at the Fermi level. The intensity of this peak is dramatically reduced in vortices on NbO$_x$ phase II. Additionally, the peak intensity is not symmetric around the Fermi level anymore. Although such an asymmetry is also found in the calculations presented in Figure 5.5(b) for an isotropic material, the observed asymmetry in the measurements on NbO$_x$ phase II might also be influenced by other factors. On NbO$_x$ phase I, the zero-bias peak vanishes almost entirely, indicating the disappearance of the energetically discrete CdGM states. Instead, the gap is homogeneously filled with quasiparticles at the center of the vortex.

Figure 7.5: Single spectra recorded at the center of a vortex on all three Nb surfaces. The increasing oxygen contamination of the surface leads to a depletion of the CdGM states as becomes evident from the decreasing peak intensity. Stabilization parameters, magnetic field and temperatures: see Figures 7.3 and 7.6. *Adapted from Ref. [316]. Copyright ©2020 by the American Physical Society.*

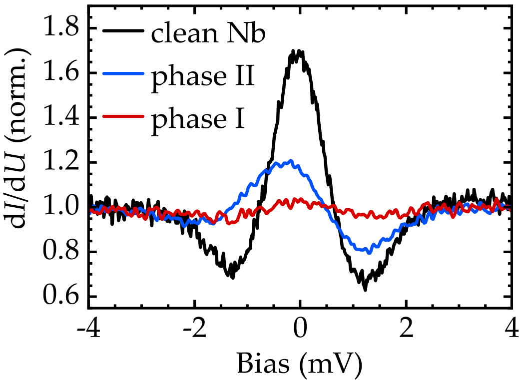

It is important to briefly discuss the potential influence of hydrogen, which has already been shown to locally suppress the CdGM states on the otherwise clean Nb surface, on the observations made on the oxygen-reconstructed surfaces. Hydrogen is not resolved on both NbO_x phase I and NbO_x phase II in topographic measurements, yet its presence cannot be excluded and instead is rather likely, given its high solubility in Nb [330]. Nevertheless, the difference in the observed CdGM intensity in the vortex centers demonstrated in Figure 7.5 clearly correlates with the oxygen induced surface disorder and the inferred changes of the mean free path on NbO_x phase I and NbO_x phase II. Thus, although an influence of hydrogen on these measurements is possible, the dominating contribution to the observed behavior is ascribed to the respective oxygen reconstructions.

To assess how the absence of the CdGM states influences the apparent vortex shape at different bias voltages, constant energy cuts from full grid measurements of single vortices on both surfaces are displayed in Figure 7.6(a) and (c), revealing qualitative differences in comparison to the measurements on clean Nb(110). On the more highly ordered NbO_x phase II surface, a very weak splitting of the vortex around -1.2 mV remains visible, yet the elliptical deformation of the vortex at 0 meV is almost entirely absent. On NbO_x phase I, the apparent vortex shape remains almost fully isotropic throughout all bias voltages. The zero-bias conductance maps of vortices on each of the three Nb surfaces displayed in Figure 7.6(e) emphasizes the qualitative difference. While the vortex on clean Nb(110) appears strongly elliptical with a ratio of about 0.6 between the minor and major axis of the ellipse, the vortices on both NbO_x phase I and NbO_x phase II are almost fully isotropic with an axes-ratio of ~ 0.9. The line grids presented in Figure 7.6(b) and (d) measured along the respective lines indicated in panel (e) confirm the significantly lower zero-bias LDOS at the center of the vortices on the oxygen-reconstructed surfaces and only show a blurred (NbO_x phase II) or no (NbO_x phase I) spatial dispersion of the in-gap stats. Line grids recorded in directions perpendicular to the presented ones exhibit comparable features, contrary to the very anisotropic picture drawn in Figure 7.3. This observation explains the lacking or depleted splitting of the vortices on NbO_x phase I and

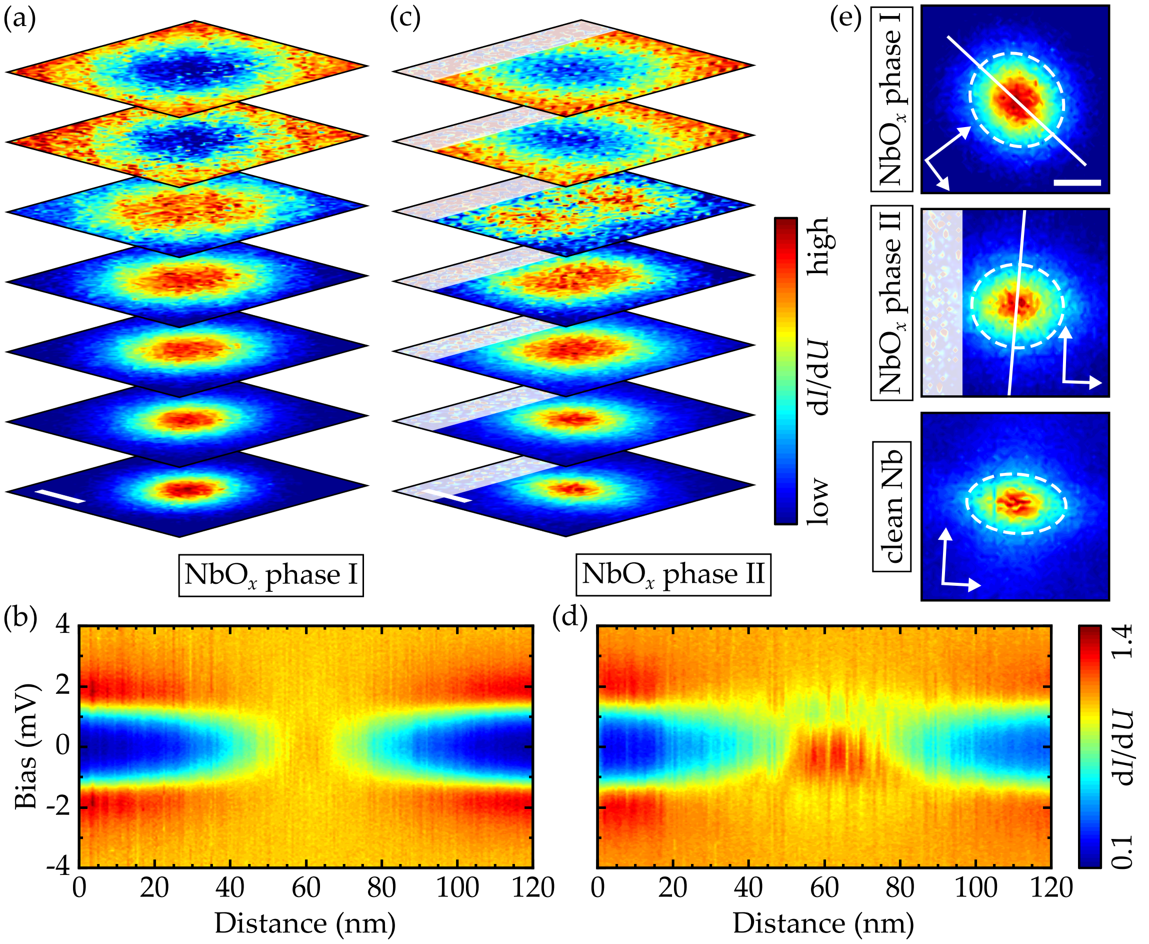

Figure 7.6: (a) Stacked differential conductance data measured on a single vortex in a full grid spectroscopy on NbO$_x$ phase I. Slices were taken at $U = (-2.0, -1.6, -1.2, -1.0, -0.8, -0.4, 0.0)$ mV (top to bottom). (b) Line grid recorded along the line indicated in the corresponding zero-bias map in (e). (c),(d) Same as (a),(b) but on NbO$_x$ phase II. A tip instability at the end of the measurements displayed in (c) caused parts of the conductance maps to be very noisy. This area is gray shaded for a clearer presentation of the data. While a small anisotropy and a weak splitting of the vortex remain on NbO$_x$ phase II, the vortex on NbO$_x$ phase I appears almost fully symmetric. This is emphasized in the the zero-bias maps of all Nb surfaces in (e). All scale bars are 30 nm. Stabilization parameters: (a),(b) $U = -5$ mV, $I = 100$ pA $U_{\mathrm{mod}} = 0.2$ mV; (c),(d) -7 mV, 200 pA, 0.2 mV. $\mu_0 H = 100$ mT; $T = 1.5$ K.

NbO$_x$ phase II, respectively, and corroborates the hypothesis that the CdGM states play a crucial role in the anisotropic appearance of the vortices on clean Nb(110).

7.3 DISCUSSION

The presented experimental results confirmed the impact of the CdGM states on the apparent vortex shape in the STM measurements. Yet, the origin of the observed anisotropy on clean Nb(110) still needs to be examined. In literature, three different possible causes for anisotropic vortices have been discussed: (i) If the inter-vortex distance is smaller or comparable to either the superconductor's penetration depth or coherence length, neighboring vortices will influence each other either by stray fields [331] or overlapping quasiparticle wave functions [332]. In the presented case, the lattice constant of the Abrikosov lattice of ≈ 160 nm (cf. Figure 7.1(a)) is significantly larger than both the penetration depth and the coherence length (39 nm, 38 nm). Further, an influence of the six-fold symmetric vortex lattice should result in vortices with the same symmetry. Instead, the two-fold symmetry observed in the experiments hints at the two remaining possible explanations, (ii) an anisotropic pairing potential or (iii) an anisotropic Fermi surface [218, 322, 333, 334], which are both expected to inherit their symmetry from the two-fold symmetric crystal structure of the Nb(110) surface. Transport measurements in tunnel junctions made from crystalline bulk Nb demonstrated a bulk gap anisotropy of no more than ~ 10 % in various crystallographic directions [335, 336]. As the size of superconducting gap on the surface closely corresponds to the average bulk value as shown in chapter 6 and the measured differential conductance is well described by an isotropic gap function, the anisotropy of the surface gap is not expected to exceed the variation of the bulk gap. Since the latter is significantly lower than the anisotropy of the vortex LDOS at zero bias, the anisotropic pairing is considered an unlikely explanation for the observed behavior.

The effect of an anisotropic Fermi surface can be investigated by self-consistently solving the Bogoliubov-de Gennes equations in a 2D system with isotropic pairing and discrete square lattice with lattice constant a. Generally, STM experiments are most sensitive to states close to the $\overline{\Gamma}$-point of the surface Brillouin zone as discussed in section 3.1 [107, 337]. First of all, this results in the conclusion that the observed specific shape of the vortices on clean Nb(110) is an outcome of the employed experimental technique, and that the full LDOS inside the vortices, which is an integral over the entire Fermi surface, will likely show a different spatial variation. Nevertheless, the observed anisotropy of the apparent vortex shape is a result of the anisotropic surface and, if well understood, allows to draw conclusions on the underlying electronic structure. As a second, related consequence of this k-selectivity of STM experiments, it is sufficient to mimic the stadium-shaped bands in the center of the Nb(110) Fermi surface marked in Figure 6.3 in the proposed simulations. For this purpose, a 2D electron gas with different effective masses $m_x/m_y \approx 0.47$ along the principal lattice directions is

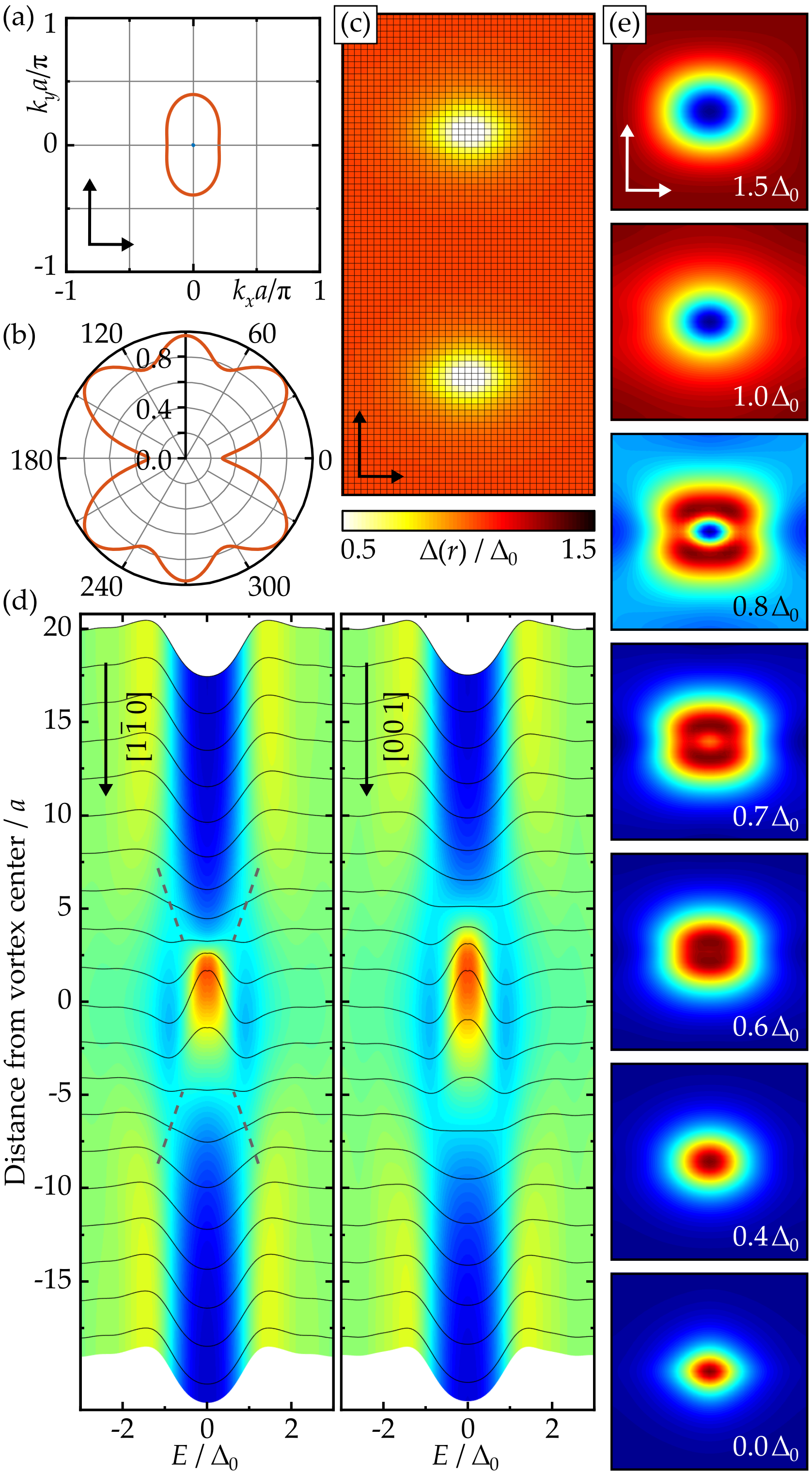

Figure 7.7: Results of the simulations described in the main text. (a),(b) The model's underlying Fermi surface and Fermi velocity, respectively. The displayed directions correspond to the (reciprocal) $[1\bar{1}0]$ and $[001]$ direction. (c) Variation of the pairing order in an external magnetic flux of $2\Phi_0$ at $k_B T = 0.26\Delta_0$. (d) Low-energy LDOS as calculated along the $\langle 1\bar{1}0\rangle$ (left panel) and $\langle 001\rangle$ direction (right panel) after thermal broadening by $k_B T = 0.26\Delta_0$. The x-shaped dispersion of the CdGM states is marked with gray lines. (e) LDOS maps at indicated energies, approximately corresponding to the bias voltages in Figures 7.2 and 7.6. Simulation parameters as labeled in Ref. [316]: $N = 40$, $t_x = 1.5t_0$, $t_y = 0.7t_0$, $t_{so} = t_0$, $V_0 = 2t_0$, $E_F = -4.4t_0$, $\omega_D = t_0$. The pairing order in the absence of fields is $\Delta_0 = 0.23t_0$. *Adapted from Ref. [316]. Copyright ©2020 by the American Physical Society.*

chosen. Additionally, spin-orbit coupling of Rashba or Dresselhaus type [338, 339] is added to obtain a truly anisotropic band structure [316]. Choosing the Fermi energy such that one band dominates, a large stadium-shaped Fermi surface and a small circular surface, depicted in orange and blue in Figure 7.7(a), respectively, are obtained, constituting a basic model of the relevant bands. Further details of the simulations can be found in Ref. [316] and the corresponding supplemental material. The x- (k_x-)direction and y- (k_y-)direction in Figure 7.7(a) correspond to the $[0\,0\,1]$ ($\overline{\Gamma} - \overline{\mathrm{H}}$) and $[1\,\bar{1}\,0]$ ($\overline{\Gamma} - \overline{\mathrm{N}}$) direction of the surface and surface Brillouin zone of Nb(110), respectively. Figure 7.7(b) illustrates the Fermi velocity corresponding to the dominant (orange) band. To study vortices in this model, a quantized flux of $2\Phi_0 = 2\mu_0 H(Na)^2$ is added to a lattice of size $(N \times 2N)a$, as displayed in Figure 7.7(c). The two resulting vortices appear as depressions of the pairing order Δ. Although the pairing order already exhibits a small anisotropy with the major axis of the recognizable ellipse oriented along the $\langle 0\,0\,1\rangle$ direction, features such as the splitting of the vortex are not evident.

As deduced in the previous section, it is necessary to consider the CdGM states of the system. Panels (d) and (e) of Figure 7.7 display the calculated quasiparticle LDOS within a single vortex broadened by $0.26\Delta_0$, corresponding to an experimental temperature of about 1.5 K, close to the experimental value. In Figure 7.7(d), the x-shaped dispersion of the CdGM states along the y- ($[1\,\bar{1}\,0]$) direction is evident, while it seems to be absent in the simulations along the x- ($[0\,0\,1]$) direction, both features identical to the presented measurements on clean Nb. The LDOS maps in Figure 7.7(e) confirm the good qualitative agreement between experiment and simulations and even allow for a quantitative comparison. The splitting of the vortex starting at an energy of about 1.2 meV in the presented measurements is reproduced at a similar energy of $0.8\Delta_0$ in the simulations. The vortex remains split down to $0.6\Delta_0$, again reflecting the experimental observations. At lower energies, the vortex shape transforms into an ellipse, with an axis ratio of about 0.7. This value is slightly larger than that of 0.6 observed in the spectroscopic measurements on clean Nb, but nevertheless confirms the good agreement between model and experiment.

As a result, the employed simulations coherently identify the anisotropic Fermi surface as the physical origin anisotropic CdGM states on the Nb(110) surface, resulting in an apparent anisotropic shape of the vortices. A closer look at the simulation results reveals that the dispersion of the CdGM states along the y-direction is only covered up by the introduced thermal broadening (the reader is referred to the supplemental material of Ref. [316] for corresponding graphs). If a lower broadening $< 0.1\Delta_0$ is used for the calculations, corresponding to a temperature significantly lower than the one accessible in the present experimental setup, non-zero-energy CdGM states with a weaker dispersion and lower intensity than along the $\langle 1\,\bar{1}\,0\rangle$ direction also appear along the $\langle 0\,0\,1\rangle$ direction.

In summary, the presented combination of STM and STS measurements on clean and oxygen-reconstructed surfaces revealed anisotropic vortices on the Nb(110) surface, with the apparent vortex shape changing from round at energies close to the gap edge to a split, coffee bean-like at intermediate energies to elliptical at the Fermi energy. By reducing the quasiparticle mean free path on the surface by increasing its oxygen content, the CdGM states found on the clean surface could be quenched, concomitant with a reduction of the asymmetry of the observed vortices. In combination with tight-binding simulations, the anisotropic Fermi surface of Nb(110) was established as the main cause for the anisotropy of the observed CdGM states and the resulting apparent vortex shape.

The presented results complement other works demonstrating the influence of Fermi surface anisotropy on the quasiparticle excitations inside vortices in type II superconductors [323–325, 334] and constitute an experimental confirmation of the theoretically calculated band structure of the Nb(110) surface. In the context of topological superconductivity, the experiments on the topologically trivial superconductor Nb(110), similarly to the subsequently published measurements on La(0001) in Ref. [325], display a suppressed spatial dispersion of the lowest-lying vortex core states caused by the Fermi surface anisotropy, while earlier works attributed spatially non-split zero-bias states inside vortices to MZMs [286, 326]. The results obtained in this chapter suggest a more reliable possibility to distinguish both topological MZMs and trivial states in vortices: If one is able to add surface disorder to the system without changing the bulk properties, trivial CdGM states are depleted while MZMs are expected to remain due to their topological protection.

Chapter 8

8 CORRELATIONS OF YU-SHIBA-RUSINOV STATES AND THE KONDO EFFECT IN FE ATOMS ON CLEAN NB(110)

Chains of magnetic adatoms on superconducting surfaces constitute one possible realization of Majorana zero modes in solid state systems. Yet, to be able to controllably engineer systems with the desired electronic properties, it is crucial to study the individual building blocks and their interactions in the system: (i) the adatom–substrate interaction, determining the energy and spatial extent of the atomic YSR states and (ii) the interatomic coupling of those individual YSR states.

Following the experimental results presented in the previous two chapters, Nb(110) is expected to constitute an interesting platform to study both of these interactions. Most importantly, the large superconducting gap facilitates the detection of in-gap states, yet also the possibility of changing the surface's reconstruction allows to tune the occurring YSR states as will be shown in the following.

In this chapter, I will focus on the adatom–substrate interaction of single Fe atoms atop the Nb(110) surface. The choice of Fe atoms was motivated by recent experiments on Fe chains on Pb(110) and Re(0001) [65, 66, 68]. To increase the energy resolution of the presented measurements beyond the limit imposed by the finite temperature of the setup, most experiments were conducted using superconducting tips. Properties of such tips will be briefly discussed in the first part of the chapter. In section 8.1, I will demonstrate that Fe atoms on the clean and oxygen-reconstructed surface of Nb(110) exhibit strongly varying adatom –substrate interactions, eventually leading to Fe atoms in both the unscreened and Kondo screened phase of the YSR phase diagram which will be discussed in section 8.2. This study highlights the strong bond between both effects, linking Kondo resonances in the normal-metallic with YSR states in the superconducting regime.

The results presented in this chapter were published in Ref. [340]. The presented simulations were performed by Domenico Di Sante, Alexander Kowalski, Ronny Thomale and Giorgio Sangiovanni from the Institute for Theoretical Physics and Astrophysics at the University of Würzburg.

8.1 Yu-Shiba-Rusinov states in single Fe atoms on Nb(110)

The preparation of the Nb(110) surface followed the procedure described in chapter 6, resulting in a surface with sufficiently low oxygen and also hydrogen concentration to observe large areas of the pristine (110) surface. After cooling the sample in the STM, Fe atoms were deposited from an Fe rod (*Alfa Aesar*, 99.995 %) onto the cold surface ($T_{\mathrm{sample}} \approx 4.2$ K), resulting in a coverage of about 0.1 atoms/nm^2. An exemplary topography of the obtained surface is displayed in Figure 8.1(a). Arrows in the scan mark Fe atoms in different adsorption positions on the Nb surface: While Fe atoms sitting on the clean surface (Fe/Nb(110)), marked by black arrows, appear with a corrugation of about 60 pm as shown in the line profile in Figure 8.1(b), Fe atoms adsorbed on remaining patches of NbO$_x$ phase II (Fe/NbO$_x$), marked by blue arrows, exhibit a corrugation of $\gtrsim 100$ pm. By atomic manipulation of single atoms onto and away from an oxygen patch it was possible to confirm that the apparent difference between these two kinds of atoms is solely based on the presence of oxygen [340]. Rarely, "bright" Fe atoms also are found on the clean surface, as marked by the gray arrow in Figure 8.1(a) [340]. However, their origin is not fully understood, and measurements on close-packed Fe dimers that will be presented in chapter 9 exhibited both similar topographic and spectroscopic features. Hence, Fe atoms sitting in potentially unconventional binding sites and randomly assembled dimers are indistinguishable by the means presented in this chapter and are thus for the moment not considered further.

The origin of this strong adsorption site-dependent corrugation of Fe atoms on clean an oxygen-reconstructed Nb was illuminated by *ab initio* DFT calculations using the VASP simulation package [317] (cf. Ref. [340] for more details on the simulations). From these calculations, the energetically most favorable adsorption site on the clean as well as on the oxygen-reconstructed surface was found to be the fourfold hollow site as displayed in Figure 8.1(c). For Fe atoms on clean Nb, this was experimentally confirmed in several different works [243, 340, 341] and will also be shown in chapter 9. Yet, the determined adatom–surface distances (defined by the center of the adatom and the plane through the center of the topmost Nb atom layer) differ significantly for the two surfaces, being 1.70 Å for Fe/Nb(110) and 1.34 Å for Fe/NbO$_x$, and at first sight contradict the experimentally observed difference in apparent height. The corresponding calculated constant LDOS contours, which are decisive for the measured height profiles in constant current

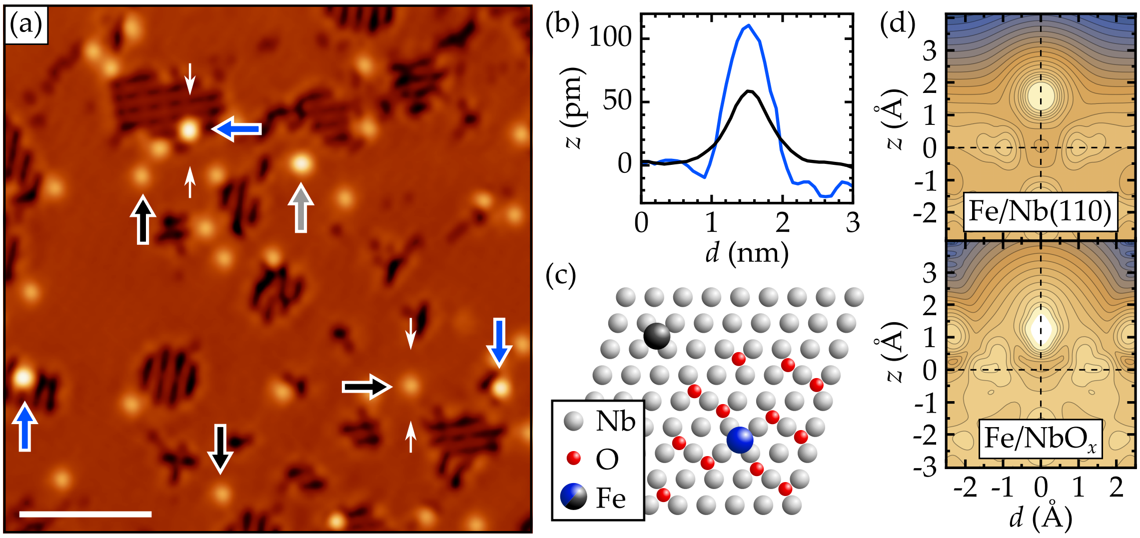

Figure 8.1: (a) Topographic scan of the Nb(110) surface after low-temperature deposition of Fe atoms appearing as bright protrusions. Arrows mark atoms in different adsorption positions: faint atoms on clean Nb(110) (black), a bright atom on clean Nb(110) (gray) and bright atoms on remaining patches of NbO$_x$ phase II (blue). Stabilization parameters: $U = -100$ mV, $I = 400$ pA. Scale bar is 5 nm. (b) Height profiles for Fe/Nb(110) and Fe/NbO$_x$ taken along the lines indicated by small white arrows in (a). (c) Ball model of the energetically favorable fourfold hollow adsorption position of Fe/Nb(110) and Fe/NbO$_x$. (d) Calculated constant LDOS lines for both types of Fe atoms. *(d) Adapted from Ref. [340]. Copyright ©2020 by the American Physical Society.*

STM images, are displayed in Figure 8.1(d) and resolve the issue. It becomes evident, that, although Fe on NbO$_x$ phase II sits closer to the surface, the constant LDOS lines are more corrugated, resulting in a larger apparent height of the adatom. Further, a significant distortion of the LDOS contour in comparison to the spherical shape for Fe/Nb(110) is visible, hinting also at a stronger hybridization between adatom and substrate, relevant for the emergent YSR states, as will be discussed below. It is noteworthy, that in contrast to the single adsorption position for Fe/Nb(110), a variety of adsorption positions exists for Fe/NbO$_x$, as will be revealed by spectroscopic data presented later in this section. Nevertheless, the topographic measurements indicate that the differences between those adsorption positions are more subtle than the difference between Fe on clean Nb(110) and Fe on the chosen position on NbO$_x$ phase II, as all Fe atoms on NbO$_x$ phase II appear with the same height of about 100 pm.

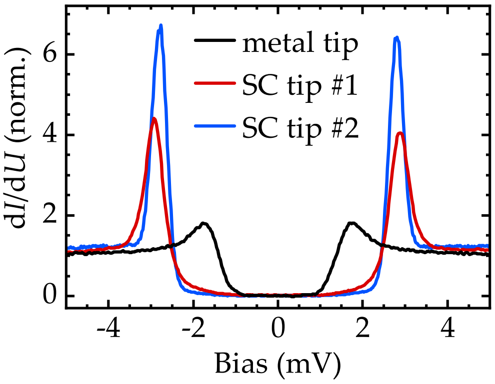

Figure 8.2: Single spectra recorded with a normal-metallic and two different superconducting tips. Fitting the latter with two convoluted Dynes functions yields $\Delta_t = 1.35$ meV, $\Gamma_t = 0.19$ meV and 1.25 meV, 0.12 meV for SC tip #1 and #2, respectively. Stabilization parameters: $U = -7$ mV, $I = 400$ pA, $U_{\mathrm{mod}} = 0.1$ mV. $T = 1.4$ K.

Measurements with superconducting tips

The spectroscopic data on single and coupled Fe atoms on Nb(110), the latter will be the topic of chapter 9, was mostly measured with superconducting tips in order to enhance the spectral resolution of the experiments beyond the thermal limit [202] (see also chapter 5). I will here therefore briefly review the process of preparing such tips and their spectroscopic properties, before discussing the results of the experiments on single Fe atoms.

In literature, mostly two ways of obtaining superconducting tips are described. One possibility is to cut or etch tips from wires made from bulk superconducting materials such as niobium [342, 343] or vanadium [344]. In contrast to the second approach described below, this approach has the advantage of producing tips with well developed, bulk-like superconducting gaps. However, due to substantial oxidation of these materials in air, it is always necessary to treat these tips by Ar-sputtering [169] or field emission [342] to remove the oxide layer after introducing them to the UHV system. The second possibility is to use standard tungsten tips and dip them into a superconducting sample in order to pick up a small cluster of the material [201, 202, 345]. This process allows to prepare superconducting tips *in situ* and if necessary to also remove the cluster by pulsing on a normal metal. Yet, the finite size of the cluster, which depends at least partially on the indentation depth, can lead to non-BCS-like gaps with significantly broadened coherence peaks and gap edges in comparison to the bulk material [346, 347]. This effect can lead to a lower energy resolution than reachable with bulk tips.

All superconducting tips used for measurements presented in this thesis were obtained by indentation into a Nb(110) crystal, as this does not require to develop a new tip fabrication process and yielded satisfactory results concerning tip stability and topographic as well as spectroscopic resolution. While the indentation depth needed to create a superconducting tip varied between tens of nanometers and several micrometers, generally deeper indentation led to more defined (but not necessarily larger) gaps in the tip spectrum. Figure 8.2 shows

spectra measured on a clean Nb(110) surface with two superconducting tips and one normal-metallic tungsten tip for comparison. It is clearly seen, that although the gap of SC tip #1 appears to be even slightly larger than that of SC tip #2 as seen from the position of the coherence peaks, the coherence peaks are significantly wider and less intense. These observations are confirmed by fitting both gaps with a convolution of two Dynes functions (cf. Equation (5.16)) with fixed sample gap $\Delta_\mathrm{s} = 1.53$ meV and quasiparticle broadening $\Gamma_\mathrm{s} = 1$ μeV as well as effective temperature $T = 1.8$ K as obtained from the fit of the spectrum measured with a normal-metallic tip (cf. section 6.2). For SC tip #1 one obtains $\Delta_{\mathrm{t},\#1} = 1.35$ meV, $\Gamma_{\mathrm{t},\#1} = 0.19$ meV and for SC tip #2 $\Delta_{\mathrm{t},\#2} = 1.25$ meV, $\Gamma_{\mathrm{t},\#2} = 0.12$ meV. As a more bulk-like tip is expected to show a smaller quasiparticle broadening, while the gap size can even be enhanced for smaller cluster by finite size effects [348, 349], the cluster of SC tip #2 is presumably larger than that of SC tip#1. This appears to be reasonable as the latter was obtained by an accidental, probably severe, tip crash, while the SC tip#1 was indented for "only" 100 nm. Still, both tips greatly enhance the energy resolution in the experiments. Observed YSR states could be fitted with a Gaussian envelope with FWHM $\lesssim 0.3$ mV, twice smaller than the thermal broadening of $3.5 k_\mathrm{B} T$ of a delta-like feature at the electronic temperature of the setup.
To extract quantitative values of e.g. YSR energies from measurements with superconducting tips, it is important to keep in mind that all features of the sample's LDOS are shifted by $\pm\Delta_\mathrm{t}$ in the recorded spectra. Therefore, the value of Δ_t was extracted from spectra taken on clean Nb(110) for all presented experiments as described above. It is sufficient to subtract this value from the bias voltages at which the YSR states appear in the measurement, although a full deconvolution of the recorded spectrum and the extracted tip spectrum is also possible [242]. Finally, I want to note that at the tunneling resistances used throughout this thesis no Cooper pair tunneling in form of a Josephson current [350] or Andreev reflections [201], that would lead to $\mathrm{d}I/\mathrm{d}U$ peaks at $U = 0$ and $|U| < \Delta_\mathrm{t}/e$, respectively, occurred.

With the understanding of the characteristics of measurements preformed with superconducting tips, it is now possible to look at spectroscopic data recorded on single Fe atoms in various adsorption positions. In Figure 8.3(a) spectra on both an Fe atom on clean Nb(110) (top panel) and two different Fe atoms on NbO_x phase II (bottom panel) are displayed. The spectrum taken on the Fe atom on clean Nb(110) only shows a small difference to a spectrum taken on the bare surface, presented as a dashed line in the same graph. Only the slight enhancement of the coherence peaks detected on top of the Fe atom indicates the presence of YSR states close to gap edges. Following the introduction of YSR states in section 5.3, it is evident that states with $E_\mathrm{YSR} \approx \Delta$ imply a very weak scattering of the itinerant

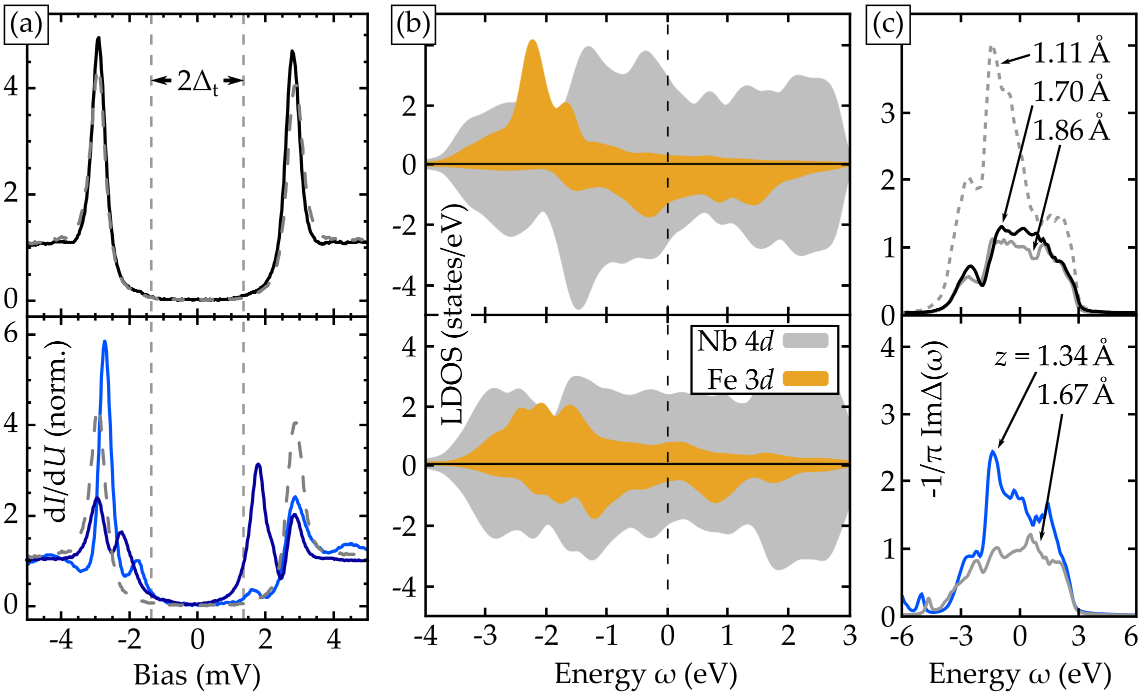

Figure 8.3: (a) Differential conductance spectra measured on single Fe atoms. All top panels correspond to Fe atoms on clean Nb(110), bottom panels to Fe atoms on NbO_x phase II. For Fe/NbO_x, spectra measured on two different atoms are displayed. The gray dashed lines correspond to a spectrum recorded on the bare surface for reference. Stabilization parameters: $U = -7$ mV, $I = 400$ pA, $U_{\mathrm{mod}} = 0.1$ mV. $T = 1.4$ K. $\Delta_t = 1.35$ meV. (b) Calculated LDOS projected on the surface Nb (gray) and Fe d states (orange). The larger asymmetry between majority (positive values) and minority (negative values) spin states for Fe/Nb(110) implies a higher magnetic moment in comparison to Fe/NbO_x. (c) Imaginary part of the hybridization function obtained from DFT calculations for different adatom–surface distances z as given in the graphs. The solid black and blue line display the curves for the respective equilibrium positions. Large values of $\mathrm{Im}\,\Delta(\omega)$ indicate a strong adatom–substrate interaction. *Partially adapted from Ref. [340]. Copyright ©2020 by the American Physical Society.*

quasiparticles at the magnetic adatom spin. In contrast to this, Fe atoms on NbO_x phase II exhibit YSR states at energies well inside the sample's superconducting gap, indicating a much stronger adatom–substrate interaction. The two spectra in the lower panel of Figure 8.3(a) differ substantially, illustrating that as mentioned before, although all Fe atoms on top of NbO_x phase II appear with a similar topography, a variety of adsorption positions within the oxygen reconstruction with slightly different adatom–substrate interactions exist. This fact is further investigated in the following section, resolving a crossing of the YSR states over the quantum phase transition depending on their precise adsorption position.

Before that, the substantial difference between Fe/Nb(110) and Fe/NbO$_x$ shall be assessed. As discussed in section 5.3, the YSR energy is determined by both the magnitude of the impurity spin as well as the interaction of this spin with the itinerant quasiparticles. Further DFT calculations of the investigated system reveal that the latter dominates the formation of the YSR states in Fe atoms on Nb: Figure 8.3(b) displays the calculated DOS projected on the surface Nb (gray) and Fe (orange) *d* states, separated into majority (positive values) and minority spin states (negative values). One can deduce the Fe atom magnetic moment to be $\mu = 2.2\mu_{\mathrm{B}}$ for Fe/Nb(110), more than twice the value of Fe/NbO$_x$ ($\mu = 0.9\mu_{\mathrm{B}}$) [340]. A reduction of the magnetic moment in proximity of oxygen has also been observed in other systems [351, 352]. This demonstrates that in order to obtain the experimentally observed YSR energies, the hybridization of the magnetic moment of Fe/NbO$_x$ must be drastically larger than for Fe/Nb(110), which is indeed corroborated by the DFT calculations: The imaginary part of the calculated hybridization function displayed in Figure 8.3(c) describes the probability amplitude of electrons to hop between the impurity and the substrate [340] (note that the presented calculations do not involve superconductivity, but the Nb surface in the normal state) and is thus a measure of the adatom–substrate interaction. For the equilibrium adatom–surface distances given earlier, displayed as solid black and blue lines, the hybridization function is much larger for Fe/NbO$_x$. Calculations performed for other, artificial heights, especially the second curve displayed for Fe/NbO$_x$ which corresponds approximately to the equilibrium height of Fe/Nb(110), demonstrate that the effect of an increased interaction is mostly distance-dependent and does not rely on the presence of oxygen other than to establish the reduced adatom–surface distance.

The measurements presented in this section demonstrate the strong influence of oxygen on the YSR states appearing in Fe atoms on the superconducting Nb(110) surface. Interestingly, these experimental results were rationalized by DFT calculations performed for Nb in its *normal* state, revealing the adsorption position-dependent hybridization of the Fe atoms to the Nb substrate. This relation between the normal and superconducting state properties of magnetic adatoms on metallic surfaces also manifests itself in the correlation of the Kondo effect and YSR states appearing on the same adatom–surface system in different electronic states of the surface as will be shown in the following section.

8.2 QUANTUM PHASE TRANSITION IN FE ATOMS ON NBO$_x$

The screening of a magnetic impurity by conduction electrons via the Kondo effect renders the system non-magnetic. This effect competes with the formation of YSR states in a superconducting host, where the impurity spin is responsible for the observed pair breaking potential. As a consequence, an increasing hybridization

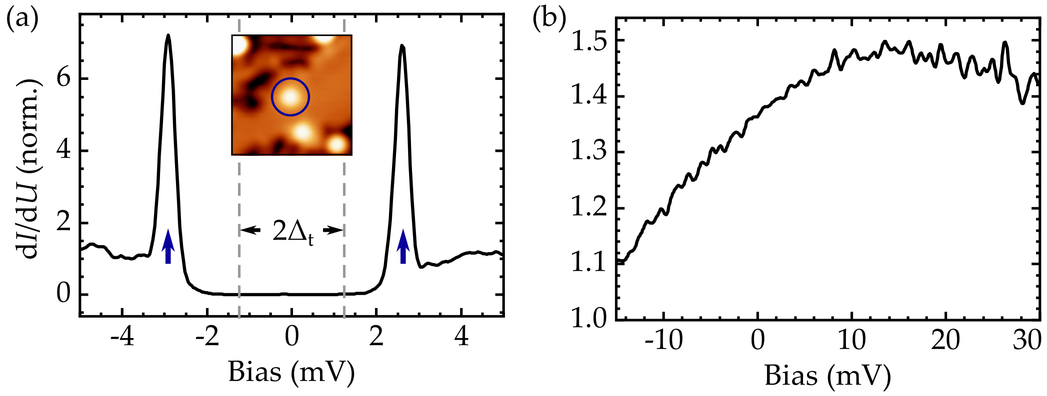

Figure 8.4: (a) Low-energy spectrum of an Fe atom on clean Nb(110), similar to the one shown in Figure 8.3. Arrows indicate the position of the YSR states. The inset shows a $5 \times 5\,\mathrm{nm}^2$ scan of the atom. $\Delta_t = 1.25\,\mathrm{meV}$. (b) Spectrum atop the same Fe atom in an external magnetic field of $\mu_0 H = 600\,\mathrm{mT}$ used to quench superconductivity in the substrate. In contrast to the measurements on Fe/NbO$_x$ presented in Figure 8.5, no pronounced Kondo resonance was detected. Stabilization parameters: (a) $U = -10\,\mathrm{mV}$, $I = 400\,\mathrm{pA}$, $U_\mathrm{mod} = 0.1\,\mathrm{mV}$; (b) $-20\,\mathrm{mV}$, $500\,\mathrm{pA}$, $1\,\mathrm{mV}$. $T = 1.5\,\mathrm{K}$.

of the magnetic adatoms initially decreases the YSR energy, as long as the spin is unscreened for $\Delta < k_\mathrm{B} T_\mathrm{K}$. At $\Delta \approx k_\mathrm{B} T_\mathrm{K}$, the system undergoes a quantum phase transition, and an increasing screening of the impurity spin leads to a simultaneously increasing YSR energy (see also chapter 5). Experimentally, the QPT has been observed on networks of uncoupled magnetic molecules forming Moiré-like structures on Pb(111) and hence giving rise to various adsorption positions on the surface [202, 226], and was artificially induced by altering the impurity–surface interaction by an STM tip [227–229]. In this section I will show that depending on the Fe atoms' adsorption position on NbO$_x$ phase II, the occurring YSR states similarly cross the QPT. The phase transition is traced by combining spectroscopic measurements on these atoms in the superconducting and normal-metallic state of the Nb surface.

To this end, experiments were executed as described in the following: First, measurements with a normal-metallic tip were performed in an out of-plane field of $\mu_0 H = 600\,\mathrm{mT}$, just above $\mu_0 H_{c2}^{\mathrm{Nb}} = 400\,\mathrm{mT}$, to quench superconductivity. Afterwards, the magnetic field was set to zero and low-energy spectra were recorded on the same set of atoms with a superconducting tip prepared by indentation into the Nb surface as described earlier.

Figure 8.4 shows the spectroscopic signatures of a single Fe atom on clean Nb(110). In panel (a), the YSR states close to the superconducting gap edge of Nb already

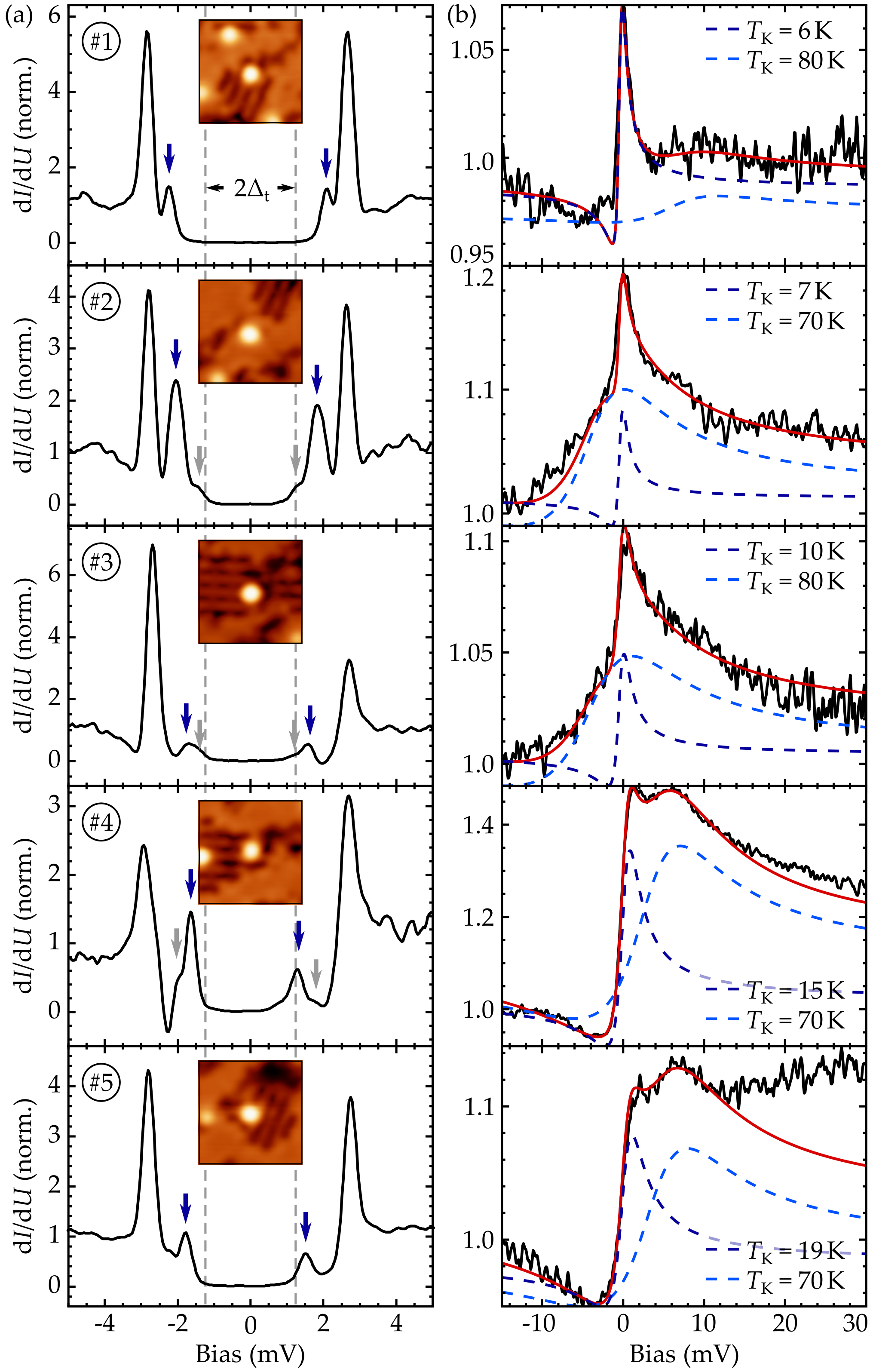

Figure 8.5: Spectroscopy of five different Fe atoms on NbO$_x$ phase II, equivalent to those in Figure 8.4. The gray arrows in (a) indicate additional YSR pairs, the red (blue dashed) lines in (b) show the fit (individual Fano curves) of the Kondo resonances.

introduced in Figure 8.3(a) are presented. In panel (b), the spectrum recorded in the normal state of the substrate is displayed. As expected for magnetic adatoms with only a very weak interaction with the surface, no pronounced peak or dip hinting at a Fano resonance as the result of the Kondo effect is detected. In Ref. [243], the observed wide feature has been interpreted as a signature of inelastic spin excitations, which is strongly broadened for Fe atoms due to a large number of electron–hole pairs excited in the process that reduce the spin excitations' lifetime [163, 353]. However, the agreement of the calculated line shape with the experimental data is limited, preventing an unambiguous interpretation.

For Fe/NbO$_x$ the picture changes dramatically. Figure 8.5 displays superconducting and normal state spectra on five different Fe atoms on NbO$_x$ phase II. All atoms exhibit clear in-gap peaks in the low-energy spectra presented in panel (a). In addition to the two dominant peaks, marked with blue arrows, atoms #2–4 exhibit a second pair of peaks with low intensity close to $eU \approx \Delta_\mathrm{t}$, as indicated by gray arrows. As discussed earlier (cf. chapter 5), coupling of individual atomic orbitals to the substrate can give rise to multiple YSR states [238, 241, 242]. Two characteristics allow to assign the observed intense YSR states of Fe/NbO$_x$ to the d_{z^2} orbital of the Fe atom: First, as this orbital protrudes the most from the surface, STM measurements should be most sensitive to this orbital, explaining the high intensity in the STS data. Second, the d_{z^2} orbital is most sensitive to changes in the adatom–substrate distance [354–356], explaining the strongly varying YSR energies of these peaks, contrary to those close to E_F. Similarly, the single pair of YSR states on Fe/Nb(110) is expected to arise from the Fe atom's d_{z^2} orbital. This was further confirmed by mapping the YSR wave function in Refs. [243, 341]. The energy of the second pair of YSR peaks on Fe/NbO$_x$ only weakly varies and is expected to originate from the $d_{xz,yz}$ orbitals [340].

The picture of two orbitals participating in the adatom–surface interaction persists when examining the normal state spectroscopic data of Fe/NbO$_x$ in Figure 8.5(b). The STS curves reveal distinct Fano-like features, uncovering Kondo resonances in these atoms.[1] After background subtraction, the data can be fitted with the sum of two Fano curves (cf. Equation (2.12)), accounting for two separate Kondo channels, similar to the picture found for Fe atoms on the Re(0001) surface [180]. The resulting curves are displayed in Figure 8.5(b) and the fitting parameters are summarized in Table 8.1. One finds that the two Kondo channels exhibit significantly different Kondo temperatures $T_\mathrm{K} = \Gamma/k_\mathrm{B}$, with one varying in the range of 5–20 K, while the other one is constant within the uncertainty of the fit at 70–80 K. It is noteworthy that all extracted Kondo temperatures are significantly

---

[1] It should be mentioned that the Fe atoms presented here are those that showed clear Fano-like line shapes. A variety of normal state (and corresponding superconducting) spectral curves could be identified during the measurement, about half of which could not be fitted in the same way as those shown in Figure 8.5(b).

Table 8.1: Fano fit parameters of the Kondo resonances in Figure 8.5(b).

Fe atom	T_{K_1} (K)	q_1	T_{K_2} (K)	q_2
#1	6	1.7	80	1.2
#2	7	1.8	70	1.8
#3	10	1.8	80	1.7
#4	15	1.8	70	1.5
#5	19	1.8	80	1.4

higher than any splitting $\Delta E = 2g\mu_\mathrm{B} \cdot \Delta S \cdot B \approx 0.2$ meV ($g = 2$, $\Delta S = 1$) of the resonance at the applied field, such that an artificial broadening can be neglected. Although it is tempting to assign each of these Kondo channels to one of the observed YSR pairs, the spin corresponding to the high-T_K channel is screened well above T_c, which should prevent the formation of YSR states [202]. Thus, the orbital origin of the high-T_K Kondo channel remains unresolved. The Kondo temperature of the low-T_K channel however closely corresponds to the superconducting gap of Nb, allowing to correlate this Kondo resonance with the high-intensity YSR states, both showing a significant adsorption position dependence.

In fact, the correlation of both effects allows to directly observe an adsorption position-dependent phase transition of the Fe atoms' YSR states: In Figure 8.6, the average of the YSR energies extracted at positive and negative bias voltage $\left(E^+_\mathrm{YSR} - E^-_\mathrm{YSR}\right)/2$ is plotted against the fitted Kondo temperature of the low-T_K Kondo channel. By replacing α in Equation (5.30) with $k_\mathrm{B}T_\mathrm{K}/0.72\Delta$ and using the simplification $\beta = 0$,[2] one finds good agreement between the measured data and the theory of the QPT of YSR states represented by the gray line in Figure 8.6. The transition Kondo temperature $T_{\mathrm{K}_\mathrm{c}} = 0.72\Delta/k_\mathrm{B}$ lies within the range of $T_{\mathrm{K}_\mathrm{c}} \approx \Delta/k_\mathrm{B}$ predicted by theory [241, 357, 358] and similar values were found for other systems [202]. It is important to note that although the YSR energies described by Equation (5.30) are based on a classical model, more recent calculations based on an Anderson model of a quantum mechanical spin corroborate the classical findings and justify its usage to describe Fe/NbO$_x$ [359, 360].

To conclude the discussion of the QPT observed in Fe/NbO$_x$, it is valuable to assess the intensity of the detected YSR states on the different Fe atoms. As explained in section 5.3, the classical picture predicts an asymmetry inversion

---

[2] This assumption corresponds to a vanishing spin-independent scattering, which would manifest itself in symmetric peak intensities of the YSR pairs (cf. section 5.3). While this is approximately true for Fe atoms #1–3, it is clearly incorrect for atoms #4 and #5, suggesting a change of not only the spin-dependent scattering reflected in the variation of T_K, but also the spin-independent scattering for different Fe atoms. Yet, similar simplifications led to a good agreement between experiment and theory in different works [202, 225, 234], suggesting that at least for a qualitative understanding $\beta \approx 0$ is justified.

Figure 8.6: YSR energies plotted against the fitted Kondo temperatures from the data set in Figure 8.5 (full dots). By taking the average of the YSR energies extracted at positive and negative bias, any voltage offset from the measurement is eliminated. Error bars indicate the experimental difference between E^+_{YSR} and E^-_{YSR}. The empty dot represents an Fe atom on clean Nb(110), where no Kondo resonance was observed. The gray line displays the model introduced in section 5.3, separating the Fe atoms into an unscreened (small T_K) and Kondo screened (high T_K) regime. The QPT occurs at $T_{\mathrm{K_c}} = 0.72\Delta/k_\mathrm{B}$.

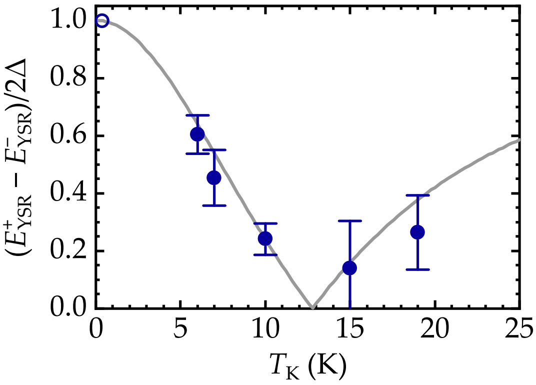

of the measured YSR peak intensities at the QPT, as long as there is no sign change of the spin-independent scattering potential V. The experimental findings however lack this feature. Instead, all low-energy spectra exhibit a higher intensity of the hole-like YSR peak, most prominently visible for atoms #2, #4 and #5. Recent experimental work on Fe-5,10,15,20-tetrapyridyl-porphyrin molecules on Pb(111) by L. Farinacci *et al.* indicates that in addition to Coulomb scattering also interfering tunneling paths through different molecular orbitals can lead to an asymmetry of both the YSR states as well as the Kondo resonance [235]. Similar results have been obtained theoretically for atomic orbitals [145]. The qualitative result of a more intense YSR peak at negative bias concomitant with a positive Fano line shape factor q presented in Ref. [235] is also found in the system presented here. Although there is no direct evidence for such interference for electrons tunneling into Fe/NbO$_x$, the observed two channel Kondo resonance indicates the participation of at least two orbitals in the tunneling process. Thus, the asymmetry of the YSR states might be be dominated by the interference of tunneling paths, which could explain the lacking asymmetry inversion of the YSR peak intensities at the QPT.

8.3 DISCUSSION

The results presented in this chapter provide a detailed picture of the impurity–substrate interaction of Fe atoms with the Nb(110) surface. Single Fe atoms on the clean surface only weakly interact with the itinerant quasiparticles in the system and hence exhibit YSR states close to the superconducting gap edge, originating from the d_{z^2} atomic orbital. Contrary, Fe atoms adsorbed onto NbO$_x$ phase II reveal much more pronounced in-gap YSR states, although DFT calculations showed that their magnetic moment is reduced by more than 1/2 in comparison to Fe/Nb(110). This apparent contradiction could be explained by the smaller adatom–surface distance of Fe/NbO$_x$, leading to an increased overlap of the atomic d_{z^2} orbitals with the substrate and hence larger scattering potential for Cooper pairs. It was found experimentally that Fe atoms occupy a variety of adsorption sites within the NbO$_x$ phase II reconstruction, leading to changes in the adatom–substrate interaction and the concomitant YSR states. Measurements in the superconducting and normal-metallic phase of Nb(110) atop the same Fe atoms revealed Fe atoms in two distinct phases of spin-screening on both sides of the QPT. Contrary to previous experiments, the QPT in the presented system is not evoked by altering the impurity–substrate distance [227–229, 361] or varying adsorption positions in a Moiré-like structure [202, 226, 234], but is based on the presence of adsorbates, here oxygen, on the surface that changes the interaction of impurity and surface. A similar effect was recently observed for Fe atoms in proximity of assemblies of interstitial Fe atoms on top of an oxygen-reconstructed Ta(110) surface [362].

As discussed in the introduction of this chapter, the substrate–adatom interaction is a key component when engineering magnetic adatom–superconductor hybrid systems aiming at the realization of MZMs in solid state systems. To enter the topologically non-trivial phase, the system needs to evolve YSR bands that cross E_F and open a topologically protected band gap (cf. section 5.4). Hence, Fe atoms on clean Nb(110) appear to be an unfavorable system, as the weak adatom –substrate interaction results in single-atom YSR states that are energetically located very close to the gap edge, i.e. far away from E_F. However, very recent combined experimental and theoretical work nevertheless suggests the appearance of delocalized MZMs along Fe chains on Nb(110) [363]. The strong influence of oxygen on the YSR states described in this chapter would allow to individually tune the YSR energies of single Fe atoms, potentially permitting to further examine the phase space of Fe chains on Nb(110). Yet, controlling the exact adsorption position of each atom on the NbO$_x$ phase II reconstruction in an engineered adatom assembly would be extremely challenging.

On the other hand, the single pair of YSR peaks that appears in STS experiments on Fe/Nb(110) is expected to be easily traceable in systems with an increasing number of adatoms, such that Fe/Nb(110) represents a interesting system to further study the coupling of YSR states of individual magnetic impurities beyond previous experimental work on different adatom dimers [248–251]. This will be the topic of the next chapter.

Chapter 9

9 COUPLED YU-SHIBA-RUSINOV STATES IN SHORT CHAINS OF FE ATOMS

Following the work on single Fe atoms from the previous chapter investigating the adatom–substrate interaction and demonstrating the reflectance of this interaction in both the atoms' superconducting and normal state LDOS, this chapter addresses the adatom–adatom coupling and the concomitant hybridization of YSR states. Generally, the capability of STM to individually position atoms or molecules by manipulation with the STM tip allows to create almost arbitrary 2D structures [43] and, most important for tuning the adatom–adatom coupling, to place atoms at desired interatomic distances and along different crystallographic directions. For the investigation of topological superconductivity in artificial systems, atom manipulation has successfully been employed to build chains from single atoms of magnetic elements such as Fe [68, 364], Mn [63, 276] or Cr [69] on various superconducting surfaces.

Although atom manipulation of Fe atoms on Nb(110) is possible [340, 363], it proofed to require extremely low tunneling resistances in the range of few kΩ, occasionally causing disruptive changes of the tip that often prevent the continuation of the experiment. To study the coupling of YSR states in assemblies of a few atoms it is also possible to instead rely on randomly formed adatom structures that assemble during the atom deposition process. However, in this case it is necessary to resolve and identify the occurring adatom configurations prior to the investigation of their electronic properties, which can become challenging at small interatomic distances, as the individual adatoms merge into a single protrusion in the topography measured with a standard metallic tip. In the presented work, this issue was resolved by functionalizing STM tips with single CO molecules, which significantly increases the topographic resolution of the experiments, as will be introduced in section 9.1. The coupling of YSR states will first be investigated in dimers with different interatomic distances in section 9.2. Afterwards, the formation of extended states in short 1D Fe chains will be assessed in section 9.3.

Finally, in section 9.4, the experimental results will be rationalized by model calculations.

Most results presented in this chapter were published in Ref. [341].

9.1 INCREASING SPATIAL RESOLUTION WITH CO-FUNCTIONALIZED METAL TIPS

The capabilities of CO-functionalized STM and also AFM (atomic force microscopy) tips to drastically enhance the spatial resolution of an experiment have been demonstrated in a variety of systems and developed a special significance for structural studies of molecules on surfaces [109, 365]. This increase in the spatial resolution is caused by the forces acting on the CO molecule when it is brought close to a surface. As a result, the CO is pulled toward or pushed away from the highest points in the topography, artificially enhancing the corrugation in the STM topography [366–368]. Most experiments with such tips are executed on noble metal surfaces and tip functionalization with CO molecules on these surfaces has become a standard procedure [369, 370]. CO molecules adsorbed on e.g. Cu(001) and (111) have further been shown to exhibit strong signatures of inelastic vibrational excitations when probed by IETS, resulting in electron–hole symmetric steps at about ± 35 meV in the $\mathrm{d}I/\mathrm{d}U$ signal for the most dominant mode, which is the hindered rotation of the molecule [117]. This allows to unambiguously identify and distinguish CO molecules from other adsorbates.

For the purpose of the presented work, the initial attempts aimed at dosing CO molecules and functionalizing the STM tip on the clean Nb(110) surface. CO molecules (*Messer Industriegase GmbH*, 99.997 %) were dosed onto the surface through the opened radiation shields of the cryostat via a leak valve connected to a narrow tube pointing toward the sample in the STM. During the 5 min deposition process, the pressure in the STM chamber was kept at 1×10^{-8} mbar and the sample temperature did not surpass 15 K. Afterwards, adsorbates appearing as depressions with a diameter of 0.5 nm and a depth of about 20 pm were observed on the surface and could clearly be distinguished from atomic oxygen impurities by scanning with a bias voltage of +2 V, where oxygen appears as a protrusion, while the small adsorbates remained depressions on the surface (see also appendix C). However, IETS failed to show the characteristic vibrational excitations and attempts to pick up these adsorbates with the standard procedures described in literature failed. It is unclear, whether the CO molecules stay intact upon adsorption on the Nb(110) surface and just behave differently than on noble metal surfaces, or whether they potentially dissociate, given the high reactivity of the surface [313, 371, 372].

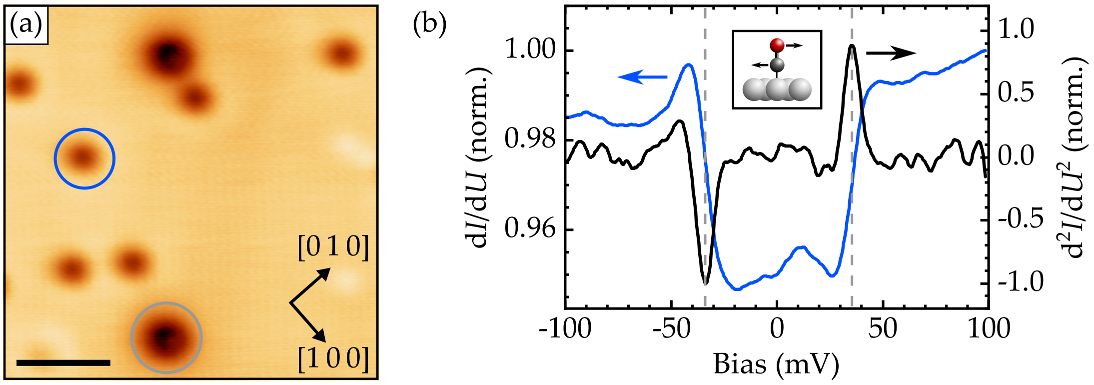

Figure 9.1: (a) Topographic scan of the Cu(001) surface with adsorbed CO molecules (blue circle) and remaining impurities, presumably nitrogen (gray circle). Scale bar is 2 nm. (b) Differential conductance (blue curve) and simultaneously measured second derivative of the tunneling current (black curve) atop a CO molecule after subtraction of the signal measured on the bare Cu surface. The excitation by inelastic tunneling of the hindered rotation mode of the CO molecule sketched in the inset leads to steps (peaks/dips) at $\pm(34 \pm 1)$ mV in the $\mathrm{d}I/\mathrm{d}U$ ($\mathrm{d}^2I/\mathrm{d}U^2$) signal, marked by dashed lines. Stabilization parameters: (a),(b) $U = 100$ mV, $I = 1$ nA; (b) $U_{\mathrm{mod}} = 5$ mV. $T = 4.2$ K.

9.1.1 Tip functionalization on Cu(001)

Following the unsuccessful attempts on Nb(110), tip functionalization was conducted on a Cu(001) surface with the plan to exchange samples from Cu(001) to Nb(110) after the functionalization. The Cu(001) surface was cleaned by sputtering the sample with Ar^+ ions at an acceleration voltage of 1 kV for 1 h, while keeping the sample at 500 °C.[1] Afterwards, the sample was annealed at the same temperature for another 30 min, resulting in a clean Cu(001) surface. A topographic scan of the surface after CO deposition as described above is shown in Figure 9.1(a), with CO molecules appearing as round depressions with a diameter of 0.5 nm and a depth of 20 pm. Additionally, larger impurities, probably single nitrogen atoms originating from a small leak in the Ar line, are found on the same surface. As described above, the hindered rotation mode of the CO molecules opens an inelastic tunneling channel at the energy of the vibrational mode, as could be verified in spectroscopy measurements atop single CO molecules. An example for such a measurement is shown in Figure 9.1(b), exhibiting a step-like increase in the $\mathrm{d}I/\mathrm{d}U$ signal symmetric around zero bias. To extract the precise excitation energy, the simultaneously recorded $\mathrm{d}^2I/\mathrm{d}U^2$ signal was fitted according to Equa-

---

[1] The reason to heat the sample during sputtering was the slow response of the radiative heater in the system. This way, the annealing time after sputtering and segregation of new defects toward the surface could be minimized.

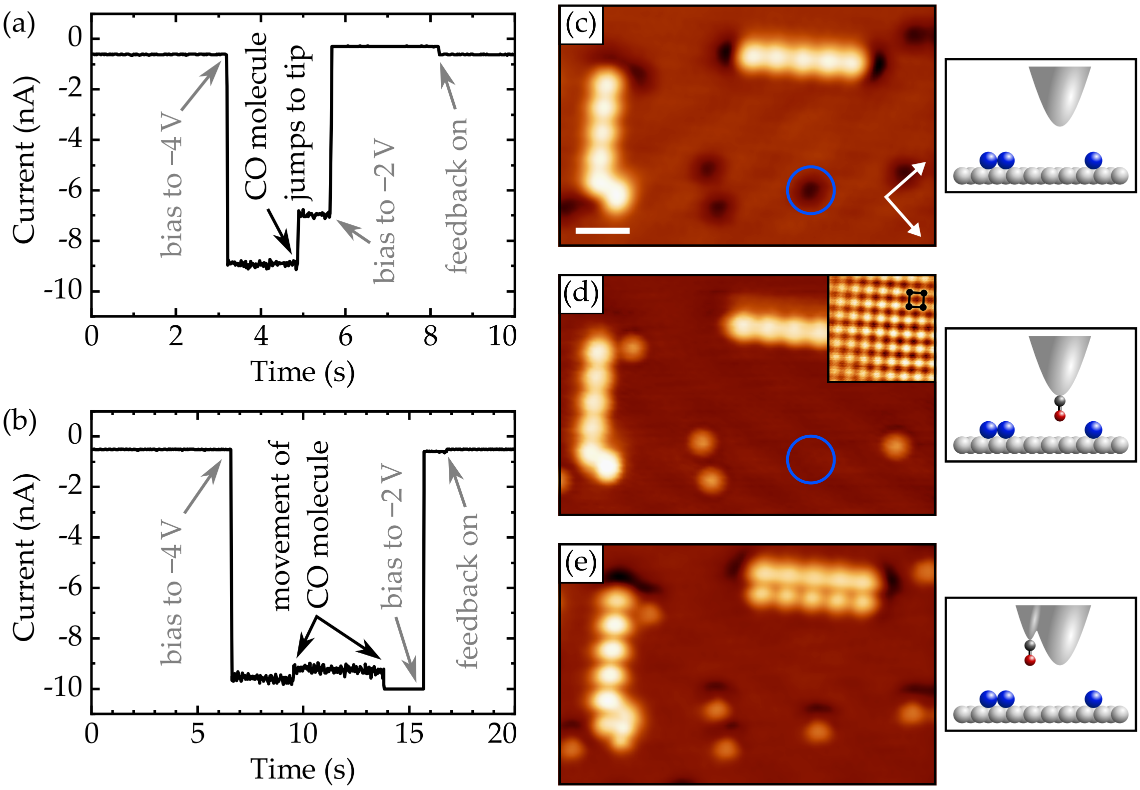

Figure 9.2: (a) Procedure and current traces of a successful transfer of a CO molecule to the tip. (b) Same as (a), but instead of picking up the CO molecule, it was only moved on the surface. (c)-(e) Topographic scans of the Cu(001) surface with adsorbed CO molecules and self-assembled Cu chains recorded before and after the functionalization with a CO molecule. Scale bar is 1 nm. Sketches on the right illustrate the different tip configurations. After picking up the CO molecule marked with a blue circle in (c) onto a metallic tip, the remaining CO molecules appear as bright protrusions in (d). The inset shows a scan with atomic resolution recorded with the CO-functionalized tip; the Cu(001) unit cell is indicated. If the CO molecule is not picked up onto the tip apex but forms a CO/metal double tip as presented in (e), the resulting scan is a superposition of the scans in (c) and (d). Stabilization parameters: (a) $U = -2$ V, $I = 0.6$ nA; (b) -2 V, 0.5 nA; (c),(e) 0.1 V, 1 nA; (d) -2 V, 1.5 nA, inset: -0.01 V, 3 nA.

tion (3.13), yielding an excitation threshold of (34 ± 1) mV. This value closely matches earlier results obtained by infrared absorption spectroscopy [373], He atom scattering [374] and other IETS measurements [117].

To pick up CO molecules from the Cu(001) surface onto the tip, the following procedure, similarly introduced by L. Bartels *et al.* in Ref. [370], was developed: First, the tip was stabilized atop a CO molecule at a bias voltage of $U = -2$ V and a tunneling current of $I = 0.5 - 1.5$ nA, varying for (microscopically) different tips. In the next step, the feedback loop of the STM electronics was opened and the bias voltage was changed to -4 V, above the activation barrier of the CO molecule on the surface [370]. This step also determined the initial current setpoint, as it was chosen to be as high as possible, but still low enough such that the tunneling current would not surpass 10 nA, the limit of the current amplifier, when changing the bias voltage to -4 V. This allowed to obtain the maximum activity of the CO molecule, as the likeliness of the CO being activated is proportional to the number of electrons tunneling into the molecule [370], while still being able to observe changes of the tunneling current. In Figure 9.2(a) and (b), traces of the tunneling current over time following this procedure are displayed. Jumps of the CO molecule onto the tip apex were detected as a sudden decrease of the absolute tunneling current (cf. panel (a)), while movements of the CO on the surface are indicated by only small alterations of the current (cf. panel (b)). Once such a change was detected, the bias voltage was changed back to -2 V and the feedback loop was closed again. The success rate of this procedure strongly depends on the microscopic tip shape,[2] where with a suitable tip, multiple subsequent successful transfers of a CO molecule were be achieved, while it could be close to impossible to succeed with a less suitable tip. Therefore, after few unsuccessful attempts, the tip was reshaped on the Cu(001) surface prior to new attempts of functionalizing the tip with a CO molecule. The results of a successful tip functionalization are nicely demonstrated by the scans presented in Figure 9.2(c)-(e), where an accidentally imperfect preparation of the Cu(001) crystal led to self-assembled atomic Cu chains along the $\langle 1\,1\,0 \rangle$ direction of the surface with an interatomic spacing of $\sqrt{2}a_{\mathrm{Cu}}$. Before the tip functionalization, CO molecules appear as depressions on the Cu surface (cf. Figure 9.2(c)). After transferring a CO molecule to the tip, the CO molecules on the surface appear as protrusions with a height of about 50 pm (cf. Figure 9.2(d)) [369]. This contrast reversal is caused by constructively interfering tunneling channels directly from the metallic tip and through the tip molecule into the molecule on the surface, which leads to an increased tunneling current above the CO molecule [375]. The functionalized tip now allows to resolve the atomic lattice of the Cu(001) surface presented in the inset of panel (d), demonstrating the strongly increased spatial resolution of such tips.

The scan in Figure 9.2(e) provides a direct comparison of both tips: Coincidentally, the transferred molecule and a Cu atom at the tip apex form a double tip of almost equal height as illustrated in the sketch in panel (e). As a result, both the Cu chains and remaining CO molecules on the surface appear doubled along the vertical

---

[2] Also the tip material might play a decisive role, as I never succeeded to pick up a CO molecule if the tip was beforehand prepared on a Nb crystal. In this case it was always necessary to pick up a Cu cluster before tip functionalization.

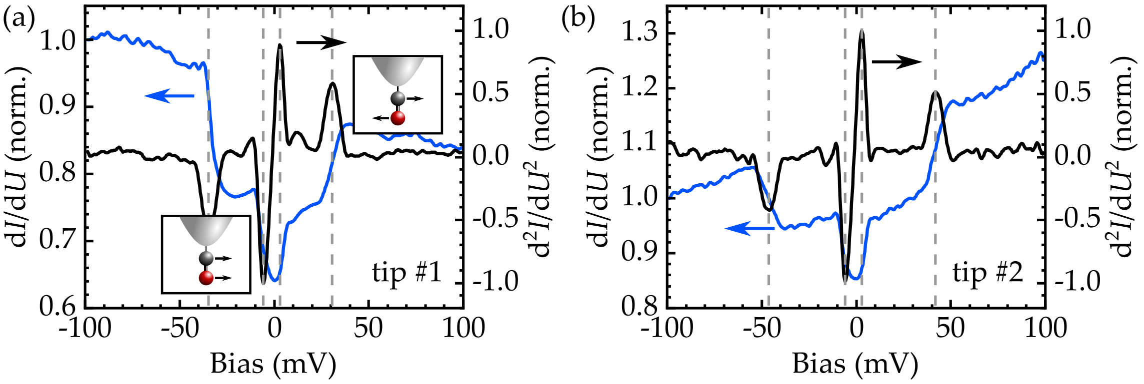

Figure 9.3: First and second derivative of the tunneling current recorded with two different CO-functionalized STM tips above the clean Nb(110) surface. Insets in (a) depict vibrational modes of the low-energy hindered translation (left) and high-energy hindered rotation mode (right). The tip-/adsorption position-dependent excitation energies amount to (a) (4 ± 1) meV and (33 ± 2) meV and (b) (4 ± 1) meV and (44 ± 2) meV for the two modes, respectively. Stabilization parameters: $U = -100$ mV, $I = 1$ nA, $U_{\mathrm{mod}} = 5$ mV. $T = 1.4$ K. *Adapted from Ref. [341]. Copyright ©2021 by the American Physical Society.*

direction of the scan. Based on the different appearance of CO molecules imaged with metallic and CO-functionalized tips, one finds that the upper reproduction of the chains and molecules stems from the metallic part of the tip, while the lower one is produced by the CO-functionalized part. Clearly, the latter produces a much better resolved image of the Cu chains with a distinctly higher contrast between the Cu atoms, directly visualizing the increased spatial resolution provided by CO-functionalized tips.

After careful tip functionalization and characterization on Cu(001), the sample in the STM had to be exchanged for the Nb(110) crystal as discussed earlier. During the exchange procedure the STM temperature did not exceed 15 K. A successful sample exchange and tip approach to the Nb(110) surface without losing the CO molecule was determined by measuring the $\mathrm{d}I/\mathrm{d}U$ and $\mathrm{d}^2I/\mathrm{d}U^2$ signal above the clean Nb(110) surface. In about four out of five attempts, the CO molecule stayed on the tip, resulting in the characteristic excitation spectra shown in Figure 9.3. Similar to the spectrum recorded atop a CO molecule on the Cu(001) surface presented in Figure 9.1(b), the hindered rotation mode is visible, with the corresponding excitation energy varying for different tips. This observation is presumably due to different adsorption sites on the corrugated tip surface, as CO molecules atop or next to a single metallic adatom on a flat surface have been shown to exhibit significantly different vibrational energies in comparison to free-standing atoms atop the same surface [376]. Additionally, the lower-energy

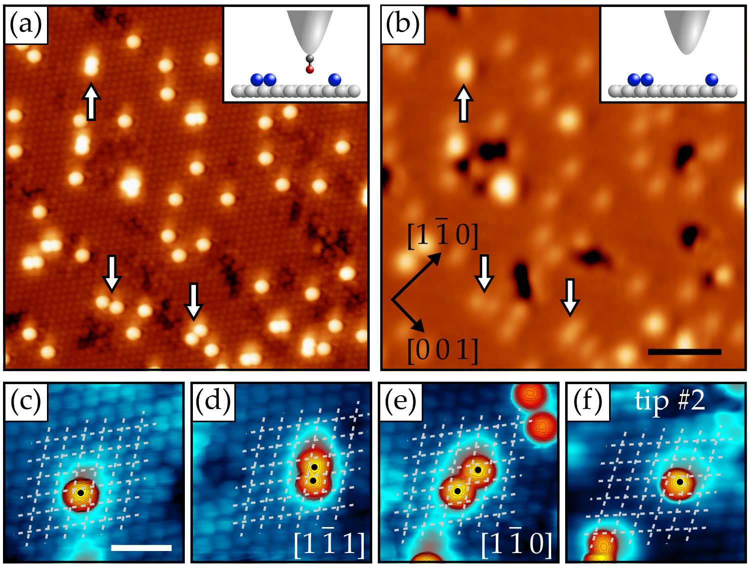

Figure 9.4: Topographic scans of the same Nb(110) surface area recorded with (a) a CO-functionalized and (b) a metal tip. With the CO-functionalized tip, the Nb lattice as well as individual Fe atoms and clusters are clearly resolved. Scale bar is 3 nm. (c)-(f) Close-ups of single atoms and two different dimers. The dashed lines highlight the Nb(110) lattice, black dots the point of maximum height of the atoms. Scale bar is 1 nm. Scan parameters: (a),(c)-(f) $U = -10\,\text{mV}$, $I = 5\,\text{nA}$; (b) $-1\,\text{V}$, $0.4\,\text{nA}$. *Adapted from Ref. [341]. Copyright ©2021 by the American Physical Society.*

hindered translation mode, which can also be observed for CO/Cu(111) [377], is detected for CO molecules attached to the STM tip at $\pm(4 \pm 1)$ mV.

9.1.2 *Topographic resolution of Fe clusters on the Nb(110) surface*

Figure 9.4 displays topographic measurements of the Fe decorated Nb(110) surface. Fe atoms with a relatively high coverage of 0.3 atoms/nm^2 to increase the chance of the formation of small clusters and chains were already deposited prior to the tip fictionalization and sample exchange to prevent any unnecessary disturbances that might cause the CO molecule to detach from the tip. The experimental data presented in Figure 9.4(a) recorded with a CO-functionalized tip reveals the Nb(110) lattice as well as a variety of different Fe clusters with atomic resolution. Similar to the measurements with metallic tips presented in chapter 6, oxygen and hydrogen impurities appear as depressions on the otherwise clean surface. Arrows mark the three Fe dimers with the shortest interatomic distance found on the Nb(110) surface, oriented along the $\langle 1\bar{1}1\rangle$, $\langle 1\bar{1}0\rangle$ and $\langle 1\bar{1}3\rangle$ directions. Surprisingly, during the whole study no dimers along the $\langle 001\rangle$ direction were observed, which might hint at short-ranged attractive interactions between two Fe atoms that force them into the $\langle 1\bar{1}1\rangle$ configuration if their initial interatomic distance upon deposition is too short [378]. This is confirmed by a closer study of the Fe atoms' adsorption positions presented below. However, more recent data published in Ref. [363] indicates that it is possible to create $\langle 0\,0\,1 \rangle$ dimers by atomic manipulation.

Contrary to the scan recorded with the CO-functionalized tip, a scan of the same area after removing the molecule from the tip displayed in Figure 9.4(b) emphasizes the importance of the tip functionalization for the identification of the different clusters, which are heavily blurred by the comparably blunt metal tip apex. This scan recorded at a bias voltage of -1 V also allows to allocate oxygen patches on the surface and differentiate them from hydrogen. Since the presence of oxygen strongly influences the YSR states of the Fe atoms as discussed in the previous chapter, all further measurements presented in this chapter were conducted on Fe atoms and clusters on clean Nb(110).

Finally, the capability of the CO-functionalized tips to individually resolve the adsorption position of single Fe atoms and atoms within clusters is assessed in Figure 9.4(c)-(f). From a comparison of panels (c) and (f) showing scans of single Fe atoms with two different CO tips it is evident that dependent on the tip, the atoms appear to be shifted within the primitive unit cell of the Nb(110) lattice indicated by dashed lines. While the same tip always shows the same shift for different atoms, different tips showed no preferred shifting direction, suggesting that the observed shift is an artifact of a non-ideal, asymmetric tip and confirming the fourfold hollow site as the actual adsorption position as calculated by DFT [340]. Interestingly, the LDOS maxima of the individual atoms in the $\langle 1\,\bar{1}\,1 \rangle$ dimer seem not to correspond to those of single atoms (cf. panel (d)). Instead, both atoms exhibit an inwards displacement of the maximum LDOS toward the center of the dimer, corroborating the suggestion of interatomic forces mentioned above. This behavior was only found for closest-packed dimers (and other clusters with the same interatomic spacing), but is absent for larger dimers (cf. panel (e)).

Conclusively, the CO-functionalized tips lead to a significant increase in topographic resolution of the STM experiments, allowing to unambiguously identify even close-packed Fe structures on the Nb surface. The presented topography measurements serve as the basis for the following experiments, that investigate the electronic properties of the examined structures.

9.2 Distance-dependent coupling in Fe dimers

In order to study the basic coupling strength between YSR states of single Fe atoms, single spectra atop various dimers were measured. To increase the spectroscopic resolution of the experiments and to exclude potential artifacts stemming from the CO molecule, the molecule was removed from the tip after recording the topographic information and identifying the different dimers on the surface, before dipping the tip into the Nb surface to render it superconducting, as already described in chapter 8. Representative spectra of different dimers are displayed in Figure 9.5(a) together with both a spectrum of a single Fe atom (blue curve) and a spectrum taken on the bare surface (gray dashed curves) for comparison. Panels (b)-(e) exhibit scans and a ball model representation of the corresponding adatom assemblies. As discussed in the previous chapter, single Fe atoms on clean Nb(110) only weakly interact with the substrate, resulting in YSR states close to the gap edge with $E_{\mathrm{YSR}} \approx \Delta_{\mathrm{Nb}}$. Coupling of two atoms in the close-packed configuration along the $\langle 1\,\bar{1}\,1 \rangle$ direction dramatically changes the picture. The purple spectrum in Figure 9.5(a) exhibits two pairs of YSR states well within the superconducting gap, with the more intense peaks at $\pm(2.3 \pm 0.1)$ mV in the convoluted tip and sample LDOS. The weaker pair appears at a bias voltage close to Δ_{t}/e, i.e. close to the Fermi level in the sample LDOS. This doubling of the number of YSR states in an impurity dimer is in accordance with the introduction of coupled YSR states in section 5.3, where the hybridization of the two single-atom YSR states was shown to lead to their splitting into states with even and odd symmetry. As will be demonstrated by further measurements presented in section 9.3, this symmetry difference of the two YSR states is also found for the Fe dimer. However, it is experimentally difficult to fully exclude an additional coupling of the single atoms' d orbitals, that further influences the occurring YSR states. Contrary to Ref. [254], where for small interatomic distances a change in the spin excitation signal attributed to the same orbital that leads to the observed YSR states was detected and directly demonstrated the orbital coupling, single Fe atoms on clean Nb(110) do not exhibit such features (cf. chapter 8). Hence, a coupling of the d_{z^2} orbitals cannot be excluded. However, as will be shown in section 9.4, the observed YSR states in the Fe dimers and longer chains can be well described without introducing this additional coupling. Therefore, the detected change of the YSR states is in the following considered to originate at least primarily from the coupling of of the single-atom YSR wave functions.

For the $\langle 1\,\bar{1}\,0 \rangle$-oriented dimer with an interatomic distance of $\sqrt{2}a$, no clear in-gap states were observed. Yet, the STS data still significantly differs from that of a single Fe atom with an increased intensity at the coherence peaks in comparison to both the single atom and the bare surface, suggesting a small, but still finite coupling between the YSR states. Contrary, spectroscopic data atop the $\langle 1\,\bar{1}\,3 \rangle$-oriented dimer or dimers with an even larger interatomic distance closely resembles that measured on a single atom, setting the minimum distance over which no coupling between the Fe atoms occurs to $\sqrt{11}a/2 = 0.55$ nm.

Before further examining the hybridized YSR states and their wave functions, I will briefly discuss the reason for the relatively short coupling distance of Fe/Nb(110). The first factor is the weak interaction of the single-atom spins with the itinerant

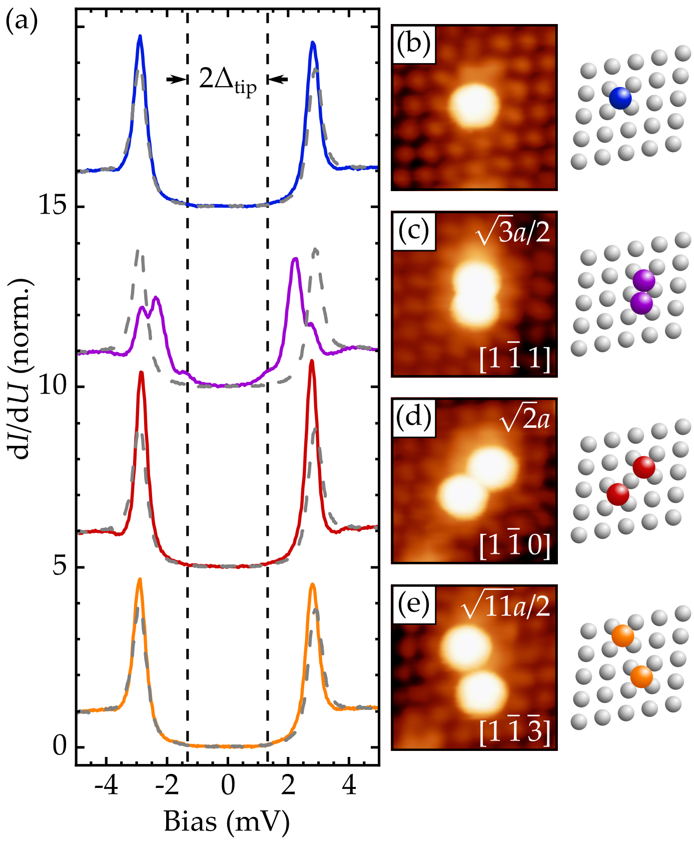

Figure 9.5: (a) Differential conductance data recorded on a single Fe atom and three different dimers. Spectra recorded on the clean Nb surface (gray, dashed lines) are presented for reference. Spectra are vertically offset for clarity. $\Delta_t = 1.31$ meV. (b)-(e), left panel: Scans of the respective atom assemblies recorded with a CO-functionalized tip (scan range: $2 \times 2\,\mathrm{nm}^2$). The interatomic distance and orientation are indicated for each dimer. Right panel: Ball model representation. Stabilization parameters: (a) $U = -7$ mV, $I = 0.4$ nA, $U_{\mathrm{mod}} = 0.1$ mV; (b)-(e) -10 mV, 5 nA. $T = 1.4$ K. *Reprinted from Ref. [341]. Copyright ©2021 by the American Physical Society.*

quasiparticles in the substrate, which mediate the coupling between the Fe atoms. Contrary to Fe atoms, Cr atoms, which have YSR states very close to E_F reflecting a strong adatom–substrate interaction, were shown to couple over much larger distances of several nanometers [254]. The second factor influencing the coupling distance is the spatial decay of the YSR wave functions, which is proportional to $1/k_F r$ (cf. section 5.3). Due to the multitude of bands crossing the Fermi level in the Nb(110) surface Brillouin zone, it is unclear to which of these bands the Fe atoms couple most dominantly, preventing a straightforward determination of k_F. However, mapping out the LDOS of the single-atom YSR state reveals a strong localization of the state to the Fe atom, suggesting a decay length < 0.5 nm.

9.3 COUPLING IN 1D CHAINS

To further evaluate the hybridization of YSR states in impurity dimers and track the YSR state coupling toward the formation of bands, the experiments were expanded to short chains along the $\langle 1\,\bar{1}\,1 \rangle$ direction, where the strongest coupling was observed in the Fe dimers. By preparing the samples as described in the previous section, chains of up to four atoms self-assembled on the Nb(110) surface with any nearby atoms having a distance larger than the minimal coupling distance

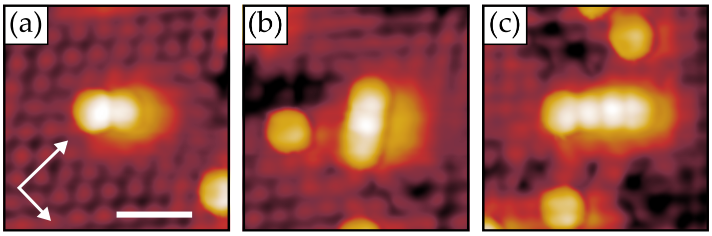

Figure 9.6: Topographic scans of an Fe (a) dimer, (b) trimer and (c) tetramer along the $\langle 1\bar{1}1\rangle$ direction recorded with a CO-functionalized tip. Scale bar is 1 nm. Scan parameters: $U = -10\,\mathrm{mV}$, $I = 3\,\mathrm{nA}$. *Adapted from Ref. [341]. Copyright ©2021 by the American Physical Society.*

of 0.55 nm to the chains. Scans of each a dimer, trimer and tetramer are displayed in Figure 9.6. In this set of measurements, a slight CO/metal double tip produced a shadow on the right side of every chain. However, as the tip was reconditioned to render it superconducting before the STS measurements, this double tip feature did not affect the results presented in the following.

In order to assess the hybridized YSR wave functions, full grid spectroscopy was performed on all chains in a range of $3 \times 3\,\mathrm{nm}^2$ with a spectrum taken every 0.05 nm. The results for all chains are presented in Figure 9.7. As already shown in the previous section, $\langle 1\bar{1}1\rangle$ dimers exhibit two pairs of YSR states with higher intensity of the electron-like states (cf. Figure 9.7(a)). Maps of the LDOS of both states extracted from the full grid measurements at a bias voltage of $U = (\Delta_\mathrm{t} + E_\mathrm{YSR})/e$ and displayed in Figure 9.7(c) and (d) reveal the YSR wave functions. The low-energy state wave function exhibits an odd symmetry, characterized by the vanishing intensity at the dimer center, while the even-symmetry wave function of the high-energy state has an intensity maximum at the dimer's center. A line grid extracted from the same measurement displayed in Figure 9.7(b) confirms this observation. To emphasize especially the low-intensity odd state, the line grid shows the numerically calculated second derivative of the conductance signal. Peaks in the $\mathrm{d}I/\mathrm{d}U$ signal hence appear as dark areas in the color-coded $\mathrm{d}^3I/\mathrm{d}U^3$ line grid. Clearly, the low-energy state is more prominent at the ends of the dimer, while the high-energy state dominates at the dimer center.

Spectra taken on the $[1\bar{1}\bar{1}]$ trimer (panel (e)) similarly reveal two clear YSR in-gap states at ±1.75 mV and ±2.30 mV. Again, wave functions of both even and odd symmetry are found in both the line grid and the differential conductance maps at the bias voltages corresponding to the YSR energies (panels (f)-(h)). For the trimer however, the low-energy state's wave function has an even symmetry, while the high-energy state's wave function is odd, exactly opposite to the picture observed for the dimer.

For the tetramer, the situation becomes more complicated. The spectrum at the chain center displayed in Figure 9.7(i) exhibits a broadened asymmetric peak that

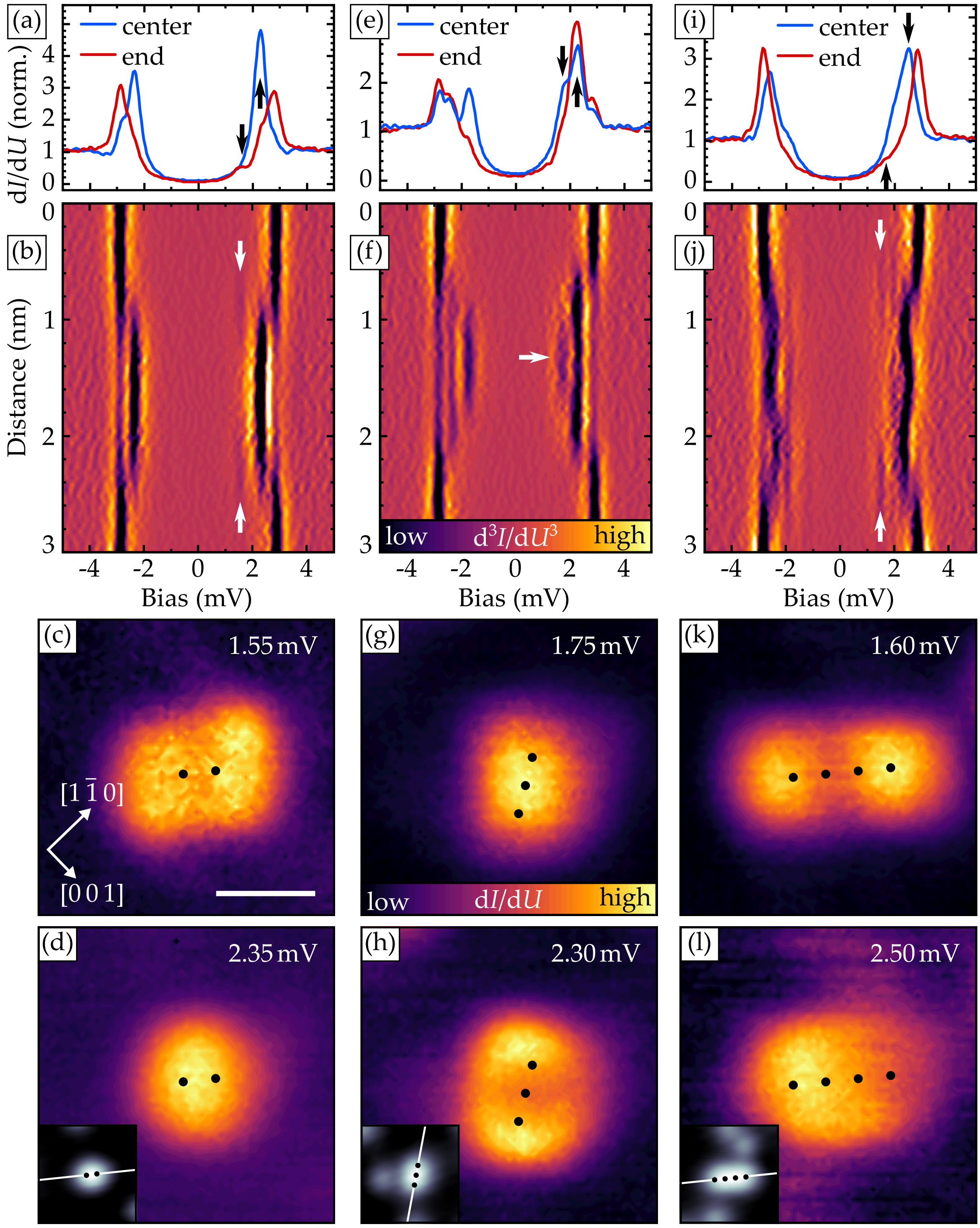

Figure 9.7: (a) Point spectra taken at the center and end of the $[1\,\bar{1}\,1]$ dimer displayed in Figure 9.6(a). (b) Calculated second derivative of the $\mathrm{d}I/\mathrm{d}U$ signal along the dimer axis indicated by the line in the inset of panel (d), white arrows highlight low-intensity YSR states. (c),(d) Maps of the differential conductance at the bias voltages indicated by black arrows in (a) and noted in the panels. Black dots mark the Fe atoms' centers. Scale bar is 1 nm. The inset shows the simultaneously recorded topography. (e)-(h), (i)-(l): Same as (a)-(d), but for a trimer and tetramer, respectively. Stabilization parameters: $U = -7$ mV, $I = 1$ nA, $U_{\mathrm{mod}} = 0.1$ mV. $T = 1.4$ K.

is slightly shifted from the coherence peak position of the bare surface. At the chain end, an additional low-intensity state appears at about ±1.6 mV. The spatial resolution in the line grid presented in panel (j) generates a clearer picture: The lowest-energy state is most pronounced at the chain ends as further confirmed by the conductance map in Figure 9.7(k). At higher energies, the broad peak found in the single-point spectrum is in the line grid shown to vary in energy in a wave-like pattern along the chain. This observation suggests the presence of at least two individual YSR states that cannot be resolved in the experiment. Adopting this description, the wave-like structure in the line grid can be separated into a state with even symmetry at high energies, also visible in the conductance map in panel (l), and a lower-energy state with an odd symmetry as indicated by the intensity minimum at the chain center visible in the line grid (see also appendix D, where $\mathrm{d}I/\mathrm{d}U$ maps of all YSR states at positive and negative bias voltage are displayed).
Reviewing the results obtained on the $\langle 1\bar{1}1\rangle$ Fe chains on Nb(110) presented above, one finds that the symmetries of both the energetically lowest and highest YSR states' wave functions alternate between odd and even whenever the chain length is increased by one atom. This finding will be rationalized in the following.

9.4 DISCUSSION

The experimental results discussed in the previous two sections revealed a significant coupling of the Fe atoms' YSR states only for close-packed structures on the Nb(110) lattice and uncovered an oscillatory behavior of the YSR states' spatial symmetries for short chains as a function of length. The aim of this section is to reproduce these findings in a simple tight-binding model, that allows to rationalize the experimental findings and provides insight into the basic characteristics of YSR state coupling. Ultimately, more rigorous calculations are presented to legitimate the simple model, but also to exhibit its limits.
The model employed to describe the coupling in Fe chains was introduced by D. K. Morr and J. Yoon in Ref. [247] and can be obtained by simplification of the extended model that will be shown in the second part of this section (see also appendix E). The advantage of the simplified version is that it only contains the single-atom YSR energy E_0 and the $n-1$ hopping constants k_i describing the coupling between atoms at sites $(j, j+i)$ in an n-atomic chain. The short coupling distance < 0.55 nm of the YSR states of Fe atoms on Nb(110) prevents the coupling of next-nearest neighbor atoms even in the close-packed chains, which have a distance of $2 \cdot \sqrt{3}\mathrm{a}/2$ nm $= 0.57$ nm. This reduces the model to only two parameters, E_0 and k_1. The resulting YSR energies as a function of both E_0 and k_1 are displayed in Figure 9.8(a)-(c).[3]

---

[3] Details of the calculations can be found in appendix E.

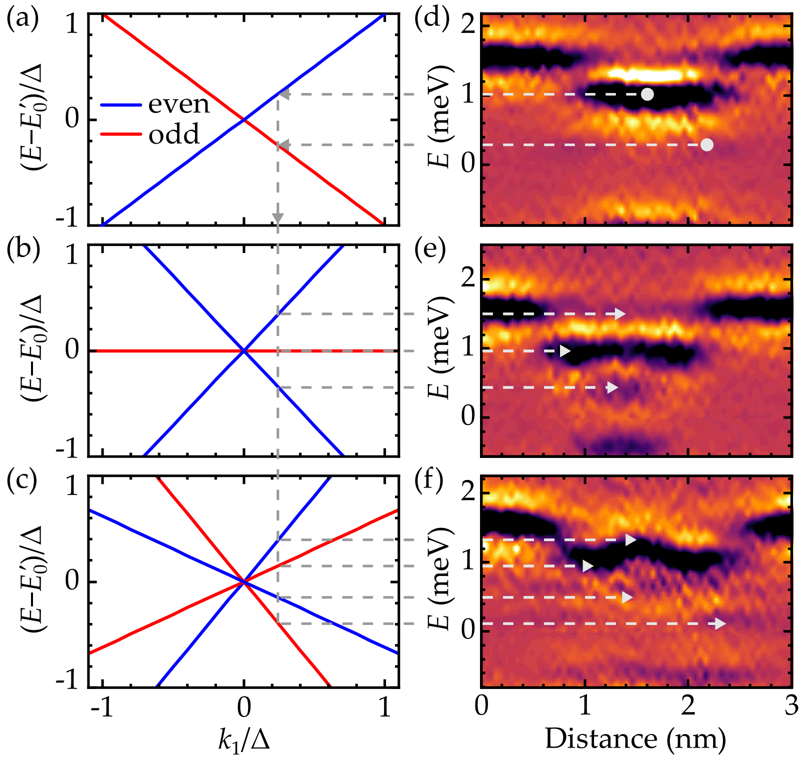

Figure 9.8: (a)-(c) Energy splitting of coupled YSR states depending on the nearest-neighbor hopping term k_1 as obtained from the simplified tight-binding model for a dimer, trimer, and tetramer, respectively. Blue (red) lines represent an even (odd) symmetry of the corresponding wave function. (d)-(f) Energies and spatial distribution of the YSR states in the $\langle 1\bar{1}1\rangle$ chains obtained by subtracting Δ_t from the data in Figure 9.7(b),(f),(j). The data is shifted to match "0" in the calculations, all y-axes extend over $2\Delta_{\mathrm{Nb}}$, ensuring an equal scaling of theory and experiment. *Reprinted from Ref. [341]. Copyright ©2021 by the American Physical Society.*

It is evident that the model does not directly map onto the experimental results, where the single-atom YSR energy of the Fe atom is approximately equal to the superconducting gap of Nb, while the observed in-gap states in the chains lie well inside the gap. The model in contrast predicts a symmetric splitting of the YSR energies around E_0 with a linear dependence on k_1, such that the center between the energetically lowest and highest YSR state remains at E_0. As will be shown below, a shift of the center energy as observed in the experiment is obtained from the full tight-binding model and can originate from Coulomb-like interactions or a finite overlap of the wave functions, which are both neglected in the simplified model. Further, a variation of the spin alignment within the chain can cause shifts in the center energy [246], and changes of the adatom–substrate interaction caused by e.g. the small change in adsorption position discussed in section 9.1.2 or an overlap of the atomic orbitals would alter the single-atom YSR energy within the chains. To acknowledge the experimentally observed variation of the center energy, the calculated data was shifted to the center energy E_0' extracted from the measurements for each chain. The result is displayed in Figure 9.8(d)-(f), where the d^3I/dU^3 line grids already presented in Figure 9.7 are aligned with the model calculations, shifted to $E_0' = 0.6$ meV for the dimer, $E_0' = 1.0$ meV for the trimer (Note that according to the model the center energy is equal to the YSR state with an odd wave function.) and $E_0' = 0.7$ meV for the tetramer.

To assess the validity of the model we first compare the theoretical and experimental results obtained for the Fe dimer: For positive k_1, the model predicts a higher energy for the even than for the odd states, as also found experimentally. Thus the dimer can serve as an input parameter to fix the hopping parameter in the model. From the relation $\left(E^{\text{even}} - E^{\text{odd}}\right) = 2k_1$, one extracts a hopping term of $k_1 \approx (0.40 \pm 0.04)$ meV $\approx (0.26 \pm 0.03)\Delta_{\text{Nb}}$, which can then be used to "predict" the experimental data of the trimer and tetramer as is graphically illustrated in Figure 9.8. For the trimer, the model predicts three YSR states. For the energetically lower two states, the extracted energies at $k_1 = 0.26\Delta_{\text{Nb}}$ as well as the states' symmetries very well match the experimental data, as indicated by the gray arrows in Figure 9.8. The third state is expected to coincide with the coherence peaks detected on the clean Nb surface, which prevents its unambiguous identification due to co-tunneling into the surface and the potential YSR state atop the Fe chain. For the tetramer, the model confirms the interpretation of the experimental results discussed in the previous section, suggesting that the wave-like structure observed around 1.2 meV consists of an even state at slightly higher and an odd state at lower energy, which is further confirmed by maps of the differential conductance at the corresponding bias voltage (cf. Figure 9.7(l) and appendix D). The low-energy odd state observed experimentally at ≈ 0.2 meV in the sample LDOS (cf. Figure 9.7(k)) is also confirmed by the calculations. Finally, the low-energy even state produced by the tight-binding model is not clearly resolved in the presented measurements, although a very weak signature of a potential peak can be identified in the d^3I/dU^3 line grid at ≈ 0.6 meV in Figure 9.8(f). Yet, the very intense odd state at higher energies dominates dI/dU maps taken at the corresponding bias voltage (cf. appendix D), preventing an assessment of the state's symmetry.

In conclusion, the simplified tight-binding model provides a satisfactory qualitative but also quantitative description of the experimentally investigated coupling of YSR states in short chains of Fe atoms. Especially the fact that knowledge about the coupling in an adatom dimer suffices to model the YSR states in longer chains demonstrates the potential of this simple model. Yet, it is instructive to compare the results of the simplified model to more extended calculations to understand the origin of the obtained results as well as their limitations.

To this end, the Hamiltonian describing a single magnetic impurity on a superconducting surface given by Equation (5.29) was extended to 1D chains.[4] As suggested

---

[4] See appendix E for details.

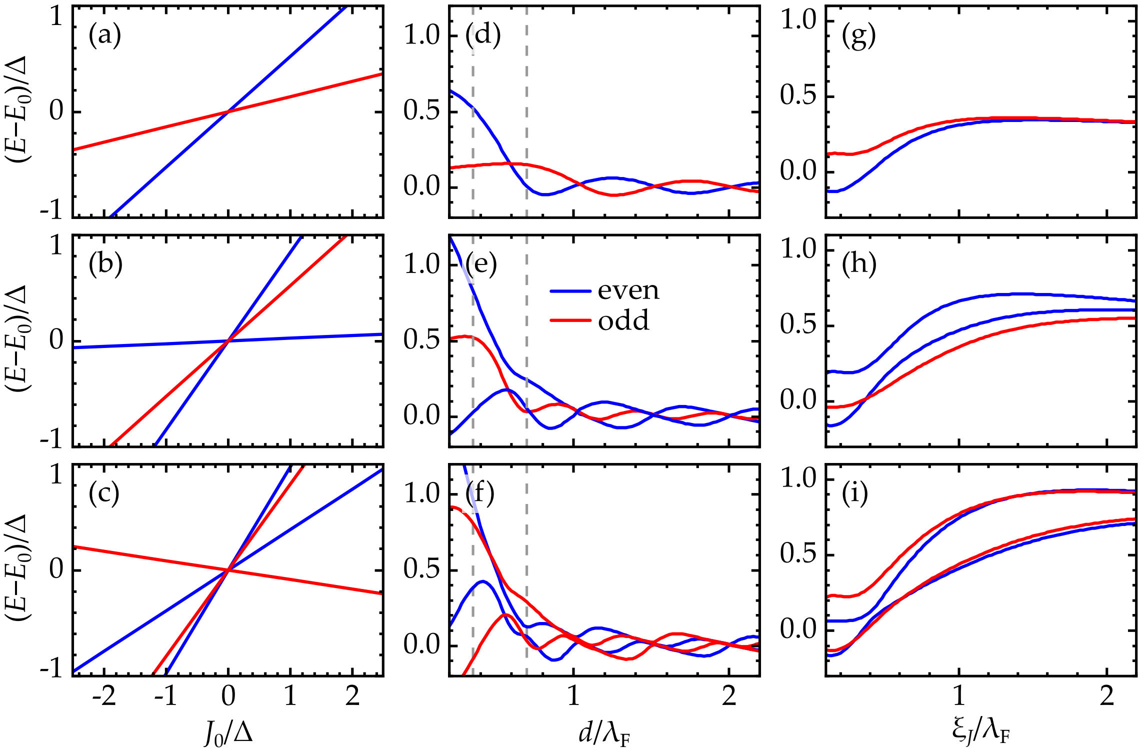

Figure 9.9: YSR energies in coupled 1D chains of two to four atoms (top to bottom) as obtained from the full model discussed in the text. Panels (a)-(c) show the dependence on the exchange potential strength, (d)-(f) on the interatomic distance and (g)-(i) on the decay length of the exchange potential. Input parameters are: (a)-(c) $\xi_J/\lambda_F = 0.4$, $d/\lambda_F = 0.35$; (d)-(f) $\xi_J/\lambda_F = 0.4$, $J_0/\Delta = 1$; (g)-(i) $d/\lambda_F = 0.7$, $J_0/\Delta = 1$. The dashed lines in (d)-(f) indicate the interatomic distances used in (a)-(c) and (g)-(i). *Reprinted from Ref. [341]. Copyright ©2021 by the American Physical Society.*

in Ref. [250], the exchange potential was described by $J(r) = J_0/\sqrt{\pi\xi_J}\exp\left(-r^2/\xi_J^2\right)$ and the normalized YSR wave function $\varphi(r) = \sqrt{2/\lambda_F}\,\mathrm{sinc}(2\pi r/\lambda_F)$ [51] was inserted into the obtained eigenvalue problem, where J_0 is the potential strength, ξ_J is the potential's decay length, λ_F is the Fermi wavelength and r points along the chain. In Figure 9.9, the derived eigenvalues of the system are displayed as a function of (a)-(c) J_0/Δ, (d)-(f) d/λ_F and (g)-(i) ξ_J/λ_F.

Similar to the simplified model, the YSR energies depend linearly on the strength of the exchange potential for all chains, yet, also the center energy shifts from E_0 with increasing potential strength. This general shift of the YSR energies is found to depend on all free parameters in the model, while it was fully absent in the simplified model and hence had to be manually compensated for to match experiments and calculations. Another significant difference between both models concerns the energetic distribution of the states with even and odd wave functions.

Although for the parameters chosen in panels (a)-(c), the symmetry oscillates as a function of energy, this is not a universal property of the full model, contrary to the simplified version. As can be seen e.g. for $d = 0.7\lambda_\mathrm{F}$ in panels (e) and (f) or $\xi_J = 2\lambda_\mathrm{F}$ in panels (h) and (i) the energetic order can be reversed or completely altered. The main reason for this effect is the variation of the phase difference between the YSR state wave functions, which is insignificant for very short interatomic distances, where both models yield the same results, but gains importance at distances comparable to λ_F.

The experimentally studied $\langle 1\,\bar{1}\,1\rangle$ chains are expected to fall into a limit where both models yield qualitatively similar results: In the nearest-neighbor adsorption position of the Fe atoms, d is expected to be much smaller than λ_F, where for an antiferromagnetic coupling between the impurity spin and the quasiparticles the energetically highest state always has an even symmetry due to the vanishing phase difference between the YSR states. Equally, the Fe chains are expected to lie within the limit of small ξ_J, where the energetic order of the YSR states is maintained, as the coupling was determined to be very short-ranged. Both observations justify a description of the studied Fe chains within the simplified model.

The results presented in this chapter provide direct access to the coupling of individual atomic YSR states. Based on the high-resolution topographic measurements with CO-functionalized tips and STS data of a variety of atomic dimers, a very short coupling distance of Fe atoms on Nb(110), originating from the strong localization of the YSR states, could be determined. Fe/Nb(110) thus constitutes a model tight-binding system, as could be shown by matching the experimental data of longer chains with simplified tight-binding calculations. Notably, the model only relies on information obtained from the measurements on Fe dimers and does not rely on the tuning of free parameters to reproduce the experimental results of larger systems.

Hence, Fe/Nb(110) nominally constitutes an excellent platform to engineer larger adatom systems whose electronic properties could be modeled rather easily to e.g. predict band crossings as were shown to occur in the electronically more complex system of Mn/Nb(110) [276]. Unfortunately, the rather difficult manipulation of Fe atoms on the Nb(110) surface and the short coupling distance that diminishes the potential to tune the interatomic coupling over a large range complicates the realization of more elaborate adatom assemblies. Yet, the presented work outlines the benefits of a profound understanding of the YSR state coupling in small adatom assemblies when looking for new adatom–surface combinations in which these advanced YSR systems could be realized. Theoretical suggestions already surpass the investigation of 1D chains [274, 379], that have been the main focus of experimental work in the past, and suggest a multitude of physical effects beyond MZMs that could be realized in engineered systems of magnetic adatoms on superconducting surfaces [380–383].

Chapter 10

10 SUMMARY AND OUTLOOK

The research presented in this thesis covered the interaction of magnetic adatoms with both metallic and superconducting surfaces and the effects resulting from this interaction, ranging from the Kondo effect in Part I to Yu-Shiba-Rusinov states in Part II.

In chapters 2 and 3 of this thesis, the physics relevant for Part I and the experimental details of the presented work were introduced.

The experiments on Co atoms on Cu(111) presented in chapter 4 reassessed the origin of the zero-bias anomaly previously observed in differential conductance measurements and revealed signatures deviating from the to date prevailing explanation within the framework of the Kondo effect. Recent theoretical work proposed spin excitations in combination with a new many-body state, the spinaron, rather than the Kondo effect as the physical origin of the zero-bias anomaly, and motivated the magnetic field-dependent and spin-polarized measurements presented in this thesis. In fields of up to 12 T, the zero-bias anomaly was shown to alter its line shape due to an asymmetric splitting of features observed in the d^2I/dU^2 signal. Comparison of this experimental finding with both a modeled Zeeman-split Kondo resonance and the proposed model of spin excitations and the spinaron failed to produce a satisfactory agreement between theory and experiment that would have allowed to discriminate between both explanations. Further experiments with spin-polarized STM tips revealed the spin character of the uncovered magnetic states or excitations in Co/Cu(111). Surprisingly, one of the features in the atoms' LDOS that was shown to shift to lower energies with increasing magnetic field strength was determined to have a minority spin character. Simultaneously, a second feature that was shown to shift to higher energies exhibited a majority spin character. While being in contradiction with standard theories of both the Kondo effect and trivial spin excitations, this shift to higher energies in combination with a majority spin character is reported for the spinaron. Nevertheless, the overall picture of the proposed model could not be matched to the experimental results presented in this thesis, as the minority spin state remained unexplained.

Hence, while further experimental and theoretical efforts are required to unveil the full physics behind this at first sight very simple system of a single Co atom on the Cu(111) surface, the performed experiments clearly reveal new intriguing physics incompatible with standard magnetic effects observed in spin systems coupled to metallic substrates.

The theoretical background of the physics discussed in Part II was presented in chapter 5, reviewing the formation of in-gap Caroli-de Gennes-Matricon states, YSR states and Majorana zero modes in superconducting systems. The platform for the experimental work, the Nb(110) surface, was introduced in chapter 6.
In chapter 7, the electronic properties of the Nb(110) surface were further studied by examining the vortex bound states on the type II superconductor. On the clean Nb(110) surface, vortices imaged at bias voltages inside the superconducting gap were shown to exhibit an anisotropic apparent shape, changing from coffee bean-like to elliptical at zero bias. In comparison, vortices on the oxygen-reconstructed surfaces were imaged as almost fully isotropic. Hence, the vortex shape could directly be linked to Caroli-de Gennes-Matricon states, that only develop in clean superconductors. These Caroli-de Gennes-Matricon states were consecutively shown to inherit their anisotropy from the two-fold symmetric shape of the Fermi surface of Nb(110) by tight-binding calculations.
In chapter 8, the interaction of Fe atoms with the clean and oxygen-reconstructed Nb(110) surface and the influence of modifications of this interaction on the arising Yu-Shiba-Rusinov states was investigated. While atoms adsorbed onto the clean surface were shown to only very weakly interact with the superconducting substrate, inducing a single pair of YSR states close to the superconducting gap, Fe atoms on NbO$_x$ were demonstrated to exhibit a wide range of atom−substrate interaction strengths and hence YSR state energies. In comparative measurements in the superconducting and normal state of the substrate, Kondo resonances in the normal state could be correlated with YSR states of the same atoms, exposing an adsorption position-dependent quantum phase transition of the Fe atoms from an unscreened to a screened YSR ground state.
Finally, motivated by proposals of realizing Majorana zero modes in chains of magnetic adatoms on superconductors, the interatomic coupling of YSR states of Fe atoms on clean Nb(110) was examined in chapter 9. STM tips functionalized with CO molecules allowed to topographically resolve close-packed dimers and short chains that self-assembled on the surface upon Fe deposition. STS measurements on various dimers demonstrated an extremely short coupling distance of the YSR states on the order of 1.5 lattice constants. By mapping the LDOS of hybridized YSR states in close-packed chains, the YSR state wave functions' symmetry was revealed, displaying an oscillating behavior between chains with even and odd numbers of Fe atoms for the energetically lowest and highest YSR state. The observed oscillation of the hybridized YSR states' symmetry was qualitatively and

the corresponding YSR energies within limits also quantitatively simulated in a simple tight-binding model, solely relying on the coupling strength extracted from the measurements on Fe dimers as an input parameter.

Based on the example of Fe/Nb(110), the results of chapters 8 and 9 demonstrate how a thorough understanding of the adatom–substrate interaction and atom–atom coupling in only small systems such as dimers can be sufficient to model and potentially also to deterministically design larger artificial coupled YSR systems with defined electronic properties.

Outlook

Although Fe atoms on Nb(110) are an ideal system to study the above-mentioned properties as single Fe atoms only exhibit a single pair of YSR states which is easily traceable in coupled geometries, the short coupling distance limits the realization of more complex geometries. Cr and Mn atoms were shown to exhibit larger interactions and were successfully assembled to magnetic adatom chains [63, 69, 244, 254, 276]. Nevertheless, even larger coupling distances are desirable to increase the flexibility of the structures' design, envisioning e.g. ring-like [380] or 2D systems [274]. This could be achieved by combining both systems investigated in the course of this thesis: By introducing superconductivity into the surface state of the noble metal (111) surfaces via the proximity effect, as has been done in thin films of Ag on Nb(110) [384, 385] and Au on V(110) [386], one could realize an effectively 2D superconducting state. This would significantly increase the YSR states decay length and hence coupling distance [237]. Further, the isotropy of the fcc (111) surfaces suppresses orientation-dependent coupling, allowing for maximum flexibility in the design of 2D magnetic adatom lattices.

The same system might also yield further insight into the physics of Co atoms on the Cu(111) surface. If the zero-bias anomaly persists on the layered noble metal/superconductor system, screening of the Co atom spin via the Kondo effect at temperatures much higher than T_c should prevent the formation of YSR states. On the other hand, the observation of YSR states would indicate the existence of a finite magnetic moment of the Co atom, disproving the prevalent Kondo-related explanation of the zero-bias anomaly.

APPENDIX

A

Appendix A

Additional Fits of Field-Dependent Spectra on Co/Cu(111)

Additional fitting results of the field-dependent spectroscopy measurements of the ZBA on Co/Cu(111) are presented in Figures A.1 and A.2. To assess the change of the overall line shape of the ZBA in an external field, the $\mathrm{d}I/\mathrm{d}U$ signal from measurements at positive and negative values of the applied field were fitted with a single Fano resonance. Although this description is unphysical in both the Kondo picture, due to the neglected splitting of the Kondo resonance, and also the SE & spinaron model, that does not contain any interference of tunneling paths that could lead to a Fano line, the applied fit helps to track the position E_0 and width Γ of the ZBA. As mentioned in the main text, the center of the ZBA shifts to lower bias voltages with increasing field strength, independent on the direction of the field, as can be seen from the data in Figure A.1(a). Equally symmetric with respect to 0 T, the width of the ZBA displayed in Figure A.1(b) increases as a consequence of the shift of the individual features discussed in the main text.

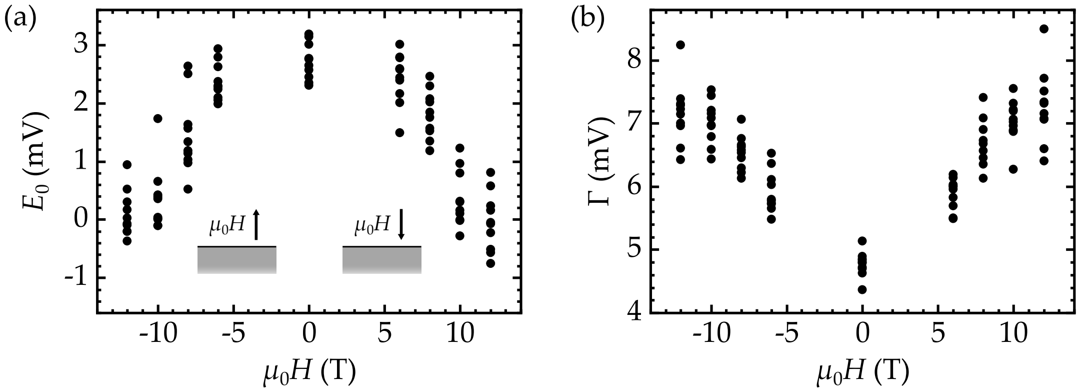

Figure A.1: Results of single-Fano line fits of the ZBA on Co/Cu(111) recorded at various fields and opposing field directions. Fitting was performed in a bias range of $(-10, +10)$ mV. The (a) position and (b) width of the ZBA change symmetrically around zero-field. The directions of the field for positive and negative values of $\mu_0 H$ are sketched in (a).

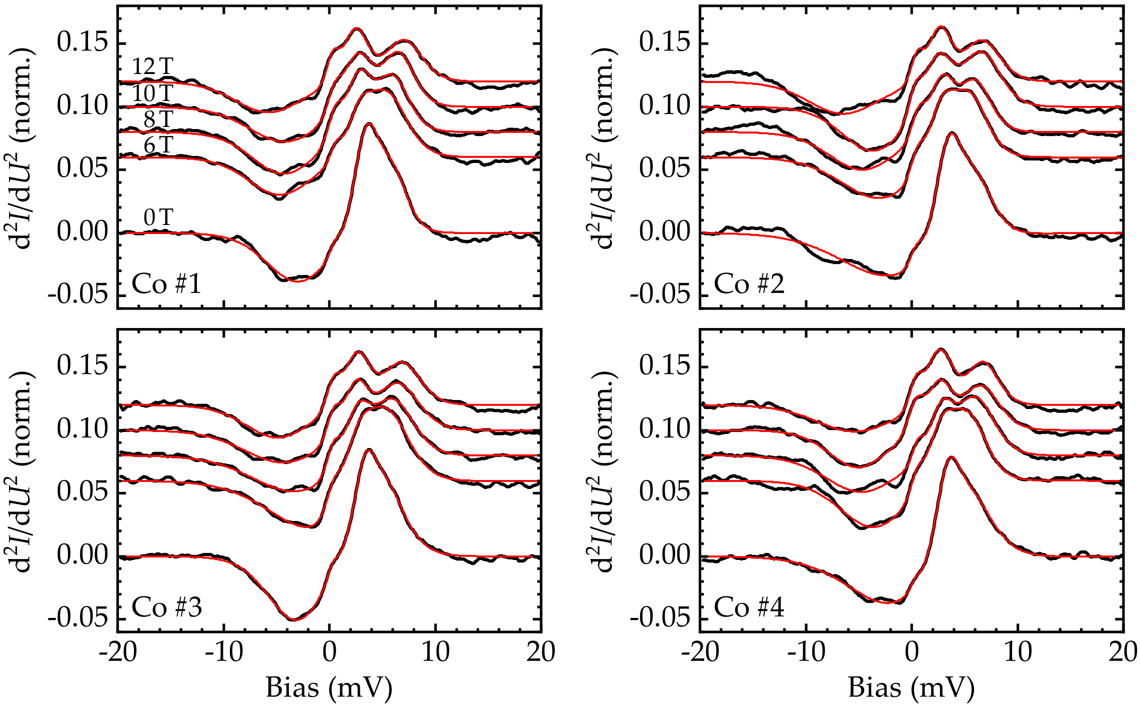

Figure A.2: Fits (red) of the d^2I/dU^2 signal (black) of four additional Co atoms within the model including four inelastic excitation-like peaks. Stabilization parameters (same as in Figure 4.4): $U = -20$ mV, $I = 1$ nA, $U_{\mathrm{mod}} = 0.5$ mV. $\mu_0 H$ as indicated; $T = 1.4$ K.

Figure A.2 displays fits of the d^2I/dU^2 signal of four additional Co atoms applying the model proposed in the main text containing four peaks used to describe inelastic excitations. Equivalent to the data presented in Figure 4.6, the fits describe the experimental signal well. The results of the fits presented here are included in the graphs of Figure 4.7.

B

Appendix B

THE ZERO-BIAS ANOMALY ON CO/AU(111)

To support the field-dependent results on Cu/Cu(111) presented in chapter 4, the same measurements were performed on Co/Au(111). The Au(111) surface was prepared by Ar^+-ion sputtering at 0.5 keV and annealing to 400 °C for 20 min. Co atoms were deposited as described in chapter 4. The resulting surface is displayed in Figure B.1(a). Panels (b) and (c) display the measured $\mathrm{d}I/\mathrm{d}U$ and calculated $\mathrm{d}^2I/\mathrm{d}U^2$ signal of a Co atom on the fcc and hcp site and on the soliton wall of the herringbone reconstruction of the Au(111) surface. Due to a failure of the experiments, no zero-field data exists for this measurement set, yet measurements on other Co atoms exhibited spectra similar to those observed at 6 T. The atoms on the fcc and hcp sites show a similar behavior than Co atoms on Cu(111). Especially the splitting of the positive bias peak in the $\mathrm{d}^2I/\mathrm{d}U^2$ signal is well observed, again with the peak at lower bias voltage exhibiting a higher intensity in comparison to the one at higher bias voltage. The Co atom on the soliton wall only exhibits a weak ZBA, as already shown in Ref. [150], which does not change as a function of the applied field, suggesting a non-magnetic origin. The results of the fitting procedure introduced in the main text for the atoms in the fcc and hcp sites are displayed in Figure B.1(d). While both types of atoms show the same shift of both the low- and high-energy (orange and red) feature at positive bias voltage, the absolute energies of the states of the fcc atoms are slightly higher.

In general, Co atoms on Au(111) are demonstrated to show the same spectroscopic response to an external field as Co atoms on Cu(111).

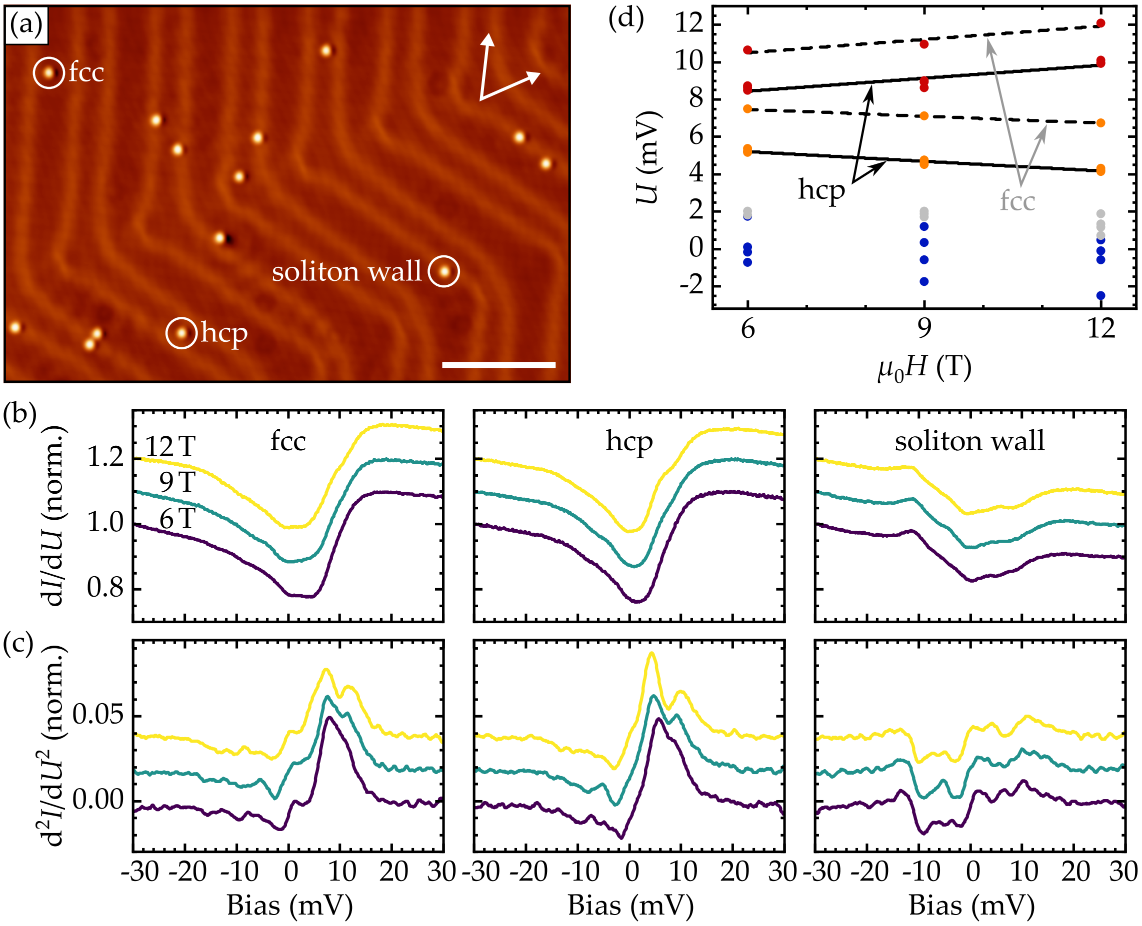

Figure B.1: (a) Topography of the Au(111) surface with deposited Fe atoms. Scale bar is 10 nm. (b) Differential conductance measured on the atoms mark in (a). (c) Numerically calculated derivative of the dI/dU signal in (b). (d) Results of the fitting model introduced in the main text. Linear fits to the positions of the two d^2I/dU^2 peaks at positive bias yield slopes of (-0.15 ± 0.02) mV/T and (0.23 ± 0.08) mV/T for atoms in both the fcc and hcp site. Stabilization parameters: $U = -30$ mV, $I = 1$ nA, $U_{\mathrm{mod}} = 0.5$ mV. $\mu_0 H$ as indicated; $T = 1.4$ K.

Appendix C

Adsorption of CO on Nb(110)

As described in the main text in chapter 9, the deposition of CO molecules onto the Nb(110) surface was unsuccessful, in that no vibrational modes of CO molecules could be detected by IETS atop the impurities found on the surface after CO deposition. Further, attempts to transfer these impurities onto the tip failed. In Figure C.1, the Nb surface after CO deposition at a substrate temperature of 4.2 K is presented. Contrary to oxygen, which can also form atomic impurities on very clean Nb surfaces, the impurities found in these scans do not change their contrast when the bias voltage is changed from -1 V to $+2$ V (cf. panels (a) and (b)), but remain depressions with a diameter of about 0.5 nm and depth of $10-20$ pm (cf. panels (c) and (d)). As such defects were only observed after CO deposition, two origins of the observed depressions are plausible: (i) The impurities might be intact CO molecules, yet absorbed differently to the Nb surface than to the Cu surface, e.g. laying horizontally on the surface, which would explain the lacking vibrational modes in IETS measurements. (ii) The CO molecules might decompose on the surface [313], with the oxygen atom attaching to a NbO_x patch, leaving the carbon atom, seen as the depression, behind.

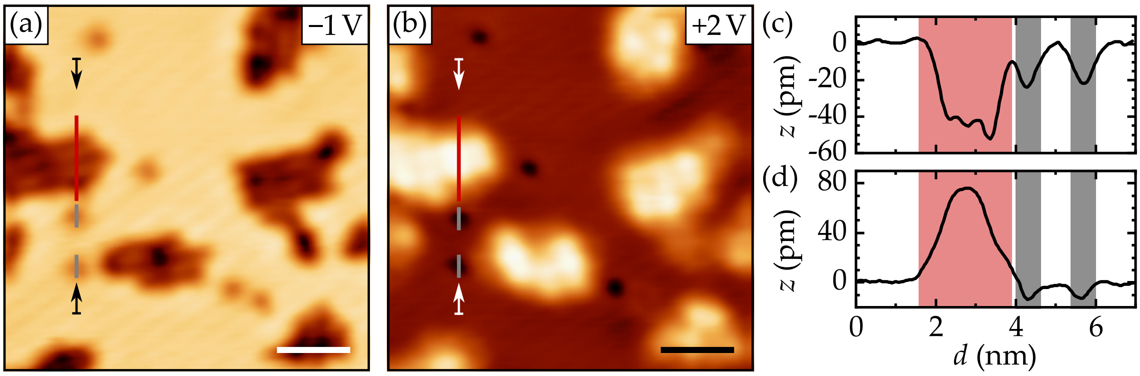

Figure C.1: Scans of the Nb(110) surface with remaining patches of NbO_x phase II and round-shaped impurities resulting from the deposition of CO molecules at a substrate temperature of 4.2 K. At a bias voltage of (a) -1 V, both oxygen and the impurities appear as depressions, while at (b) $+2$ V, oxygen exhibits a positive height above the clean Nb(110) surface. The impurities remain dark in the used color code. Scale bars are 2 nm. Line profiles indicated by arrows in (a) and (b) are displayed in (c) and (d). Oxygen is marked in red, the CO-related impurities are marked in gray. The same colors are used to indicate the respective positions in the scans. Scan parameters: (a) $U = -1$ V, $I = 1$ nA; (b) 2 V, 1 nA.

D

Appendix D

DIFFERENTIAL CONDUCTANCE MAPS OF $\langle 1\bar{1}1\rangle$ CHAINS

The following figure demonstrates the electron–hole symmetry of the YSR states in $\langle 1\bar{1}1\rangle$ chains of Fe atoms on Nb(110) discussed in chapter 9. The weak enhancement at the coherence peaks on the single atom in panel (a) is strongly localized to the topographic lateral extension of the atom. The additional conductance maps for the trimer (±2.85 mV) in panel (c) and tetramer (±1.95 mV and ±2.35 mV) in panel (d) not shown in the main text correspond to the values where the simplified model predicts additional states that are spectrally unresolved in the point spectra shown in Figure 9.7 of the main text. The similar shape of the tetramer LDOS at ±1.60 mV and ±1.95 mV suggests that the appearance of the less intense state at ±1.95 mV is covered by the more intense state at ±1.60 mV, hiding the true symmetry of the first.

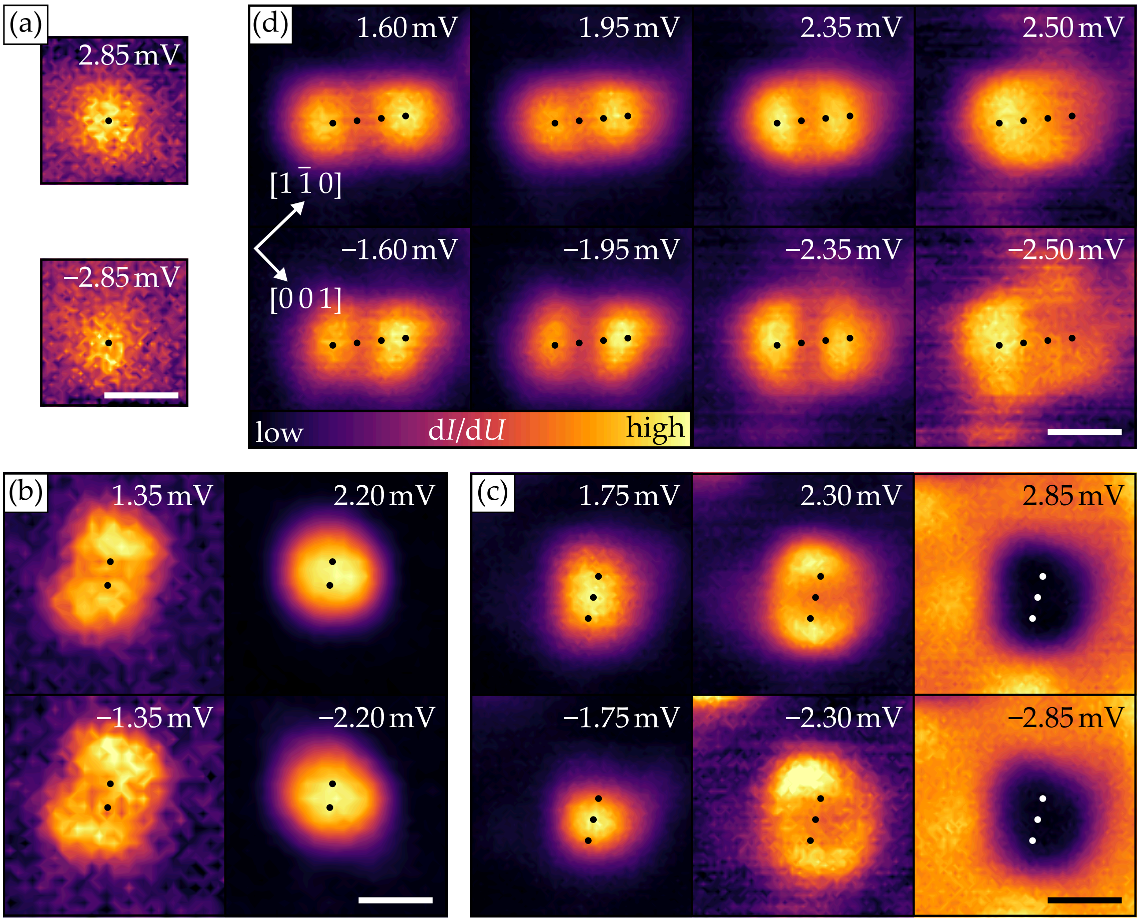

Figure D.1: Supplemental differential conductance maps of a (a) single atom ($\Delta_t = 1.31$ meV), (b) dimer, (c) trimer and (d) trimer (all $\Delta_t = 1.33$ meV). Scale bars are 1 nm. Stabilization parameters: $U = -7$ mV, $I = 1$ nA, $U_{\text{mod}} = 0.1$ mV. $T = 1.4$ K. *Reprinted from Ref. [341]. Copyright ©2021 by the American Physical Society.*

Appendix E

E DETAILS OF THE TIGHT-BINDING MODELS DESCRIBING THE YU-SHIBA-RUSINOV STATE COUPLING

E.1 SIMPLIFIED MODEL

The simplified model was introduced for YSR states by D. K. Morr and J. Yoon in Ref. [247] and is generally known from a basic description of the H_2^+ molecule. Approximating the solution of the n-atomic coupled system as a linear combination of the single-atom YSR wave functions with coefficients c_j, $j \in [1, n]$, and hopping constants k_i describing the coupling between atoms in sites $(j, j+i)$, $i \in [1, n-1]$, yields the following eigenvalue problems for a dimer, trimer and tetramer, respectively:

$$\begin{pmatrix} E_0 & k_1 \\ k_1 & E_0 \end{pmatrix} \begin{pmatrix} c_1 \\ c_2 \end{pmatrix} = E \begin{pmatrix} c_1 \\ c_2 \end{pmatrix}, \tag{E.1}$$

$$\begin{pmatrix} E_0 & k_1 & k_2 \\ k_1 & E_0 & k_1 \\ k_2 & k_1 & E_0 \end{pmatrix} \begin{pmatrix} c_1 \\ c_2 \\ c_3 \end{pmatrix} = E \begin{pmatrix} c_1 \\ c_2 \\ c_3 \end{pmatrix}, \tag{E.2}$$

$$\begin{pmatrix} E_0 & k_1 & k_2 & k_3 \\ k_1 & E_0 & k_1 & k_3 \\ k_2 & k_1 & E_0 & k_1 \\ k_3 & k_2 & k_1 & E_0 \end{pmatrix} \begin{pmatrix} c_1 \\ c_2 \\ c_3 \\ c_4 \end{pmatrix} = E \begin{pmatrix} c_1 \\ c_2 \\ c_3 \\ c_4 \end{pmatrix}. \tag{E.3}$$

E_0 is the single-atom YSR energy. Diagonalizing the matrices yields the eigenvalues of these equations, which can be separated for states with even $(c_i = c_{n-i+1})$

and odd ($c_i = -c_{n-i+1}$) symmetry:

$$E_{\mathrm{dimer,e}} = E_0 + k_1, \tag{E.4}$$
$$E_{\mathrm{dimer,o}} = E_0 - k_1, \tag{E.5}$$

$$E_{\mathrm{trimer,e}} = E_0 + \frac{k_2}{2} \pm \sqrt{2k_1^2 + \frac{k_2^2}{4}}, \tag{E.6}$$
$$E_{\mathrm{trimer,o}} = E_0 - k_2, \tag{E.7}$$

$$E_{\mathrm{tetramer,e}} = E_0 + \frac{k_1}{2} + \frac{k_3}{2} \pm \sqrt{\frac{5k_1^2}{4} + 2k_1k_2 - \frac{k_1k_3}{2} + k_2^2 + k_3^3}, \tag{E.8}$$
$$E_{\mathrm{tetramer,o}} = E_0 - \frac{k_1}{2} - \frac{k_3}{2} \pm \sqrt{\frac{5k_1^2}{4} - 2k_1k_2 - \frac{k_1k_3}{2} + k_2^2 + k_3^3}. \tag{E.9}$$

Figure 9.8(a)-(c) reproduces these solutions for $k_2,\ k_3 = 0$.

E.2 COMPLETE MODEL

The complete model was introduced in Ref. [250] for dimers and was extended to trimers and tetramers in this thesis, describing the YSR state coupling in chapter 9. For a system with n magnetic impurities coupled to a superconductor, the Hamiltonian of the single impurity in 5.29 is extended to

$$\mathcal{H} = \mathcal{H}_{\mathrm{BCS}} + \sum_j^n J_j(r), \tag{E.10}$$

with $J_j(r) := J(r - r_j)$ being the the exchange potential of the impurity at site r_j. The impurity spin was fixed to 1 [250]. Again, considering small coupling, a linear combination of the single-atom wave functions $|\varphi_i\rangle = |\varphi(r - r_i)\rangle$ is assumed as the solution of the above Hamiltonian:

$$|\Phi(r)\rangle = \sum_i^n c_i \, |\varphi_i\rangle \,. \tag{E.11}$$

Inserting this ansatz into the Schrödinger equation containing the Hamiltonian in Equation (E.10) and multiplying with $\langle\varphi_l|$, one obtains

$$\sum_i^n \sum_{i \neq j}^n c_i \, \langle\varphi_l|J_j|\varphi_i\rangle = (E - E_0) \sum_i^n c_i \, \langle\varphi_l|\varphi_i\rangle \,. \tag{E.12}$$

Writing out the equation for a dimer yields

$$\begin{pmatrix} C_1 & D_1 \\ D_1 & C_1 \end{pmatrix} \begin{pmatrix} c_1 \\ c_2 \end{pmatrix} = (E - E_0) \begin{pmatrix} 1 & S_1 \\ S_1 & 1 \end{pmatrix} \begin{pmatrix} c_1 \\ c_2 \end{pmatrix}, \tag{E.13}$$

with the overlap integral

$$S_i := \langle \varphi_1 | \varphi_{i+1} \rangle \,, \tag{E.14}$$

the Coulomb-like integral

$$C_i := \langle \varphi_1 | J_{i+1} | \varphi_1 \rangle \tag{E.15}$$

and the exchange-like integral

$$D_i := \langle \varphi_1 | J_1 | \varphi_{i+1} \rangle \,. \tag{E.16}$$

The eigenvalues of this problem are given by

$$E = E_0 + \frac{C_1 \pm D_1}{1 \pm S_1}. \tag{E.17}$$

Arguing that the overlap between the atomic YSR wave functions is sufficiently small such that $S_1 = 0$ and that the exchange potential decays fast enough such that $C_1 = 0$, one obtains the solutions of the simplified model by replacing D_1 with the hopping term k_1.

The eigenvalue equations of the complete model for the trimer and tetramer are

$$\begin{pmatrix} C_1 + C_2 & B_1 + D_1 & A_2 + D_1 \\ B_1 + D_1 & 2C_1 & B_1 + D_1 \\ A_2 + D_2 & B_1 + D_1 & C_1 + C_2 \end{pmatrix} \begin{pmatrix} c_1 \\ c_2 \\ c_3 \end{pmatrix} = (E - E_0) \begin{pmatrix} 1 & S_1 & S_2 \\ S_1 & 1 & S_1 \\ S_2 & S_1 & 1 \end{pmatrix} \begin{pmatrix} c_1 \\ c_2 \\ c_3 \end{pmatrix} \tag{E.18}$$

and

$$\begin{aligned} &\begin{pmatrix} C_1 + C_2 + C_3 & B_1 + B_1' + D_1 & A_2 + B_2' + D_2 & 2A_3 + D_3 \\ B_1 + B_1' + D_1 & 2C_1 + C_2 & 2B_1 + D_1 & A_2 + B_2' + D_2 \\ A_2 + B_2' + D_2 & 2B_1 + D_1 & 2C_1 + C_2 & B_1 + B_1' + D_1 \\ 2A_3 + D_3 & A_2 + B_2' + D_2 & B_1 + B_1' + D_1 & C_1 + C_2 + C_3 \end{pmatrix} \begin{pmatrix} c_1 \\ c_2 \\ c_3 \\ c_4 \end{pmatrix} \\ &\qquad = (E - E_0) \begin{pmatrix} 1 & S_1 & S_2 & S_3 \\ S_1 & 1 & S_1 & S_2 \\ S_2 & S_1 & 1 & S_1 \\ S_3 & S_2 & S_1 & 1 \end{pmatrix} \begin{pmatrix} c_1 \\ c_2 \\ c_3 \\ c_4 \end{pmatrix}, \end{aligned} \tag{E.19}$$

respectively, with the following additional definitions:

$$A_i := \langle \varphi_1 | J_2 | \varphi_{i+1} \rangle \,, \tag{E.20}$$

$$B_1 := \langle \varphi_1 | J_3 | \varphi_2 \rangle \,, \tag{E.21}$$

$$B_i' := \langle \varphi_1 | J_4 | \varphi_{i+1} \rangle \,. \tag{E.22}$$

The results displayed in Figure 9.9 in chapter 9 were obtained by introducing the exchange potential $J(r) = J_0/\sqrt{\pi\xi_\mathrm{J}}\exp\left(-r^2/\xi_\mathrm{J}^2\right)$ [250] and a normalized YSR wave function of the form $\sqrt{2/\lambda_\mathrm{F}}\,\mathrm{sinc}(2\pi r/\lambda_\mathrm{F})$ [51] in one dimension, where J_0 is the potential strength, ξ_J is the potential's decay length, λ_F is the Fermi wavelength and r points along the chain. The integrals and solutions of the eigenvalue problems were numerically evaluated with *python*.

LIST OF ABBREVIATIONS

1D	one-dimensional
2D	two-dimensional
3D	three-dimensional
AFM	atomic force microscopy
AES	Auger electron spectroscopy
bcc	body-centered cubic
BCS	Bardeen-Cooper-Schrieffer
CdGM	Caroli-de Gennes-Matricon
DFT	density functional theory
DOS	density of states
fcc	face-centered cubic
FWHM	full width at half maximum
G-L	Ginzburg-Landau
hcp	hexagonal close-packed
IETS	inelastic tunneling spectroscopy
LEED	low-energy electron diffraction
LDOS	local density of states
MONA	molecular nanoprobe
MZM	Majorana zero mode
Nc	nickelocene
QPT	quantum phase transition
UHV	ultra-high vacuum
SE	spin excitation
SP-STM	spin-polarized scanning tunneling microscopy
SP-STS	spin-polarized scanning tunneling spectroscopy
STM	scanning tunneling microscopy / microscope
STS	scanning tunneling spectroscopy
XMCD	x-ray magnetic circular dichroism
YSR	Yu-Shiba-Rusinov
ZBA	zero-bias anomaly

LIST OF PUBLICATIONS

Parts of this thesis have been published in...

- A. Odobesko, D. Di Sante, A. Kowalski, S. Wilfert, F. Friedrich, R. Thomale, G. Sangiovanni, and M. Bode, "Observation of tunable single-atom Yu-Shiba-Rusinov states", Phys. Rev. B **102**, 174504 (2020)
- A. Odobesko, F. Friedrich, S.-B. Zhang, S. Haldar, S. Heinze, B. Trauzettel, and M. Bode, "Anisotropic vortices on superconducting Nb(110)", Phys. Rev. B **102**, 174502 (2020)
- F. Friedrich, R. Boshuis, M. Bode, and A. Odobesko, "Coupling of Yu-Shiba-Rusinov states in one-dimensional chains of Fe atoms on Nb(110)", Phys. Rev. B **103**, 235437 (2021)

Additional work has been published in...

- S. Krämmer, F. Laye, F. Friedrich, C. Vannahme, C. L. C. Smith, A. C. Mendes, I. S. Chronakis, J. Lahann, A. Kristensen, and H. Kalt, "Electrospun Polymer Fiber Lasers for Applications in Vapor Sensing", Adv. Optical Mater. **5**, 1700248 (2017)
- N. Maleeva, L. Grünhaupt, T. Klein, F. Levy-Bertrand, O. Dupre, M. Calvo, F. Valenti, P. Winkel, F. Friedrich, W. Wernsdorfer, A.V. Ustinov, H. Rotzinger, A. Monfardini, M.V. Fistul, and I.M. Pop, "Circuit quantum electrodynamics of granular aluminum resonators", Nat. Commun. **9**, 3889, (2018)
- F. Friedrich, P. Winkel, K. Borisov, H. Seeger, C. Sürgers, I. M. Pop, and W. Wernsdorfer, "Onset of phase diffusion in high kinetic inductance granular aluminum micro- SQUIDs", Supercond. Sci. Technol. **32**, 125008 (2019)
- R. Boshuis, A. Odobesko, F. Friedrich, J. Jung, and M. Bode, "Comparative growth study of ultrathin Bi films on clean and oxygen-reconstructed Nb(110)", Phys. Rev. Mat. **5**, 054801 (2021)

BIBLIOGRAPHY

[1] W. de Haas, J. de Boer, and G. van dën Berg, “The Electrical Resistance of Gold, Copper and Lead at Low Temperatures”, Physica **1**, 1115–1124 (1934) (cited on pages 1, 16).

[2] G. Van den Berg and J. de Nobel, “Les propriétés à basses températures des alliages des métaux «normaux» avec des solutés de transition”, J. Phys. Radium **23**, 665–671 (1962) (cited on page 1).

[3] J. Kondo, “Resistance Minimum in Dilute Magnetic Alloys”, Progress of Theoretical Physics **32**, 37–49 (1964) (cited on pages 1, 14).

[4] A. A. Abrikosov, “Electron Scattering on Magnetic Impurities in Metals and Anomalous Resistivity Effects”, Physics Physique Fizika **2**, 5–20 (1965) (cited on pages 1, 15).

[5] Y. Nagaoka, “Self-Consistent Treatment of Kondo’s Effect in Dilute Alloys”, Phys. Rev. **138**, A1112–A1120 (1965) (cited on pages 1, 15).

[6] H. Suhl, “Dispersion Theory of the Kondo Effect”, Phys. Rev. **138**, A515–A523 (1965) (cited on pages 1, 15).

[7] F. Donati, S. Rusponi, S. Stepanow, C. Wackerlin, A. Singha, L. Persichetti, R. Baltic, K. Diller, F. Patthey, E. Fernandes, J. Dreiser, Ž. Šljivančanin, K. Kummer, C. Nistor, P. Gambardella, and H. Brune, “Magnetic Remanence in Single Atoms”, Science **352**, 318–321 (2016) (cited on pages 1, 54).

[8] F. Jelezko, T. Gaebel, I. Popa, M. Domhan, A. Gruber, and J. Wrachtrup, “Observation of Coherent Oscillation of a Single Nuclear Spin and Realization of a Two-Qubit Conditional Quantum Gate”, Phys. Rev. Lett. **93**, 130501 (2004) (cited on page 1).

[9] L. Childress, M. V. Gurudev Dutt, J. M. Taylor, A. S. Zibrov, F. Jelezko, J. Wrachtrup, P. R. Hemmer, and M. D. Lukin, “Coherent Dynamics of Coupled Electron and Nuclear Spin Qubits in Diamond”, Science **314**, 281–285 (2006) (cited on page 1).

[10] J. J. Pla, K. Y. Tan, J. P. Dehollain, W. H. Lim, J. J. L. Morton, D. N. Jamieson, A. S. Dzurak, and A. Morello, “A Single-Atom Electron Spin Qubit in Silicon”, Nature **489**, 541–545 (2012) (cited on page 1).

[11] J. J. Pla, K. Y. Tan, J. P. Dehollain, W. H. Lim, J. J. L. Morton, F. A. Zwanenburg, D. N. Jamieson, A. S. Dzurak, and A. Morello, “High-Fidelity Readout and Control of a Nuclear Spin Qubit in Silicon”, Nature **496**, 334–338 (2013) (cited on page 1).

[12] A. Laucht, R. Kalra, S. Simmons, J. P. Dehollain, J. T. Muhonen, F. A. Mohiyaddin, S. Freer, F. E. Hudson, K. M. Itoh, D. N. Jamieson, J. C. McCallum, A. S. Dzurak, and A. Morello, “A Dressed Spin Qubit in Silicon”, Nat. Nanotech. **12**, 61–66 (2017) (cited on page 1).

[13] T. F. Watson, B. Weber, Y.-L. Hsueh, L. C. L. Hollenberg, R. Rahman, and M. Y. Simmons, “Atomically Engineered Electron Spin Lifetimes of 30 s in Silicon”, Sci. Adv. **3**, e1602811 (2017) (cited on page 1).

[14] S. Thiele, F. Balestro, R. Ballou, S. Klyatskaya, M. Ruben, and W. Wernsdorfer, “Electrically Driven Nuclear Spin Resonance in Single-Molecule Magnets”, Science **344**, 1135–1138 (2014) (cited on page 1).

[15] C. Godfrin, A. Ferhat, R. Ballou, S. Klyatskaya, M. Ruben, W. Wernsdorfer, and F. Balestro, “Operating Quantum States in Single Magnetic Molecules: Implementation of Grover’s Quantum Algorithm”, Phys. Rev. Lett. **119**, 187702 (2017) (cited on page 1).

[16] C. Godfrin, R. Ballou, E. Bonet, M. Ruben, S. Klyatskaya, W. Wernsdorfer, and F. Balestro, “Generalized Ramsey Interferometry Explored with a Single Nuclear Spin Qudit”, npj Quantum Inf **4**, 53 (2018) (cited on page 1).

[17] K. Yang, W. Paul, S.-H. Phark, P. Willke, Y. Bae, T. Choi, T. Esat, A. Ardavan, A. J. Heinrich, and C. P. Lutz, “Coherent Spin Manipulation of Individual Atoms on a Surface”, Science **366**, 509–512 (2019) (cited on page 1).

[18] P. Willke, T. Bilgeri, X. Zhang, Y. Wang, C. Wolf, H. Aubin, A. Heinrich, and T. Choi, “Coherent Spin Control of Single Molecules on a Surface”, ACS Nano **15**, 17959–17965 (2021) (cited on pages 1, 2).

[19] L. M. Veldman, L. Farinacci, R. Rejali, R. Broekhoven, J. Gobeil, D. Coffey, M. Ternes, and A. F. Otte, “Free Coherent Evolution of a Coupled Atomic Spin System Initialized by Electron Scattering”, Science **372**, 964–968 (2021) (cited on page 1).

[20] A. F. G. Wyatt, “Anomalous Densities of States in Normal Tantalum and Niobium”, Phys. Rev. Lett. **13**, 401–404 (1964) (cited on page 2).

[21] L. Y. L. Shen and J. M. Rowell, “Zero-Bias Tunneling Anomalies–Temperature, Voltage, and Magnetic Field Dependence”, Phys. Rev. **165**, 566–577 (1968) (cited on page 2).

[22] R. H. Wallis and A. F. G. Wyatt, "Exchange Scattering in Ti-doped Al/Al Oxide/Ag Tunnel Junctions. II. Magnetic Field", J. Phys. C: Solid State Phys. 7, 1293–1302 (1974) (cited on page 2).

[23] A. N. Pasupathy, R. C. Bialczak, J. Martinek, J. E. Grose, L. A. K. Donev, P. L. McEuen, and D. C. Ralph, "The Kondo Effect in the Presence of Ferromagnetism", Science **306**, 86–89 (2004) (cited on page 2).

[24] R. Sessoli, D. Gatteschi, A. Caneschi, and M. A. Novak, "Magnetic Bistability in a Metal-Ion Cluster", Nature **365**, 141–143 (1993) (cited on page 2).

[25] W. Wernsdorfer and R. Sessoli, "Quantum Phase Interference and Parity Effects in Magnetic Molecular Clusters", Science **284**, 133–135 (1999) (cited on page 2).

[26] W. Wernsdorfer, "From Micro- to Nano-SQUIDs: Applications to Nanomagnetism", Supercond. Sci. Technol. **22**, 064013 (2009) (cited on page 2).

[27] P. Gambardella, S. S. Dhesi, S. Gardonio, C. Grazioli, P. Ohresser, and C. Carbone, "Localized Magnetic States of Fe, Co, and Ni Impurities on Alkali Metal Films", Phys. Rev. Lett. **88**, 047202 (2002) (cited on pages 2, 54).

[28] P. Gambardella, S. Rusponi, M. Veronese, S. S. Dhesi, C. Grazioli, A. Dallmeyer, I. Cabria, R. Zeller, P. H. Dederichs, K. Kern, C. Carbone, and H. Brune, "Giant Magnetic Anisotropy of Single Cobalt Atoms and Nanoparticles", Science **300**, 1130–1133 (2003) (cited on pages 2, 54).

[29] F. Jelezko, I. Popa, A. Gruber, C. Tietz, J. Wrachtrup, A. Nizovtsev, and S. Kilin, "Single Spin States in a Defect Center Resolved by Optical Spectroscopy", Appl. Phys. Lett. **81**, 2160–2162 (2002) (cited on page 2).

[30] S. Thiele, R. Vincent, M. Holzmann, S. Klyatskaya, M. Ruben, F. Balestro, and W. Wernsdorfer, "Electrical Readout of Individual Nuclear Spin Trajectories in a Single-Molecule Magnet Spin Transistor", Phys. Rev. Lett. **111**, 037203 (2013) (cited on page 2).

[31] G. Binnig, H. Rohrer, C. Gerber, and E. Weibel, "Tunneling through a Controllable Vacuum Gap", Appl. Phys. Lett. **40**, 178–180 (1982) (cited on pages 2, 19).

[32] G. Binnig, H. Rohrer, C. Gerber, and E. Weibel, "Surface Studies by Scanning Tunneling Microscopy", Phys. Rev. Lett. **49**, 57–61 (1982) (cited on pages 2, 19).

[33] V. Madhavan, W. Chen, T. Jamneala, M. F. Crommie, and N. S. Wingreen, "Tunneling into a Single Magnetic Atom: Spectroscopic Evidence of the Kondo Resonance", Science **280**, 567–569 (1998) (cited on pages 2, 3, 17, 31, 32, 36).

[34] H. C. Manoharan, C. P. Lutz, and D. M. Eigler, “Quantum Mirages Formed by Coherent Projection of Electronic Structure”, Nature **403**, 512–515 (2000) (cited on pages 2, 3, 17, 31, 32, 36).

[35] N. Knorr, M. A. Schneider, L. Diekhöner, P. Wahl, and K. Kern, “Kondo Effect of Single Co Adatoms on Cu Surfaces”, Phys. Rev. Lett. **88**, 096804 (2002) (cited on pages 2, 3, 17, 31, 36, 37).

[36] M. A. Schneider, L. Vitali, N. Knorr, and K. Kern, “Observing the Scattering Phase Shift of Isolated Kondo Impurities at Surfaces”, Phys. Rev. B **65**, 121406 (2002) (cited on pages 2, 3, 17, 31, 32).

[37] A. F. Otte, M. Ternes, K. von Bergmann, S. Loth, H. Brune, C. P. Lutz, C. F. Hirjibehedin, and A. J. Heinrich, “The Role of Magnetic Anisotropy in the Kondo Effect”, Nat. Phys. **4**, 847–850 (2008) (cited on pages 2, 17, 33).

[38] A. J. Heinrich, J. A. Gupta, C. P. Lutz, and D. M. Eigler, “Single-Atom Spin-Flip Spectroscopy”, Science **306**, 466–469 (2004) (cited on pages 2, 11, 25).

[39] S. Baumann, W. Paul, T. Choi, C. P. Lutz, A. Ardavan, and A. J. Heinrich, “Electron Paramagnetic Resonance of Individual Atoms on a Surface”, Science **350**, 417–420 (2015) (cited on pages 2, 11).

[40] T. Choi, W. Paul, S. Rolf-Pissarczyk, A. J. Macdonald, F. D. Natterer, K. Yang, P. Willke, C. P. Lutz, and A. J. Heinrich, “Atomic-Scale Sensing of the Magnetic Dipolar Field from Single Atoms”, Nat. Nanotech. **12**, 420–424 (2017) (cited on page 2).

[41] M. Ormaza, N. Bachellier, M. N. Faraggi, B. Verlhac, P. Abufager, P. Ohresser, L. Joly, M. Romeo, F. Scheurer, M.-L. Bocquet, N. Lorente, and L. Limot, “Efficient Spin-Flip Excitation of a Nickelocene Molecule”, Nano Lett. **17**, 1877–1882 (2017) (cited on pages 2, 47).

[42] M. Ormaza, P. Abufager, B. Verlhac, N. Bachellier, M.-L. Bocquet, N. Lorente, and L. Limot, “Controlled Spin Switching in a Metallocene Molecular Junction”, Nat. Commun. **8**, 1974 (2017) (cited on pages 2, 10, 47).

[43] D. M. Eigler and E. K. Schweizer, “Positioning Single Atoms with a Scanning Tunnelling Microscope”, Nature **344**, 524–526 (1990) (cited on pages 2, 115).

[44] M. Ternes, C. P. Lutz, C. F. Hirjibehedin, F. J. Giessibl, and A. J. Heinrich, “The Force Needed to Move an Atom on a Surface”, Science **319**, 1066–1069 (2008) (cited on page 2).

[45] C. F. Hirjibehedin, C. P. Lutz, and A. J. Heinrich, “Spin Coupling in Engineered Atomic Structures”, Science **312**, 1021–1024 (2006) (cited on pages 2, 12, 25).

[46] S. Loth, S. Baumann, C. P. Lutz, D. M. Eigler, and A. J. Heinrich, "Bistability in Atomic-Scale Antiferromagnets", Science **335**, 196–199 (2012) (cited on page 2).

[47] A. A. Khajetoorians, B. Baxevanis, C. Hübner, T. Schlenk, S. Krause, T. O. Wehling, S. Lounis, A. Lichtenstein, D. Pfannkuche, J. Wiebe, and R. Wiesendanger, "Current-Driven Spin Dynamics of Artificially Constructed Quantum Magnets", Science **339**, 55–59 (2013) (cited on page 2).

[48] L. Yu, "Bound State in Superconductors with Magnetic Impurities", Acta Phys. Sin. **21**, 75 (1965) (cited on pages 2, 70).

[49] H. Shiba, "Classical Spins in Superconductors", Prog. Theor. Phys. **40**, 435–451 (1968) (cited on pages 2, 70, 73).

[50] A. I. Rusinov, "On the Theory of Gapless Superconductivity in Alloys Containing Paramagnetic Impurities", Soviet JETP **29**, 1101 (1969) (cited on pages 2, 70, 73).

[51] A. I. Rusinov, "Superconductivity near a Paramagnetic Impurity", Soviet JETP Letters **9**, 85 (1969) (cited on pages 2, 70, 72, 130, 150).

[52] A. Yazdani, B. A. Jones, C. P. Lutz, M. F. Crommie, and D. M. Eigler, "Probing the Local Effects of Magnetic Impurities on Superconductivity", Science **275**, 1767–1770 (1997) (cited on pages 2, 71).

[53] T.-P. Choy, J. M. Edge, A. R. Akhmerov, and C. W. J. Beenakker, "Majorana Fermions Emerging from Magnetic Nanoparticles on a Superconductor without Spin-Orbit Coupling", Phys. Rev. B **84**, 195442 (2011) (cited on pages 2, 74, 77, 78).

[54] B. Braunecker and P. Simon, "Interplay between Classical Magnetic Moments and Superconductivity in Quantum One-Dimensional Conductors: Toward a Self-Sustained Topological Majorana Phase", Phys. Rev. Lett. **111**, 147202 (2013) (cited on pages 2, 74, 77, 78).

[55] J. Klinovaja, P. Stano, A. Yazdani, and D. Loss, "Topological Superconductivity and Majorana Fermions in RKKY Systems", Phys. Rev. Lett. **111**, 186805 (2013) (cited on pages 2, 74, 77, 78).

[56] S. Nadj-Perge, I. K. Drozdov, B. A. Bernevig, and A. Yazdani, "Proposal for Realizing Majorana Fermions in Chains of Magnetic Atoms on a Superconductor", Phys. Rev. B **88**, 020407 (2013) (cited on pages 2, 74, 77, 78).

[57] F. Pientka, L. I. Glazman, and F. von Oppen, "Topological Superconducting Phase in Helical Shiba Chains", Phys. Rev. B **88**, 155420 (2013) (cited on pages 2, 78).

[58] A. Heimes, P. Kotetes, and G. Schön, “Majorana Fermions from Shiba States in an Antiferromagnetic Chain on Top of a Superconductor”, Phys. Rev. B **90**, 060507 (2014) (cited on pages 2, 78).

[59] J. Li, H. Chen, I. K. Drozdov, A. Yazdani, B. A. Bernevig, and A. H. MacDonald, “Topological Superconductivity Induced by Ferromagnetic Metal Chains”, Phys. Rev. B **90**, 235433 (2014) (cited on pages 2, 78).

[60] Y. Peng, F. Pientka, L. I. Glazman, and F. von Oppen, “Strong Localization of Majorana End States in Chains of Magnetic Adatoms”, Phys. Rev. Lett. **114**, 106801 (2015) (cited on pages 2, 78, 79).

[61] A. Y. Kitaev, “Unpaired Majorana Fermions in Quantum Wires”, Phys.-Usp. **44**, 131–136 (2001) (cited on pages 2, 76, 77, 80).

[62] A. Stern, “Non-Abelian States of Matter”, Nature **464**, 187–193 (2010) (cited on pages 2, 80).

[63] L. Schneider, P. Beck, J. Neuhaus-Steinmetz, L. Rózsa, T. Posske, J. Wiebe, and R. Wiesendanger, “Precursors of Majorana Modes and Their Length-Dependent Energy Oscillations Probed at Both Ends of Atomic Shiba Chains”, Nat. Nanotech. **17**, 384–389 (2022) (cited on pages 2, 3, 79, 115, 135).

[64] J. Bouaziz, F. S. Mendes Guimarães, and S. Lounis, “A New View on the Origin of Zero-Bias Anomalies of Co Atoms atop Noble Metal Surfaces”, Nat. Commun. **11**, 6112 (2020) (cited on pages 3, 31, 33–35, 38, 42, 43).

[65] S. Nadj-Perge, I. K. Drozdov, J. Li, H. Chen, S. Jeon, J. Seo, A. H. MacDonald, B. A. Bernevig, and A. Yazdani, “Observation of Majorana Fermions in Ferromagnetic Atomic Chains on a Superconductor”, Science **346**, 602–607 (2014) (cited on pages 3, 79, 101).

[66] M. Ruby, F. Pientka, Y. Peng, F. von Oppen, B. W. Heinrich, and K. J. Franke, “End States and Subgap Structure in Proximity-Coupled Chains of Magnetic Adatoms”, Phys. Rev. Lett. **115**, 197204 (2015) (cited on pages 3, 74, 79, 101).

[67] R. Pawlak, M. Kisiel, J. Klinovaja, T. Meier, S. Kawai, T. Glatzel, D. Loss, and E. Meyer, “Probing Atomic Structure and Majorana Wavefunctions in Mono-Atomic Fe Chains on Superconducting Pb Surface”, npj Quantum Inf **2**, 16035 (2016) (cited on pages 3, 79).

[68] H. Kim, A. Palacio-Morales, T. Posske, L. Rózsa, K. Palotás, L. Szunyogh, M. Thorwart, and R. Wiesendanger, “Toward Tailoring Majorana Bound States in Artificially Constructed Magnetic Atom Chains on Elemental Superconductors”, Sci. Adv. **4**, eaar5251 (2018) (cited on pages 3, 79, 101, 115).

[69] F. Küster, S. Brinker, R. Hess, D. Loss, S. S. P. Parkin, J. Klinovaja, S. Lounis, and P. Sessi, "Non-Majorana Modes in Diluted Spin Chains Proximitized to a Superconductor", PNAS **119**, e2210589119 (2022) (cited on pages 3, 79, 115, 135).

[70] R. Gross and A. Marx, *Festkörperphysik* (Oldenbourg, München, 2012) (cited on pages 7, 58, 63, 64, 67).

[71] P. Bruno, "Tight-Binding Approach to the Orbital Magnetic Moment and Magnetocrystalline Anisotropy of Transition-Metal Monolayers", Phys. Rev. B **39**, 865–868 (1989) (cited on page 8).

[72] J. C. Oberg, M. R. Calvo, F. Delgado, M. Moro-Lagares, D. Serrate, D. Jacob, J. Fernández-Rossier, and C. F. Hirjibehedin, "Control of Single-Spin Magnetic Anisotropy by Exchange Coupling", Nat. Nanotech. **9**, 64–68 (2014) (cited on page 8).

[73] P. Jacobson, T. Herden, M. Muenks, G. Laskin, O. Brovko, V. Stepanyuk, M. Ternes, and K. Kern, "Quantum Engineering of Spin and Anisotropy in Magnetic Molecular Junctions", Nat. Commun. **6**, 8536 (2015) (cited on page 8).

[74] O. Eriksson, B. Johansson, R. C. Albers, A. M. Boring, and M. S. S. Brooks, "Orbital Magnetism in Fe, Co, and Ni", Phys. Rev. B **42**, 2707–2710 (1990) (cited on page 8).

[75] B. Chilian, A. A. Khajetoorians, S. Lounis, A. T. Costa, D. L. Mills, J. Wiebe, and R. Wiesendanger, "Anomalously Large g Factor of Single Atoms Adsorbed on a Metal Substrate", Phys. Rev. B **84**, 212401 (2011) (cited on page 9).

[76] D. Gatteschi, R. Sessoli, and J. Villain, *Molecular Nanomagnets* (Oxford University Press, 2006) (cited on pages 9–11).

[77] C. F. Hirjibehedin, C.-Y. Lin, A. F. Otte, M. Ternes, C. P. Lutz, B. A. Jones, and A. J. Heinrich, "Large Magnetic Anisotropy of a Single Atomic Spin Embedded in a Surface Molecular Network", Science **317**, 1199–1203 (2007) (cited on pages 10–12, 25).

[78] K. von Bergmann, M. Ternes, S. Loth, C. P. Lutz, and A. J. Heinrich, "Spin Polarization of the Split Kondo State", Phys. Rev. Lett. **114**, 076601 (2015) (cited on pages 10, 16, 25, 27, 33, 39, 44, 53).

[79] M. Ternes, "Spin Excitations and Correlations in Scanning Tunneling Spectroscopy", New J. Phys. **17**, 063016 (2015) (cited on pages 11, 12, 14, 48, 49).

[80] P. Willke, Y. Bae, K. Yang, J. L. Lado, A. Ferrón, T. Choi, A. Ardavan, J. Fernández-Rossier, A. J. Heinrich, and C. P. Lutz, "Hyperfine Interaction of Individual Atoms on a Surface", Science **362**, 336–339 (2018) (cited on page 11).

[81] S. Loth, C. P. Lutz, and A. J. Heinrich, "Spin-Polarized Spin Excitation Spectroscopy", New J. Phys. **12**, 125021 (2010) (cited on pages 12–14, 25, 27, 44).

[82] Creative Commons Attribution-NonCommercial-ShareAlike 3.0 Unported License (CC BY-NC-SA 3.0) , `https://creativecommons.org/licenses/by-nc-sa/3.0/` (cited on page 13).

[83] B. Verlhac, N. Bachellier, L. Garnier, M. Ormaza, P. Abufager, R. Robles, M.-L. Bocquet, M. Ternes, N. Lorente, and L. Limot, "Atomic-Scale Spin Sensing with a Single Molecule at the Apex of a Scanning Tunneling Microscope", Science **366**, 623–627 (2019) (cited on pages 14, 25, 47).

[84] P. W. Anderson, "Localized Magnetic States in Metals", Phys. Rev. **124**, 41–53 (1961) (cited on page 14).

[85] M. Ternes, A. J. Heinrich, and W.-D. Schneider, "Spectroscopic Manifestations of the Kondo Effect on Single Adatoms", J. Phys.: Condens. Matter **21**, 053001 (2009) (cited on pages 14, 16, 17, 34).

[86] A. C. Hewson, *The Kondo Problem to Heavy Fermions*, 1st pbk. ed. with corrections, Cambridge Studies in Magnetism 2 (Cambridge University Press, Cambridge ; New York, 1997) (cited on pages 15, 16, 52).

[87] Y. Meir, N. S. Wingreen, and P. A. Lee, "Low-Temperature Transport through a Quantum Dot: The Anderson Model out of Equilibrium", Phys. Rev. Lett. **70**, 2601–2604 (1993) (cited on page 16).

[88] C. Zener, "Interaction Between the d Shells in the Transition Metals", Phys. Rev. **81**, 440–444 (1951) (cited on page 16).

[89] J. Owen, M. Browne, W. D. Knight, and C. Kittel, "Electron and Nuclear Spin Resonance and Magnetic Susceptibility Experiments on Dilute Alloys of Mn in Cu", Phys. Rev. **102**, 1501–1507 (1956) (cited on page 16).

[90] T. Kasuya, "A Theory of Metallic Ferro- and Antiferromagnetism on Zener's Model", Prog. Theor. Phys. **16**, 45–57 (1956) (cited on page 16).

[91] K. Yosida, "Magnetic Properties of Cu-Mn Alloys", Phys. Rev. **106**, 893–898 (1957) (cited on page 16).

[92] K. Yosida, "Anomalous Electrical Resistivity and Magnetoresistance Due to an s-d Interaction in Cu-Mn Alloys", Phys. Rev. **107**, 396–403 (1957) (cited on page 16).

[93] J. R. Schrieffer and P. A. Wolff, "Relation between the Anderson and Kondo Hamiltonians", Phys. Rev. **149**, 491–492 (1966) (cited on page 16).

[94] J. Fernández, P. Roura-Bas, and A. A. Aligia, "Theory of Differential Conductance of Co on Cu(111) Including Co s and d Orbitals, and Surface and Bulk Cu States", Phys. Rev. Lett. **126**, 046801 (2021) (cited on pages 16, 32).

[95] U. Fano, "Effects of Configuration Interaction on Intensities and Phase Shifts", Phys. Rev. **124**, 1866–1878 (1961) (cited on page 17).

[96] M. Pivetta, M. Ternes, F. Patthey, and W.-D. Schneider, "Diatomic Molecular Switches to Enable the Observation of Very-Low-Energy Vibrations", Phys. Rev. Lett. **99**, 126104 (2007) (cited on page 17).

[97] J. Li, W.-D. Schneider, R. Berndt, and B. Delley, "Kondo Scattering Observed at a Single Magnetic Impurity", Physical Review Letters **80**, 2893–2896 (1998) (cited on page 17).

[98] H. O. Frota and L. N. Oliveira, "Photoemission spectroscopy for the spin-degenerate Anderson model", en, Physical Review B **33**, 7871–7874 (1986) (cited on page 17).

[99] H. O. Frota, "Shape of the Kondo resonance", en, Physical Review B **45**, 1096–1099 (1992) (cited on page 17).

[100] H. Prüser, M. Wenderoth, P. E. Dargel, A. Weismann, R. Peters, T. Pruschke, and R. G. Ulbrich, "Long-range Kondo signature of a single magnetic impurity", en, Nature Physics **7**, 203–206 (2011) (cited on page 17).

[101] M. Gruber, A. Weismann, and R. Berndt, "The Kondo resonance line shape in scanning tunnelling spectroscopy: instrumental aspects", Journal of Physics: Condensed Matter **30**, 424001 (2018) (cited on page 17).

[102] N. Néel, J. Kröger, M. Schüler, B. Shao, T. O. Wehling, A. Kowalski, and G. Sangiovanni, "Single-Co Kondo Effect in Atomic Cu Wires on Cu(111)", Phys. Rev. Research **2**, 023309 (2020) (cited on pages 18, 32).

[103] R. Wiesendanger, *Scanning Probe Microscopy and Spectroscopy: Methods and Applications* (Cambridge University Press, Cambridge [England] ; New York, 1994) (cited on pages 19, 23).

[104] C. J. Chen, *Introduction to Scanning Tunneling Microscopy* (Oxford University Press, 2021) (cited on pages 19, 20).

[105] J. Bardeen, "Tunnelling from a Many-Particle Point of View", Phys. Rev. Lett. **6**, 57–59 (1961) (cited on page 20).

[106] J. Tersoff and D. R. Hamann, "Theory and Application for the Scanning Tunneling Microscope", Phys. Rev. Lett. **50**, 1998–2001 (1983) (cited on page 21).

[107] J. Tersoff and D. R. Hamann, "Theory of the Scanning Tunneling Microscope", Phys. Rev. B **31**, 805–813 (1985) (cited on pages 21, 96).

[108] S. Ohnishi and M. Tsukada, "Molecular Orbital Theory for the Scanning Tunneling Microscopy", Solid State Communications **71**, 391–394 (1989) (cited on page 23).

[109] L. Gross, N. Moll, F. Mohn, A. Curioni, G. Meyer, F. Hanke, and M. Persson, "High-Resolution Molecular Orbital Imaging Using a p-Wave STM Tip", Phys. Rev. Lett. **107**, 086101 (2011) (cited on pages 23, 116).

[110] C. J. Chen, "Origin of Atomic Resolution on Metal Surfaces in Scanning Tunneling Microscopy", Phys. Rev. Lett. **65**, 448–451 (1990) (cited on page 23).

[111] C. J. Chen, "Tunneling Matrix Elements in Three-Dimensional Space: The Derivative Rule and the Sum Rule", Phys. Rev. B **42**, 8841–8857 (1990) (cited on page 23).

[112] I. Horcas, R. Fernández, J. M. Gómez-Rodríguez, J. Colchero, J. Gómez-Herrero, and A. M. Baro, "WSXM : a software for scanning probe microscopy and a tool for nanotechnology", Rev. Sci. Instrum. **78**, 013705 (2007) (cited on page 23).

[113] D. Nečas and P. Klapetek, "Gwyddion: An Open-Source Software for SPM Data Analysis", Open Physics **10**, 181–188 (2012) (cited on page 23).

[114] J. Lambe and R. C. Jaklevic, "Molecular Vibration Spectra by Inelastic Electron Tunneling", Phys. Rev. **165**, 821–832 (1968) (cited on pages 25, 33).

[115] R. C. Jaklevic and J. Lambe, "Molecular Vibration Spectra by Electron Tunneling", Phys. Rev. Lett. **17**, 1139–1140 (1966) (cited on page 25).

[116] B. C. Stipe, M. A. Rezaei, and W. Ho, "Single-Molecule Vibrational Spectroscopy and Microscopy", Science **280**, 1732–1735 (1998) (cited on page 25).

[117] L. J. Lauhon and W. Ho, "Single-Molecule Vibrational Spectroscopy and Microscopy: CO on Cu(001) and Cu(110)", Phys. Rev. B **60**, R8525–R8528 (1999) (cited on pages 25, 116, 118).

[118] D. P. E. Smith, G. Binnig, and C. F. Quate, "Detection of Phonons with a Scanning Tunneling Microscope", Appl. Phys. Lett. **49**, 1641–1643 (1986) (cited on page 25).

[119] M. Bode, "Spin-Polarized Scanning Tunnelling Microscopy", Rep. Prog. Phys. **66**, 523–582 (2003) (cited on page 25).

[120] R. Wiesendanger, H.-J. Güntherodt, G. Güntherodt, R. J. Gambino, and R. Ruf, "Observation of Vacuum Tunneling of Spin-Polarized Electrons with the Scanning Tunneling Microscope", Phys. Rev. Lett. **65**, 247–250 (1990) (cited on page 25).

[121] R. Wiesendanger, I. V. Shvets, D. Bürgler, G. Tarrach, H. J. Güntherodt, J. M. D. Coey, and S. Gräser, “Topographic and Magnetic-Sensitive Scanning Tunneling Microscope Study of Magnetite”, Science **255**, 583–586 (1992) (cited on page 25).

[122] M. Bode, M. Getzlaff, and R. Wiesendanger, “Spin-Polarized Vacuum Tunneling into the Exchange-Split Surface State of Gd(0001)”, Phys. Rev. Lett. **81**, 4256–4259 (1998) (cited on page 25).

[123] O. Pietzsch, A. Kubetzka, M. Bode, and R. Wiesendanger, “Real-Space Observation of Dipolar Antiferromagnetism in Magnetic Nanowires by Spin-Polarized Scanning Tunneling Spectroscopy”, Phys. Rev. Lett. **84**, 5212–5215 (2000) (cited on page 25).

[124] S. Loth, K. von Bergmann, M. Ternes, A. F. Otte, C. P. Lutz, and A. J. Heinrich, “Controlling the State of Quantum Spins with Electric Currents”, Nat. Phys. **6**, 340–344 (2010) (cited on pages 25, 27, 44).

[125] A. A. Khajetoorians, J. Wiebe, B. Chilian, S. Lounis, S. Blügel, and R. Wiesendanger, “Atom-by-Atom Engineering and Magnetometry of Tailored Nanomagnets”, Nat. Phys. **8**, 497–503 (2012) (cited on page 25).

[126] M. Julliere, “Tunneling between Ferromagnetic Films”, Physics Letters A **54**, 225–226 (1975) (cited on page 26).

[127] D. Wortmann, S. Heinze, P. Kurz, G. Bihlmayer, and S. Blügel, “Resolving Complex Atomic-Scale Spin Structures by Spin-Polarized Scanning Tunneling Microscopy”, Phys. Rev. Lett. **86**, 4132–4135 (2001) (cited on page 26).

[128] M. Bode, R. Pascal, and R. Wiesendanger, “Scanning Tunneling Spectroscopy of Fe/W(110) Using Iron Covered Probe Tips”, J. Vac. Sci. Technol. A: Vacuum, Surfaces, and Films **15**, 1285–1290 (1997) (cited on page 27).

[129] A. Kubetzka, M. Bode, O. Pietzsch, and R. Wiesendanger, “Spin-Polarized Scanning Tunneling Microscopy with Antiferromagnetic Probe Tips”, Phys. Rev. Lett. **88**, 057201 (2002) (cited on page 27).

[130] L. Berbil-Bautista, S. Krause, M. Bode, and R. Wiesendanger, “Spin-Polarized Scanning Tunneling Microscopy and Spectroscopy of Ferromagnetic Dy(0001)/W(110) Films”, Phys. Rev. B **76**, 064411 (2007) (cited on page 27).

[131] O. Storz, “Aufbau eines Rastertunnelmikroskops für Landau Level - Spektroskopie auf topologischen Isolator - Oberflächen”, PhD thesis (Universität Würzburg, Würzburg, 2016) (cited on pages 28, 29).

[132] S. Wilfert, “Rastertunnelmikroskopische und -spektroskopische Untersuchung von Supraleitern und topologischen Supraleitern”, PhD thesis (Universität Würzburg, Würzburg, 2019) (cited on pages 28, 81, 89, 92).

[133] S. Pan, *Piezoelectric Motor*, Patent Publication Number WO/1993/019494, 1993 (cited on page 28).

[134] M. Weissmann, A. Saúl, A. M. Llois, and J. Guevara, “Cobalt Impurities on Noble-Metal Surfaces”, Phys. Rev. B **59**, 8405–8407 (1999) (cited on page 32).

[135] A. Schiller and S. Hershfield, “Theory of Scanning Tunneling Spectroscopy of a Magnetic Adatom on a Metallic Surface”, Phys. Rev. B **61**, 9036–9046 (2000) (cited on page 32).

[136] M. Weissmann and A. M. Llois, “Adsorbed 3d Transition-Metal Atoms and Dimers on Au(111): Signatures Derived from One-Electron Calculations”, Phys. Rev. B **63**, 113402 (2001) (cited on page 32).

[137] Y. Shimada, H. Kasai, H. Nakanishi, W. Agerico Diño, A. Okiji, and Y. Hasegawa, “Spatial and temperature dependence of the spectroscopic profile of a magnetic atom adsorbed on a metal surface—Co/Cu(111)”, Journal of Applied Physics **94**, 334–341 (2003) (cited on page 32).

[138] J. Merino and O. Gunnarsson, “Role of Surface States in Scanning Tunneling Spectroscopy of (111) Metal Surfaces with Kondo Adsorbates”, Phys. Rev. Lett. **93**, 156601 (2004) (cited on page 32).

[139] J. Merino and O. Gunnarsson, “Simple Model for Scanning Tunneling Spectroscopy of Noble Metal Surfaces with Adsorbed Kondo Impurities”, Phys. Rev. B **69**, 115404 (2004) (cited on page 32).

[140] M. A. Barral, A. M. Llois, and A. A. Aligia, “Hybridization of Impurity States with the Shockley Surface Band versus Bulk States”, Phys. Rev. B **70**, 035416 (2004) (cited on page 32).

[141] C.-Y. Lin, A. H. Castro Neto, and B. A. Jones, “Microscopic Theory of the Single Impurity Surface Kondo Resonance”, Phys. Rev. B **71**, 035417 (2005) (cited on page 32).

[142] C.-Y. Lin, A. H. Castro Neto, and B. A. Jones, “First-Principles Calculation of the Single Impurity Surface Kondo Resonance”, Phys. Rev. Lett. **97**, 156102 (2006) (cited on page 32).

[143] K. R. Patton, S. Kettemann, A. Zhuravlev, and A. Lichtenstein, “Spin-Polarized Tunneling Microscopy and the Kondo Effect”, Phys. Rev. B **76**, 100408 (2007) (cited on pages 32, 33).

[144] P. Roura-Bas, M. A. Barral, and A. M. Llois, “Co Impurities on Ag and Cu: Kondo Temperature Dependence on Substrate Orientation”, Phys. Rev. B **79**, 075410 (2009) (cited on page 32).

[145] S. Frank and D. Jacob, “Orbital Signatures of Fano-Kondo Line Shapes in STM Adatom Spectroscopy”, Phys. Rev. B **92**, 235127 (2015) (cited on pages 32, 112).

[146] P. P. Baruselli, R. Requist, A. Smogunov, M. Fabrizio, and E. Tosatti, "Co Adatoms on Cu Surfaces: Ballistic Conductance and Kondo Temperature", Phys. Rev. B **92**, 045119 (2015) (cited on page 32).

[147] M. S. Tacca, T. Jacob, and E. C. Goldberg, "Influence of Surface States on the Conductance Spectra for Co Adsorbed on Cu(111)", Phys. Rev. B **103**, 245419 (2021) (cited on page 32).

[148] W. Chen, T. Jamneala, V. Madhavan, and M. F. Crommie, "Disappearance of the Kondo Resonance for Atomically Fabricated Cobalt Dimers", Phys. Rev. B **60**, R8529–R8532 (1999) (cited on pages 32, 33).

[149] M. Crommie, "Observing Electronic Scattering in Atomic-Scale Structures on Metals", Journal of Electron Spectroscopy and Related Phenomena **109**, 1–17 (2000) (cited on page 32).

[150] V. Madhavan, W. Chen, T. Jamneala, M. F. Crommie, and N. S. Wingreen, "Local Spectroscopy of a Kondo Impurity: Co on Au(111)", Phys. Rev. B **64**, 165412 (2001) (cited on pages 32, 33, 36, 141).

[151] L. Limot and R. Berndt, "Kondo effect and surface-state electrons", Applied Surface Science **237**, 572–576 (2004) (cited on page 32).

[152] L. Limot, E. Pehlke, J. Kröger, and R. Berndt, "Surface-State Localization at Adatoms", Phys. Rev. Lett. **94**, 036805 (2005) (cited on page 32).

[153] M. A. Schneider, P. Wahl, L. Diekhöner, L. Vitali, G. Wittich, and K. Kern, "Kondo Effect of Co Adatoms on Ag Monolayers on Noble Metal Surfaces", Jpn. J. Appl. Phys. **44**, 5328–5331 (2005) (cited on pages 32, 34).

[154] J. Henzl and K. Morgenstern, "Contribution of the Surface State to the Observation of the Surface Kondo Resonance", Phys. Rev. Lett. **98**, 266601 (2007) (cited on page 32).

[155] L. Vitali, R. Ohmann, S. Stepanow, P. Gambardella, K. Tao, R. Huang, V. S. Stepanyuk, P. Bruno, and K. Kern, "Kondo Effect in Single Atom Contacts: The Importance of the Atomic Geometry", Phys. Rev. Lett. **101**, 216802 (2008) (cited on pages 32, 36, 37).

[156] N. Néel, J. Kröger, R. Berndt, T. O. Wehling, A. I. Lichtenstein, and M. I. Katsnelson, "Controlling the Kondo Effect in CoCu$_n$ Clusters Atom by Atom", Phys. Rev. Lett. **101**, 266803 (2008) (cited on pages 32, 36).

[157] N. Néel, J. Kröger, and R. Berndt, "Kondo Effect of a Co Atom on Cu(111) in Contact with an Iron Tip", Phys. Rev. B **82**, 233401 (2010) (cited on page 32).

[158] S. L. Kawahara, J. Lagoute, V. Repain, C. Chacon, Y. Girard, J. Klein, and S. Rousset, "Kondo Peak Splitting on a Single Adatom Coupled to a Magnetic Cluster", Phys. Rev. B **82**, 020406 (2010) (cited on pages 32, 33).

[159] M. Moro-Lagares, J. Fernández, P. Roura-Bas, M. R. Ibarra, A. A. Aligia, and D. Serrate, “Quantifying the Leading Role of the Surface State in the Kondo Effect of Co/Ag(111)”, Phys. Rev. B **97**, 235442 (2018) (cited on pages 32, 36).

[160] Q. L. Li, C. Zheng, R. Wang, B. F. Miao, R. X. Cao, L. Sun, D. Wu, Y. Z. Wu, S. C. Li, B. G. Wang, and H. F. Ding, “Role of the Surface State in the Kondo Resonance Width of a Co Single Adatom on Ag(111)”, Phys. Rev. B **97**, 035417 (2018) (cited on pages 32, 36).

[161] N. Knorr, H. Brune, M. Epple, A. Hirstein, M. A. Schneider, and K. Kern, “Long-Range Adsorbate Interactions Mediated by a Two-Dimensional Electron Gas”, Phys. Rev. B **65**, 115420 (2002) (cited on page 33).

[162] K. Nagaoka, T. Jamneala, M. Grobis, and M. F. Crommie, “Temperature Dependence of a Single Kondo Impurity”, Phys. Rev. Lett. **88**, 077205 (2002) (cited on page 33).

[163] B. Schweflinghaus, M. dos Santos Dias, A. T. Costa, and S. Lounis, “Renormalization of Electron Self-Energies via Their Interaction with Spin Excitations: A First-Principles Investigation”, Phys. Rev. B **89**, 235439 (2014) (cited on pages 33, 110).

[164] S. Brinker, F. Küster, S. S. P. Parkin, P. Sessi, and S. Lounis, “Anomalous Excitations of Atomically Crafted Quantum Magnets”, Sci. Adv. **8**, eabi7291 (2022) (cited on page 34).

[165] Creative Commons Attribution 4.0 International License (CC BY 4.0), `https://creativecommons.org/licenses/by/4.0/` (cited on page 34).

[166] M. Moro-Lagares, R. Korytár, M. Piantek, R. Robles, N. Lorente, J. I. Pascual, M. R. Ibarra, and D. Serrate, “Real Space Manifestations of Coherent Screening in Atomic Scale Kondo Lattices”, Nat. Commun. **10**, 2211 (2019) (cited on page 34).

[167] M. Bode, A. Kubetzka, S. Heinze, O. Pietzsch, R. Wiesendanger, M. Heide, X. Nie, G. Bihlmayer, and S. Blügel, “Spin Orbit Induced Local Band Structure Variations Revealed by Scanning Tunnelling Spectroscopy”, J. Phys.: Condens. Matter **15**, S679–S692 (2003) (cited on page 35).

[168] J. Friedel, “XIV. The Distribution of Electrons Round Impurities in Monovalent Metals”, The London, Edinburgh, and Dublin Philosophical Magazine and Journal of Science **43**, 153–189 (1952) (cited on page 36).

[169] M. Ternes, “Scanning Tunneling Spectroscopy at the Single Atom Scale”, PhD thesis (École Polytechnique Fédérale de Lausanne, Lausanne, 2006) (cited on pages 36, 104).

[170] J. Cui, J. D. White, and R. D. Diehl, “Anomalous Inelastic He-atom Scattering Intensities for the Vibrational Modes of Alkali Metals on Graphite”, Surface Science Letters **293**, L841–L846 (1993) (cited on page 42).

[171] H. Gawronski, M. Mehlhorn, and K. Morgenstern, “Imaging Phonon Excitation with Atomic Resolution”, Science **319**, 930–933 (2008) (cited on page 42).

[172] E. Minamitani, R. Arafune, N. Tsukahara, Y. Ohda, S. Watanabe, M. Kawai, H. Ueba, and N. Takagi, “Surface Phonon Excitation on Clean Metal Surfaces in Scanning Tunneling Microscopy”, Phys. Rev. B **93**, 085411 (2016) (cited on page 42).

[173] F. M. Leibsle, C. F. J. Flipse, and A. W. Robinson, “Structure of the Cu{100}-*c*(2×2)N Surface: A Scanning-Tunneling-Microscopy Study”, Phys. Rev. B **47**, 15865–15868 (1993) (cited on page 45).

[174] L. Gerhard, T. K. Yamada, T. Balashov, A. F. Takács, R. J. H. Wesselink, M. Däne, M. Fechner, S. Ostanin, A. Ernst, I. Mertig, and W. Wulfhekel, “Magnetoelectric Coupling at Metal Surfaces”, Nat. Nanotech. **5**, 792–797 (2010) (cited on page 46).

[175] S.-H. Phark, J. A. Fischer, M. Corbetta, D. Sander, K. Nakamura, and J. Kirschner, “Reduced-Dimensionality-Induced Helimagnetism in Iron Nanoislands”, Nat. Commun. **5**, 5183 (2014) (cited on page 46).

[176] B. Verlhac, “Atomic-Scale Spin Sensing with a Single Molecule at the Apex of a Scanning Tunneling Microscope”, PhD thesis (Université de Strasbourg, Strasbourg, 2019) (cited on pages 48, 49).

[177] P. Nozières and A. Blandin, “Kondo Effect in Real Metals”, J. Phys. France **41**, 193–211 (1980) (cited on page 52).

[178] P. Schlottmann and P. Sacramento, “Multichannel Kondo Problem and Some Applications”, Advances in Physics **42**, 641–682 (1993) (cited on page 52).

[179] A. Rosch, J. Paaske, J. Kroha, and P. Wölfle, “Nonequilibrium Transport through a Kondo Dot in a Magnetic Field: Perturbation Theory and Poor Man’s Scaling”, Phys. Rev. Lett. **90**, 076804 (2003) (cited on page 52).

[180] L. Schneider, M. Steinbrecher, L. Rózsa, J. Bouaziz, K. Palotás, M. dos Santos Dias, S. Lounis, J. Wiebe, and R. Wiesendanger, “Magnetism and In-Gap States of 3d Transition Metal Atoms on Superconducting Re”, npj Quantum Mater. **4**, 42 (2019) (cited on pages 53, 110).

[181] J. A. Stroscio and R. J. Celotta, “Controlling the Dynamics of a Single Atom in Lateral Atom Manipulation”, Science **306**, 242–247 (2004) (cited on page 53).

[182] G. Schütz, W. Wagner, W. Wilhelm, P. Kienle, R. Zeller, R. Frahm, and G. Materlik, "Absorption of Circularly Polarized x Rays in Iron", Phys. Rev. Lett. **58**, 737–740 (1987) (cited on page 54).

[183] J. Stöhr and H. C. Siegmann, *Magnetism: From Fundamentals to Nanoscale Dynamics*, Springer Series in Solid-State Sciences 152 (Springer, Berlin ; New York, 2006) (cited on page 54).

[184] J. Kügel, M. Leisegang, M. Böhme, A. Krönlein, A. Sixta, and M. Bode, "Remote Single-Molecule Switching: Identification and Nanoengineering of Hot Electron-Induced Tautomerization", Nano Lett. **17**, 5106–5112 (2017) (cited on page 54).

[185] M. Leisegang, "Eine neue Methode zur Detektion ballistischen Transports im Rastertunnelmikroskop: Die Molekulare Nanosonde", PhD thesis (Universität Würzburg, Würzburg, 2021) (cited on page 54).

[186] F. Ladstädter, U. Hohenester, P. Puschnig, and C. Ambrosch-Draxl, "First-Principles Calculation of Hot-Electron Scattering in Metals", Phys. Rev. B **70**, 235125 (2004) (cited on page 54).

[187] H. Kamerlingh Onnes, "Further Experiments with Liquid Helium", Leiden Comm. **120b, 122 b, 124c** (1911) (cited on page 57).

[188] W. Meissner and R. Ochsenfeld, "Ein neuer Effekt bei Eintritt der Supraleitfähigkeit", Naturwissenschaften **21**, 787–788 (1933) (cited on page 57).

[189] F. London and H. London, "The Electromagnetic Equations of the Supraconductor", Proc. R. Soc. Lond. A **149**, 71–88 (1935) (cited on page 57).

[190] M. Tinkham, *Introduction to Superconductivity*, 2nd ed, International Series in Pure and Applied Physics (McGraw Hill, New York, 1996) (cited on pages 58, 63, 65–67, 89).

[191] S. Hunklinger, *Festkörperphysik* (Oldenbourg, München, 2011) (cited on pages 58, 60).

[192] H. Ibach and H. Lüth, *Festkörperphysik: Einführung in die Grundlagen*, Springer-Lehrbuch (Springer, Berlin, 2009) (cited on page 58).

[193] J. Bardeen, L. N. Cooper, and J. R. Schrieffer, "Theory of Superconductivity", Phys. Rev. **108**, 1175–1204 (1957) (cited on page 58).

[194] L. N. Cooper, "Bound Electron Pairs in a Degenerate Fermi Gas", Phys. Rev. **104**, 1189–1190 (1956) (cited on page 58).

[195] E. Maxwell, "Isotope Effect in the Superconductivity of Mercury", Phys. Rev. **78**, 477–477 (1950) (cited on page 58).

[196] C. A. Reynolds, B. Serin, W. H. Wright, and L. B. Nesbitt, "Superconductivity of Isotopes of Mercury", Phys. Rev. **78**, 487–487 (1950) (cited on page 58).

[197] H. Fröhlich, “Theory of the Superconducting State. I. The Ground State at the Absolute Zero of Temperature”, Phys. Rev. **79**, 845–856 (1950) (cited on page 58).

[198] D. A. Wollman, D. J. Van Harlingen, W. C. Lee, D. M. Ginsberg, and A. J. Leggett, “Experimental Determination of the Superconducting Pairing State in YBCO from the Phase Coherence of YBCO-Pb Dc SQUIDs”, Phys. Rev. Lett. **71**, 2134–2137 (1993) (cited on page 59).

[199] C. C. Tsuei, J. R. Kirtley, C. C. Chi, L. S. Yu-Jahnes, A. Gupta, T. Shaw, J. Z. Sun, and M. B. Ketchen, “Pairing Symmetry and Flux Quantization in a Tricrystal Superconducting Ring of $YBa_2Cu_3O_{7-\delta}$”, Phys. Rev. Lett. **73**, 593–596 (1994) (cited on page 59).

[200] A. Mathai, Y. Gim, R. C. Black, A. Amar, and F. C. Wellstood, “Experimental Proof of a Time-Reversal-Invariant Order Parameter with a π shift in $YBa_2Cu_3O_{7-\delta}$”, Phys. Rev. Lett. **74**, 4523–4526 (1995) (cited on page 59).

[201] M. Ternes, W.-D. Schneider, J.-C. Cuevas, C. P. Lutz, C. F. Hirjibehedin, and A. J. Heinrich, “Subgap Structure in Asymmetric Superconducting Tunnel Junctions”, Phys. Rev. B **74**, 132501 (2006) (cited on pages 61, 104, 105).

[202] K. J. Franke, G. Schulze, and J. I. Pascual, “Competition of Superconducting Phenomena and Kondo Screening at the Nanoscale”, Science **332**, 940–944 (2011) (cited on pages 62, 72, 104, 108, 111, 113).

[203] R. C. Dynes, V. Narayanamurti, and J. P. Garno, “Direct Measurement of Quasiparticle-Lifetime Broadening in a Strong-Coupled Superconductor”, Phys. Rev. Lett. **41**, 1509–1512 (1978) (cited on page 63).

[204] V. L. Ginzburg and L. D. Landau, “On the Theory of Superconductivity”, Zh. Eksp. Teor. Fiz. **20**, 1064 (1950) (cited on page 63).

[205] L. P. Gor’kov, “Microscopic Derivation of the Ginzburg-Landau Equations in the Theory of Supercondcutivity”, Soviet JETP **9**, 1364 (1959) (cited on page 63).

[206] T. M. Riseman, P. G. Kealey, E. M. Forgan, A. P. Mackenzie, L. M. Galvin, A. W. Tyler, S. L. Lee, C. Ager, D. M. Paul, C. M. Aegerter, R. Cubitt, Z. Q. Mao, T. Akima, and Y. Maeno, “Observation of a Square Flux-Line Lattice in the Unconventional Superconductor Sr_2RuO_4”, Nature **396**, 242–245 (1998) (cited on page 67).

[207] R. Gilardi, J. Mesot, A. Drew, U. Divakar, S. L. Lee, E. M. Forgan, O. Zaharko, K. Conder, V. K. Aswal, C. D. Dewhurst, R. Cubitt, N. Momono, and M. Oda, “Direct Evidence for an Intrinsic Square Vortex Lattice in the Overdoped High-T_c Superconductor $La_{1.83}Sr_{0.17}CuO_{4+\delta}$”, Phys. Rev. Lett. **88**, 217003 (2002) (cited on page 67).

[208] N. Nakai, P. Miranović, M. Ichioka, and K. Machida, "Reentrant Vortex Lattice Transformation in Fourfold Symmetric Superconductors", Phys. Rev. Lett. **89**, 237004 (2002) (cited on page 67).

[209] P.-G. de Gennes, *Superconductivity of Metals and Alloys* (CRC Press, Boca Raton, 2018) (cited on page 68).

[210] J. D. Shore, M. Huang, A. T. Dorsey, and J. P. Sethna, "Density of States in a Vortex Core and the Zero-Bias Tunneling Peak", Phys. Rev. Lett. **62**, 3089–3092 (1989) (cited on pages 68, 69).

[211] D. Rainer, J. A. Sauls, and D. Waxman, "Current Carried by Bound States of a Superconducting Vortex", Phys. Rev. B **54**, 10094–10106 (1996) (cited on page 68).

[212] N. Hayashi, T. Isoshima, M. Ichioka, and K. Machida, "Low-Lying Quasiparticle Excitations around a Vortex Core in Quantum Limit", Phys. Rev. Lett. **80**, 2921–2924 (1998) (cited on pages 68, 69).

[213] C. Caroli, P. De Gennes, and J. Matricon, "Bound Fermion States on a Vortex Line in a Type II Superconductor", Physics Letters **9**, 307–309 (1964) (cited on pages 68, 69).

[214] J. Bardeen, R. Kümmel, A. E. Jacobs, and L. Tewordt, "Structure of Vortex Lines in Pure Superconductors", Phys. Rev. **187**, 556–569 (1969) (cited on page 68).

[215] C. Renner, A. D. Kent, P. Niedermann, Ø. Fischer, and F. Lévy, "Scanning Tunneling Spectroscopy of a Vortex Core from the Clean to the Dirty Limit", Phys. Rev. Lett. **67**, 1650–1652 (1991) (cited on pages 69, 87).

[216] H. F. Hess, R. B. Robinson, R. C. Dynes, J. M. Valles, and J. V. Waszczak, "Scanning-Tunneling-Microscope Observation of the Abrikosov Flux Lattice and the Density of States near and inside a Fluxoid", Phys. Rev. Lett. **62**, 214–216 (1989) (cited on pages 69, 87).

[217] C. Chen, Q. Liu, W.-C. Bao, Y. Yan, Q.-H. Wang, T. Zhang, and D. Feng, "Observation of Discrete Conventional Caroli–de Gennes–Matricon States in the Vortex Core of Single-Layer FeSe/SrTiO$_3$", Phys. Rev. Lett. **124**, 097001 (2020) (cited on page 69).

[218] F. Gygi and M. Schluter, "Electronic Tunneling into an Isolated Vortex in a Clean Type-II Superconductor", Phys. Rev. B **41**, 822–825 (1990) (cited on pages 69, 96).

[219] B. W. Heinrich, J. I. Pascual, and K. J. Franke, "Single Magnetic Adsorbates on s-Wave Superconductors", Progress in Surface Science **93**, 1–19 (2018) (cited on pages 70–72).

[220] M. E. Flatté and J. M. Byers, "Local Electronic Structure of a Single Magnetic Impurity in a Superconductor", Phys. Rev. Lett. **78**, 3761–3764 (1997) (cited on pages 71, 72).

[221] M. E. Flatté and J. M. Byers, "Local Electronic Structure of Defects in Superconductors", Phys. Rev. B **56**, 11213–11231 (1997) (cited on pages 71, 72).

[222] M. I. Salkola, A. V. Balatsky, and J. R. Schrieffer, "Spectral Properties of Quasiparticle Excitations Induced by Magnetic Moments in Superconductors", Phys. Rev. B **55**, 12648–12661 (1997) (cited on pages 71, 72).

[223] L. Farinacci, "Tuning the Interactions of Magnetic Molecules on a Superconductor", PhD thesis (Freie Universität Berlin, Berlin, 2019) (cited on page 71).

[224] F. von Oppen, Y. Peng, and F. Pientka, "Topological Superconducting Phases in One Dimension", in *Topological Aspects of Condensed Matter Physics*, edited by C. Chamon, M. O. Goerbig, R. Moessner, and L. F. Cugliandolo (Oxford University Press, 2017), pp. 387–450 (cited on pages 72, 75, 76, 78, 79).

[225] J. Bauer, J. I. Pascual, and K. J. Franke, "Microscopic Resolution of the Interplay of Kondo Screening and Superconducting Pairing: Mn-phthalocyanine Molecules Adsorbed on Superconducting Pb(111)", Phys. Rev. B **87**, 075125 (2013) (cited on pages 72, 111).

[226] N. Hatter, B. W. Heinrich, M. Ruby, J. I. Pascual, and K. J. Franke, "Magnetic Anisotropy in Shiba Bound States across a Quantum Phase Transition", Nat. Commun. **6**, 8988 (2015) (cited on pages 72, 108, 113).

[227] L. Malavolti, M. Briganti, M. Hänze, G. Serrano, I. Cimatti, G. McMurtrie, E. Otero, P. Ohresser, F. Totti, M. Mannini, R. Sessoli, and S. Loth, "Tunable Spin-Superconductor Coupling of Spin 1/2 Vanadyl Phthalocyanine Molecules", Nano Lett. **18**, 7955–7961 (2018) (cited on pages 72, 108, 113).

[228] L. Farinacci, G. Ahmadi, G. Reecht, M. Ruby, N. Bogdanoff, O. Peters, B. W. Heinrich, F. von Oppen, and K. J. Franke, "Tuning the Coupling of an Individual Magnetic Impurity to a Superconductor: Quantum Phase Transition and Transport", Phys. Rev. Lett. **121**, 196803 (2018) (cited on pages 72, 108, 113).

[229] H. Huang, R. Drost, J. Senkpiel, C. Padurariu, B. Kubala, A. L. Yeyati, J. C. Cuevas, J. Ankerhold, K. Kern, and C. R. Ast, "Quantum Phase Transitions and the Role of Impurity-Substrate Hybridization in Yu-Shiba-Rusinov States", Commun. Phys. **3**, 199 (2020) (cited on pages 72, 108, 113).

[230] L. Cornils, A. Kamlapure, L. Zhou, S. Pradhan, A. A. Khajetoorians, J. Fransson, J. Wiebe, and R. Wiesendanger, "Spin-Resolved Spectroscopy of the Yu-Shiba-Rusinov States of Individual Atoms", Phys. Rev. Lett. **119**, 197002 (2017) (cited on page 72).

[231] L. Schneider, P. Beck, J. Wiebe, and R. Wiesendanger, "Atomic-Scale Spin-Polarization Maps Using Functionalized Superconducting Probes", Sci. Adv. **7**, eabd7302 (2021) (cited on pages 72, 74).

[232] S. Jeon, Y. Xie, J. Li, Z. Wang, B. A. Bernevig, and A. Yazdani, "Distinguishing a Majorana Zero Mode Using Spin-Resolved Measurements", Science **358**, 772–776 (2017) (cited on pages 72, 79).

[233] T. Matsuura, "The Effects of Impurities on Superconductors with Kondo Effect", Progress of Theoretical Physics **57**, 1823–1835 (1977) (cited on page 72).

[234] N. Hatter, B. W. Heinrich, D. Rolf, and K. J. Franke, "Scaling of Yu-Shiba-Rusinov Energies in the Weak-Coupling Kondo Regime", Nat. Commun. **8**, 1–7 (2017) (cited on pages 72, 111, 113).

[235] L. Farinacci, G. Ahmadi, M. Ruby, G. Reecht, B. W. Heinrich, C. Czekelius, F. von Oppen, and K. J. Franke, "Interfering Tunneling Paths through Magnetic Molecules on Superconductors: Asymmetries of Kondo and Yu-Shiba-Rusinov Resonances", Phys. Rev. Lett. **125**, 256805 (2020) (cited on pages 72, 112).

[236] F. von Oppen and K. J. Franke, "Yu-Shiba-Rusinov States in Real Metals", Phys. Rev. B **103**, 205424 (2021) (cited on pages 72, 73).

[237] G. C. Ménard, S. Guissart, C. Brun, S. Pons, V. S. Stolyarov, F. Debontridder, M. V. Leclerc, E. Janod, L. Cario, D. Roditchev, P. Simon, and T. Cren, "Coherent Long-Range Magnetic Bound States in a Superconductor", Nat. Phys. **11**, 1013–1016 (2015) (cited on pages 72, 73, 135).

[238] M. Ruby, Y. Peng, F. von Oppen, B. W. Heinrich, and K. J. Franke, "Orbital Picture of Yu-Shiba-Rusinov Multiplets", Phys. Rev. Lett. **117**, 186801 (2016) (cited on pages 72, 73, 110).

[239] E. Liebhaber, S. Acero González, R. Baba, G. Reecht, B. W. Heinrich, S. Rohlf, K. Rossnagel, F. von Oppen, and K. J. Franke, "Yu-Shiba-Rusinov States in the Charge-Density Modulated Superconductor $NbSe_2$", Nano Lett. **20**, 339–344 (2020) (cited on page 73).

[240] H. Kim, L. Rózsa, D. Schreyer, E. Simon, and R. Wiesendanger, "Long-Range Focusing of Magnetic Bound States in Superconducting Lanthanum", Nat. Commun. **11**, 4573 (2020) (cited on page 73).

[241] R. Žitko, O. Bodensiek, and T. Pruschke, “Effects of Magnetic Anisotropy on the Subgap Excitations Induced by Quantum Impurities in a Superconducting Host”, Phys. Rev. B **83**, 054512 (2011) (cited on pages 73, 110, 111).

[242] D.-J. Choi, C. Rubio-Verdú, J. de Bruijckere, M. M. Ugeda, N. Lorente, and J. I. Pascual, “Mapping the Orbital Structure of Impurity Bound States in a Superconductor”, Nat. Commun. **8**, 15175 (2017) (cited on pages 73, 105, 110).

[243] F. Küster, A. M. Montero, F. S. M. Guimarães, S. Brinker, S. Lounis, S. S. P. Parkin, and P. Sessi, “Correlating Josephson Supercurrents and Shiba States in Quantum Spins Unconventionally Coupled to Superconductors”, Nat. Commun. **12**, 1108 (2021) (cited on pages 73, 79, 102, 110).

[244] P. Beck, L. Schneider, L. Rózsa, K. Palotás, A. Lászlóffy, L. Szunyogh, J. Wiebe, and R. Wiesendanger, “Spin-Orbit Coupling Induced Splitting of Yu-Shiba-Rusinov States in Antiferromagnetic Dimers”, Nat. Commun. **12**, 2040 (2021) (cited on pages 73, 74, 135).

[245] M. E. Flatté and D. E. Reynolds, “Local Spectrum of a Superconductor as a Probe of Interactions between Magnetic Impurities”, Phys. Rev. B **61**, 14810–14814 (2000) (cited on page 74).

[246] D. K. Morr and N. A. Stavropoulos, “Quantum interference between impurities: Creating novel many-body states in s-wave superconductors”, Phys. Rev. B **67**, 020502 (2003) (cited on pages 74, 128).

[247] D. K. Morr and J. Yoon, “Impurities, Quantum Interference, and Quantum Phase Transitions in s -Wave Superconductors”, Phys. Rev. B **73**, 224511 (2006) (cited on pages 74, 127, 147).

[248] S.-H. Ji, T. Zhang, Y.-S. Fu, X. Chen, X.-C. Ma, J. Li, W.-H. Duan, J.-F. Jia, and Q.-K. Xue, “High-Resolution Scanning Tunneling Spectroscopy of Magnetic Impurity Induced Bound States in the Superconducting Gap of Pb Thin Films”, Phys. Rev. Lett. **100**, 226801 (2008) (cited on pages 74, 113).

[249] D.-J. Choi, C. G. Fernández, E. Herrera, C. Rubio-Verdú, M. M. Ugeda, I. Guillamón, H. Suderow, J. I. Pascual, and N. Lorente, “Influence of Magnetic Ordering between Cr Adatoms on the Yu-Shiba-Rusinov States of the $\beta-\mathrm{Bi_2Pd}$ Superconductor”, Phys. Rev. Lett. **120**, 167001 (2018) (cited on pages 74, 113).

[250] M. Ruby, B. W. Heinrich, Y. Peng, F. von Oppen, and K. J. Franke, “Wave-Function Hybridization in Yu-Shiba-Rusinov Dimers”, Phys. Rev. Lett. **120**, 156803 (2018) (cited on pages 74, 113, 130, 148, 150).

[251] S. Kezilebieke, M. Dvorak, T. Ojanen, and P. Liljeroth, "Coupled Yu-Shiba-Rusinov States in Molecular Dimers on $NbSe_2$", Nano Lett. **18**, 2311–2315 (2018) (cited on pages 74, 113).

[252] N. Y. Yao, C. P. Moca, I. Weymann, J. D. Sau, M. D. Lukin, E. A. Demler, and G. Zaránd, "Phase Diagram and Excitations of a Shiba Molecule", Phys. Rev. B **90**, 241108 (2014) (cited on page 74).

[253] T. Meng, J. Klinovaja, S. Hoffman, P. Simon, and D. Loss, "Superconducting Gap Renormalization around Two Magnetic Impurities: From Shiba to Andreev Bound States", Phys. Rev. B **92**, 064503 (2015) (cited on page 74).

[254] F. Küster, S. Brinker, S. Lounis, S. S. P. Parkin, and P. Sessi, "Long Range and Highly Tunable Interaction between Local Spins Coupled to a Superconducting Condensate", Nat. Commun. **12**, 6722 (2021) (cited on pages 74, 123, 124, 135).

[255] E. Liebhaber, L. M. Rütten, G. Reecht, J. F. Steiner, S. Rohlf, K. Rossnagel, F. von Oppen, and K. J. Franke, "Quantum Spins and Hybridization in Artificially-Constructed Chains of Magnetic Adatoms on a Superconductor", Nat. Commun. **13**, 2160 (2022) (cited on page 74).

[256] M. F. Crommie, C. P. Lutz, and D. M. Eigler, "Imaging Standing Waves in a Two-Dimensional Electron Gas", Nature **363**, 524–527 (1993) (cited on page 74).

[257] F. Wilczek, "Majorana Returns", Nat. Phys. **5**, 614–618 (2009) (cited on page 75).

[258] E. Majorana and G. F. Bassani, *Ettore Majorana, Scientific Papers: On Occasion of the Centenary of His Birth* (Springer, Berlin ; New York, 2006) (cited on page 75).

[259] R. Mohapatra and A. Smirnov, "Neutrino Mass and New Physics", Annu. Rev. Nucl. Part. Sci. **56**, 569–628 (2006) (cited on page 75).

[260] S. R. Elliott and M. Franz, "*Colloquium* : majorana fermions in nuclear, particle, and solid-state physics", Rev. Mod. Phys. **87**, 137–163 (2015) (cited on pages 75, 76).

[261] F. Vissani, S. Dell'Oro, and S. Marcocci, "Testing Creation of Matter with Neutrinoless Double Beta Decay", in Proceedings of XVII International Workshop on Neutrino Telescopes — PoS(NEUTEL2017) (Mar. 2018), p. 030 (cited on page 75).

[262] M. Agostini et al. (GERDA Collaboration), "Probing Majorana Neutrinos with Double-β Decay", Science **365**, 1445–1448 (2019) (cited on page 75).

[263] X.-L. Qi and S.-C. Zhang, "Topological Insulators and Superconductors", Rev. Mod. Phys. **83**, 1057–1110 (2011) (cited on page 75).

[264] J. Alicea, "New Directions in the Pursuit of Majorana Fermions in Solid State Systems", Rep. Prog. Phys. **75**, 076501 (2012) (cited on pages 75, 79).

[265] M. Sato and Y. Ando, "Topological Superconductors: A Review", Rep. Prog. Phys. **80**, 076501 (2017) (cited on page 75).

[266] M. Leijnse and K. Flensberg, "Introduction to Topological Superconductivity and Majorana Fermions", Semicond. Sci. Technol. **27**, 124003 (2012) (cited on pages 76, 78).

[267] M. Z. Hasan and C. L. Kane, "*Colloquium*: topological insulators", Rev. Mod. Phys. **82**, 3045–3067 (2010) (cited on page 77).

[268] N. Read and D. Green, "Paired States of Fermions in Two Dimensions with Breaking of Parity and Time-Reversal Symmetries and the Fractional Quantum Hall Effect", Phys. Rev. B **61**, 10267–10297 (2000) (cited on pages 77, 79).

[269] D. A. Ivanov, "Non-Abelian Statistics of Half-Quantum Vortices in p-Wave Superconductors", Phys. Rev. Lett. **86**, 268–271 (2001) (cited on pages 77, 79).

[270] Y. Maeno, S. Kittaka, T. Nomura, S. Yonezawa, and K. Ishida, "Evaluation of Spin-Triplet Superconductivity in Sr_2RuO_4", J. Phys. Soc. Jpn. **81**, 011009 (2012) (cited on pages 77, 79).

[271] R. M. Lutchyn, J. D. Sau, and S. Das Sarma, "Majorana Fermions and a Topological Phase Transition in Semiconductor-Superconductor Heterostructures", Phys. Rev. Lett. **105**, 077001 (2010) (cited on pages 77, 78).

[272] Y. Oreg, G. Refael, and F. von Oppen, "Helical Liquids and Majorana Bound States in Quantum Wires", Phys. Rev. Lett. **105**, 177002 (2010) (cited on pages 77, 78).

[273] L. Fu and C. L. Kane, "Superconducting Proximity Effect and Majorana Fermions at the Surface of a Topological Insulator", Phys. Rev. Lett. **100**, 096407 (2008) (cited on pages 77, 79).

[274] J. Röntynen and T. Ojanen, "Topological Superconductivity and High Chern Numbers in 2D Ferromagnetic Shiba Lattices", Phys. Rev. Lett. **114**, 236803 (2015) (cited on pages 77, 131, 135).

[275] J. Li, T. Neupert, Z. Wang, A. H. MacDonald, A. Yazdani, and B. A. Bernevig, "Two-Dimensional Chiral Topological Superconductivity in Shiba Lattices", Nat. Commun. **7**, 12297 (2016) (cited on page 77).

[276] L. Schneider, P. Beck, T. Posske, D. Crawford, E. Mascot, S. Rachel, R. Wiesendanger, and J. Wiebe, "Topological Shiba Bands in Artificial Spin Chains on Superconductors", Nat. Phys. **17**, 943–948 (2021) (cited on pages 78, 79, 115, 131, 135).

[277] R. M. Lutchyn, E. P. A. M. Bakkers, L. P. Kouwenhoven, P. Krogstrup, C. M. Marcus, and Y. Oreg, “Majorana Zero Modes in Superconductor-Semiconductor Heterostructures”, Nat. Rev. Mater. **3**, 52–68 (2018) (cited on page 78).

[278] A. Das, Y. Ronen, Y. Most, Y. Oreg, M. Heiblum, and H. Shtrikman, “Zero-Bias Peaks and Splitting in an Al-InAs Nanowire Topological Superconductor as a Signature of Majorana Fermions”, Nat. Phys. **8**, 887–895 (2012) (cited on page 78).

[279] V. Mourik, K. Zuo, S. M. Frolov, S. R. Plissard, E. P. A. M. Bakkers, and L. P. Kouwenhoven, “Signatures of Majorana Fermions in Hybrid Superconductor-Semiconductor Nanowire Devices”, Science **336**, 1003–1007 (2012) (cited on page 78).

[280] M. T. Deng, S. Vaitiekėnas, E. B. Hansen, J. Danon, M. Leijnse, K. Flensberg, J. Nygård, P. Krogstrup, and C. M. Marcus, “Majorana Bound State in a Coupled Quantum-Dot Hybrid-Nanowire System”, Science **354**, 1557–1562 (2016) (cited on page 78).

[281] B. Jäck, Y. Xie, and A. Yazdani, “Detecting and Distinguishing Majorana Zero Modes with the Scanning Tunnelling Microscope”, Nat. Rev. Phys. **3**, 541–554 (2021) (cited on page 78).

[282] B. E. Feldman, M. T. Randeria, J. Li, S. Jeon, Y. Xie, Z. Wang, I. K. Drozdov, B. Andrei Bernevig, and A. Yazdani, “High-Resolution Studies of the Majorana Atomic Chain Platform”, Nat. Phys. **13**, 286–291 (2017) (cited on page 79).

[283] M. Ruby, B. W. Heinrich, Y. Peng, F. von Oppen, and K. J. Franke, “Exploring a Proximity-Coupled Co Chain on Pb(110) as a Possible Majorana Platform”, Nano Lett. **17**, 4473–4477 (2017) (cited on page 79).

[284] L. Schneider, S. Brinker, M. Steinbrecher, J. Hermenau, T. Posske, M. dos Santos Dias, S. Lounis, R. Wiesendanger, and J. Wiebe, “Controlling In-Gap End States by Linking Nonmagnetic Atoms and Artificially-Constructed Spin Chains on Superconductors”, Nat. Commun. **11**, 4707 (2020) (cited on page 79).

[285] A. Kamlapure, L. Cornils, J. Wiebe, and R. Wiesendanger, “Engineering the Spin Couplings in Atomically Crafted Spin Chains on an Elemental Superconductor”, Nat. Commun. **9**, 3253 (2018) (cited on page 79).

[286] J.-P. Xu, M.-X. Wang, Z. L. Liu, J.-F. Ge, X. Yang, C. Liu, Z. A. Xu, D. Guan, C. L. Gao, D. Qian, Y. Liu, Q.-H. Wang, F.-C. Zhang, Q.-K. Xue, and J.-F. Jia, “Experimental Detection of a Majorana Mode in the Core of a Magnetic Vortex inside a Topological Insulator-Superconductor $Bi_2Te_3/NbSe_2$ Heterostructure”, Phys. Rev. Lett. **114**, 017001 (2015) (cited on pages 79, 87, 99).

[287] H.-H. Sun, K.-W. Zhang, L.-H. Hu, C. Li, G.-Y. Wang, H.-Y. Ma, Z.-A. Xu, C.-L. Gao, D.-D. Guan, Y.-Y. Li, C. Liu, D. Qian, Y. Zhou, L. Fu, S.-C. Li, F.-C. Zhang, and J.-F. Jia, “Majorana Zero Mode Detected with Spin Selective Andreev Reflection in the Vortex of a Topological Superconductor”, Phys. Rev. Lett. **116**, 257003 (2016) (cited on page 79).

[288] D. Wang, L. Kong, P. Fan, H. Chen, S. Zhu, W. Liu, L. Cao, Y. Sun, S. Du, J. Schneeloch, R. Zhong, G. Gu, L. Fu, H. Ding, and H.-J. Gao, “Evidence for Majorana Bound States in an Iron-Based Superconductor”, Science **362**, 333–335 (2018) (cited on pages 79, 87).

[289] T. Machida, Y. Sun, S. Pyon, S. Takeda, Y. Kohsaka, T. Hanaguri, T. Sasagawa, and T. Tamegai, “Zero-Energy Vortex Bound State in the Superconducting Topological Surface State of Fe(Se,Te)”, Nat. Mater. **18**, 811–815 (2019) (cited on pages 79, 87).

[290] Q. Liu, C. Chen, T. Zhang, R. Peng, Y.-J. Yan, C.-H.-P. Wen, X. Lou, Y.-L. Huang, J.-P. Tian, X.-L. Dong, G.-W. Wang, W.-C. Bao, Q.-H. Wang, Z.-P. Yin, Z.-X. Zhao, and D.-L. Feng, “Robust and Clean Majorana Zero Mode in the Vortex Core of High-Temperature Superconductor $(\mathrm{Li}_{0.84}\mathrm{Fe}_{0.16})$OHFeSe”, Phys. Rev. X **8**, 041056 (2018) (cited on pages 79, 87).

[291] Y. S. Hor, A. J. Williams, J. G. Checkelsky, P. Roushan, J. Seo, Q. Xu, H. W. Zandbergen, A. Yazdani, N. P. Ong, and R. J. Cava, “Superconductivity in $\mathrm{Cu}_x\mathrm{Bi}_2\mathrm{Se}_3$ and its Implications for Pairing in the Undoped Topological Insulator”, Phys. Rev. Lett. **104**, 057001 (2010) (cited on page 79).

[292] L. Fu and E. Berg, “Odd-Parity Topological Superconductors: Theory and Application to $\mathrm{Cu}_x\mathrm{Bi}_2\mathrm{Se}_3$”, Phys. Rev. Lett. **105**, 097001 (2010) (cited on page 79).

[293] S. Wilfert, P. Sessi, Z. Wang, H. Schmidt, M. C. Martínez-Velarte, S. H. Lee, Y. S. Hor, A. F. Otte, Y. Ando, W. Wu, and M. Bode, “Scanning Tunneling Spectroscopy Investigations of Superconducting-Doped Topological Insulators: Experimental Pitfalls and Results”, Phys. Rev. B **98**, 085133 (2018) (cited on page 79).

[294] B. Jäck, Y. Xie, J. Li, S. Jeon, B. A. Bernevig, and A. Yazdani, “Observation of a Majorana Zero Mode in a Topologically Protected Edge Channel”, Science **364**, 1255–1259 (2019) (cited on page 79).

[295] G. C. Ménard, S. Guissart, C. Brun, R. T. Leriche, M. Trif, F. Debontridder, D. Demaille, D. Roditchev, P. Simon, and T. Cren, “Two-Dimensional Topological Superconductivity in Pb/Co/Si(111)”, Nat. Commun. **8**, 2040 (2017) (cited on page 79).

[296] G. Ménard, A. Mesaros, C. Brun, F. Debontridder, D. Roditchev, P. Simon, and T. Cren, "Isolated Pairs of Majorana Zero Modes in a Disordered Superconducting Lead Monolayer", Nat. Commun. **10**, 2587 (2019) (cited on page 79).

[297] A. Palacio-Morales, E. Mascot, S. Cocklin, H. Kim, S. Rachel, D. K. Morr, and R. Wiesendanger, "Atomic-Scale Interface Engineering of Majorana Edge Modes in a 2D Magnet-Superconductor Hybrid System", Sci. Adv. **5**, eaav6600 (2019) (cited on page 79).

[298] S. Kezilebieke, M. N. Huda, V. Vaňo, M. Aapro, S. C. Ganguli, O. J. Silveira, S. Głodzik, A. S. Foster, T. Ojanen, and P. Liljeroth, "Topological Superconductivity in a van Der Waals Heterostructure", Nature **588**, 424–428 (2020) (cited on page 79).

[299] J. Bedow, E. Mascot, T. Posske, G. S. Uhrig, R. Wiesendanger, S. Rachel, and D. K. Morr, "Topological Superconductivity Induced by a Triple-**q** Magnetic Structure", Phys. Rev. B **102**, 180504 (2020) (cited on page 79).

[300] N. B. Kopnin and M. M. Salomaa, "Mutual Friction in Superfluid He3: Effects of Bound States in the Vortex Core", Phys. Rev. B **44**, 9667–9677 (1991) (cited on page 79).

[301] G. E. Volovik, "Fermion Zero Modes on Vortices in Chiral Superconductors", Soviet JETP Lett. **70**, 609–614 (1999) (cited on page 79).

[302] V. Gurarie, L. Radzihovsky, and A. V. Andreev, "Quantum Phase Transitions across a P-Wave Feshbach Resonance", Phys. Rev. Lett. **94**, 230403 (2005) (cited on page 79).

[303] S. Tewari, S. Das Sarma, C. Nayak, C. Zhang, and P. Zoller, "Quantum Computation using Vortices and Majorana Zero Modes of a $p_x + ip_y$ Superfluid of Fermionic Cold Atoms", Phys. Rev. Lett. **98**, 010506 (2007) (cited on page 79).

[304] S. Das Sarma, C. Nayak, and S. Tewari, "Proposal to stabilize and detect half-quantum vortices in strontium ruthenate thin films: Non-Abelian braiding statistics of vortices in a $p_x + ip_y$ superconductor", Phys. Rev. B **73**, 220502 (2006) (cited on page 79).

[305] G. Moore and N. Read, "Nonabelions in the Fractional Quantum Hall Effect", Nuclear Physics B **360**, 362–396 (1991) (cited on page 79).

[306] P. Townsend and J. Sutton, "Investigation by Electron Tunneling of the Superconducting Energy Gaps in Nb, Ta, Sn, and Pb", Phys. Rev. **128**, 591–595 (1962) (cited on page 81).

[307] T. McConville and B. Serin, "Specific Heat of Type II Superconductors in a Magnetic Field", Phys. Rev. Lett. **13**, 365–367 (1964) (cited on page 81).

[308] B. W. Maxfield and W. L. McLean, "Superconducting Penetration Depth of Niobium", Phys. Rev. **139**, A1515–A1522 (1965) (cited on page 81).

[309] D. K. Finnemore, T. F. Stromberg, and C. A. Swenson, "Superconducting Properties of High-Purity Niobium", Phys. Rev. **149**, 231–243 (1966) (cited on page 81).

[310] A. B. Odobesko, S. Haldar, S. Wilfert, J. Hagen, J. Jung, N. Schmidt, P. Sessi, M. Vogt, S. Heinze, and M. Bode, "Preparation and Electronic Properties of Clean Superconducting Nb(110) Surfaces", Phys. Rev. B **99**, 115437 (2019) (cited on pages 81, 83–85).

[311] J. Hagen, "Präparation und Charakterisierung von Nb(110)-Oberflächen", Bachelor's Thesis (Universität Würzburg, Würzburg, 2017) (cited on page 81).

[312] T. Haas, "A Study of the Niobium (110) Surface Using Low Energy Electron Diffraction Techniques", Surface Science **5**, 345–358 (1966) (cited on page 81).

[313] T. W. Haas, A. G. Jackson, and M. P. Hooker, "Adsorption on Niobium (110), Tantalum (110), and Vanadium (110) Surfaces", The Journal of Chemical Physics **46**, 3025–3033 (1967) (cited on pages 81, 116, 143).

[314] C. Sürgers, M. Schöck, and H. v. Löhneysen, "Oxygen-Induced Surface Structure of Nb(110)", Surface Science **471**, 209–218 (2001) (cited on pages 81, 82).

[315] A. S. Razinkin and M. V. Kuznetsov, "Scanning Tunneling Microscopy (STM) of Low-Dimensional NbO Structures on the Nb(110) Surface", Phys. Metals Metallogr. **110**, 531–541 (2010) (cited on pages 81, 82).

[316] A. Odobesko, F. Friedrich, S.-B. Zhang, S. Haldar, S. Heinze, B. Trauzettel, and M. Bode, "Anisotropic Vortices on Superconducting Nb(110)", Phys. Rev. B **102**, 174502 (2020) (cited on pages 84, 87, 90, 94, 97, 98).

[317] G. Kresse and J. Furthmüller, "Efficient Iterative Schemes for *Ab Initio* Total-Energy Calculations Using a Plane-Wave Basis Set", Phys. Rev. B **54**, 11169–11186 (1996) (cited on pages 84, 102).

[318] see: `https://vasp.at/` (cited on page 84).

[319] P. E. Blöchl, "Projector Augmented-Wave Method", Phys. Rev. B **50**, 17953–17979 (1994) (cited on page 84).

[320] G. Kresse and D. Joubert, "From Ultrasoft Pseudopotentials to the Projector Augmented-Wave Method", Phys. Rev. B **59**, 1758–1775 (1999) (cited on page 84).

[321] H. Träuble and U. Essmann, "Ein hochauflösendes Verfahren zur Untersuchung magnetischer Strukturen von Supraleitern", phys. stat. sol. (b) **18**, 813–828 (1966) (cited on page 87).

[322] N. Hayashi, M. Ichioka, and K. Machida, "Star-Shaped Local Density of States around Vortices in a Type-II Superconductor", Phys. Rev. Lett. **77**, 4074–4077 (1996) (cited on pages 87, 96).

[323] C.-L. Song, Y.-L. Wang, P. Cheng, Y.-P. Jiang, W. Li, T. Zhang, Z. Li, K. He, L. Wang, J.-F. Jia, H.-H. Hung, C. Wu, X. Ma, X. Chen, and Q.-K. Xue, "Direct Observation of Nodes and Twofold Symmetry in FeSe Superconductor", Science **332**, 1410–1413 (2011) (cited on pages 87, 99).

[324] Z. Du, D. Fang, Z. Wang, Y. Li, G. Du, H. Yang, X. Zhu, and H.-H. Wen, "Anisotropic Superconducting Gap and Elongated Vortices with Caroli-De Gennes-Matricon States in the New Superconductor $Ta_4Pd_3Te_{16}$", Scientific Reports **5**, 9408 (2015) (cited on pages 87, 99).

[325] H. Kim, Y. Nagai, L. Rózsa, D. Schreyer, and R. Wiesendanger, "Anisotropic Non-Split Zero-Energy Vortex Bound States in a Conventional Superconductor", Applied Physics Reviews **8**, 031417 (2021) (cited on pages 87, 99).

[326] Y. Yuan, J. Pan, X. Wang, Y. Fang, C. Song, L. Wang, K. He, X. Ma, H. Zhang, F. Huang, W. Li, and Q.-K. Xue, "Evidence of Anisotropic Majorana Bound States in $2M-WS_2$", Nat. Phys. **15**, 1046–1051 (2019) (cited on pages 87, 99).

[327] U. Essmann and H. Träuble, "The Direct Observation of Individual Flux Lines in Type II Superconductors", Physics Letters A **24**, 526–527 (1967) (cited on page 88).

[328] F. Bitter, "On Inhomogeneities in the Magnetization of Ferromagnetic Materials", Phys. Rev. **38**, 1903–1905 (1931) (cited on page 88).

[329] A. F. Mayadas, R. B. Laibowitz, and J. J. Cuomo, "Electrical Characteristics of rf-Sputtered Single-Crystal Niobium Films", Journal of Applied Physics **43**, 1287–1289 (1972) (cited on page 92).

[330] T. W. Haas, "Low-Energy Electron Scattering from Clean and Hydrogen-Covered Nb(110) Surfaces", Journal of Applied Physics **39**, 5854–5858 (1968) (cited on page 94).

[331] F. Gygi and M. Schlüter, "Self-Consistent Electronic Structure of a Vortex Line in a Type-II Superconductor", Phys. Rev. B **43**, 7609–7621 (1991) (cited on page 96).

[332] A. S. Mel'nikov, D. A. Ryzhov, and M. A. Silaev, "Local Density of States around Single Vortices and Vortex Pairs: Effect of Boundaries and Hybridization of Vortex Core States", Phys. Rev. B **79**, 134521 (2009) (cited on page 96).

[333] N. Hayashi, M. Ichioka, and K. Machida, “Effects of Gap Anisotropy upon the Electronic Structure around a Superconducting Vortex”, Phys. Rev. B **56**, 9052–9063 (1997) (cited on page 96).

[334] H. Hess, R. Robinson, and J. Waszczak, “STM Spectroscopy of Vortex Cores and the Flux Lattice”, Physica B: Condensed Matter **169**, 422–431 (1991) (cited on pages 96, 99).

[335] M. L. A. MacVicar and R. M. Rose, “Anisotropic Energy-Gap Measurements on Superconducting Niobium Single Crystals by Tunneling”, Journal of Applied Physics **39**, 1721–1727 (1968) (cited on page 96).

[336] M. L. A. MacVicar, “Distribution of the Energy Gap in k Space for Superconducting Nb”, Phys. Rev. B **2**, 97–100 (1970) (cited on page 96).

[337] S. Heinze, S. Blügel, R. Pascal, M. Bode, and R. Wiesendanger, “Prediction of Bias-Voltage-Dependent Corrugation Reversal for STM Images of Bcc (110) Surfaces: W(110), Ta(110), and Fe(110)”, Phys. Rev. B **58**, 16432–16445 (1998) (cited on page 96).

[338] E. I. Rashba, “Properties of Semiconductors with an Extremum Loop. I. Cyclotron and Combinational Resonance in a Magnetic Field Perpendicular to the Plane of the Loop”, Sov. Phys. Solid State **2**, 1109–1122 (1960) (cited on page 98).

[339] G. Dresselhaus, “Spin-Orbit Coupling Effects in Zinc Blende Structures”, Phys. Rev. **100**, 580–586 (1955) (cited on page 98).

[340] A. Odobesko, D. Di Sante, A. Kowalski, S. Wilfert, F. Friedrich, R. Thomale, G. Sangiovanni, and M. Bode, “Observation of Tunable Single-Atom Yu-Shiba-Rusinov States”, Phys. Rev. B **102**, 174504 (2020) (cited on pages 102, 103, 106, 107, 110, 115, 122).

[341] F. Friedrich, R. Boshuis, M. Bode, and A. Odobesko, “Coupling of Yu-Shiba-Rusinov States in One-Dimensional Chains of Fe Atoms on Nb(110)”, Phys. Rev. B **103**, 235437 (2021) (cited on pages 102, 110, 116, 120, 121, 124, 125, 128, 130, 146).

[342] S. H. Pan, E. W. Hudson, and J. C. Davis, “Vacuum Tunneling of Superconducting Quasiparticles from Atomically Sharp Scanning Tunneling Microscope Tips”, Appl. Phys. Lett. **73**, 2992–2994 (1998) (cited on page 104).

[343] Y. Uehara, T. Fujita, M. Iwami, and S. Ushioda, “Superconducting Niobium Tip for Scanning Tunneling Microscope Light Emission Spectroscopy”, Rev. Sci. Instrum. **72**, 2097–2099 (2001) (cited on page 104).

[344] M. Eltschka, B. Jäck, M. Assig, O. V. Kondrashov, M. A. Skvortsov, M. Etzkorn, C. R. Ast, and K. Kern, "Superconducting Scanning Tunneling Microscopy Tips in a Magnetic Field: Geometry-controlled Order of the Phase Transition", Appl. Phys. Lett. **107**, 122601 (2015) (cited on page 104).

[345] H. Suderow, M. Crespo, P. Martinez-Samper, J. Rodrigo, G. Rubio-Bollinger, S. Vieira, N. Luchier, J. Brison, and P. Canfield, "Scanning tunneling microscopy and spectroscopy at very low temperatures", Physica C: Superconductivity **369**, 106–112 (2002) (cited on page 104).

[346] S. Bose, P. Raychaudhuri, R. Banerjee, P. Vasa, and P. Ayyub, "Mechanism of the Size Dependence of the Superconducting Transition of Nanostructured Nb", Phys. Rev. Lett. **95**, 147003 (2005) (cited on page 104).

[347] S. Bose, A. M. García-García, M. M. Ugeda, J. D. Urbina, C. H. Michaelis, I. Brihuega, and K. Kern, "Observation of Shell Effects in Superconducting Nanoparticles of Sn", Nat. Mater. **9**, 550–554 (2010) (cited on page 104).

[348] R. W. Cohen and B. Abeles, "Superconductivity in Granular Aluminum Films", Phys. Rev. **168**, 444–450 (1968) (cited on page 105).

[349] S. Bose and P. Ayyub, "A Review of Finite Size Effects in Quasi-Zero Dimensional Superconductors", Rep. Prog. Phys. **77**, 116503 (2014) (cited on page 105).

[350] O. Naaman, W. Teizer, and R. C. Dynes, "Fluctuation Dominated Josephson Tunneling with a Scanning Tunneling Microscope", Phys. Rev. Lett. **87**, 097004 (2001) (cited on page 105).

[351] F. Passek and M. Donath, "Magnetic Surface State Becomes Nonmagnetic by Oxygen Adsorption", Phys. Rev. Lett. **71**, 2122–2125 (1993) (cited on page 107).

[352] M. Getzlaff, J. Bansmann, and G. Schönhense, "Oxygen on Fe(110): Magnetic Properties of the Adsorbate System", Journal of Magnetism and Magnetic Materials **192**, 458–466 (1999) (cited on page 107).

[353] M. dos Santos Dias, B. Schweflinghaus, S. Blügel, and S. Lounis, "Relativistic Dynamical Spin Excitations of Magnetic Adatoms", Phys. Rev. B **91**, 075405 (2015) (cited on page 110).

[354] M. Imada, A. Fujimori, and Y. Tokura, "Metal-Insulator Transitions", Rev. Mod. Phys. **70**, 1039–1263 (1998) (cited on page 110).

[355] P. Limelette, A. Georges, D. Jérome, P. Wzietek, P. Metcalf, and J. M. Honig, "Universality and Critical Behavior at the Mott Transition", Science **302**, 89–92 (2003) (cited on page 110).

[356] J. Kügel, M. Karolak, A. Krönlein, D. Serrate, M. Bode, and G. Sangiovanni, "Reversible Magnetic Switching of High-Spin Molecules on a Giant Rashba Surface", npj Quant. Mater. **3**, 53 (2018) (cited on page 110).

[357] K. Satori, H. Shiba, O. Sakai, and Y. Shimizu, "Numerical Renormalization Group Study of Magnetic Impurities in Superconductors", J. Phys. Soc. Jpn. **61**, 3239–3254 (1992) (cited on page 111).

[358] O. Sakai, Y. Shimizu, H. Shiba, and K. Satori, "Numerical Renormalization Group Study of Magnetic Impurities in Superconductors. II. Dynamical Excitation Spectra and Spatial Variation of the Order Parameter", J. Phys. Soc. Jpn. **62**, 3181–3197 (1993) (cited on page 111).

[359] R. Žitko, J. S. Lim, R. López, and R. Aguado, "Shiba States and Zero-Bias Anomalies in the Hybrid Normal-Superconductor Anderson Model", Phys. Rev. B **91**, 045441 (2015) (cited on page 111).

[360] A. Villas, R. L. Klees, H. Huang, C. R. Ast, G. Rastelli, W. Belzig, and J. C. Cuevas, "Interplay between Yu-Shiba-Rusinov States and Multiple Andreev Reflections", Phys. Rev. B **101**, 235445 (2020) (cited on page 111).

[361] S. Kezilebieke, R. Žitko, M. Dvorak, T. Ojanen, and P. Liljeroth, "Observation of Coexistence of Yu-Shiba-Rusinov States and Spin-Flip Excitations", Nano Lett. **19**, 4614–4619 (2019) (cited on page 113).

[362] A. Kamlapure, L. Cornils, R. Žitko, M. Valentyuk, R. Mozara, S. Pradhan, J. Fransson, A. I. Lichtenstein, J. Wiebe, and R. Wiesendanger, "Correlation of Yu-Shiba-Rusinov States and Kondo Resonances in Artificial Spin Arrays on an s-Wave Superconductor", Nano Lett. **21**, 6748–6755 (2021) (cited on page 113).

[363] D. Crawford, E. Mascot, M. Shimizu, L. Schneider, P. Beck, J. Wiebe, R. Wiesendanger, H. O. Jeschke, D. K. Morr, and S. Rachel, "Majorana modes with side features in magnet-superconductor hybrid systems", arXiv:2109.06894 [cond-mat.supr-con] (2021) (cited on pages 113, 115, 122).

[364] A. Kamlapure, L. Cornils, J. Wiebe, and R. Wiesendanger, "Engineering the Spin Couplings in Atomically Crafted Spin Chains on an Elemental Superconductor", Nat. Commun. **9**, 3253 (2018) (cited on page 115).

[365] L. Gross, F. Mohn, N. Moll, P. Liljeroth, and G. Meyer, "The Chemical Structure of a Molecule Resolved by Atomic Force Microscopy", Science **325**, 1110–1114 (2009) (cited on page 116).

[366] L. Gross, F. Mohn, N. Moll, B. Schuler, A. Criado, E. Guitián, D. Peña, A. Gourdon, and G. Meyer, "Bond-Order Discrimination by Atomic Force Microscopy", Science **337**, 1326–1329 (2012) (cited on page 116).

[367] P. Hapala, G. Kichin, C. Wagner, F. S. Tautz, R. Temirov, and P. Jelínek, "Mechanism of High-Resolution STM/AFM Imaging with Functionalized Tips", Phys. Rev. B **90**, 085421 (2014) (cited on page 116).

[368] P. Hapala, R. Temirov, F. S. Tautz, and P. Jelínek, "Origin of High-Resolution IETS-STM Images of Organic Molecules with Functionalized Tips", Phys. Rev. Lett. **113**, 226101 (2014) (cited on page 116).

[369] L. Bartels, G. Meyer, and K.-H. Rieder, "Controlled Vertical Manipulation of Single CO Molecules with the Scanning Tunneling Microscope: A Route to Chemical Contrast", Appl. Phys. Lett. **71**, 213–215 (1997) (cited on pages 116, 119).

[370] L. Bartels, G. Meyer, K.-H. Rieder, D. Velic, E. Knoesel, A. Hotzel, M. Wolf, and G. Ertl, "Dynamics of Electron-Induced Manipulation of Individual CO Molecules on Cu(111)", Phys. Rev. Lett. **80**, 2004–2007 (1998) (cited on pages 116, 118, 119).

[371] G. J. Dooley and T. W. Haas, "Behavior of Refractory Metal Surfaces in Ultrahigh Vacuum as Observed by Low-Energy Electron Diffraction (LEED) and Auger Electron Spectroscopy", J. Vac. Sci. Technol. **7**, S90–S100 (1970) (cited on page 116).

[372] D. A. King and D. P. Woodruff, *The Chemical Physics of Solid Surfaces and Heterogeneous Catalysis* (Elsevier, Amsterdam Oxford New York, 1990) (cited on page 116).

[373] C. J. Hirschmugl, G. P. Williams, F. M. Hoffmann, and Y. J. Chabal, "Adsorbate-Substrate Resonant Interactions Observed for CO on Cu(100) in the Far Infrared", Phys. Rev. Lett. **65**, 480–483 (1990) (cited on page 118).

[374] A. P. Graham, F. Hofmann, J. P. Toennies, G. P. Williams, C. J. Hirschmugl, and J. Ellis, "A High Resolution Helium Atom Scattering and Far Infrared Study of the Dynamics and the Lateral Potential Energy Surface of CO Molecules Chemisorbed on Cu(001)", The Journal of Chemical Physics **108**, 7825–7834 (1998) (cited on page 118).

[375] J. A. Nieminen, E. Niemi, and K.-H. Rieder, "Interference between Competing Tunneling Channels and Chemical Resolution of STM", Surface Science **552**, L47–L52 (2004) (cited on page 119).

[376] D. Kuhness, J. Pal, H. J. Yang, N. Mammen, K. Honkala, H. Häkkinen, W.-D. Schneider, M. Heyde, and H.-J. Freund, "Binding Behavior of Carbonmonoxide to Gold Atoms on Ag(001)", Top. Catal. **63**, 1578–1584 (2020) (cited on page 120).

[377] A. J. Heinrich, C. P. Lutz, J. A. Gupta, and D. M. Eigler, "Molecule Cascades", Science **298**, 1381–1387 (2002) (cited on page 121).

[378] M. Bode, R. Pascal, M. Dreyer, and R. Wiesendanger, "Nanostructural and Local Electronic Properties of Fe/W(110) Correlated by Scanning Tunneling Spectroscopy", Phys. Rev. B **54**, R8385–R8388 (1996) (cited on page 122).

[379] S. Körber, B. Trauzettel, and O. Kashuba, "Collective Yu-Shiba-Rusinov States in Magnetic Clusters at Superconducting Surfaces", Phys. Rev. B **97**, 184503 (2018) (cited on page 131).

[380] D. K. Morr and N. A. Stavropoulos, "Quantum Corrals, Eigenmodes, and Quantum Mirages in s-Wave Superconductors", Phys. Rev. Lett. **92**, 107006 (2004) (cited on pages 132, 135).

[381] N. A. Stavropoulos and D. K. Morr, "Quantum Imaging and Selection Rules in Triangular Quantum Corrals", Phys. Rev. B **71**, 140501 (2005) (cited on page 132).

[382] J. F. Steiner, C. Mora, K. J. Franke, and F. von Oppen, "Quantum Magnetism and Topological Superconductivity in Yu-Shiba-Rusinov Chains", Phys. Rev. Lett. **128**, 036801 (2022) (cited on page 132).

[383] H. Schmid, J. F. Steiner, K. J. Franke, and F. von Oppen, "Quantum Yu-Shiba-Rusinov Dimers", Phys. Rev. B **105**, 235406 (2022) (cited on page 132).

[384] T. Tomanic, C. Sürgers, R. Heid, M. Alcántara Ortigoza, K.-P. Bohnen, D. Stöffler, and H. v. Löhneysen, "Local-Strain Mapping on Ag(111) Islands on Nb(110)", Appl. Phys. Lett. **101**, 063111 (2012) (cited on page 135).

[385] T. Tomanic, M. Schackert, W. Wulfhekel, C. Sürgers, and H. v. Löhneysen, "Two-Band Superconductivity of Bulk and Surface States in Ag Thin Films on Nb", Phys. Rev. B **94**, 220503 (2016) (cited on page 135).

[386] P. Wei, S. Manna, M. Eich, P. Lee, and J. Moodera, "Superconductivity in the Surface State of Noble Metal Gold and Its Fermi Level Tuning by EuS Dielectric", Phys. Rev. Lett. **122**, 247002 (2019) (cited on page 135).

ACKNOWLEDGMENTS

At the end of this thesis, I want to thank all people who supported me during the last years and contributed to the presented work:

First of all, I thank Prof. Dr. Matthias Bode, who gave me the opportunity to work in his group and to discover the world of single atoms. His advice and our many discussions were essential to this thesis. I also want to thank him for giving me the opportunity to present my research on several conferences.

Secondly, I would like to thank Prof. Dr. Friedrich Reinert for agreeing to act as second reviewer of my thesis and for his interest in my work.

I am grateful to Dr. Artem Odobesko, who introduced me to all the tricks in scanning tunneling microscopy, ultra-high vacuum, and sample preparation. I want to thank him for the time we spent in the lab together, for the times he spent in the lab alone, when he agreed to take care of night shifts measuring, and for countless discussions. And most importantly, I thank him for his never-ending optimism: *Everything is going to work, Felix, the only question is when.*

Many thanks go to my office mates Robin Boshuis and Dr. Johannes Jung for many (scientific and non-scientific) conversations and the nice atmosphere. I was lucky to share the 1 K system with Robin and enjoyed working there together.

Dr. Markus Leisegang and Patrick Härtl I thank for many more discussions and their support and ideas concerning all kinds of issues in the lab.

Artem and Patrick are further thanked for proofreading this thesis.

I am thankful that I had the opportunity to supervise the bachelor's thesis of Christian Mayer. I very much enjoyed our joint work.

Without Anita Gebhardt, none of the presented work could have been realized. She takes care of all the small and bigger things outside the lab, making sure I had everything I needed for my work.

I thank Rosmarie Riegel and Hiltrud Eaton for their support with all administrative concerns.

Very importantly, I thank the whole team of the Experimental Physics II for the friendly atmosphere, the many cakes, our barbecues and volleyball matches, and other outside-university activities that I enjoyed a lot.

I am grateful to Prof. Dr. Samir Lounis, who initiated the project of Co atoms on Cu(111) with his work, patiently explained the theory to me several times, and together with Dr. Juba Bouaziz and Dr. Sascha Brinker, provided valuable input for the interpretation of the experimental results.

I further want to thank Prof. Dr. Björn Trauzettel and Dr. Song-Bo Zhang, as well as Prof. Dr. Giorgio Sangiovanni, Dr. Domenico Di Sante, and Alexander Kowalski who provided the theory for the projects of vortices and single Fe atoms on Nb(110).

I would like to thank Philipp Kagerer for his involvement in our ongoing research and for always taking his time when I need something.
Dr. Laëtitia Farinacci I thank for providing valuable advice for the spin-polarized STS measurements.
Sebastian Vettermann kindly allowed me to use his glove box to transfer the nickelocene molecules.
And I thank our workshop, especially Rainer Brauner and Dr. Utz Baß, who helped planning and realized all special parts and devices I needed.

Finally, I am thankful to my family, who provided me with the possibility to pursue my studies and always supported me on the way.
And I thank Jessi, for proofreading this thesis, but more importantly for her support, her encouragement, and her understanding, whenever I was too occupied with my work. I would not have come this far without you.